Synchrotron-based In Situ Electron Spectroscopy Applied to Oxide Formation and Catalysis

Johansson, Niclas

2017

Document Version:
Publisher's PDF, also known as Version of record

Synchrotron-based *In Situ* Electron Spectroscopy Applied to Oxide Formation and Catalysis

NICLAS JOHANSSON
FACULTY OF SCIENCE | LUND UNIVERSITY

Synchrotron-based *In Situ* Electron Spectroscopy Applied to Oxide Formation and Catalysis

Synchrotron-based *In Situ* Electron Spectroscopy Applied to Oxide Formation and Catalysis

by Niclas Johansson

LUND
UNIVERSITY

Thesis for the degree of Doctor of Philosophy
Thesis advisors: Prof. Joachim Schnadt, Dr Jan Knudsen
Faculty opponent: Prof. Wendy Flavell

To be presented, with the permission of the Faculty of Science of Lund University, for public criticism in lecture hall F (K404) at the Department of Physics on Thursday, 9 November 2017 at 13:15.

Organization
LUND UNIVERSITY

Department of Physics
Box 118
SE–221 00 LUND
Sweden

Document name
DOCTORAL DISSERTATION

Date of disputation
2017-11-09

Sponsoring organization

Author(s)
Niclas Johansson

Title and subtitle
Synchrotron-based *In Situ* Electron Spectroscopy Applied to Oxide Formation and Catalysis

Abstract
In this thesis, *in situ* ambient pressure X-ray photoelectron spectroscopy has been used to address chemical reactions on surfaces. The presented work aims at the invesstigation of the relation between pressure and adsorbate surface structures during catalytic reactions. Various materials have been investigated ranging from single crystal surfaces to an immobilized homogeneous catalyst in an effort to apply the surface science methodology to materials which more closely resembles working catalysts.

Adsorbate structures in ultrahigh vacuum conditions have been studied for decades and are well known. However, it is unclear how these structures relate to those in the mbar regime. Here, I investigate this relation by two reactions on single crystals: the oxidation of CO over Ir(111) and the Sonogashira cross-coupling over Au(111). The results show that the adsorbate structure in the two pressure regimes can be related. In fact, knowledge of the ultrahigh vacuum structures is vital for an understanding of the surface structures in the mbar regime.

Ultrathin oxides are often employed as model systems to mimic the support-particle interactions of a working catalyst. One such oxide is the bilayer FeO(111) grown atop a Pt(111) surface. In this thesis, an O-enriched trilayer phase of this film has been investigated and its spectroscopic fingerprint has been characterized unambiguously. It is shown that the trilayer has a high affinity for water dissociation. This concept is expanded upon by the growth of a stepped FeO film which contains FeO-FeO steps. These steps share the O-Fe-O structural motif of the trilayer film and also have an affinity for water splitting. Hence, the introduction of an interfacial O atom heavily modifies the properties of the oxide surface.

Immobilization of homogeneous catalysts has the possibility of combining their high yield and selectivity with the high throughput of heterogeneous catalysis. To this end, a homogeneous catalyst, a Mn(III)-salen complex, was immobilized and characterized on an Au(111) support. The oxidative capabilities of the compound remain after the immobilization even if the liquid environment is exchanged for gas phase reactants.

Key words
CO oxidation, Sonogashira cross-copuling, trilayer FeO, vicinal FeO, Mn(III)-Salen, APXPS, XAS

Classification system and/or index terms (if any)

Supplementary bibliographical information

Language
English

ISSN and key title

ISBN
978-91-7753-437-2 (print)
978-91-7753-438-9 (pdf)

Recipient's notes

Number of pages
216

Price

Security classification

Synchrotron-based *In Situ* Electron Spectroscopy Applied to Oxide Formation and Catalysis

by Niclas Johansson

LUND
UNIVERSITY

Cover illustration front: A picture of a sample transfer to the reaction cell at the APXPS instrument of the SPECIES beamline.

Funding information: The thesis work was financially supported by the natural science faculty at Lund University.

Faculty of Science, Department of Physics

ISBN: 978-91-7753-437-2 (print)
ISBN: 978-91-7753-438-9 (pdf)

Printed in Sweden by Media-Tryck, Lund University, Lund 2017

Pressure will turn you either into dust or a diamond

Abstract

In this thesis, *in situ* ambient pressure X-ray photoelectron spectroscopy has been used to address chemical reactions on surfaces. The presented work aims at the invesstigation of the relation between pressure and adsorbate surface structures during catalytic reactions. Various materials have been investigated ranging from single crystal surfaces to an immobilized homogeneous catalyst in an effort to apply the surface science methodology to materials which more closely resembles working catalysts.

Adsorbate structures in ultrahigh vacuum conditions have been studied for decades and are well known. However, it is unclear how these structures relate to those in the mbar regime. Here, I investigate this relation by two reactions on single crystals: the oxidation of CO over Ir(111) and the Sonogashira cross-coupling over Au(111). The results show that the adsorbate structure in the two pressure regimes can be related. In fact, knowledge of the ultrahigh vacuum structures is vital for an understanding of the surface structures in the mbar regime.

Ultrathin oxides are often employed as model systems to mimic the support-particle interactions of a working catalyst. One such oxide is the bilayer FeO(111) grown atop a Pt(111) surface. In this thesis, an O-enriched trilayer phase of this film has been investigated and its spectroscopic fingerprint has been characterized unambiguously. It is shown that the trilayer has a high affinity for water dissociation. This concept is expanded upon by the growth of a stepped FeO film which contains FeO-FeO steps. These steps share the O-Fe-O structural motif of the trilayer film and also have an affinity for water splitting. Hence, the introduction of an interfacial O atom heavily modifies the properties of the oxide surface.

Immobilization of homogeneous catalysts has the possibility of combining their high yield and selectivity with the high throughput of heterogeneous catalysis. To this end, a homogeneous catalyst, a Mn(III)-salen complex, was immobilized and characterized on an Au(111) support. The oxidative capabilities of the compound remain after the immobilization even if the liquid environment is exchanged for gas phase reactants.

Populärvetenskaplig sammanfattning

Det är svårt att tänka sig dagens samhälle utan katalys då många av de produkter som vi använder dagligen framställs med någon form av katalysator med tillämpningar som sträcker sig från kemikalieproduktion till avgasrening. Den mest kända katalysatorn är nog bilkatalysatorn som används för att omvandla de mest skadliga bilavgaserna till mindre skadliga gaser. En mindre känd katalytisk process som har en mer indirekt påverkan på våra liv är Haber-Bosch-processen. Denna används som ett steg vid framställandet av konstgödsel och har uppskattats vara anledningen till att en världsbefolkning över 3 miljarder är möjlig. Haber-Bosch-processens betydelse påvisar vikten av katalysatorer.

För att en kemisk process ska ske måste en energibarriär övervinnas. Denna barriär kan liknas vid en kulle som måste överskridas där en katalysator är ett ämne som visar en 'genväg' kring kullen. Den nya vägen gör så att reaktioner som vanligtvis sker långsamt fortgår snabbare. Ibland är denna kulle så hög att vissa reaktioner inte kan genomföras utan en katalytisk genväg. Genvägen innebär en lägre energiförbrukning då produktion går fortare och enklare. Katalysatorer medför även färre biprodukter då en mindre mängd kemikalier behövs i den kemiska framställningsprocessen. En lägre energiförbrukning och färre kemikalier är viktigt ekonomiskt, men det är även viktigt för miljön.

Utvecklandet av nya katalysatorer fortgår med den så kallade *trial-and-error*-metoden. Här prövas olika katalysatorer för att se vilken som ger bäst resultat. Denna metodik har visat sig effektiv och har lett till stora framsteg relativt snabbt. Tyvärr visar inte trial-and-error-metoden varför molekylerna använder katalysatorns genväg. Kunskap behövs på en molekylär skala om varför de katalytiska reaktionerna sker för att kunna skräddarsy nya katalysatorer till specifika reaktioner. Det är detta som den ytfysikaliska katalysforskningen ämnar att förstå. Verkliga katalysatorer är väldigt komplicerade och svåra att förstå på en molekylär nivå. Därför använder ytfysikforskare modellsystem som enbart innehåller några av katalysatorns viktigaste beståndsdelar. För att underlätta förståelsen ytterligare brukar dessa förenklade katalysatorer studeras i vakuum. Detta medför att de studerade kemiska reaktionerna sker som de skulle göra långt ute i rymden och därför inte är representativa för hur de sker här på jorden.

I denna avhandling har jag studerat kemiska reaktioner på katalysatormodellsystem vid tryck som närmar sig trycket hos de verkliga katalysatorerna. Jag har utfört dessa undersökningar med hjälp av den nya metoden högtryckröntgenfotoelektronspektroskopi. Denna metod ger möjligheten att undersöka molekylerna

medan de kemiska reaktionerna sker vilket medför att katalysatorns genväg kan studeras istället för hur det ser ut innan och/eller efter kullen. Detta medför att ytfysikmetodiken närmar sig de faktiska katalysatorerna istället för att studera reaktioner som de händer i rymden.

Med den nya metoden har jag undersökt hur olika kemiska reaktioner och ytor förändras nära atmosfärstrycket gentemot vakuum och hur detta påverkar de katalytiska vägarna. En av de reaktioner jag undersökt används inom kemikalieproduktion. Denna reaktion kopplar samman små molekyler med hjälp av en guldkatalysator och producerar större och mer användbara varianter. Här har jag undersökt hur olika molekyler tar olika vägar till att kopplas samman även om slutprodukten är densamma, och hur dessa vägar påverkas av ett högre tryck. Därmed bidrar denna avhandling till en större förståelse för de katalytiska vägarna och till att katalysatorer kan skräddarsys i framtiden.

Om dagens katalysatorer jämförs med de katalysatorer som finns i naturen förefaller de som ineffektiva. Denna skillnad visar att det finns ett stort utrymme för att förbättra våra katalysatorer, och för att göra detta behövs det insikter som påvisar hur molekylerna växelverkar med katalysatorerna. Möjligheten att studera de kemiska reaktionerna medan de händer är ett steg i riktningen mot effektivare katalysatorer vilket leder till energibesparingar och en bättre miljö.

Populärwissenschaftliche Zusammenfassung

Die heutige Gesellschaft lässt sich kaum ohne die Errungenschaften der Katalyse vorstellen. Täglich benutzen wir unterschiedlichste Formen von Katalysatoren und deren Produkte, welche in der chemischen Industrie genauso wie in der Abgasreinigung verwendet werden. Einer der bekanntesten Katalysatoren ist der Abgaskatalysator im Auto, der die meisten der schädlichen Abgase in weniger schädliche Gase umwandelt. Ein etwas weniger bekannter aber durchaus für unsere Leben bedeutsamer Katalysator findet Anwendung im Haber-Bosch-Verfahren. Dieses katalytische Verfahren ermöglicht unter anderem die Herstellung von Kunstdünger, ohne dessen Verwendung in der Landwirtschaft kaum eine Weltbevölkerung von über drei Milliarden Menschen möglich wäre. Dies zeigt direkt die außerordentlich Bedeutung von Katalysatoren.

Um eine chemiche Reaktionen in Gang zu setzen, muss eine Energiebarriere überwunden werden. Diese Barriere kann man sich wie einen Hügel, der bezwungen werden muss, vorstellen. Ein Katalysator kann auf der anderen Seite wie ein Tunnel durch den Hügel gesehen werden. Solch ein Tunnel ermöglicht, dass Reaktionen, die normalerweise sehr langsam ablaufen, beschleunigt werden. Manchmal ermöglich auch erst der Einsatz eines Katalysatortunnels eine chemische Reaktion, da die Überwindung des Berges unmöglich ist. Der durch den Katalysator geöffnete Tunnel verringert den Energieverbrauch, da die Herstellung schneller und einfacher erfolgen kann. Ein weiterer Vorteil ist, dass die eingesetzte Menge an Chemikalien reduziert werden kann, was auch zu weniger Beiprodukten führt. Ein niedrigerer Energieverbrauch ist nicht nur wirtschaftlich sinnvoll sondern auch gut für die Umwelt.

Die Entwicklung von neuen Katalysatoren geschieht meist in einem Versuch-und-Irrtum Verfahren, wobei unterschiedliche Katalysatoren getestet werden, um den besten zu finden. Diese Methode hat sich als effektiv erwiesen und führt meist relativ schnell zu großen Fortschritten. Um neue Katalysatoren direkt nach Mass zu schneidern, bedarf es doch ein Verständnis von katalytischen Reaktionen auf einer molekularen Ebene. Dies ist es, was sich die oberflächenphysikalische Katalysatorforschung zum Ziel gesetzt hat. Da es aber durchaus kompliziert ist, richtige Katalysatoren auf einer molekularen Ebene zu verstehen, verwenden Oberflächenphysiker Modellsysteme, welche nur einige der wichtigsten Bestandteile beinhalten. Um das Verständnis dieser vereinfachten Katalysatoren zu erleichtern, werden diese im Vakuum erforscht. Das bedeutet, dass die Reaktionen ablaufen, als ob sie im Weltall stattfinden würden. Daher ist es fraglich, ob man Rückschlüsse auf die Reaktionen, wie sie auf der Erde ablaufen würden, ziehen kann. In dieser Arbeit habe ich chemische Reaktionen von

Modellsystemen in einem Druck, der sich dem des tatsächlichen Katalysators nähert, untersucht. Die Experimente konnte ich dank der neuen Messmethode der Hochdruckröntgenphotoelektronenspektroskopie durchführen. Diese Methode erlaubt es, die Moleküle während der chemischen Reaktion im Katalysatortunnel zu untersuchen, anstatt sie nur auf der einen oder der anderen Seite des Energieberges zu beobachten. Damit nähert sich die Oberflächenphysik mehr und mehr den richtigen Katalysatoren.

Mit dieser neuen Messmethode habe ich untersucht, wie sich chemische Reaktionen und Oberflächen für Katalysatoren verändern, wenn ein atmosphärischer Druck anstelle des Vakuums verwendet wird. Eine der Reaktionen, die ich untersucht habe, wird in der chemischen Industrie verwendet um zwei kleine Moleküle mithilfe eines Goldkatalysators zu einem größeren und nützlicheren Molekül zu verbinden. Des Weiteren habe ich untersucht, wie unterschiedliche Moleküle verschiedene Wege nehmen, um sich zu einem Endprodukt zu verbinden und wie diese Wege, die sie einschlagen, vom Druck abhängen. Damit leistet meine Arbeit einen Beitrag zum Verständnis von katalytischen Prozessen auf molekularere Ebene, was die Entwicklung neuer Katalysatoren in der Zukunft erleichtern kann.

Wenn wir aber die heutigen Katalysatoren mit denen vergleichen, die in der Natur vorkommen, sehen wir, dass es noch viele Verbesserungsmöglichkeiten gibt. Um jedoch die Katalysatoren zu verbessern, brauchen wir noch ein besseres Verständnis von den Wechselwirkungen zwischen den Molekülen und Katalysatoren. Ein erster Schritt zur Herstellung effektiverer Katalysatoren ist, chemische Reaktionen zu untersuchen, während sie geschehen. Diese Forschung wird in Zukunft dazu beitragen können, dass chemische Reaktionen in der Industrie oder im Auto weniger Energie verbrauchen und die Umwelt weniger belastet wird.

Acknowledgements

The work behind a Ph.D. thesis is a long process. During this time I have been fortunate to meet and work with a lot of different people at many different laboratories around the world. I would like to take this opportunity to thank everyone which have made this possible.

First and foremost, I'd like to thank my main supervisor Joachim Schnadt. Achim, we have been working together for a long time and I'd like to thank you for your patience and guidance. You have allowed me to follow my own ideas and conduct my research in my own way. Your door was always open and you never turned down a discussion, whether it was about data, underlying phenomena or recent politics. Working with you has been a very positive experience.

I'd also like to take this opportunity to thank my co-supervisor Jan Knudsen. Jan, I've also worked with you for a long time and we have shared many beamtimes together. I think you have thought me most of what I know about vacuum systems and how to use them, and for this, I am very grateful. You always have a very positive attitude and many helpful ideas, even if it felt like the whole experiment was collapsing. Jan, thank you for teaching me how to 'keep cool' in these difficult situations and I'm happy to have worked with you.

There are many past and present colleagues that have contributed to this work. I would like to thank Payam Shayesteh for assistance during beamtimes and for giving me someone to annoy whenever I felt like taking a break. I'd also like to thank you for showing me how an 'intended' plasma discharge in a vacuum system looks like. Similarly, I'd like to thank Mohammad Alif Arman for great help during beamtimes and good company. Ashley Head and Shilpi Chaudhary, we were for some time the 'dream team' of beamtimes and you have greatly contributed to a good working environment, I'll always remember the "banana dance" adn you have my gratitude. On the topic of beamtimes, I'd like to thank Karsten Handerup, Robert Temperton, and Benjamin Reinecke for helping and inviting me to various projects. Further, I'd like to extend my gratitude to Olesia Snezhkova for being a great colleague. On this topic, I'd like to thank Elin Grånäs for having 'Roligt nästan jämt' in the STM lab. and tricking me into running Lidingöloppet. On the topic of STM, I'd like to thank Lindsay Merte for assistance in the lab and providing me with images. I'd also like to thank Tripta Kamra and Sheetal Sisodiya for helping me with basic chemistry and introducing me to new and exciting projects. Further, I'd like to thank Anneli Nilsson Ahlm and Anne Petersson Jungbeck for administrative support. Also deserving my gratitude is Johan Knutsson, we've had many good times since we

were both bachelor students. Patrik Wirgin, you have been a great help when it comes to any form of paperwork, sending parcels or just about anything and no topic is taboo in a conversation. A place for conversations without taboos was always the SLJUS-lunchroom and for that, I'd like to thank the 'lunchroom-gang'. I'd also like to thank all my colleagues at SLJUS for keeping a warm and welcoming atmosphere, which makes it a great place to work at.

I'd also like to take this opportunity to thank my colleagues at the MAX IV Laboratory. Samuli Urpelainen, I'd like to thank you for being a great co-worker and sharing the experience of putting up and down the APXPS instrument a few times. On this topic, I'd also like to thank Mikko-Heikki Mikkelä and Margit Andersson. Further, Jacek Osiecki and Karina Schulte Thånell, thank you for assistance during the many beamtimes at I311. I'd also like to extend my gratitude to all the MAX IV Laboratory staff for making it a great place for science.

Petra Reinke, I'd like to thank you and Ehsan Monazami for a great time measuring STM in Virginia.

I'd like to thank Mie Andersen, Petter Persson, and Fredric Ericson for kindly providing me with DFT calculations. Further, I'd also like to thank all of the co-authors of my papers. I'd like to extend my gratitude to everyone which I've met at the beamtimes. Sometimes I was support for you, and sometimes you supported me. Thank you for making work at synchrotron radiation facilities such a great experience.

I would also like to take this opportunity to thank my friends and family. Kenneth and Karolina, you never turned down an opportunity for beer and it is never too late in the evening/night/morning. I would also like to thank my parents, Ann and Jörgen, for supporting me through my studies and always helping with various construction/digging projects. I'd also like to thank my siblings, Eva and Fredrik, for their indulgence.

Finally, I'd like to thank Lisa. You have supported me by always being there when I needed you and you have pushed me into widening my horizons. I'm really glad that the APXPS instrument isn't only a tool for catalysis research, but also a catalyst for researchers.

Preface and list of publications

This doctoral thesis presents my contribution to the field of surface science by using model catalysts to investigate CO oxidation, Sonogashira cross-coupling, oxide formation and propylene oxidation. The work uses insights from previous studies in the literature and new herein reported knowledge gained from UHV studies and combines it with *in situ* spectroscopy to fully characterize the investigated catalysts and reactions at *ambient* conditions.

This thesis is based on the following publications, referred to by their Roman numerals:

I **Sonogashira cross-coupling over Au(111): from UHV to ambient pressure**

N. Johansson, S. Sisodiya, P. Shayesteh, S. Chaudhary, J. N. Andersen, J. Knudsen, O. F. Wendt, and J. Schnadt
In press: J. Phys.: Condens. Matter
I was main responsible for planning, preparing and carrying out of the ambient pressure X-ray photoelectron spectroscopy measurements. I was the experimental lead in the X-ray photoelectron and X-ray adsorption spectroscopy experiments. I analyzed all data and wrote the manuscript.

II **Mn-salen supported by Au(111): adsorption and catalysis**

N. Johansson, O. Snezhkova, S. Chaudhary, E. Monazami, F. Ericson, R. Jensen, A.-L. Christoffersen, A. R. Head, S. Urpelainen, B.N. Reinecke, I. Chorkendorff, P. Reincke, P. Persson, J. Knudsen, and J. Schnadt
In manuscript
I was main responsible for planning, preparing, and leading several ambient pressure X-ray photoelectron spectroscopy beamtimes, the scanning tunneling microscopy measurements, and μ-reactor measurements. I analyzed all the data and wrote the manuscript.

III **Ambient pressure phase transitions over Ir(111): at the onset of CO oxidation**

N. Johansson, M. Andersen, Y. Monya, J. N. Andersen, H. Kondoh, J. Schnadt, and J. Knudsen
In press: J. Phys.: Condens. Matter
I was main responsible for planning, preparing and carrying out of the ambient pressure X-ray photoelectron spectroscopy measurements. I was main responsible for the analysis of the data and wrote the manuscript except for the section on the density functional theory results.

IV **Oxidation of ultrahin FeO(111) grown on Pt(111): spectroscopic evidence for hydroxylation**

N. Johansson, L. R. Merte, E. Grånäs, S. Wendt, J.N. Andersen, J. Schnadt, and J. Knudsen
Top. Catal. 2016, **59**, 506
I was main responsible for planning and leading the ambient pressure X-ray photoelectron and X-ray adsorption spectroscopy experiments. I analyzed the data and wrote the manuscript.

V **Ultrathin stepped iron oxide films grown on high index Pt surfaces – a new catalytic model system**

E. Grånäs, **N. Johansson**, M. A. Arman, J. Osiecki, K. Schulte Thånell, J. N. Andersen, J. Schnadt, and J. Knudsen
In manuscript
I participated in the planning, preparation and measurement of the X-ray photoelectron, X-ray adsorption spectroscopy, and scanning tunneling microscopy data. I participated in discussions about the data and contributed to writing the manuscript.

VI **The SPECIES beamline at the MAX IV Laboratory: a facility for soft X-ray RIXS and APXPS**

S. Urpelainen, C. Såthe, W. Grizolli, M. Agåker, A. R. Head, M. Andersson, S.-W. Huang, B. N. Jensen, E. Wallén, H. Tarawneh, R. Sankari, R. Nyholm, M. Lindberg, P. Sjöblom, **N. Johansson**, B. N. Reinecke, M. A. Arman, L. R. Merte, J. Knudsen, J. Schnadt, J. N. Andersen, and F. Hennies
J. Synchrotron Radiat. 2017, **24**, 344
I was deeply involved in the commissioning of the ambient pressure X-ray photoelectron spectroscopy instrument and participated in the commissioning of the SPECIES beamline.

Publications to which I have contributed, but which are not included in this thesis:

VII **Polymer-supported palladium(II) carbene complexes: catalytic activity, recyclability, and selectivity in C-H acetoxylation of arenes**

M. H. Majeed, P. Shayesteh, L. R. Wallenberg, A. R. Persson, **N. Johansson**, L. Ye, J. Schnadt, and O. F. Wendt
Chem. Eur. J. 2017, **23**, 8457

VIII **Iron phthalocyanine on Cu(111): coverage-dependent assembly and symmetry breaking, temperature-induced homocoupling, and modification of the adsorbate-surface interaction by annealing**

O. Snezhkova, F. Bischoff, Y. He, A. Wiengarten, S. Chaudhary, **N. Johansson**, K. Schulte, J. Knudsen, J. V. Barth, K. Seufert, W. Auwärter, and J. Schnadt
J. Chem. Phys. 2016, **144**, 094702

IX **Covalent immobilization of molecularly imprinted polymer nanoparticles using an epoxy silane.**

T. Kamra, S. Chaudhary, C. Xu, **N. Johansson**, L. Montelius, J. Schnadt and L. Ye
J. Colloid. Interf. Sci. 2015, **445**, 277

x **Intrinsic ligand effect governing the catalytic activity of Pd oxide thin films**

N. M. Martin, M. Van den Bossche, A. Hellman, H. Grönbeck, C. Hakanoglu, J. Gustafson, S. Blomberg, **N. Johansson**, Z. Liu, S. Axnanda, J. F. Weaver, and E. Lundgren
ACS Catal. 2014, **4**, 3330-3334

xi **The new ambient-pressure X-ray photoelectron spectroscopy instrument at MAX-lab**

J. Schnadt, J. Knudsen, J. N. Andersen, H. Siegbahn, A. Pietzsch, F. Hennies, **N. Johansson**, N. Mårtensson, G. Öhrwall, S. Bahr, S. Mähl and O. Schaff
J. Synchrotron Rad. 2012, **19**, 701-704

List of Abbreviations

AEY	Auger electron yield
AFM	Atomic force microscopy
ALS	Advanced light source
APXP	Ambient pressure X-ray photoelectron
APXPS	Ambient pressure X-ray photoelectron spectroscopy
BrB	Bromobenzene
ClB	Chlorobenzene
DFT	Density functional theory
EPU	Elliptically polarizing undulator
ESCA	Electron spectroscopy for chemical analysis
EXAFS	Extended X-ray absorption fine structure
FWHM	Full width at half maximum
FY	Fluorescence yield
HOMO	Highest occupied molecular orbital
IB	Iodobenzene
IMFP	Inelastic mean free path
IRRAS	Infrared reflection absorption spectroscopy
LBNL	Lawrence Berkeley National Laboratory
LDOS	Local density of states
LEED	Low energy diffraction
LUMO	Lowest unoccupied molecular orbital
MCP	Multichannel plate
NEXAFS	Near edge X-ray absorption fine structure
PA	Phenylacetylene
PES	Photoelectron spectroscopy
PEY	Partial electron yield
PROX	Preferred oxidation
RIXS	Resonant inelastic X-ray scattering
STM	Scanning tunneling microscopy
TEY	Total electron yield
UHV	Ultrahigh vacuum
UPS	Ultraviolet photoelectron spectroscopy
XA	X-ray absorption
XAFS	X-ray absorption fine structure
XAS	X-ray absorption spectroscopy
XP	X-ray Photoelectron
XPS	X-ray photoelectron spectroscopy

Contents

Chapter 1

Introduction

Our modern society and many of the products we use daily rely on efficient production of large quantities of chemicals with the help of catalysts. These applications range from fertilizers and fuels to pollutant removal. One of the most well-known catalysts is the three-way automotive converter in which harmful pollutants are converted into less harmful species and is today vital for the environment, especially in urban areas.

Other catalytic reactions, however, have a more indirect impact on human life. One of these is the ammonia production from nitrogen and hydrogen over an iron-based catalyst. This process is extremely important as ammonia is essential for the production of artificial fertilizer, which is believed to be vital to sustain a world population above 3 billion [1]. The catalytic ammonia synthesis, which is referred to as the Haber-Bosch process, was discovered by Fritz Haber in the beginning of the 20th century and later optimized for industry by Carl Bosch. In recognition of their efforts, Haber and Bosch were awarded the Nobel Prize in Chemistry in 1918 and 1931, respectively [2, 3]. Later, the awarding to Haber sparked some ethical debate due to his involvement in chemical weapons during the First World War. Regardless, many consider the Haber-Bosch process the most important invention of the 20th century. It is estimated that nearly 90% of all chemicals are manufactured using a catalyst [4] and many of these would not be feasible without catalysis. Hence, research on catalysis is not only performed out of scientific curiosity but due to the impact on society.

The term catalysis was introduced in 1835 by Jöns Jacob Berzelius who described the process 'to awaken affinities, which are asleep at a particular temperature, by their mere presence and not their own affinity'. His work was

expanded by Wilhelm Ostwald who worked on reactions catalyzed in the presence of acids and bases. Ostwald's definition from 1895, which is often used today, states that 'catalysts are substances which change the velocity of the reaction without modification of the energy factors of the reaction'. For his work on catalysts, Ostwald was awarded the Nobel Prize in Chemistry in 1909 [5].

The field of catalysis can be roughly divided into *homogeneous* and *heterogeneous* catalysis. The distinction of the categories is found in the aggregation states of the catalyst and reactants, *i.e.* whether they are in solid, liquid, or gas phase. In homogeneous catalysis, the catalysts and reactants are in the same aggregation state, typically in a liquid. In contrast, in heterogeneous catalysis the reactants and the catalyst are not in the same aggregation phase. The most common configuration of heterogeneous catalysis is gas phase reactants and a solid catalyst. In both categories, the catalysts introduce an alternative path to the reaction with lower activation barriers, as defined by Ostwald. As a result, a reaction proceeds spontaneously where otherwise the reaction is unlikely to happen or it proceeds at a very slow rate.

Chemical reactions at surfaces

Since heterogeneous catalysis typically occurs at the solid-gas interface, an understanding of surface structures and chemistry is essential to gain insight into the catalytic mechanisms. In figure 1.1, the three main catalytic reaction mechanisms are illustrated. As an example, consider the oxidation of CO over a metal surface. According to the *Langmuir-Hinshelwood* mechanism, the reaction cycle start with adsorption of CO and O_2 on the catalyst surface. Secondly, the O_2 molecule dissociates into atomic O, which diffuses over the surface. As the adsorbed CO diffuse together with atomic O they react to form CO_2, which desorbs, and the catalytic cycle is closed. In contrast, the *Eley-Rideal* mechanism

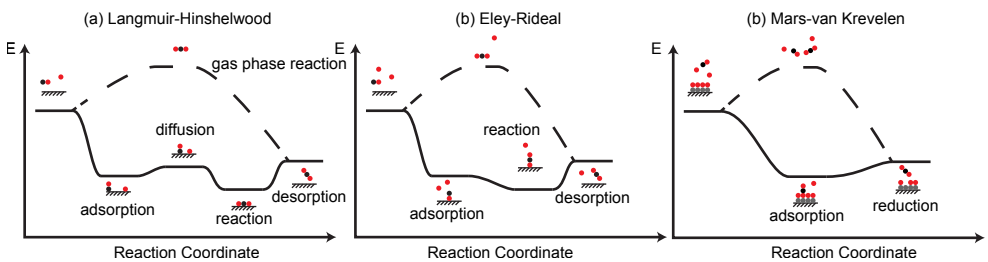

Figure 1.1: A schematic illustration of three mechanisms of heterogeneous catalysis. The red and black balls represents O and C atoms while the grey balls represents metal atoms of the surface oxide. The energy is plotted as a function of the reaction coordinate.

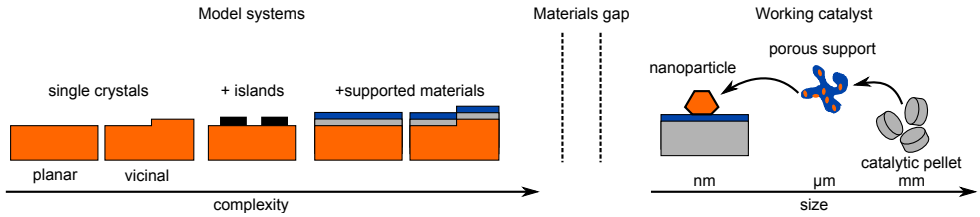

Figure 1.2: Simplified model systems in relation to the compositions of a working catalyst. The right side of the figure shows the composition of a working catalyst at different length scales. The working catalyst is often composed of nanoparticles dispersed onto a porous support material. The support typically is formed as a pellet that is used in the reactor. The surface science approach is to investigate single crystals of the active materials where the complexity can be increased by adding steps and other materials to the surface as shown in the left side of the figure. The inability of the model systems to mimic the working catalyst is referred to as the materials gap.

involves direct reaction of a gas phase CO molecule with adsorbed atomic O. Finally, if the surface is oxidized the reaction can proceed via the *Mars-van Krevelen* mechanism. It is similar to Eley-Rideal in that gas phase CO interacts directly with O at the surface. However, it differs as the process reduces the oxide which would need to regenerate by gas phase O_2 for further cycles. Depending on the reaction and the surface, all three mechanisms have been found to be valid. These mechanisms were studied by Gerhard Ertl who detailed the molecular mechanisms during the Haber-Bosch process and observed structural oscillations on Pt surfaces. Ertl was awarded the Nobel Prize in Chemistry in 2007 'for his studies of chemical processes on solid surfaces' [6].

The material gap

In large-scale industrial applications catalytic reactions are carried out in a reactor, in which temperature and pressure can be controlled. The right side of figure 1.2 illustrates the catalytic material in such a reactor at different length scales. Often the reactors are filled with catalytic pellets composed of a porous material that the catalytically active particles are dispersed onto. The support, which is typically some form of oxide, hold a complex structure that maximizes its surface area. A large surface area allows for an enhanced gas exposure to the active, often metallic, particles. This leads to a system which is rather complex. The structure of the support is quite intricate and the active particles themselves contain multiple facets. In addition, the support-particle interaction might influence the activity. These factors make it difficult to study industrial catalysts and achieve a detailed atomic-scale understanding of their catalytic properties.

To achieve atomic scale understanding of working catalysts, their complexity needs to be reduced. In the so-called surface science approach, the complexity reduction is performed by replacing the real catalysts with model systems. The simplest of model systems is a single crystal surface of the same material as the active particles. Such a single crystal surface contains many identical sites and it is easy to determine surface structures formed upon adsorption and co-adsorption as well as desorption energies. However, these materials are not particularly representative of the actual working catalyst. For instance, the active particles typically contains multiple surface facets, steps, and other irregularities. Further, the support-particle interaction is completely ignored. To mimic the real system more accurately, a stepwise increase in complexity is employed as schematically illustrated in the left side of figure 1.2. As a single crystal is the simplest model system it is desirable to use it while simultaneously model the steps and multiple facets of the active particles. Therefore, the first step in increased complexity is to cut the single crystal at a plane in the vicinity of the low index planes. These so-called vicinal surfaces contain multiple facets and therefore resembles more closely the active particle compared to a planar single crystal. However, the interactions with the support material is still ignored. To mimic support-particle interaction of the working catalyst, the next step in complexity is to grow islands or films of the support material on the single crystals. This creates a so-called inverted catalyst and the interactions can be studies. Even though the complexity of the model systems is increasing for every modeling step, it still does not meet that of the working catalysts and this inability is referred to as the *material gap* of surface science.

The pressure gap

As with the material gap, there is also a *pressure gap*. The working heterogeneous catalysts typically operate at pressures of several, if not hundreds bars. In the homogeneous case, the catalysts typically operates in liquids. This results in systems with high chemical potentials, a comparatively high Gibs free energy, turbulent gas dynamics and multiple interactions with the surfaces as the gases often contain multiple components. Similarly to the material approach, the complexity of these systems is reduced in surface science by using ultra-high vacuum (UHV) conditions ($\leq 10^{-10}$ mbar) during the measurements with gases being dosed in the 10^{-6} mbar range. Pressures below 10^{-6} mbar are often necessary for techniques such as X-ray photoelectron spectroscopy (XPS) and low energy electron diffraction (LEED) as to detect the information carrying electrons and operate the detectors. The use of UHV conditions, however, also allows for highly controlled environments. Within this pressure regime it

is rather straightforward to investigate the surface-gas interactions with 'clean' gases compared to what is possible in air.

However, it is not certain that the adsorbate structures found at UHV can be extrapolated to the pressure regime used in a working catalyst. An example of the pressure gap for a common catalytic material is found on the Pd(100) surface. At UHV conditions, exposure to O_2 leads to a surface of chemisorbed atomic O in a p(2 × 2)-O structure that after increased UHV exposure to O_2 forms a c(2×2) phase [7]. These UHV structures are composed of chemisorbed O by the surface and do not induce a significant change to the Pd surface. However, at exposures to O_2 in the mbar regime the same Pd surface forms surface- or bulk oxides [8]. Hence, the surface interactions and the resulting surface structures are quite different from the ones observed in UHV studies. This example clearly demonstrates the pressure gap and that the relation between surface structures and reactivity at realistic conditions cannot be deduced from UHV type studies.

Bridging the gaps

In recent years much effort has been directed towards bridging the pressure gap and photon based techniques are commonly used. Techniques using photons are generally non-intrusive and able to operate at atmospheric pressure and above. However, they typically do not hold the same ability to investigate the chemistry of surfaces as electron spectroscopies.

The electron spectroscopies were extended into the mbar regime with the development of ambient pressure XPS (APXPS) in the 1970s, but due to the available light sources, only a few instrument were built. The technique saw an upswing in the 00's with the development of synchrotron-based instruments. APXPS holds the ability to investigate the chemistry of the solid/gas interface and allows for so-called *in situ* measurements. Here, *in situ* refers to a measurement in which the processes are probed as they occur in a realistic pressure. In addition, *in situ* APXPS is the technique which most of my work is based on.

The ability to bring surface science methods to more 'realistic' conditions is the first step in producing more suitable models for the catalytic processes. Typically, catalysis research is based on a *trial and error* methodology which has lead to major advances in a relatively short time frame but do not detail the catalytic mechanisms. The aim of catalysis research within surface science is to gain insight into the fundamental processes to produce catalysts from *first principle*. Being able to investigate reactions *in situ* brings the field closer to this goal.

This thesis

In this thesis I have investigated catalytic reactions over a variety of systems ranging from diatomic molecules adsorbed on single crystals to oxide phase changes and, finally, to reactions over large molecular complexes. These studies bridge the pressure gap by the use of *in situ* electron spectroscopy while simultaneously striving to bridge the material gap with model systems of increasing complexity. In the least complex system, I studied the the pressure gap of the oxidation of CO over a single crystal surface. However, to approach real catalysts the complexity must be increased. The increase in complexity is approached in three fashions. In the first approach, large reactants are used on a single crystal catalyst to investigate their coupling. Not only is the reaction more complicated as more atoms are included, but the surface structures become also more difficult as the possible structures and interactions increase with the molecular size. The second approach is to use an ultrathin hetero-oxide and study its phase transformation during exposure to mbar pressures of oxygen. This concept is explored further as a vicinal version of the hetero-oxide is also produced and its structure and reactivity is characterized. Lastly, the most complex system is that of an immobilized large homogeneous catalyst. Here, the complexity arise from the support-molecule, molecule-molecule, and gas-molecule interactions during the reaction studies.

From the results in the included papers it is demonstrated that the insights gained during UHV studies can be applied to those found at mbar conditions. Not only are they helpful, but in some cases necessary for a detailed understanding. Hence, UHV studies are, and will be, relevant for future investigations. Instruments that facilitate both UHV and ambient pressure measurements are therefore vital to catalysis research within the field of surface science.

Outline

In the next chapter I present the techniques that I used during the experimental work behind this thesis with focus on APXPS. In chapter 3, I discuss the model systems investigated and I summarize the included research papers in chapter 4. Finally, in chapter 5 I give my final remarks and suggestions for future investigations.

Chapter 2

Techniques for probing solid surfaces and solid/gas interfaces

The main techniques of my experimental work have been X-ray photoelectron and adsorption spectroscopies at synchrotron radiation facilities. I have also been heavily involved in the commissioning of the first APXPS end station in Sweden, and partly in the commissioning of the SPECIES beamline that hosts this end station now. In the following, the experimental techniques employed are discussed in light of acquisition and data treatment. As it constituted a major part of my work, the APXPS technique and instrumentation are discussed in some detail.

2.1 Electron spectroscopies

The investigation of adsorbates on surfaces has been of primary interest for the surface science community since the mid 20th century. One group of experimental methods that have proven extremely valuable for these investigations is the one of electron spectroscopies. The use of electrons is advantageous for several reasons: (i) they are easy to detect, (ii) electrons have a short effective escape depth from solids which makes the techniques surface sensitive, and (iii) they can be easily manipulated by external fields, which makes energy assignment straightforward.

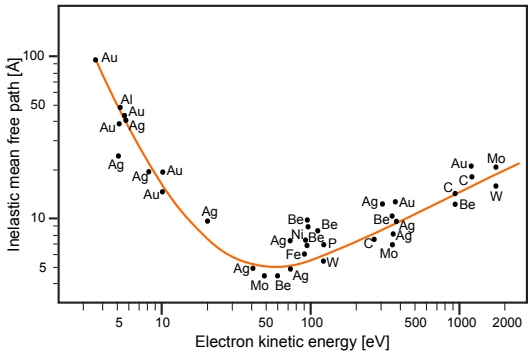

Figure 2.1: The inelastic mean free path for electrons traveling through various materials as a function of kinetic energy. The curve demonstrates that for for the energy ranges relevant for XPS, the IMFP at the minimum (2-5 Å). The image is adapted from Ref. [9]

The short effective escape depth is due to a high cross section for electrons to interact with matter. As such, electrons can on average only travel a short distance before being scattered inelastically, and this distance is referred to as the inelastic mean free path (IMFP). If we consider electrons traveling through solid matter, it is observed that the electron IMFP depends primarily on the kinetic energy of the electron more than the nature of the material it travels through. Hence, the IMFP of electrons is described by the so-called universal IMFP curve illustrated in figure 2.1. The shortest IMFP is observed for electrons with a kinetic energy between 20 and 100 eV and is about 2-5 Å. Electron spectroscopies in the soft X-ray regime ($h\nu < 5$ keV) primarily use electrons with kinetic energies up to 1000 eV and, hence, the vast majority of detected electrons originate from the first few atomic layers of the solid. Therefore, electron spectroscopy methods are inherently very surface sensitive.

Electron spectroscopy experiments are typically performed under UHV conditions in an effort to keep the surfaces adsorbate-free. Due to the high surface sensitivity of the technique, about 50% of the signal originates from the very first atomic layer of the solid and, hence, impurities highly affect the measurement. UHV also implies the ability to precisely control the gas environment which, in turn, allows for detailed adsorbate species investigations. There are, however, residual gases remaining in the vacuum system which might affect the measurements and an example of this is seen in **Paper IV**.

One of the most widely employed electron spectroscopy techniques is photoelectron spectroscopy (PES). PES make use of the photoelectric effect, which was first discovered by Heinrich Hertz in 1887[1]. The phenomenon was later, in 1905, explained by Albert Einstein[2], an achievement for which he was awarded the Nobel Prize in Physics in 1921 [12]. Einstein introduced the quantum hypothesis

[1] The original publication is found in Ref. [10].
[2] The original publication is found in Ref. [11].

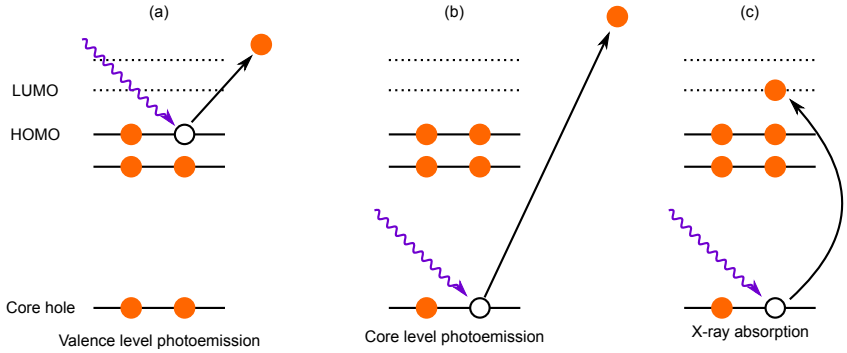

Figure 2.2: Schematic view of some the primal ways of interaction between X-rays and matter. (a) in valence band spectroscopy, an electron from the valence band, or highest occupied molecular orbital (HOMO) in the case of molecules, is promoted into the vacuum. (b) a similar process occurs during core level photoemission with the distinction that the ejected electron originates from a core level. (c) during X-ray absorption, an electron from the core levels is promoted either to the valence band or to the lowest occupied molecular orbital (LUMO) depending on which type of material is investigated.

for the photon and the relation between the incident photon energy and the kinetic energy of the emitted electron.

In the energy range of interest for the work in this thesis, the photon-electron interaction can be described by two main mechanisms: *photoemission* (cf. figures 2.2(a) and (b)) and *photoabsorption* (cf. figure 2.2(c)). In photoemission experiments the emitted electron can originate either from the valence band or from the core levels. Valence band investigations can be performed with ultraviolet radiation and are often referred to as ultraviolet photoemission spectroscopy (UPS) while the core level investigations employ X-rays and are hence referred to as X-ray photoelectron spectroscopy. Both XPS and UPS probe occupied states and the emitted electrons are typically detected by a hemispherical electron energy analyzer.

In X-ray absorption spectroscopy (XAS), X-rays of a well-defined energy impinge onto a sample. If the photon energy is equal to the energy difference between a core level and an unoccupied valence state, the electron may be promoted into this state. Therefore, by changing the photon energy, the unoccupied levels may be mapped.

2.1.1 X-ray photoelectron spectroscopy

Photoelectron spectroscopy has proven to be one of the most versatile methods for studying surface chemistry. Since element-specific information is obtained, the technique is commonly referred to as electron spectroscopy for chemical analysis (ESCA). The technique itself was developed by Kai Siegbahn, who was awarded the Nobel Prize in Physics in 1981 [13] for his contribution to the development of high-resolution electron spectroscopy. Today, XPS is one of the cornerstones of surface science and commonly available.

The photoemission process

To visualize the photoemission process the so-called three-step model is often employed. Within this model, the photoemission event is illustrated as follows: (i) an impinging photon promotes a bound electron into a nearly-free wave packet in the unoccupied band structure of the solid. (ii) This wave packet is transported to the surface and (iii) then penetrates the surface barrier as a plane wave. This is a purely phenomenological approach developed by Berglund and Spicer [14, 15], which, however, has proven to be successful and describes the phenomenon rather well.

From the above description, and from the conservation of energy, it follows that

$$E_i + h\nu = E_f + E_k, \tag{2.1}$$

where E_i is the initial state energy, $h\nu$ is the photon energy, E_f is the final state energy, and E_k the kinetic energy of the emitted electron. The difference between the initial and final state energies equals the ionization potential. When employing XPS to investigate surfaces, it is more useful to reference to the Fermi energy. With this in mind and a slight re-arrangement, Eq. 2.1 becomes

$$E_k = h\nu - (E_B + \Phi)\,, \tag{2.2}$$

where E_B is the binding energy of the emitted electron and Φ is the surface work function. Hence, if $h\nu$ is known, information about the electron binding energy can be found from analyzing the kinetic energy of the emitted electrons. In reality, the kinetic energy is measured inside an electron energy analyzer and the relevant surface work function is that of the analyzer, cf. figure 2.12.

A more accurate description of the photoemission event is given in the one-step model, which is illustrated in figure 2.3. In this description, the electron is promoted from its bound state into a free electron described by a plane wave.

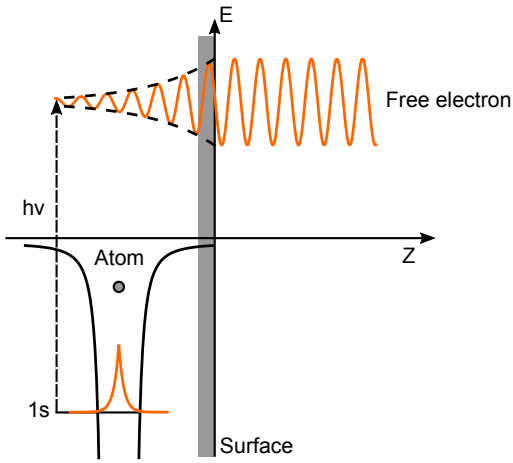

Figure 2.3: A schematic representation of the photoemission process. The transition probability is illustrated by the overlap of the orbital radial wave function and the decaying plane wave of the free electron.

The wave function, however, decays rapidly within the solid and, hence, the distance from the surfaces heavily influences the transition probability. This decay arises from various scattering mechanisms and the decay length relates to the IMFP.

The relevant information about the direct photon-induced transition is contained within the *transition matrix element*, M_{fi}. If the wavelength of the incoming radiation is long compared to that of the atomic dimensions, the reduced transition matrix element can, within the *electric dipole approximation*, be expressed as

$$M_{fi} = \langle \psi_f | - e \cdot \mathbf{r} | \psi_i \rangle, \tag{2.3}$$

where ψ_f and ψ_i are the final and initial state wave functions, respectively, and $-e \cdot \mathbf{r}$ is the dipole operator. The initial and final state wave functions are generally not known, but may in the *one-electron view* approximation be expressed as a product between the electron of the singe-electron wave function and the (N-1) electron wave function of the remaining system. Hence, the final state wave function is expressed as a product of a plane wave, ϕ^{f,E_k}, and the remaining ion, $\psi^f(N-1)$. The initial state wave function is expressed as a product of the orbital from which the electron originated, $\phi^{i,k}$, and the wave function describing the remaining electrons, $\psi^i(N-1)$. Now equation 2.3 can be expressed as [16]

$$M_{fi} \langle \psi_f | - e \cdot \mathbf{r} | \psi_i \rangle = \langle \phi^{f,E_k} | - e \cdot \mathbf{r} | \phi^{i,k} \rangle \langle \psi^f(N-1) | \psi^i(N-1) \rangle. \tag{2.4}$$

According to Fermi's golden rule, the transition probability is proportional to the square of the transition matrix element. Hence, from equation 2.4 it follows that the cross section for photoemission for any given photon energy is given by the product between a one-electron matrix element and a (N-1)-electron overlap integral in accordance with the one-step model.

In photoemission experiments, the binding energy of the emitted electron is of interest. However, due to the nature of many-electron-systems, some approximations are needed to extract the binding energies. In one of the simplest approximations, the *frozen orbital approximation*, the orbitals not directly involved in the photoemission event are considered stationary, which implies that the (N-1) overlap integral in equation 2.4 is unity. Here, the measured energy is the negative Hartee-Fock orbital energy, which is often referred to as Koopmans' binding energy. However, this is intuitively inaccurate as the remaining charges will re-arrange as to minimize their energy. This is called *relaxation* and shifts the measured binding energy towards lower values and constitutes the *main line*. However, there are several excited non-orthogonal final states which will result in photoemission. As understood from equation 2.4, a different final ionic state will modify the electron final state and the (N-1) overlap integral. These excited final states result in *satellite* lines at higher binding energy compared to Koopmans' energy. The energies of the main and satellite lines are given by the projection of the initial-state Hamiltonian eigenstates onto the eigenstates of the final-state Hamiltonian. Hence, if the interactions between the emitted electron and the remaining system are neglected, as in the *sudden approximation*, the *first moment* of the photoemission events remain at Koopmans' energy.

The two main satellite features are divided into *shake-ups* and *shake-offs*. Both are excited final states with the distinction that shake-off satellites are doubly ionized. For molecular samples, these appear in X-ray Photoelectron (XP) spectra as discrete peaks, as illustrated in figure 2.4(b), while it is slightly different for metals. The most common excited final state in metals involves the creation of *electron-hole pairs*. Here, an electron is lifted from the top of the valence band just above the Fermi energy into the conduction band. Due to the band structure, there exists a near infinite amount of possible final states. The probability to promote these follows the inverse square law with respect to their energy and is observed in XP spectra as an asymmetry towards higher binding energy of the main line, as illustrated in figure 2.4(a).

As chemical bonds are formed, the overall attractive potential of the ion is altered and induces a shift in the measured binding energy. This is called a *chemical shift*, which allows the XPS measurements to probe the chemical surrounding of the atom. For instance, in **Paper I** chemical shifts in the binding

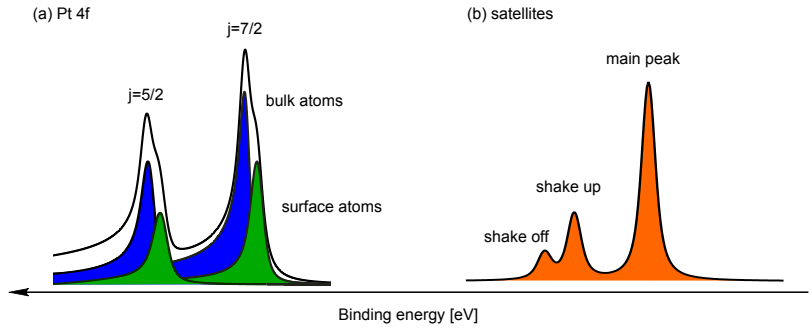

Figure 2.4: An illustration of a measured XP spectra. (a) shows a Pt $4f$ XP spectrum, which exhibit spin-orbit splitting and chemical shifts. (b) shows the an example spectrum with shake-up and shake-off satellite peaks.

energy of carbon atoms are observed. Here, the C $1s$ binding energy depends on whether it is bound to chlorine, bromine, or iodine in direct relation to the electronegativity of the halogen. Chemical shifts are also observed for atoms located at surfaces. Due to the surface termination, the coordination of the surface atoms is reduced which induces a so-called *surface core-level shift*. This shift is typically towards lower binding energy, which is observed in the Ir and Pt spectra in **Paper III**, **Paper IV**, and **Paper V** and is illustrated in figure 2.4(a).

The final state includes the ion from which the photoelectron was emitted and as such, an unpaired electron must be considered. The total spin of the final state in XPS is 1/2 as only one unpaired electron is created (*i.e.* a single core hole). If the orbital angular momentum of the electron is larger than zero, *e.g.* it resides in a p, d, or f orbital, the energy level is split into two levels in accordance to *LS coupling*. This splitting results in two peaks in the XP spectrum and is referred to as *spin-orbit splitting*. As an example, consider photoemission from the Pt $4f$ core level. An electron in a f orbital has an angular orbital momentum of 3, hence, the resulting total angular momenta are $J = 5/2$ and $7/2$ as shown in figure 2.4(a). The occupancy of each level is given by the number of possibilities for the secondary total angular momentum quantum number, M_j, which ranges from $-J$ to J, giving $2J + 1$ possibilities. With the Pt $4f$ example, this yields a ratio of 6:8 which gives the measured intensity between the Pt $4f_{5/2}$ and Pt $4f_{7/2}$ orbitals. However, this is not a general rule as additional effects influences the measured spectrum.

In special cases a splitting can also be observed for s orbitals. This is true if the investigated system have an unfilled valence shell configuration [16]. For instance, molecular O_2 has a valence electron spin of S=1 which couples to the angular momentum of the core hole after photoemission. This splits the energy

level and gives two peaks in the measured spectra. The splitting due to the open valence-state is called *core polarization* and is observed in the O 1*s* spectra in **Paper III** and **Paper IV**.

Practical approach to XPS data analysis

Depending on the goal, analysis of XP spectra varies from near-trivial to quite advanced. For instance, the analysis of the elemental composition of a sample is rather straightforward as databases of core-level binding energies for the elements are available, *e.g.* from NIST [17]. However, for a detailed understanding of the surface chemistry, the analysis effort scales quickly with the number of possible surface species.

A typical XP spectrum is composed of two parts: the *background* and the photoemission *peaks*. The peaks are composed of one or more *components* whose appearance is detailed below. The background for any given excitation energy is mostly composed of inelastically scattered electrons that originate from any orbitals with an ionization energy less or equal that particular photon energy. In addition, excitations of plasmons and other secondary excitations by the outgoing electrons also contribute to the background [18]. In the near-peak region, these effects are reasonably modeled by the *Shirley* background [19]. This background is based on intensity continuity of the measured data and appears as a step under the peak in the XP spectrum. The Shirley background determines the background shape iteratively and is one of the most commonly used backgrounds. Another step-like background that many use is the *Tougaard* background [20], however, the Tougaard background has not been used in this work. The purpose of these backgrounds is to describe the asymmetry due to the rapid increase of emitted electrons at the binding energy of an orbital. However, there are some exceptions to this step-like behavior. For instance, at metallic peaks the asymmetry is mainly due to satellites and the inelastically scattered electrons are included in the curve fitted lineshape. Hence, a linear background should be used when curve fitting metallic peaks if such a lineshape is used. Another example is shown in figure 2.5. This C 1*s* XP spectrum exhibits a highly linear background. The linearity originates from the inelastic scattering of photoelectrons at lower binding energy and Pt Auger electrons. A Shirley background would not adequately model this type of background, which demonstrate the phenomenological nature of background subtraction in XPS analysis.

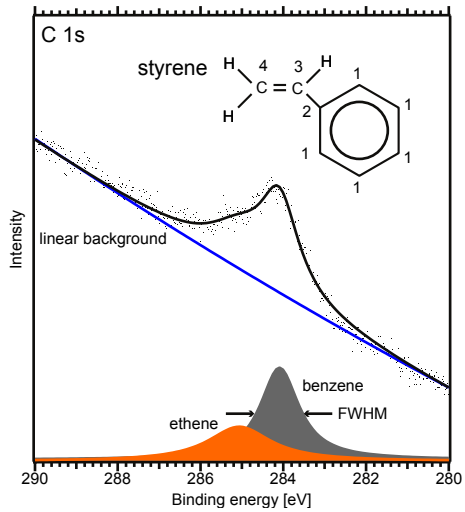

Figure 2.5: A C 1s XP spectrum acquired of styrene adsorbed on Ag clusters dispersed on FeO(111) supported by Pt(111). The spectrum exhibits a linear background and two components are fitted in accordance to the benzene ring and ethane derivative.

The lineshape of a component in an XP spectrum is a combination of different phenomena. Firstly, the measured final state have a finite lifetime which give rise to a broadening in accordance with Heisenberg's uncertainty principle. This is referred to as the natural linewidth and is modeled by a Lorentzian function. Secondly, broadening mechanisms, such as uncertainties from the instrumentation and vibrations in the solid lattice of the surface, have a Gaussian appearance. To model these mechanisms a Voigt function is used which is a convolution between a Lorenztian and a Gaussian. In the case of gases, the vibrational components are typically well resolved and by fitting a Voigt function to the peaks in the XP spectrum, the full width at half maximum (FWHM) of the contributions can be separated. For solids, however, the vibrational components are typically not resolved and therefore the above discussion is not applicable. Here, the line broadening by a multitude of lattice vibrations completely obscures the natural linewidth. In practice, even if a Voigt function is fitted to the data, the Lorentzian FWHM will not hold any physical meaning. However, it is often needed in order to get a good fit and is therefore included in some fashion.

For metallic peaks, the situation is slightly different. Since there is no band gap there is a large electron-hole pair generation which renders the peaks asymmetric. This is well described by the Doniach-Šunjić lineshape [18]. This lineshape hold a Lorentzian width and is convoluted with a Gaussian for curve fitting.

The typical approach to XPS analysis is to separate the background and components by first subtracting a background and secondly curve-fitting components according to the lineshapes outlined above. Often, the measured spectrum is a

sum of several different species. For instance, figure 2.5 show a C 1*s* XP spectrum of styrene adsorbed on Ag clusters supported by a bilayer FeO(111) on a Pt(111) substrate. The spectrum clearly exhibits a linear background and one peak with a shoulder component on the high-binding energy side. The chemical inequality of the C atoms in the styrene molecules results in four different C species (cf. figure 2.5). However, most of the expected shifts are small and will not be resolved adequately in the spectrum. This leads to the observation of two components and, thus, it is sufficient to curve-fit two components assigned to the benzene ring and the ethane derivative. This is a fairly straightforward example as it involves relatively few components. If larger systems are investigated, more complex curve-fitting models are required. One such situation is presented in **Paper II** where the carbon atoms in the investigated molecular complex can be described by three components. However, upon forming multiple adlayers the measured signal will be a sum of three components per layer with relatively small energy separations in between. By only fitting uncorrelated components, the internal energy separation between the adlayers and their internal intensity ratio would be impossible to extract. Hence, when performing curve fitting it is important to employ a model based on pre-existing knowledge of the investigated system, such as molecular stoichiometry and/or elemental composition.

2.1.2 X-ray absorption spectroscopy

A range of techniques which is almost as commonly employed at synchrotron radiation facilities as photoelectron spectroscopies are the X-ray absorption spectroscopies. Similarly to XPS, the data obtained is element specific, but also influenced by the chemistry and geometry of the neighboring atoms. When a photon interacts with an electron, depending on the photon energy, it can either promote the electron into the (i) vacuum , *i.e.* it becomes a photoelectron, or (ii) to an unoccupied state. If the photoelectrons are measured as a function of photon energy there will be a rapid increase in intensity, seen as an *edge*, as the photon energy equals the ionization energy of the investigated orbital. With increasing photon energy, the amount of photoelectrons will decrease monotonously as the cross section for photoionization decreases with the exception of low intensity oscillations. These oscillations occur up to several hundreds of eV over the absorption edge and are due to interference between the photoelectron and the nearest coordination sphere. Thus, the oscillations are related to the local geometry of the probed atom. In the second case, a well-defined and intense absorption structure is characteristic at energies of 5-10 eV below the absorption edge up to 50 eV above. The former is generally referred

to as the pre-edge structure, while the latter is called the near-edge structure. X-ray absorption (XA) spectra cover a wide range of energies and hence, there are different names used for the appropriate energy range. The studies of the high energy oscillations are typically referred to as extended X-ray absorption fine structure (EXAFS) due to the wide range of energies, while studies of the pre- and near-edge regions are typically referred to as near-edge X-ray absorption fine structure (NEXAFS) or X-ray absorption fine structure (XAFS). These are in principle synonymous as they both concern the near edge, however, the name NEXAFS is often used when discussing absorption of the 1 s orbital (K-edge) of low Z elements (*e.g.* C, O, or N) [21]. In this thesis both the pre- and near-edges are used as they both contain information of the local environment of the atom.

The ability of XAS to detect bonding specificity of the probed atoms is used in **Paper I**. Here, the chemical bonding of the probed C atom shifts the photon energy at which the resonances appear. In addition, the XAS signal also contains information about the local electronic arrangement which in **Paper IV** and **Paper V** is used to investigate the oxidation state of Fe atoms as the XAS signal is more sensitive to such effects compared to XPS.

Determination of angles by XAS

In addition to information about the chemical state of the absorbing atom, XAS can in certain cases provide information about the orientation of the investigated sample. This is true for samples that have only a few directions of their orbitals. For instance, molecules containing phenyl rings, graphene adlayers, and certain thin films.

As for XPS, the cross section of the photon interacting with the electron is derived by the transition matrix element (equation 2.3). In XPS, the final state of the electron can be approximated by a plane wave that has little directional dependence. In contrast, the final state in XAS is a bound state which makes it highly localized. To maximize the transition probability, the momentum transfer induced by the photon needs to be directed towards the maximum of the final state orbital lobes. Hence, if the light source is highly polarized, as for example found in beamlines of electron storage rings, the tilt angle of adsorbates can be determined.

The intensity of a transition in XAS can be approximated by [22]

$$I \propto A \cdot \cos^2 \delta, \tag{2.5}$$

where A is the square of the matrix element and δ is the angle between the electric field vector of the impinging radiation and the direction of the orbital. As outlined in Ref. [21], if a threefold symmetry of the sample is assumed the azimuthally averaged resonance intensity can be expressed as

$$I = B\left(P\cos^2\theta(1-\frac{3}{2}\sin^2\alpha)+\frac{1}{2}\sin^2\alpha\right), \tag{2.6}$$

where B is a constant representing the total intensity, P is the degree of polarization of the radiation and θ is its incidence angle, and α is the orbital tilt angle. As illustrated in figure 2.6, the incidence angle is defined as the angle between the surface plane and the incoming radiation. Hence, if the degree of polarization is known, and by measuring the resonance intensities as a function of photon incidence angle, equation 2.6 can be fitted to the resulting curve and the adsorption angles can be extracted. P depends on the light source and, for instance, was assumed to be between 0.9 and 0.95 for the now decommissioned beamline D1011 at the MAX-II storage ring where the XAS data in **Paper I** were measured.

The angular dependence of XAS data is illustrated by the two iodobenzene XA spectra shown in figure 2.6. The top spectrum is acquired with a grazing incidence angle of 20°, while the bottom spectrum is acquired at normal incidence. In the top spectrum a large enhancement of the π^* resonances is seen which indicates that their respective orbital vectors are directed along the surface normal. In the normal incidence measurement, an enhancement of the σ^* resonances is

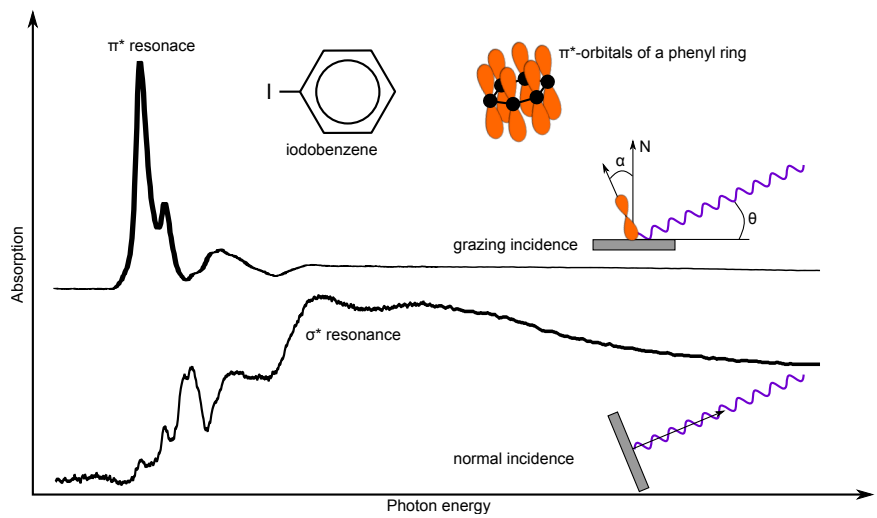

Figure 2.6: A depiction of the angular dependence when promoting electrons into highly directed materials. The measured signal strongly depends on the overlap of the radiation E-vector and the direction of the final state orbital.

seen which suggests that their orbital vectors are pointing parallel to the surface. Thus, the angle between the plane of the benzene ring and the surface plane, *i.e.* the *tilt angle*, of the ring can be determined. The above outlined method is used in **Paper I** to determine the tilt angle of halogenated benzenes and a more detailed discussion of the angular dependence in XAS is found in Ref. [21].

Acquisition of XAS data

There are several ways to observe X-ray absorption. The most direct approach is to measure the X-ray intensity before and after passing through the object of interest. A severe drawback with this method is that it requires the sample to be transparent to X-rays. Most often, this is not the case in surface science investigations and, hence, indirect methods of measuring the rate of absorption are used. Here, indirect refers to the fact that a decay must occur before detection is possible. For soft X-ray XAS measurements the most relevant decays are fluorescence and Auger decay, cf. figure 2.7. In an Auger decay, the core hole is filled by one of the valence electrons, however, instead of emitting light, the energy is transfered to another valence electron which is subsequently emitted as an *Auger electron*. Hence, the detection methods possible are fluorescence- and electron yield modes.

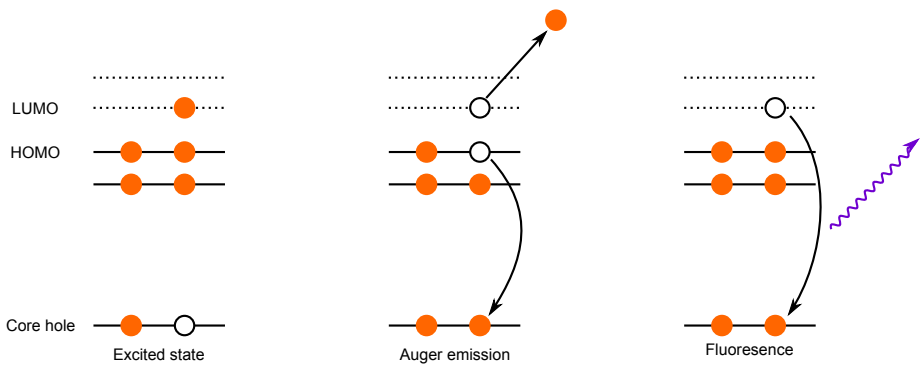

Figure 2.7: A schematic drawing of the excited state decay with a core hole present. The core hole is filled either by Auger decay after emission of an Auger electron or fluorescence decay which results in the emission of a photon.

Fluorescence yield (FY) experiments hold two major drawbacks for the investigations presented in this thesis: (i) the low Z-elements, such as carbon, nitrogen, and oxygen, predominately exhibit Auger decay. (ii) X-rays have a long escape depth and the measured signal is hence dominated by the bulk, which renders FY not particularly surface sensitive. Therefore, FY has not been used in the work of this thesis as I have mostly studied low Z-elements at surfaces.

Instead, three methods for detecting absorption are available: Auger electron yield (AEY), total electron yield (TEY), and partial electron yield (PEY). The AEY mode is beneficial as it can be recorded by the same equipment as used for XPS measurements. The energy of an Auger decay is element specific and the Auger electrons can readily be distinguished from other measured electrons. In addition, since the Auger decay process is independent of the incoming photon energy, the Auger electrons always appear at the same kinetic energies. Hence, an AEY absorption spectrum is acquired by monitoring a constant kinetic energy with the recorded intensity as a function of photon energy. The measured intensity is proportional to the X-ray absorption cross section for the promotion of a core electron into an unoccupied orbital and, hence, the unoccupied states are mapped by the spectrum [21].

In TEY mode, all ejected electrons are measured. This implies that also photoelectrons and inelastically scattered electrons are measured. The vast majority of emitted electrons are those which have been scattered inelastically, which means that a TEY measurement is dominated by the signal from the bulk. Just as FY, TEY is not ideal for surface measurements. In PEY mode, however, only electrons above a certain kinetic energy threshold are considered. Hence, this threshold is chosen so that most of the collected electrons have not been scattered inelastically. As a result, the collected electrons originate mostly from the surface which makes PEY a suitable collection mode for investigations of surfaces. In a typically PEY mode measurement, the emitted electrons are detected by an multichannel plate (MCP) detector with a mesh in front of it. An electric field is applied to the mesh, which sets the electron detection threshold.

2.1.3 Synchrotron radiation

Spectroscopy is by the oxford dictionary defined as 'the branch of science concerned with the investigation and measurement of spectra produced when matter interacts with or emits electromagnetic radiation' [23]. As the light plays such a central role in spectroscopy, the possible experiments are ultimately limited to the available light sources. For instance, to investigate the core levels of atoms, high energy light is required.

In 1895 Wilhelm Carl Röntgen discovered an unknown type of radiation while investigating electricity passing through a gas at low pressure. The discovery of these 'X-rays' was followed by William Henry Bragg and William Lawrence Bragg's discovery of the radiations diffraction by crystalline samples. Later, in 1912, Max von Laue described X-rays as waves. In recognition of their achievements, all four were awared Nobel Prizes. Clearly, X-rays have become an

important tool for all fields of natural science, but also for applications in other fields such as medicine and material science.

Conventionally, X-rays are produced by accelerating electrons in vacuum and subsequently bombarding a target material with these electrons. The impinging electrons eject core electrons from their inner shells and fluorescence decay leads to emitted X-rays having well defined photon energies. In addition, the bombarding electrons produce bremsstrahlung and the final X-ray spectra is thus broad with some sharp features. The production of bremsstrahlung is due to the emission of radiation by accelerated charges as readily explained by classic electrodynamics.

The power emitted by accelerating charges is, in general, low but increases with the square of their momentum. This is used at the electron storage ring of a typical synchrotron radiation facility. In a storage ring, the electrons travel close to the speed of light. Due to relativistic effects, light is emitted in a cone in the forward direction of the electrons movement as the electron is accelerated onto a curved trajectory. The acceleration of the electrons in an electron storage ring is achieved mainly in two ways: by bending magnets which produce a wide energy spectrum or by the use of undulators or wigglers. Undulators and wigglers are devices which contain arrays of magnets with alternating polarity that create an alternating magnetic field perpendicular to the electrons trajectory. Due to the magnetic field, the electrons travel in a sinusoidal path and each of the pairs of magnets in the array acts as a bending magnet [16], cf. figure 2.8. The total yield is enhanced by nearly a factor N compared to a single bending magnet, where N is the number of periods in the device. In addition, the produced radiation interferes at the many co-linear points as the bends of the sinusoidal path are multiples of the wanted wavelength and a spectrum of quasi-monochromatic peaks is produced [24]. By tuning the gap distance of the undulator the sinusoidal path is altered, which allows for tuning of the energy of the produced radiation. The ability to finely tune the energy of the radiation along with other advantages, such as high flux of collimated and highly polarized light, makes storage rings some of the most versatile light sources available for spectroscopic investigations.

A majority of the included work was performed at the MAX IV Laboratory, which is the Swedish national synchrotron radiation facility located in Lund. Some of the presented work was performed at the old laboratory which housed the MAX-I to MAX-III storage rings, where I mainly measured at the MAX-II ring. Today, the old laboratory is closed down and a new laboratory has started operations. The new laboratory houses two storage rings: A 3 GeV ring with a circumference of 528 m and a 1.5 GeV ring with a circumference of 96 m.

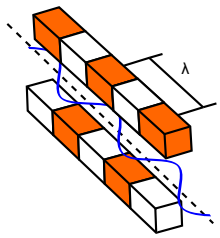

Figure 2.8: Schematic illustration of an undulator. The electrons traveling in the magnetic field deviate from their nominal trajectory and emit radiation in every bend of the sinusoidal path. The emitted power is proportional to the number of periods with length λ.

The 3 GeV ring uses the newly developed seven-bend achromat magnet lattice where the magnets are formed from a single solid block, which allows for a low emittance electron beam [25]. Commonly, free-electron lasers (FELs) are often counted among the 4th generation synchrotron radiation facilitates. However, as they do not produce light from a storage ring, the MAX IV Laboratory is arguably the first 4th generation synchrotron radiation facility in operation.

2.1.4 The SPECIES beamline

During my Ph.D. studies I was involved in the commissioning of the SPECIES beamline discussed in **Paper VI**. The SPECIES beamline is an undulator beamline at the 1.5 GeV ring of the MAX IV Laboratory, which hosts two branchlines with the resonant inelastic X-ray scattering (RIXS) and the APXPS endstations. Below, a short description of the beamline follows, which highlights the important features with focus on APXPS investigations.

A schematic view of the SPECIES beamline layout is shown in Fig. 2.9. The light source of the beamline is an elliptically polarizing undulator (EPU). The EPU was manufactured in house and is of the APPLE-II type. It has 41.5 periods with a period length of 61 mm. This undulator is constructed with four instead of two magnetic arrays, which allows for variable polarizations. The undulator is capable of producing circularly polarized light with photon energies between 40 and 300 eV and fully linearly polarized light with adjustable direction over the full photon energy range between 27 and 1500 eV. Thus, the SPECIES beamline covers the lower end of the soft X-ray regime. SPECIES is complemented by the HIPPIE beamline (110-2000 eV photon energy) which also hosts an APXPS instrument. Hence, the MAX IV Laboratory has APXPS capabilities over the full soft X-ray regime.

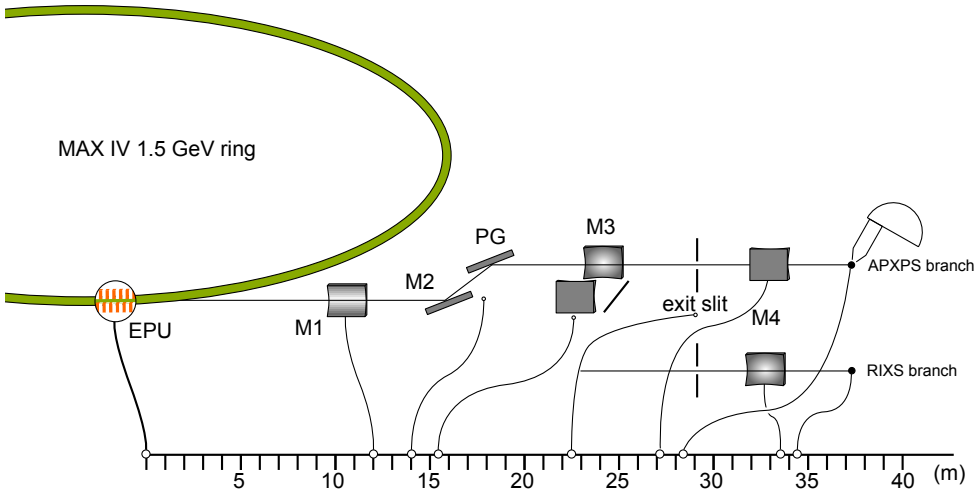

Figure 2.9: Schematic layout of the SPECIES beamline.

The monochromator of the SPECIES beamline houses two plane blazed gratings: a Au-coated grating with 1221 lines/mm and a Ni-coated grating with 250 lines/mm. The Ni-coated grating provides an increase in flux over the Au-coated grating in the 200-600 eV photon energy range. The beamline allows for switching between two refocusing mirrors (M3), which focus onto two different exit slits for the different branchlines. Each of the branchlines hosts a separate refocusing mirror (M4). The two end stations have very different requirements in terms of the X-ray spot size. RIXS requires a small spot with high photon density while a larger spot has been chosen at the APXPS beamline to match the acceptance of the electron energy analyzer.

The RIXS branchline utilizes an ellipsoidal refocusing mirror (M4) to achieve the small spot and this is the most common type of mirror used at the soft X-ray beamlines at the MAX IV Laboratory. For the APXPS branchline, in contrast, a torroidal mirror is employed. Since the spectrometers field of view is fixed, a spot size independent of photon energy and exit slit size is desirable. In addition, a larger spot size decrease the amount of beam induced effects, or beam damage, of the samples under investigation. This is realized by defocusing the beam waist at the sample location by the monochromator magnification and an astigmatically focused torroidal mirror [26]. By having the horizontal focus at the sample location and the vertical focus tens of millimeters further downstream, the vertical size becomes dependent on the source divergence, which can easily be controlled. This scheme allows for the single refocusing mirror and yield a beam spot of about 100 μm, independent of choice of exit slit size and/or photon energy.

2.1.5 Ambient pressure X-ray photoelectron spectroscopy

XPS is a popular and very powerful technique for the investigation of the electronic structure and thus the chemistry of surfaces. One of the main reasons is the limited IMFP of electrons in solids which makes the technique very surface sensitive. The same mechanisms causing the short electron IMFP in solids also limits the IMFP of electrons in gases. For instance, electrons with a kinetic energy of about 100 eV have an IMFP of about 1 mm when traveling through 1 mbar of water vapor [27]. This distance is short compared to the typical distance between sample and spectrometer entrance, commonly a few centimeters. In addition, in order to operate the spectrometers, the pressure at the MCP in the detector needs to be kept in the 10^{-5} to 10^{-6} mbar regime. It is, however, possible to increase the gas pressure above the sample surface substantially and still keep the MCP at a pressure in the 10^{-8} mbar scale in APXPS instruments.

The group of Kai Siegbahn at Uppsala University built the first APXPS instrument already in the early 1970s [28, 29]. Here, a differential pumping scheme was positioned in front of the electrostatic lens system of a hemispherical electron energy analyzer. This allowed for APXPS investigations of liquids and of the liquid/vapor interface. Towards the end of the decade, Richard Joyner and Wyn Roberts investigated the vapor/solid interface using a similar scheme [30]. All these instruments employed laboratory X-ray anodes with a comparatively low flux and, hence, only a few instruments were built. First in the late 1990s a synchrotron-based APXPS instrument was developed by the Lawrence Berkeley National Laboratory (LBNL). This instrument combined the high flux of a synchrotron radiation facility with a differentially pumped electrostatic lens system on the hemispherical analyzer, which vastly improved the transmission [31]. The instrument was soon followed by a second-generation instrument developed jointly by LBNL, the Fritz Haber Institute, Berlin, and SPECS GmbH, Berlin [27]. In the last decade, APXPS has seen an upswing and is now available at a number of synchrotron facilities and commercial laboratory instruments are available.

Instrumentation

Various APXPS systems realize the sample environment in different ways, as is detailed below. The electron energy analyzer, however, operates on the same principle for most systems. The spectrometer used at the APXPS instrument of the SPECIES beamline is a SPECS Phoibos 150 NAP analyzer and is schematically illustrated in figure 2.10. The analyzer has four pumping stages: pre-lens,

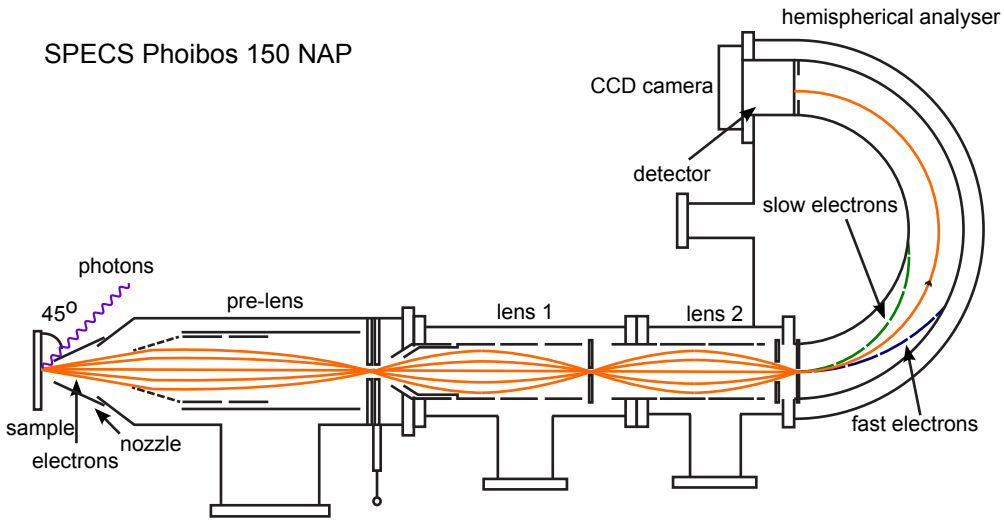

Figure 2.10: A schematic image of the SPECS Phoibos 150 NAP analyzser used at the SPECIES beamline. The image is adapted from [32].

lens 1, lens 2, and the hemisphere. All stages are separated by apertures and the apertures between lenses 1 and 2 are variable in size. The pre-lens, lens 1, and lens 2 are equipped with electrostatic lenses, which focus the electrons collected by the first aperture onto each consecutive pinhole. These lenses also perform the electron retardation before energy separation in the hemisphere. This arrangement reduces the pressure by about four orders of magnitude between the sample environment and the pre-lens. Hence, the IMFP is significantly increased already at the first differential stage. The aperture nozzle of the first stage is typically positioned within a millimeter of the sample. Thus, the sample can be exposed to pressures in the mbar regime as the emitted electrons travel only a very short distance through the gas.

The simplest approach to APXPS instrumentation, which I used in **Paper II**, is to attach a cone with a pinhole permanently on the differentially pumped electron energy analyzer, cf. figure 2.11(a). This is the method chosen at, among others, beamlines 9.3.2 and 11.0.2 at the advanced light source (ALS), and the TEMPO beamline at synchrotron SOLEIL in Paris. The major benefit of this method is the ease of operation, which ties well into the operation of synchrotron radiation facilities with multiple user groups. There are, however, a few drawbacks with this approach. The volume of the 'reactor', *i.e.* the vacuum chamber hosting the analyzer, is typically many liters. This, coupled with the fact that

the chamber is usually only pumped through the small nozzle, makes gas exchange quite slow. In addition, the nozzle itself typically constrains the effective collection angle of the spectrometer which impacts the acquisition time while not measuring at ambient conditions, *e.g.* for UHV reference measurements before or after a reaction. The acquisition time is important as the available time at synchrotrons is highly limited and prolonged exposure to the intense beam run the risk of damaging the sample. However, the largest drawback is that UHV pressures are practically unobtainable without a bake-out of the instrument after the first APXPS measurement. The loss of UHV capabilities makes the pre-reaction characterization harder and, typically, it is more difficult to correlate the APXPS results to UHV studies.

The second approach make use of an analyzer with a fixed nozzle, just as described above, with the distinction that the reactor chamber is exchangeable, cf. figure 2.11(b). This allows for highly specialized sample environments, *e.g.* corrosive gases, liquids, electrochemical cells *etc.* In addition, since the chambers are exchangeable, the risk of pollution from a previous instrument user is minimized. The benefit with this approach is quite self-explanatory as specialized sample environments allow for investigations that otherwise would need several dedicated instruments. In addition, the reactor size is highly customizable and the volume can be kept small, which allows for flow measurements with a high gas exchange rate. The drawbacks are, however, that it typically means that the ability to measure in UHV is lost and surface science preparation tools are in general not accessible. Hence, the exchangeable chamber approach enables highly specialized sample environments but the linking of UHV studies with the results in ambient conditions becomes less accessible. Setups of this type are available at, for instance, beamline 11.0.2 at the ALS, the VERSOX beamline at Diamond, and at the HIPPIE beamline of the MAX IV Laboratory.

An approach that was developed in collaboration between Lund University and SPECS GmbH is the so-called 'Lund' or cell-in-cell concept, cf. figure 2.11(c). This concept aims to combine the benefits of the above discussed approaches with none of the drawbacks and was used in the work leading to **Paper I**, **Paper III**, and **Paper IV**. Here, a reaction cell is positioned within the main vacuum system that, when attached to the spectrometer, allows for ambient investigations. It is important to note here that the nozzle is located at the reaction cell itself, thus allowing for rapid UHV XPS measurements when the reaction cell is not in use. This, coupled with the ability to host a larger vacuum system that allows for UHV preparations, enables investigations in the full pressure range from UHV into the mbar regime. The cell itself is exchangeable, which allows for fully customized sample environments just as in the exchangeable chamber

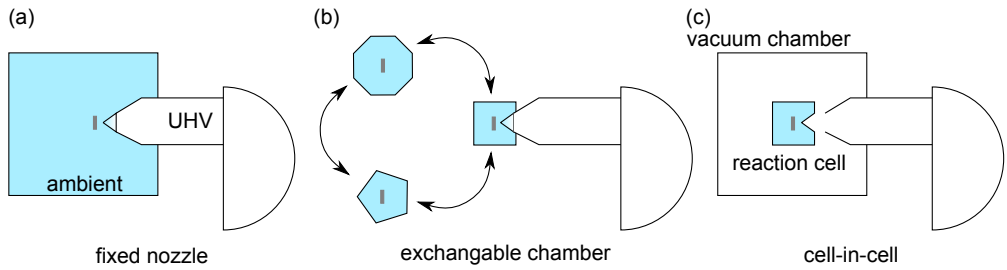

Figure 2.11: The principle layout of *in situ* environments used in current APXPS systems. The ambient environment is marked by the blue background.

concept. Additionally, due to its design, the reactor volume is kept small, which enables fast gas exchange and measurements in both batch and flow modes. Hence, the Lund concept allows for a wide range of sample environments, the full UHV to mbar pressure range, flow and batch mode investigations, and fast gas exchange. The disadvantage of this approach is that it is mechanically complex and the sample needs to be transferred from the overall vacuum system to the reactor. This is done by in vacuum manipulators which, for unexperienced users, can pose an issue. This is not a problem for laboratory systems but can present a problem at a synchrotron facility since many different, often new, users operate the instrument. The cell-in-cell concept is the chosen approach for the APXPS instruments at the SPECIES and HIPPIE beamlines at the MAX IV laboratory and is employed by many laboratory instruments.

Experimental considerations

The introduction of a gas in an APXPS experiment requires a few experimental considerations that set apart the APXPS measurements from standard XPS. For instance, surface phases are highly dependent on the gas environment. In addition, there will be a signal in the ambient pressure XP (APXP) spectra which originate from the gas just above the surface. In fact, using an APXPS instrument, it is fairly straightforward to study the gas phase species of the gas/vapor of interest, if the vapor pressure is above the detection limit. Typically, the instrument offers the positioning to move the sample along the analyzer axis, which allows for gas composition analysis as a function of distance from the sample surface. Hence, a single APXP spectrum can contain information from a few atomic layers below the surface, the solid/gas interface, and the gas just above the surface.

Pressure limitations

Pressure limitations arise from multiple factors. As the MCP of the detector needs to be kept in high vacuum, the differential pumping puts a fundamental limit to which pressures are attainable with a specific setup. Another concern is how the instrument is separated from the beamline itself. This is achieved mainly in two ways, either by a differential pumping scheme (TEMPO) similar to that of the analyzer, or by an X-ray transparent window (beamlines SPECIES, HIPPIE, 9.3.2, and 11.0.2). The pumping efficiency sets the limit in the former, and the strength of the window (commonly SiN_2) in the latter. Currently, for the APXPS instrument at the SPECIES beamline this limit is 25 mbar. An important consideration regarding pressure is related to the fact that significant pumping occurs through the aperture nozzle, as visualized in Ref. [33].

The influence of the aperture nozzle on the pressure was investigated [34] by Ogletree *et al.* In this study, it was found that the surface should be positioned around two aperture nozzle diameters away from the spectrometer opening if the pressure in the field of view of the spectrometer at the surface should be homogeneous and the same as the background pressure. For instance, the diameter of the aperture nozzle at the SPECIES beamline is currently 0.3 mm and thus, the sample should be positioned 0.6 mm away from the nozzle to obtain a homogeneous pressure in the spectrometer field of view at the surface. Hence, a smaller aperture nozzle allows for higher working pressures in two ways. Firstly, the sample can be positioned closer to the nozzle, which reduces the distance the electrons need to travel trough gas. Secondly, a smaller nozzle improves the differential pumping, which helps in maintaining the pressure at the MCP.

Energy referencing at the solid/gas interface

In photoemission experiments the binding energies are often referenced to the Fermi level. This is a robust approach to correct for the generally unknown analyzer work function and inaccuracies in the photon energy. However, molecules in the gas phase do not have a Fermi energy. Therefore, the ionization potential is measured which is referenced to the vacuum level. Commonly, the ionization potentials of molecules are a few eV higher compared to the binding energy of their adsorbed counterparts and, thus, the different contributions to the spectra can be distinguished easily [35]. As an example, the lines of CO, CO_2, and O_2 in the gas phase are separated by several eV from those of adsorbed CO and O on Ir(111) and Pt(111) as observed in **Paper III**. However, since APXP spectra typically are calibrated to the Fermi energy of the solid, the observed ionization energies of the gas warrant further discussion.

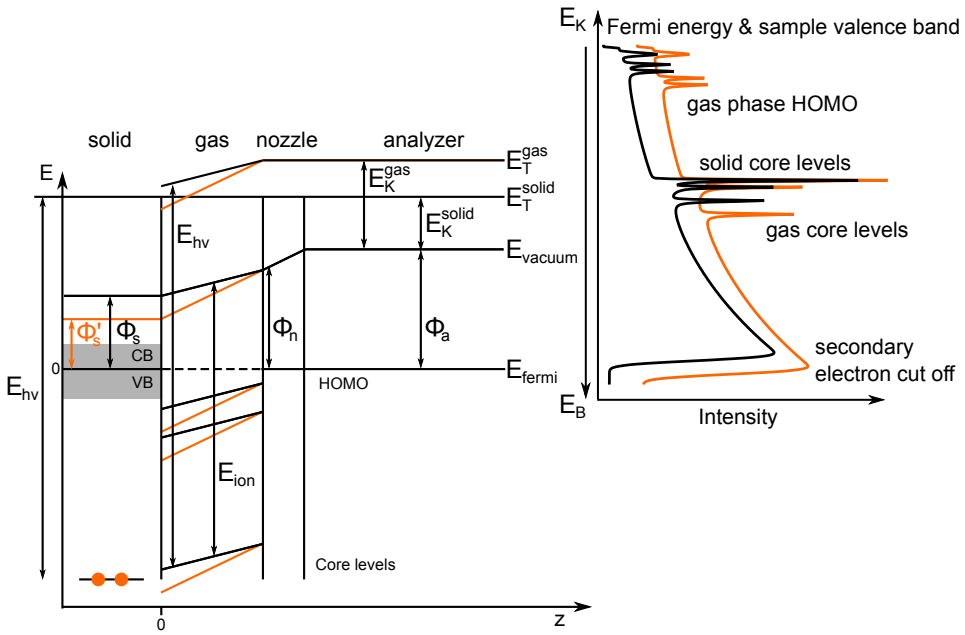

Figure 2.12: Energy diagram of the energies involved in the photoemission process. The black lines represent the situation which generates the black spectrum. The orange lines are the relevant energies after a surface work function change which lead to the orange spectrum. After a work function change, the energy levels of the gas phase peaks shift as does the secondary electron cutoff, while the peaks from the solid remain at the same energy.

Figure 2.12 shows an energy diagram of an APXPS measurement. The sample and analyzer are electrically connected so that the Fermi energies are aligned. This enables the binding energy calibration for the solid sample. In the photoemission event, a bound electron from the solid is promoted to a total energy of E_T^{solid} by the photon with an energy of $E_{h\nu}$. The electron will remain at this total energy while traveling to the analyzer where the observed kinetic energy, E_K^{solid}, is the difference between the analyzer work function, Φ_a, and the total energy of the electron

$$E_K^{solid} = E_T^{solid} - \Phi_a. \tag{2.7}$$

If the energy is assigned to be zero at the Fermi level, the total energy of the electron is $E_T^{solid} = E_{h\nu} - E_B$, where E_B is the binding energy. Hence, equation 2.7 becomes

$$E_K^{solid} = E_{h\nu} - (E_B + \Phi_a), \tag{2.8}$$

which is exactly equation 2.2 and demonstrates that it is indeed the analyzer work function which needs to be considered. Further, it shows that the observed kinetic energy from a solid is independent of the surface work function of the solid.

For measurements of the gas the situation is slightly different. Following the argument of photoemission from the solid, photoemission from a core level of the gas promotes the bound electron to the total energy E_T^{gas}. The observed kinetic energy is, just as for the solid, the difference between the total energy and the analyzer work function. As there is no Fermi energy for the gas, the total energy of the emitted electron is referred to the vacuum level $E_{vacuum}(z)$, which depends on where it is measured, and the ionization potential, E_{ion}. Hence, the observed kinetic energy from the gas can be expressed as

$$E_K^{gas}(z) = E_{h\nu} - (E_{ion} - E_{vacuum}(z)) - \Phi_a. \tag{2.9}$$

The vacuum level of the gas aligns to the work function of the surrounding material. In the situation depicted in figure 2.12 the surface work function, Φ_s, is smaller than the work function of the nozzle, Φ_n. This gives rise to the continuously increasing vacuum level of the gas shown in figure 2.12. As the experiments probes a small volume above the sample, this slope results in a broadening of the measured peaks, although this effect is small. Instead, consider an APXPS measurement where the gas is probed just above the sample and the gas and surface vacuum levels have aligned, equation 2.9 now becomes

$$E_K^{gas}(z = 0) = E_{h\nu} - E_{ion} - (\Phi_a - \Phi_s). \tag{2.10}$$

Hence, in an APXPS measurement the observed kinetic energy of electrons emitted by the gas is affected by the surface work function of the solid sample.

In this discussion the influence on the gas vacuum level by the ions created from other photoemission events is omitted. During an experiment, the remaining gas ions will generate a field that modifies E_{vacuum} and, hence, the observed kinetic energy. This effect is referred to as *space charging* and makes accurate determination of E_{vacuum} difficult. However, for the purpose of the described scenario, the space charging effect it is considered a constant and therefore is disregarded.

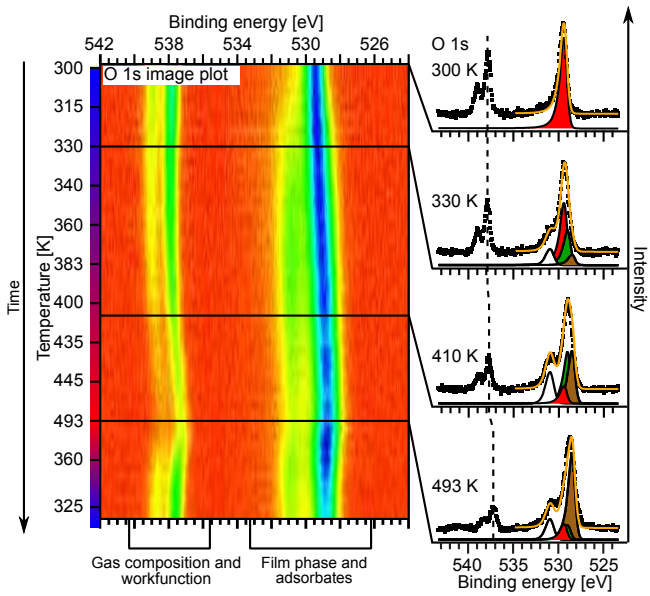

Figure 2.13: An image plot of O 1*s* APXP spectra acquired during the bilayer FeO to trilayer FeO_2 phase transition. The surface is exposed to 0.6 mbar O_2 during the entire measurement and the heating ramp starts at the top of the figure. The sample is heated to 493 K and subsequently cooled. The image plot shows that the gas phase peaks binding energy shift coincides with the change in surface phase. Hence, the surface work function shift is an indication of a surface phase change.

The surface work function depends on the adsorbate structure, and hence, it is expected to change during the course of *in situ* APXPS experiments. In figure 2.12 the orange lines depict a situation were the surface work function is lowered. For photoemission from the sample, the observed kinetic energies are unaffected in accordance with equation 2.8. For the gas, in contrast, the observed kinetic energy shift with the surface work function in agreement with equation 2.10. This results in a measured spectrum where the peaks from the solid remain at fixed binding energies while the gas phase peaks and secondary electron cutoff shift in apparent binding energy, as depicted by the orange spectrum in figure 2.12. Therefore, the shift in surface work function can be accurately determined by monitoring the measured binding energy position of the gas phase peaks in APXPS experiments and this is used in **Paper III** and **Paper IV**. Figure 2.13 shows APXP spectra of the surface phase change investigated in **Paper IV**. The investigated iron-oxide film is exposed to 0.6 mbar O_2 while heating the surface. The gas phase components shift in binding energy as the bilayer FeO transforms into trilayer FeO_2, which is evident from the spectra extracted from the image plot. Hence, the surface work function shift is an indication of surface phase changes. A similar situation similar to the gas shifts is found for measurements on thin liquid films, as is detailed in Refs. [29, 36]. Further discussions of energy referencing in APXPS and XPS are found in Refs. [35, 37, 38].

Recent developments and future of APXPS

The current interest in APXPS has lead to commercial laboratory systems being available, however, these systems are predominately directed towards academic users. Recently, a 'turn-key' APXPS system, the EnvironESCA [39], was developed by SPECS GmbH with emphasis on sample throughput and easy operation to expand the user base outside the academic area. Other instrumental advances includes the HiPP-3 analyzer [40] manufactured by Scienta Omicron. This spectrometer has a new lens mode called *swift acceleration* which improves electron transmission by up to a factor of 10 and an imaging mode with a resolution better than 10 μm. This analyzer is employed at the HIPPIE endstation. Additionally, the detectors at the APXPS instruments at the SPECIES and HIPPIE beamlines have a maximum acquisition rate of 120 Hz. These fast detectors allows for pump-probe measurements and fast acquisition of gas-surface interactions for, among others, atomic layer deposition growth characteristics, but also the surface chemistry in varying gas compositions.

A new scientific area in the APXPS community is to use so-called tender X-rays (2-5 keV). The increase in photon energy from a typical soft X-rays experiment leads a longer electron IMFP which allows for the measurement of the vapor/liquid interface but also the liquid/solid interface of thin liquid films in the same measurement. These have, for example, been applied to the electrochemical measurement of the oxygen reduction reaction [41], but also the so-called electrochemical double layer has been investigated [42].

Other recent advances involves combining APXPS with other spectroscopic techniques. As for instance, APXPS has been combined with infrared spectroscopy [43]. In this study, the ability of APXPS to obtain a complete elemental- and chemical environment profile was combined with the ability to provide information on the orientation and chemical bonding of molecular adsorbates of infrared reflection absorption spectroscopy (IRRAS) to investigate CO absorption on Pd(100) at mbar pressures. The combination lead to the identification of a CO species adsorbed at atop sites which is deemed uncommon for Pd(100). Another combination approach is between APXPS and standing wave spectroscopy [44]. Here, it was shown that the spacial arrangement of bulk- and interface chemical species could be determined with sub-nm accuracy along the direction perpendicular to the interface on a NaCl and CsOH hydrated α-Fe_2O_3 model system.

2.2 Scanning tunneling microscopy

While XPS and XAS are excellent techniques to study the chemistry of surfaces, it does not give any structural information. Structural sensitive techniques based on photons and electrons are, for instance, surface X-ray diffraction and low electron energy diffraction. Both these methods are averaging techniques and have proven useful in determining surface structures. It is, however, possible to obtain highly localized structural information by so-called scanning probe techniques, such as scanning tunneling microscopy (STM) and atomic force microscopy (AFM).

The scanning tunneling microscope was invented in 1983 by Gerd Binnig and Heinrich Rohrer and rapidly became a standard surface science technique [45]. Later, in 1986, Binning and Rohrer were awarded the Nobel Prize [46] for the invention as it had revolutionized the field of surface science. The strength of STM is its ability to provide high-resolution real space images with a spatial resolution of about $\sim$1 Å in the surface plane and as low as 0.1 Å along the surface normal [47]. STM can also provide images of large scale areas in a short time, as fast as 15 msec/image [48, 49]. However, this is only possible in specialized instruments and the typical image acquisition time is significantly longer. In addition, STM images can be recorded at elevated pressures, with current designs allowing for pressures up to 6 bar [50]. Due to the possibility for short acquisition time and elevated pressures, STM has been employed during, among others, the oxidation of CO over Rh(110) [51], Pt(111) [52], and Pd(100) [53]. However, STM measurements in higher pressures are not without challenges. For instance, the ability for atomic resolution is typically lost.

Theoretical description of STM imaging

STM measurements are rather straightforward: an atomically clean and sharp tip is brought within a fraction of a nm to a conductive surface. This allows the wave function of the electrons at the surface to overlap with the tip. By applying a small bias, a finite tunneling current is generated. By convention, the bias V is applied to the sample. The bias results in an offset of the Fermi level of the sample, cf. figure 2.14. The offset creates a potential difference over the vacuum barrier which establishes a net tunneling current between tip and sample. The tunneling current is within the the Wentzel-Kramers-Brillouin

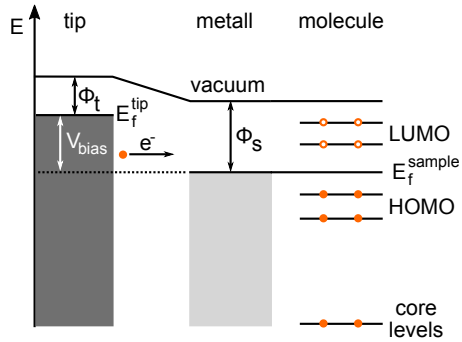

Figure 2.14: Energy diagram of an STM tip close to a metallic sample and a molecule. The bias is applied to the sample so electrons tunnel from the tip. In addition, the bias is large enough to allow for detection of the molecule since E_f^{tip} is above the LUMO of the molecule.

(WKB) approximation given by

$$I = \rho_T \rho_S V_A \exp\left(-2\sqrt{\frac{m(\phi_T + \phi_S)}{\hbar^2 z}}\right), \tag{2.11}$$

where ρ_T and ρ_S are the local density of states(LDOS) of tip and sample, respectively, V_A is the applied bias, m is the rest mass of the tunneling electron, ϕ_T and ϕ_S are the tip and surface work functions with z being the separation between them [54]. This equation highlights the strong dependence of the tunneling current to the separation, which is the origin of the high resolution attainable with the STM probe. The surface topography is imaged by raster scanning the tip over the surface while monitoring either (i) the tunneling current (constant height mode) or the (ii) z-position of the tip, while keeping the tunneling current constant with a feedback loop (constant current mode). Constant current mode is the most common and exclusively used in the work of this thesis.

As shown in equation 2.11, the tunneling current is highly dependent on the density of states, which may lead to some misconceptions. The resulting image is a convolution between the topography and the LDOS of the tip and sample. Thus, interpretation of STM images can be non trivial as changes of the tip, *e.g.* a new tip structure or tip chemistry by picking up atoms/molecules from the surface, may drastically change the apparent topography. For instance, the absolute height of an adsorbed species cannot readily determined with STM as atoms with high chemical affinity are imaged with larger apparent height due to the higher tunneling conductance [54].

Experimental setup of the scanning tunneling microscope

A schematic view of a typical STM instrument is shown in figure 2.15 where the most crucial components are indicated: the atomically sharp tip and the piezocylinder stack to which it is attached. Piezoelectric materials deform as a bias is applied over it. A finely tuned bias allows for Å precise positioning and raster scanning of the tip. In newer STM instruments, a piezocylinder is more common while in older instruments a tripod with one piezoelement per Cartesian axis is used. In my work, I have used both types of instrument with the piezocylinder in the work for **Paper II** and the tripod in the work of **Paper V**.

As the tip is positioned in the nm range from the surface and lateral raster scans in the Å range are executed, it is clear that even very small mechanical vibrations will severely influence the imaging. To minimize mechanical vibrations, the STM stage (scanner and sample) is placed on a platform which is partly suspended by springs inside the vacuum system and the rim of the platform is decorated with copper blocks. Before imaging, the platform is lowered so that these blocks are wedged in between magnets, which results in the platform resting on a magnetic field that decouples the STM stage from outside vibrations. This method of vibrational isolation is effective and referred to as *Eddycurrent* damping. Additionally, it is common to host the entire vacuum system on a platform which is vibrationally isolated from the building, *e.g.* by springs or resting on gas columns.

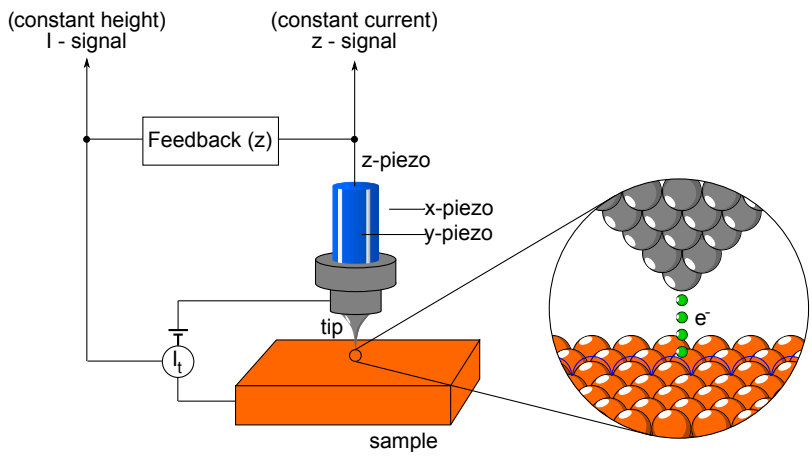

Figure 2.15: Schematic image of an STM instrument. Scanning is realized by varying the voltage over the x- and y piezoelectric elements while simultaneously monitoring either the tunneling current in constant height mode or the change in z position while employing constant current mode.

Chapter 3

Model systems

Pt-group metals are often highly active for oxidative catalysis and therefore often employed as catalysts. As they are rare in nature, much effort is put into minimizing the amount of noble metal required for active catalyst or replacing them with alloys of more abundant materials. This has lead to a widespread use of active nanoparticles dispersed inactive supports, which makes a complex system. The inherent complex nature of working catalysts makes them difficult to study with surface science methods and, therefore, model systems are often used. The purpose of the model systems is to simplify the real catalyst and mimic its most important properties. The following chapter introduces the model systems studied in my work. Starting at catalytic reactions over single crystal surfaces.

3.1 Single crystal catalysis

Crystals have long been admired due to their regularity and have been investigated since the 17th century, ever since Johannes Kepler proposed that the symmetry of snow flakes was due to a regular packing of spherical water particles[1]. Later, in 1669, Nicolas Steno demonstrated that for a particular type of crystal, the facets are the same for every exemplar. In 1784 the facets were decribed by René J. Haüy as a stacking of blocks, and William H. Miller indexed the different facets by a small sequence of integer numbers in 1839. Since then, the labels are referred to as Miller indices and are still used today for describing

[1] A copy of the original publication can be found at Ref. [55]

single crystal surfaces[2]. Prior to 1925, only naturally occurring single crystals could be studied until Percy W. Bridgman [57] reported on a technique to grow artificial single crystals which was later named after him. Ever since, investigations performed on single crystal surfaces have been the hallmark of surface science as they provide a unique possibility to study surface processes on large crystal lattices with millions of identical atoms without grain boundaries.

Catalytic oxidation over noble metal surfaces

In 1915 Irving Langmuir demonstrates that chemical reactions on the hot filaments of light bulbs were responsible for the 'clean up' of residual gases [58] in the bulb. From subsequent studies he concluded that gas impinging on a surface does not rebound elastically, but rather adsorbs by some cohesive force until it evaporates. With this in mind, Langmuir developed a model of adsorption [59], which states that every molecule that impinges onto a surface adsorbs, regardless of surface temperature. The coverage is determined by the rate of evaporation, which in turn is dictated by the interaction between the adsorbates and the surface. In addition, the model implies that molecular adlayers, *i.e.* the layer created by adsorbed molecules, are generally limited to a thickness of one molecule as the molecule-molecule interactions are weak. The development of the model sparked some controversy which lead Langmuir to investigate the adsorption of gases on plane surfaces of glass, mica and platinum foil [60]. Not only did Langmuir prove his adsorption model to be accurate, he also demonstrated the catalytic oxidation of CO over a Pt surface. Langmuir was awarded with the Nobel Prize in Chemistry 'for his discoveries and investigations in surface chemistry' in 1932 [61].

Ever since Langmuir's study of adsorption, late transition metal surfaces have been studied extensively and often focus has been on their catalytic properties. These investigations include structural studies of various adsorbates and surface reconstructions. Particularly relevant for this thesis are adsorption and reaction kinetics studies of CO on (111) surfaces of late transitions metals.

UHV studies of the adsorption of CO on Pt(111) have revealed a multitude of structures with various site coverages including p(4×4)[3], c(4×2) or c($\sqrt{3}$×2)rect structures [62, 63]. CO occupies both atop and bridge sites as illustrated in figure 3.1. Additional structures have been reported [64, 65], but will not be considered here. Further, the adsorption of O over Pt(111) surface has also been

[2]For a definition of Miller indices, cf. Ref. [56].

[3]For an introduction to Wood's notation, cf. Ref [47].

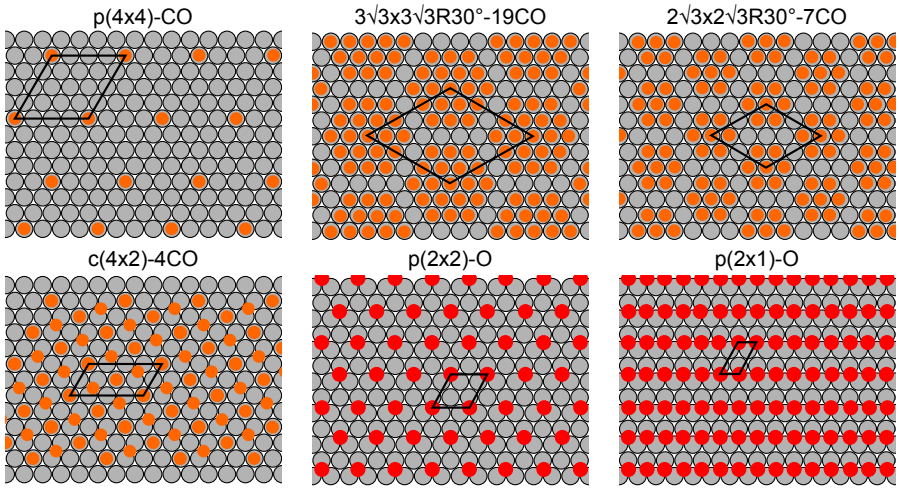

Figure 3.1: The most common CO and O adsorption structures in UHV and ambient conditions reported for Pt(111) and Ir(111). The gray balls represent Pt and Ir atoms while the orange and red balls represent CO molecules and O atoms, respectively.

investigated. These studies report that O predominately adsorbs at hollow sites in a p(2×2) structure [62], cf. figure 3.1.

Increasing the pressure to ranges between 10^{-6} and 1000 mbar reveals new adsorption structures not found in UHV. These structures are dense hexagonal moiré structures with a continuously varying coverage. The densest of these is the $(\sqrt{19} \times \sqrt{19})$R23.4°-13CO structure [65, 66]. Clearly, there exists a pressure gap for the adsorption of CO Pt surfaces.

The Pt(111) surface has been the subject of many reactions studies [67–69]. They conclude that the CO oxidation reaction over Pt(111) proceeds via the Langmuir-Hinshelwood mechanism in two phases. The first regime exhibits low activity over a CO-covered surface, while the other takes place over a high-activity O-covered phase. In recent years, the UHV reaction studies have been extended to measurements at ambient conditions, and the oxidation of CO has, for example, been studied over Rh[70–72], Pd [53, 73–76], and Pt [77, 78]. It is heavily debated whether the active surface phase is metallic or a surface oxide. In particular, the highly reactive phases of noble metal surfaces are so active that the reaction rate is limited by the diffusion of molecules through a boundary layer. This effect is commonly referred to as the *mass transfer limit*.

Different highly active phases have been reported of different Pt-group metals. For instance, it has been found that the Rh surface phase depends on the total

pressure. The Rh(111) [70] and (100) [71] surfaces exhibit a surface oxide at the mass transfer limit in CO:O_2 mixtures between 10 and 300 mbar total pressure. In contrast, at lower pressures between 0.01 and 1 mbar the active phase on Rh(100) is metallic [72]. In contrast to Rh, which either is metallic or oxide-covered depending on the gas pressure, the Pd(100) and (111) surfaces are always covered by an oxide at mass transfer limit conditions for the CO oxidation reaction. The nature of this oxide depends, however, on the CO to O_2 ratio [53, 73–76]. Hence, the nature of the active phase under mass transfer limit conditions is highly material-dependent.

For Ir surfaces the active phase during the oxidation of CO has not yet been determined in the mbar regime, but the adsorption structures in UHV and ambient pressures have been investigated [79]. CO adsorbs only in atop sites on Ir(111) in a $(\sqrt{3} \times \sqrt{3})$R30° structure in UHV conditions, which is converted into a $(2\sqrt{3} \times 2\sqrt{3})$R30°-7CO structure at low temperature or high exposure. As for Pt, a dense adsorption structure is formed in mbar pressure of CO and a $(3\sqrt{3} \times 3\sqrt{3})$R30°-19CO structure has been observed [80, 81]. In contrast to the case of Pt, the high-density CO structures on Ir(111) consist of hexagonal CO clusters of 7-19 CO molecules as depicted in figure 3.1. The observed cluster formation is explained by the strong atop site preference of CO and strong CO-CO repulsion.

O adsorption on Ir also exhibits a pressure-dependent behavior. In the UHV pressure regime, O adsorbs in the hollow sites of a $p(2 \times 2)$ structure. Increased exposure in the UHV regime leads to the formation of a $p(2 \times 1)$ phase [82]. At mbar pressure of O_2, a O-Ir-O trilayer surface oxide forms on the Ir(110) [83] and (111) [84] surfaces. This trilayer is reported to be active for low-temperature methane activation [84], and a natural question is to ask if the Ir surface is covered by an oxide in CO oxidation conditions or if it is metallic.

The coupling between UHV and ambient conditions is important for the atomic-scale understanding of reactions on noble metal surfaces, which is the topic of the investigation in **Paper III**. Interestingly, the data indicate that the structures of the inactive phases are those found in the mbar pressure studies, while the active phases are more similar to the UHV adsorption structures. Hence, UHV studies are essential for determination of pure phases both at UHV and mbar pressures.

Presently, adsorption and reaction studies under mbar pressure conditions share many similarities with the surface science studies of the 1960s. This is signified by the primitive model systems in the form of planar single crystal surfaces and the use of ultraclean gases for adsorption and reaction studies. It is without

a doubt that topics for future researchers will include materials that aim at bridging the material gap with, *e.g.* vicinal surfaces or surface films (cf. figure 1.2), but also with impurities in the gas feed to study poison effects and kinetics of the phase change.

Cross-coupling reactions

In bridging the pressure and material gaps, not only is the employed surfaces of interest, but the reactions itself need to be considered. The oxidation of CO is a very common reaction to study since it implies reaction mechanisms with a manageable amount of reaction intermediates. However, the oxidation of CO is only of minor significance for catalysis. Hence, a step in approaching catalysts used in industry is to study reactions which are performed for chemical synthesis.

A group of chemical reactions which are widely applied in organic synthesis are the carbon-carbon coupling reactions. As the name suggests, these reactions couple reactants with a carbon bond to form larger molecules. This group of reactions has a wide range of applications for fine chemicals and pharmaceuticals [85–87]. The reactions are most often catalyzed by molecular catalysts or particles containing paladium or nickel [88]. Among the carbon-carbon coupling reactions, the Sonogashira cross-coupling, cf. figure 3.2, is unique in that it is catalyzed primarily by Au nanoparticles [89–95]. However, extended gold surfaces (Au(100) and Au(111)) have also been demonstrated to be active [96, 97]. As a consequence, the Sonogashira cross-coupling fits the criteria for a more complex reaction that can be studied by *in situ* photoelectron spectroscopy.

The Sonogashira cross-coupling reaction couples unfunctionalized acetylenes with a resulting product that retains a sp-hybridized bond at the coupled carbon atom [98]. Previous studies have mainly used iodobenzene (IB) and phenylacetylene (PA) for the investigations of the coupling reaction. A mechanism

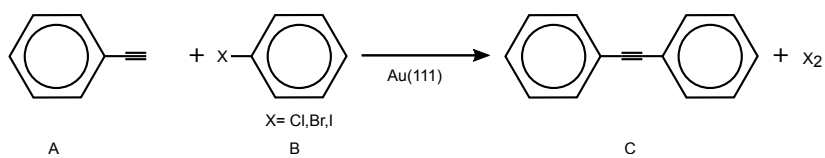

Figure 3.2: A scheme depicting the Sonogashira cross-coupling reaction where phenylacetylene (A), is coupled to a halogenated benzene (B) forming diphenylacetylene (C).

was suggested which involves C-I bond cleavage over the Au(111) surface [99], and this agrees with previous adsorption studies [100] of IB on the Au(111) surface. The study concluded that IB dissociates at a temperature of 175 K on the Au(111) surface and subsequently forms chemisorbed phenyl, biphenyl and atomic I.

It would be advantageous to substitute IB in the cross-coupling in favor for the cheaper and more available bromo- and chlorobenzenes (BrB and ClB) [101], however, a drawback is that these are less reactive. This concept has hardly been explored for the Sonogashira cross-coupling and only a few studies involving ClB and BrB have been published [93, 101, 102]. Density functional theory (DFT) calculations performed by Boronat *et al.* [102] shows that ClB has the highest activation energy for dissociation on gold nanoparticles and surfaces of the investigated halogenated benzenes. A study by Oliver-Meseguer *et al.* [93] agrees insofar as out of the investigated iodo-, bromo-, and chloroderivatives, the chloroderivatives result in the lowest yield.

I report on the first experimental data of the Sonogashira cross-coupling reaction of unfunctionalized BrB and ClB using IB as reference reactant in **Paper I**. Here, PA together with IB or ClB are seen to form the cross-coupling product, whereas BrB and PA do not. This outcome is in slight disagreement with the previously reported results [93, 102] and highlights that further studies are necessary.

The ambient pressure data in **Paper I** are understood on the basis of a thorough UHV characterization of the adsorbates. Without this characterization the ambient pressure data would be very difficult to interpret. Just as for the oxidation of CO, this demonstrates the continued importance of UHV-type studies when approaching more applied reactions. In addition, the results demonstrates the pressure gap in that the reaction pathways are seemingly pressure dependent.

3.2 Ultrathin surface oxides

A way of modeling a real catalytic system is to grow islands of the support material atop an active single crystal surface, cf. figure 1.2, and thereby create an 'inverse' catalytic model system. The reason that such systems are called inverse catalysts is that they support inactive islands on an active catalyst, while real catalysts support the active catalyst on inactive support materials. These systems reduce the complexity of a working catalyst and yet, enable the

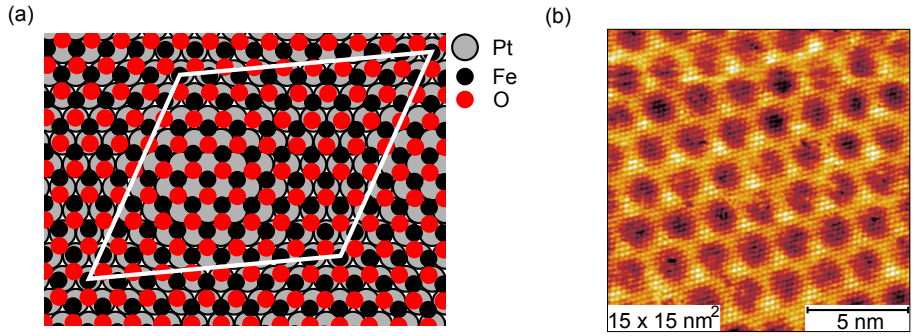

Figure 3.3: (a) ball model of the FeO surface. (b) shows an atomically resolved STM image of a monolayer FeO(111)/Pt(111) surface where the distinct moiré pattern is illustrated.

study of the metal-oxide interactions. The oxides are formed by depositing a material on the support and subsequently oxidizing it. Often the metal is different from the support, which forms a hetero-oxide hybrid system. Ultrathin hetero-oxide hybrid systems have received much attention in recent years as it has been found that many of their structures do not have a bulk counterpart; their formation is due to the support-oxide interaction and therefore hold unique characteristics [103].

One ultrathin metal oxide film that has been studied extensively is the bilayer FeO(111) film supported by a Pt(111) surface. This oxide was first reported by Vurens *et al.* in 1988 [104] and has since been subject to numerous investigations [105–112]. Today, it is one of the most well-characterized hetero-oxide hybrid systems. Hence, the structure and spectroscopic fingerprint are well documented.

The FeO(111) bilayer consists of hexagonal closed-packed O- and Fe-layers. The oxide grows layer-by-layer with an O-termination up to a coverage of 2.5 monolayers [113]. The atomic lattice of FeO (∼3.1 Å) is expanded by about 12 % to that of Pt(111) (∼2.77 Å) and rotated by 0.6°. The mismatch gives rise to a $(\sqrt{91} \times \sqrt{91})$R5.2° superlattice with a ∼25 Å periodicity. The superlattice exhibits a distinct moiré pattern upon imaging, as demonstrated in figures 3.3(a) and (b). The O-termination (cf. figure 3.5(a)) of the film makes it very inert, and, for example, CO and H_2O do not adsorb on the oxide surface in UHV conditions.

Even though the film is very inert in UHV conditions, it has been suggested that the bilayer FeO is more active for the oxidation of CO in the mbar regime than the bare Pt(111) surface. An investigation by Sun *et al.* [114] ascribed the

enhanced activity to an O-enriched phase of the FeO film and that it proceed by the Mars-van Krevelen mechanism. The investigation of Sun *et al.* was followed by a multitude of investigations [115–120], in which the film structure was characterized by both experimental and theoretical methods. It was concluded that the O-enrichment of the ultrathin bilayer FeO(111) strongly depends on the bilayer FeO(111) stacking towards the Pt-support, and the resulting film was only partially O-enriched. The transformed film had a O-Fe-O-$Pt_{substrate}$ stacking and, hence, a trilayer stoichiometry, cf. figure 3.5(b). In addition, high resolution STM images revealed a $(\sqrt{3} \times \sqrt{3})R30°$ superstructure on the trilayer FeO_2 islands. On the basis of DFT calculation this was explained as that the preferred location of the interface O atoms was atop the Pt atoms of the substrate [112].

Although extensively studied, no spectroscopic data of a clean trilayer FeO_2 film had previously been reported. Ringleb *et al.* had demonstrated that hydroxylated FeO_2 forms if H_2O and O_2 are dosed simultaneously at ambient pressure, which resulted in a H-O-Fe-O-$Pt_{substrate}$ structural motif [121]. In an effort to assign the spectroscopic fingerprint of the trilayer FeO_2 film I undertook an *in situ* APXPS investigation of the phase change, which is reported in **Paper IV**. From the APXPS and STM measurements, the film stoichiometry and the spectroscopic fingerprint are determined unambiguously. The trilayer FeO_2 film exhibits a high affinity for hydroxylation and is shown in figure 3.5(b). The hydroxylation is closely associated with the phase transition as evident from *in situ* APXPS data. Hence, the interfacial O layer heavily modifies the surface interactions of the generally inert bilayer film.

Interestingly, other trilayer-oxide films have shown similar trends both for H_2O dissociation as well as for other reactions. A hetero-oxide hybrid system with fairly similar properties to that of the iron oxides is the cobalt oxides. Cobalt oxides can also form a bilayer structure with O-termination, and it has been shown that islands of bilayer CoO transforms into trilayer CoO_2 with a O-Co-O structural motif [122] in high O chemical potentials. Similarly to the trilayer FeO_2, these trilayer CoO_2 islands show an increased affinity for water dissociation and trilayer CoO_2 has been suggested as the active phase for oxygen evolution reactions over cobalt oxide catalysts.

On some single crystal surfaces, the trilayer structural motif is also formed as a precursor to bulk-oxide formation. As discussed previously, the Ir(111) [84] and (110) [83] surfaces form a trilayer IrO_2 phase, which has been found to be active for low temperature methane activation [83]. A similar effect is found for the precursor to bulk oxide formation on Pd(100). Here a $(\sqrt{5} \times \sqrt{5})R27°$ phase forms in high O chemical potentials. The phase is active in CO [73] and

H_2 [123] oxidation. Although, the Pd-oxide does not contain a true trilayer building block, it does contains interface O atoms.

The interface O atoms seem to modify the activity of the above-mentioned metal oxides and it seems that this conclusion can be generalized. It would be interesting to investigate in future experiments if the induced activity is due to the disconnection from the support caused by these interface O atoms. An approach of investigating this, and the substrate influence, is to employ an oxide that can be formed on multiple supports. The bilayer FeO(111) film has been reported to form on Cu, Ru, Pd, Au, and Ag surfaces [124] and, hence, it would be possible to determine the influence of the support by a comparative study of FeO_2 trilayers on the surfaces of these materials.

Vicinal surfaces

Typically, the active component of a working catalyst is not a flat surface, but instead includes multiple facets, steps and other irregularities. As illustrated in figure 1.2, the use of vicinal surfaces as model systems is a step towards real catalytic systems. A vicinal surface includes *regular* facets, steps, and under-coordinated edge atoms, which mimic step atoms found on the real catalytic particles and allow for investigations of multiple sites simultaneously. For instance, the Pt(322) surface, as demonstrated in figure 3.4, has (111) terraces that are five atoms wide, which is about 12.7 Å. The steps themselves appear as (100) microfacets and contain the under-coordinated edge atoms.

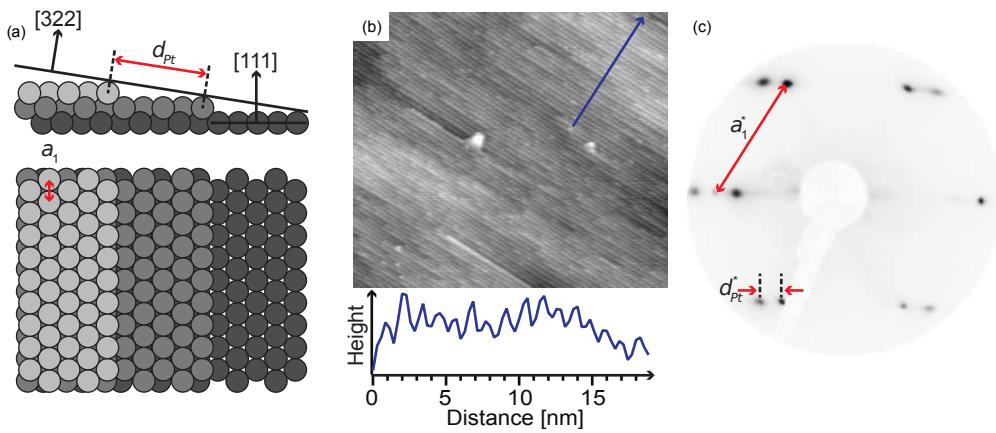

Figure 3.4: The Pt(322) surface. (a) Ball model of the surface from a side and top view. (b) STM image of the surface with a line scan of the topography marked by the blue arrow. (c) LEED image of the surface.

Vicinal surfaces have previously been employed in adsorption and reactivity measurements [125–129]. When interacting with the adsorbates, these systems are prone to restructuring in the form of step bunching. During step bunching, the low-index facets are extended, forming larger terraces and higher steps. The change in surface structure of vicinal surfaces is an indication that the real catalytic particles might not be stable either, which further demonstrates the pressure gap.

Although vicinal surfaces approach the catalytic particle, they still only allow for the study of a few sites at a time. It has recently been demonstrated that a sample with multiple crystal cuts can be studied with a cylindrically shaped crystal. The cylindrical shape of these surfaces generates multiple crystal planes, which allow for comparison between different surface cuts under identical conditions [130, 131].

Ultrathin vicinal oxides

The activity of a metal oxide is not only modified by interfacial oxygen, but also by step edges. For example, bilayer FeO(111) islands have an activity that is not observed for the complete film [132–135], and this effect is also found for CoO islands [136]. The observed activity is attributed to the coordinatively unsaturated metal edge sites of the islands. These edge sites share similarities with the working catalysts as they mimic the interaction between the active metal particle and the supporting metal oxide. In the case of bilayer FeO(111) islands on a Pt single crystal, these active sites are step edges with a FeO-Pt structure. Since the under-coordinated atoms of these sites are active, a natural question to ask is whether the under-coordinated atoms at the oxide steps (FeO-FeO) are also active.

Hetero-oxide island edge sites are difficult to study, however, due to the low number of edge atoms compared to sites in the basal planes. The use of averaging technique such as XPS results in a weak signal originating from the edge sites. In addition, the use of islands introduce structures with several types of edge-site coordination. Further, the edge sites of inverse-model catalyst islands are in direct contact with the underlying support and, as such, they only can model the oxide-to-metal-step. Hence, another approach is required to model oxide-to-oxide steps.

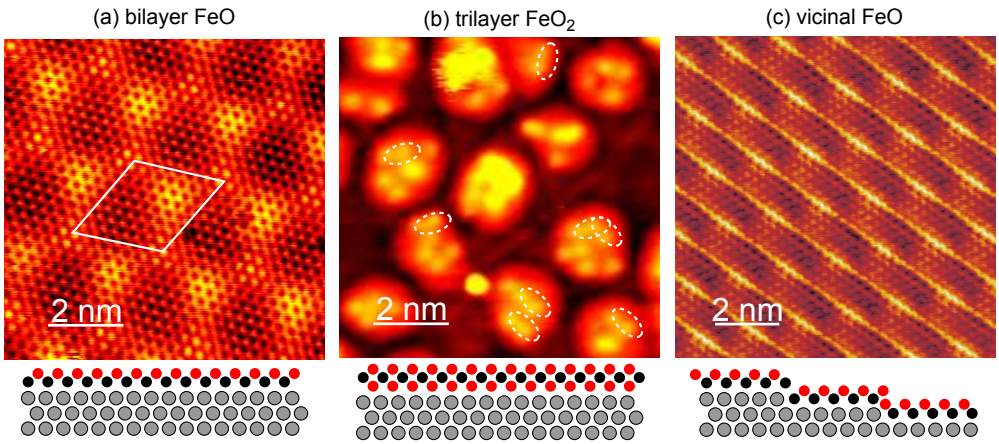

Figure 3.5: STM images and side view ball models of the investigated FeO films where the gray, black, and red balls represents Pt, Fe, and O atoms, respectively. (a) shows the bilayer FeO film while (b) shows the hydroxylated trilayer FeO_2 where some hydroxyl groups are marked. (c) shows the regular steps of the vicinal FeO film.

Bilayer FeO(111) grows epitaxially over the Pt(111) surface. Hence, by replacing the planar surface with a vicinal equivalent, it is possible to imagine that a stepped FeO film could be obtained. This concept has been demonstrated for MgO and VO_x, but also for FeO_x films [137–139]. Ketteler and Ranke [140] show that FeO exhibits the same general growth behavior on the high-index Pt(9 11 11) surface as on Pt(111). However, the FeO growth induced severe substrate-step bunching, and the obtained FeO did not overgrow the steps. The Pt(9 11 11) terraces are about 25 Å wide, which is about the size of the FeO(111)/Pt(111) moiré unit cell. Hence, the growth of FeO is confined to a single terrace, which explaines the observed FeO-Pt steps. Instead, consider the Pt(322) surface where the terrace steps are about half of the bilayer FeO(111) unit cell. If the super lattice periodicity is to be conserved, the FeO must overgrow the steps. I studied the bilayer FeO/Pt(322) film in the work leading to **Paper V**. The resulting film overgrows the terrace steps and contains highly regular FeO-FeO steps, cf. figure 3.5(c). From dosing water in UHV conditions, the film becomes partially hydroxylated and, thus, it is concluded that the FeO-FeO steps show an affinity towards water splitting. The hydroxylation is related to the under-coordinated atoms at the steps which have an O-Fe-O-Fe structural motif. This structure contains the trilayer motif, which suggests that the interface O atom might modify the activity as it disconnects the top layer from otherwise metallic species.

Unpublished data that my colleagues and I have measured further support this notion. The data show that CO_2 dissociates at the steps leading to an O-enrichment of the terraces of the vicinal FeO film. The O-enrichment results

in a similar XPS signature as that of the trilayer FeO_2 film over Pt(111). This further suggests that even the trilayer formation investigated in **Paper IV** starts from O_2 dissociating at the terrace steps. It would be interesting to study the vicinal FeO film in mbar pressures of O_2 to confirm this hypothesis.

Relatively few studies have been presented on the topic of stepped ultrathin oxides and the results presented in **Paper V** show that they have interesting properties. The possibilities for future studies range from structural characterization of other vicinal oxides, but also adsorption and reactivity studies of the film presented in **Paper V**. For instance, the reactivity of the oxide steps could be probed by CO.

3.3 Supported molecular catalysts

Molecular catalysts are often unavailable for electron spectroscopy investigations as they tend to be working under homogeneous conditions. However, many homogeneous catalysts are very effective in high yield and selectivity. An example of a process where the homogeneous catalyst is more beneficial than its heterogeneous counterpart is the *olefin metathesis*. This catalytic process redistributes olefin fragments by scission and regeneration of carbon-carbon double bonds and has been used for the production of basic chemicals ever since it was discovered [141]. The catalyst is typically a group 6-7 oxide dispersed on a porous support, and the operation temperature of the catalyst is rather high ($> 150°C$). The corresponding homogeneous catalyst operates at much lower temperature and allows the addition of more functional groups while retaining high selectivity [142].

In recent years, a branch of catalysis research has emerged in which homogeneous catalysts are immobilized on a support material with the goal of coupling the throughput and reliability of heterogeneous catalysis with the low reaction temperature, high conversion, and selectivity of the homogeneous catalysts. One such catalyst is the Mn(III)-salen complex (bis(3,5,di-t-butylsalycylidene), 1,2, cyclohexanediaminomanganese(III)chloride) depicted in Fig. 3.6. Mn(III)-salen was independently identified by the groups of Jacobsen [143–145] and Katsuki [146] to be an effective catalyst for asymmetric epoxidation of unfunctionalized olefins. In recognition of their finding, the epoxidation reaction over Mn(III)-salen complexes is referred to as Jacobsen-Katsuki epoxidation. In addition, the epoxidation exhibits a high enantioselective yield, *i.e.* the product is predominately one of the two enatiomers. This often is refereed to as chirality, referring to the greek word for hand, $\chi\epsilon\iota\rho$ (Kheir).

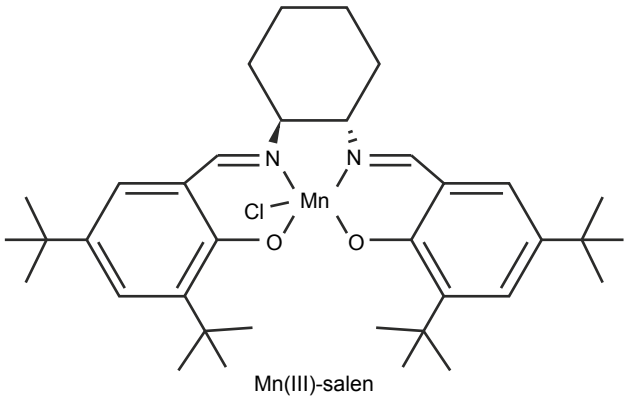

Figure 3.6: Scheme of the Mn(III)-salen molecule displaying the Mn cordination center and the ligands.

The ability to control the chirality of the reaction product is of paramount importance in the pharmaceutical industry as the chemically indistinguishable enantiomers exhibit different biological activity. An example of the importance is the release of the thalidomide drug sold under the name Contergan in the early 1960s. The drug was administered to pregnant women as it was effective against nausea and hence alleviated morning sickness. Shortly thereafter many children were born with phocomelia, which is a malformation of the limbs. It was found that one of the enantiomers of thalidomide caused deformation in fetuses. It now serves as a warning example of the importance of enantioselective pharmaceutical production.

Since the finding by Jacobsen and Katsuki, an array of studies involving derivatives of the Mn(III)-salen complex have been conducted. It is demonstrated that the catalyst, and variations of it, is active in not only oxidation of olefins [143, 144, 147–162] but also in sulfide oxidation [163] and synthesis processes such as olefin polymerization [164] and formation of cyclic organics from carbonates [165]. Hence, the molecular complex is a versatile catalyst and *in situ* investigations of the chemistry during reaction are highly desirable.

In the above-mentioned reactions, the catalyst is typically dissolved in dichloromethane (DCM) and sodiumhypochloride (NaOCl) is used as the oxidizing agent. To enable investigations by electron spectroscopy, it is necessary to immobilize the catalyst on a support and by doing so, the gain is twofold: (i) detailed investigations of the electronic structure can be conducted by electron spectroscopies and (ii) the ability to immobilize the catalyst with retained activity is demonstrated. In addition, the use of large amounts of solvent and environmentally harmful oxidizers may be circumvented.

Various methods to immobilize the Mn(III)-salen complex and its derivatives have been reported. For instance, the Mn(III)-salen complex has been anchored to various supports such as silica [161, 165, 166], quartz [162], and clay [151–153], but also to mesoporous materials [156, 158]. It has also been attached to polyoxometalates [167, 168] and carbon supports such as activated carbon [157, 160] and polymers [159]. Common to these approaches is the continued use of a solvent, which contains the oxidizing agent and the reactants. Another common theme is a measured drop in yield and selectivity during catalysis. Hence, the link between immobilization and retained activity is not clear.

For the purpose of surface science studies, a straightforward immobilization procedure is necessary. Anchoring techniques introduce several new compounds and carbon-based materials would severely interfere with the measurements as spectral features would overlap. In the only two surface science studies of a salen complex, Schwartz [169] and Lämmle [170] immobilized a Co-salen complex on NaCl single crystals by sublimation of the molecular complex in vacuum. The studies report on the orientation dependence towards the substrate of the adsorbed Co-salen as observed by AFM.

In an effort to investigate the applicability of the Mn(III)-salen complex in a heterogeneous system, I undertook the study presented in **Paper II**. The catalyst was sublimated onto a Au(111) support according to the procedure reported by Lämmle and Schwartz [169, 170] and the adsorption was spectroscopically characterized. It is shown in the paper that the molecule retains its oxidative properties after immobilization on the Au(111) single crystal. However, instead of an epoxidation reaction, complete oxidation was observed. Therefore, it would be interesting to investigate if the outcome of the reaction can be tuned into an epoxide by *e.g.* using less oxidative condition or possibly larger probe molecules. By performing these experiments, insight into the catalytic cycle with gases can be gained, which will be vital to generalize the behavior of immobilized homogeneous catalysts.

Chapter 4

Summary of papers

Complex catalytic reactions over Au(111) surfaces

Paper I: Sonogashira cross-coupling over Au(111): from UHV to ambient pressure

In this paper, my colleagues and I report on the Sonogashira cross-coupling reaction between PA and unfunctionalized ClB, BrB, and IB over an extended Au(111) surface. The adsorption properties are characterized by XPS and XAS. All investigated molecules adsorb in a flat geometry, with ClB adsorbing in a nearly perfectly flat geometry. Here, I investigate the cross-coupling in two approaches: first by dosing PA on surfaces pre-dosed with one of the halogenated benzenes at liquid nitrogen temperature, and secondly by using vapors of the reactants in the mbar regime. In both approaches is the temperature increased while measuring XPS. Both IB and ClB couple with PA to form diphenylacetylene on the Au(111) surface as is evident from a peak that develops while heating the surface. In contrast, BrB does not couple to PA. For IB the coupling proceeds first by IB dissociating on the surface, and the remaining phenyl couples to PA. ClB couples to PA by an alternate mechanism as no chemisorbed atomic-Cl species is present in the XP spectra.

IB and ClB also couple to PA at mbar pressure conditions. The peak identified as diphenylacetylene is present in the APXP spectra, although at highe temperature compared to in UHV. For IB this is due to the Au(111) surface being iodine poisoned which inhibit PA adsorption. In the ClB case, in contrast, no chemisorbed atomic-Cl species is present and the reaction must proceed with an alternative mechanism, similarly to the UHV case.

The results show that there is a discrepancy in reaction mechanism between the two pressure regimes. In addition, the data demonstrate that UHV-type experiments are highly relevant. Assigning molecular species at ambient pressures without this data is very difficult. Hence, classic surface science investigations will play an important role when trying to understand more applied and complex systems.

Paper II: Mn-salen supported by Au(111): adsorption and catalysis

This investigation is divided into two parts: (i) adsorption characteristics and (ii) reactivity of the immobilized Mn(III)-salen complexes. In the first part of the paper XPS, STM and DFT data are used to characterize the adsorption properties of different sublimation thicknesses on the Au(111) support. For submonolayer coverages, the Mn(III)-salen exhibits a degree of interaction with the Au(111) support, which is seen as a disruption from the expected sp^3 to sp^2 type carbon ratio compared to the molecular stoichiometry. This is assigned to geometrical effects where the *t*-butyl groups of the molecule are bent towards the surface. The sp^3 to sp^2 type C ratio disruption changes as the coverage is increased. For multilayer preparations this agrees with the *t*-butyl pointing outward from the surface. In addition, the O 1s signature suggests presence of a Mn(V)-oxo salen species the multilayer preparations.

The second part investigates the reactivity of Mn(III)-salen with gas phase reactants by APXPS and μ-reactor measurements. In both approaches are the Mn(III)-salen exposed to mbar pressures of propylene and O_2. The APXP spectra of multilayers of Mn(III)-salen in the gas mixture show that CO_2 forms, which indicates propylene oxidation. The μ-reactor measurements data also exhibit CO_2, albeit at a higher temperature. The temperature discrepancy is tentatively explained by the presence of the Mn(V)-oxo salen in the multilayer film. This species is one of the reaction intermediates in oxidation over Mn(III)-salen and, hence, the multilayer is primed for reaction, most likely by the sublimation procedure.

CO oxidation over single crystal surfaces

Paper III: Ambient pressure phase transitions over Ir(111): at the onset of CO oxidation

In this paper, my colleagues and I report on an investigation of the oxidation of CO over an Ir(111) surface using APXPS and DFT calculations. The interpretation of the results is based on similar measurements over Pt(111). The results show that where the Pt(111) surface demonstrates a sharp transition between inactive and active phase, the Ir(111) surface exhibit a slower transition with an intermediate phase. In this phase, both chemisorbed O and CO are present, which is never observed for Pt(111) surfaces. This discrepancy is explained by the DFT calculations in terms of adsorption energies. The adsorption energies for CO and O are greater on the Ir(111) surface compared to the Pt(111) surface. The increased adsorption energies compensate for the CO to O repulsion and, hence, stabilize the co-existence of CO and O on the Ir(111) surface. In addition, the paper reports the various CO and O coverages over the Pt and Ir surfaces as a function of temperature. Interestingly, the CO coverages of the inactive phases correspond to those of structures found at mbar pressures, while the O coverages of the active phases are more similar to coverages of structures found in UHV.

Ultrahin iron oxides grown on Pt surfaces

Paper IV: Oxidation of ultrahin FeO(111) grown on Pt(111): spectroscopic evidence for hydroxylation

Many studies have been performed on the trilayer FeO_2 films grown on the Pt(111) surface. However, very few spectroscopy investigations have been reported and none on a clean trilayer FeO_2 film. This paper reports on a full spectroscopic characterization of the trilayer FeO_2 film grown on Pt(111) using XPS, XAS, and STM. The trilayer is grown by two approaches: first by using mbar pressures of O_2 while heating a bilayer FeO(111) film and secondly by exposing a bilayer FeO(111) film to 10^{-7} mbar NO_2 at room temperature. Both approaches lead to a partly hydroxylated trilayer FeO_2 film. Hence, the trilayer has a mixture of the O-Fe-O-Pt and H-O-Fe-O-Pt structural motifs. Since the NO_2 is dosed in high vacuum conditions using ultraclean gas, the the hydroxylation must proceed by the rest-gases in the UHV system. This suggests that the trilayer FeO_2 film has a high affinity for water splitting. This is confirmed

by the *in situ* APXPS data, which show that the film becomes hydroxylated immediately as it forms.

Paper V: Ultrathin stepped iron oxide films grown on high index Pt surfaces – a new catalytic model system

This paper reports on an effort to create an FeO model system with a high density of regular steps that contain under-coordinated atoms. The film is grown on a Pt(322) surface and the resulting structure is characterized using XPS, XAS, LEED, and STM. The obtained vicinal FeO film exhibits regular steps and the same general growth as FeO on Pt(111) surfaces along the steps. However, the overall moiré pattern is perturbed in the direction orthogonal to the steps. The edge sites are almost indistinguishable in the XPS data and only a minor signal differentiates it from the planar FeO(111) film grown on Pt(111). However, the influence of the steps is visible after water exposure as they dissociate water, which is in contrast to the inert planar FeO(111) film. This result suggests that the film contains Fe terminated FeO-FeO steps. This study opens up for future studies where the FeO edge site chemistry can be studied in detail and the FeO-FeO edge sites can be compared with the FeO-metal sites.

Instruments

Paper VI: The SPECIES beamline at the MAX IV Laboratory: a facility for soft X-ray RIXS and APXPS

Here, I report on the layout and optical elements of the SPECIES beamline at the MAX IV Laboratory. The concept of the astigmatic re-focusing of the APXPS branchline is described and measurements of the spot size confirm that it is constant, independent of monochromator exit slit and photon energy. The beamline uses two separate monochromator refocusing mirrors, which allows for a fast switching between the branchlines. The low energy reach of the undulator allows for valence band investigations, which in turn allows for full characterization of the electronic structure of the samples. The SPECIES beamline was first constructed and characterized at the MAX-II storage ring which is now decommissioned. Currently, the SPECIES beamline is being rebuilt at the new 1.5 GeV storage ring at the new laboratory and is expected to be opened for regular users in early 2018.

Chapter 5

Concluding remarks and outlook

This thesis reflects the current trend in the surface science community to investigate systems of increasing complexity. The transition to more representative samples and environments is a natural progression of the 'classic' UHV-type studies. As more synchrotron and laboratory-based APXPS instruments have become available, new approaches and systems are explored. For instance, technologically relevant processes such as atomic layer deposition can be studied *in situ*. With the commercial availability of laboratory-based 'turn-key' APXPS systems, the APXPS field is further simplified as the need of UHV systems are circumvented. The ease of operation and sample throughput are likely to attract users outside of the academic field, *e.g.* the catalysis and pharmaceutical industries. The diversity of the APXPS technique and instrumentation, together with the ability of 'classical' photoemission measurements with the Lund approach, makes it a very powerful technique. I am positive that APXPS will replace UHV-based XPS as the 'workhorse' of surface science. The fact that the MAX IV Laboratory hosts two dedicated APXPS instruments is an indication of the future development.

The results in **Paper I** and **Paper III** show that the continued use of single crystals as model systems is highly relevant. APXPS allow more complex systems to be approached, however, it is still not clear if the insights gained during UHV type studies can be extrapolated into the mbar pressure regime. The results in this thesis show that the pressure gap indeed is present. The results of **Paper I** show this as the surface reaction for iodobenzene and phenylacetylene behaves differently between the UHV and mbar pressure regimes. In addition,

the inactive Pt and Ir surface phases in **Paper III** also exhibit the pressure gap. Further, it is not clear either if the structures and reactions pathways in the mbar regime are representative of structures at even higher pressures, which is likely not the case. Therefore, future use of single crystal model systems is motivated in order to step-by-step investigate adsorbate structures at higher-and-higher pressures. However, for single crystal model systems to remain relevant to catalysis research, other reactions than the oxidation of CO need to be investigated. This can be approached in multiple ways. For instance, by the use of larger reactants as in **Paper I** or by mixing impurities in the gas feed. The latter is relevant as impurities may poison reactions and, hence, investigations of the dynamics is motivated. An approach to use the previous insights gained from the oxidation of CO in **Paper III** could be to add hydrogen in the gas feed. In this case, water formation and the oxidation of CO are competing reactions. Often is it preferred to oxidize CO and not H_2, which is referred to as preferred oxidation (PROX). For instance, fuel cell technology requires clean H_2 to operate and CO is a major poison. Hence, a catalyst which is highly effective in removing CO and not in water formation is necessary and the proposed investigation will contribute towards this.

With the APXPS technique it is not only possible to bridge the pressure gap and investigate more complex reactions, it is also possible to investigate phase transformations of oxides. The results in **Paper IV** show that spectroscopic information is vital for a full characterization. As the trilayer FeO_2 exhibit such a high affinity for water splitting reactions, it is of interest to probe its reactivity further. As the trilayer film is suggested to be the active phase for the oxidation of CO by bilayer FeO, the reactivity could be studied *in situ* by APXPS. For instance, the trilayer FeO_2 film could be exposed to alternating pulses of CO and O_2 while measuring APXPS to follow the reduction and re-oxidation of the film. Alternatively, the water splitting could be investigated further by mixing water vapor into the gas feed.

To further mimic the working catalyst, a material containing steps of the oxide material is of interest. As **Paper V** reports, it is possible to grow a vicinal FeO film that contain FeO-FeO steps. This film allows for the study of the undercoordinated atoms at the step sites and the results in the paper show that these atoms exhibit a high affinity for water splitting. This affinity is not shared by the atoms in the basal plane and, hence, the edge atoms show an increased activity. Therefore, it is of interest to further study this reactivity. In addition, it is possible that these edge atoms are the nucleation site for trilayer formation. This could be shown by exposing the vicinal FeO film to a less oxidative agent or environment compared to O_2, *e.g.* CO_2 at low temperature. Toward this, my

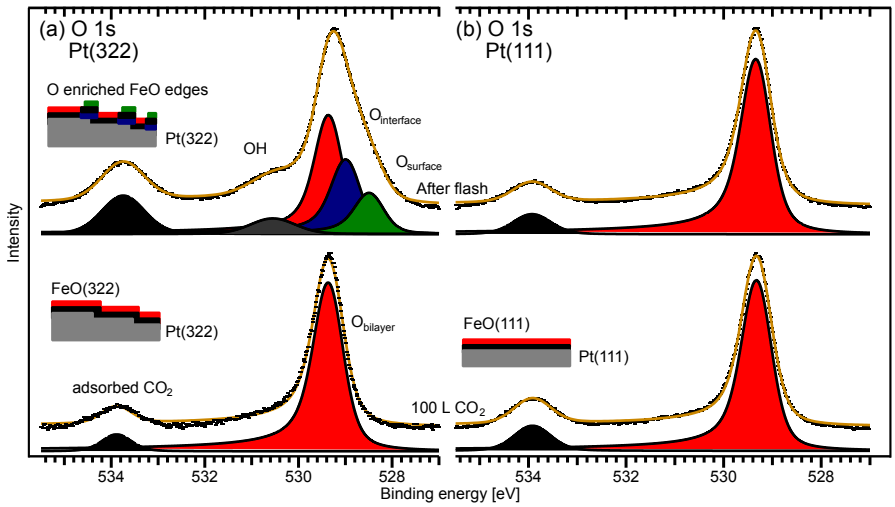

Figure 5.1: O 1s XP spectra acquired of (a) vicinal FeO and (b) planar FeO. The bottom spectra illustrate the signal of the FeO films after dosing CO_2 at liquid nitrogen temperatures while the top spectra are acquired after flashing the surfaces.

colleagues and I have performed initial experiments that demonstrate just this behavior. The spectra shown in figure 5.1(a) and (b) show O 1s XP spectra of vicinal FeO and planar FeO, respectively. The bottom spectra show the XPS fingerprints of the FeO films after dosing CO_2 at liquid nitrogen temperature, while the top spectra are acquired after subsequent flashing. The O 1s XP spectrum of the vicinal film share similarities with the trilayer film in **Paper IV**. Hence, the vicinal FeO film is partly O-enriched at the steps whereas the planar FeO film shows no sign of O-enrichment. This study could be expanded by using other molecules and reactions which the planar FeO(111) film is generally considered to be inert toward. In addition, the active sites can potentially be investigated by blocking some of the sites, *e.g.* by decorating the terraces or active sites with Au. This might demonstrate that the under coordinated atoms at the steps indeed are responsible for the activity, which the spectra in figure 5.1 suggests.

Most studies of homogeneous catalysts immobilized on supports have resulted in lower yields and selectivity, which is typically attributed to the reduced mixing of catalyst and reactants. It is, however, unclear how the anchoring affects the chemistry of the catalyst itself. To this end, the results in **Paper II** show that there is a change in chemistry for the carbon atoms while the O and N atoms seem to remain mostly unaffected. In the multilayer case, however, the change is attributed to the sublimation and not to interactions with the support. In

addition, the presented results also indicate that the Mn(III)-salen complex also is active in oxidation reactions using gas reactants, which have not been demonstrated previously. As the Mn(III)-salen is found to be active in the oxidation of propylene, it is of interest to further investigate if propylene epoxidation may be achieved with immobilized Mn(III)-salen. One approach to investigate this could be to apply a less oxidative environment, *e.g.* by reducing the O_2 partial pressure, lower the temperature, or a less oxidative gas. Since propylene epoxide is a chiral molecule, the enantioselectivity of the immobilized complex with gas phase reactants could be investigated. Further, instead of tuning the oxidative capacity of the oxidizing agent, a larger unfunctionalized olefins, *e.g.* styrene, could also be used as these are less prone to complete oxidation. In principle, the only restriction for APXPS measurements of molecular complexes is that the vapor pressure needs to be sufficiently high to facilitate dosing. Hence, a comparative study of a multitude of unfunctionalized olefins could be conducted. Finally, it is noteworthy that in studying an immobilized homogeneous catalyst, an actual working catalyst is studied. Hence, the obtained results might be directly applicable to the catalytic process which makes further studies of homogeneous catalysts with surface science methods relevant.

Bibliography

[1] V. Smil. "Detonator of the population explosion". *Nature*, **400**, 415, 1999. doi:10.1038/22672.

[2] The Nobel Prize in Chemistry 1918. Nobelprize.org. Nobel Media AB 2014. Web. 4 Sep 2017. `http://www.nobelprize.org/nobel_prizes/chemistry/laureates/1918/`.

[3] The Nobel Prize in Chemistry 1931. Nobelprize.org. Nobel Media AB 2014. Web. 4 Sep 2017. `http://www.nobelprize.org/nobel_prizes/chemistry/laureates/1931/`.

[4] I. Chorkendorff and J. W. Niemantsverdriet. *Concepts of modern catalysis*. Wiley-VCH Verlag, Weinheim, 2nd edition, 2007.

[5] The Nobel Prize in Chemistry 1909. Nobelprize.org. Nobel Media AB 2014. Web. 12 Sep 2017. `http://www.nobelprize.org/nobel_prizes/chemistry/laureates/1909/`.

[6] The Nobel Prize in Chemistry 2007. Nobelprize.org. Nobel Media AB 2014. Web. 4 Sep 2017. `http://www.nobelprize.org/nobel_prizes/chemistry/laureates/2007/`.

[7] M. Todorova, E. Lundgren, V. Blum, A. Mikkelsen, S. Gray, M. B. J. Gustafson, J. Rogal, K. Reuter, J. Andersen and M. Scheffler. "The Pd(100)−R27°-O surface oxide revisited". *Surf. Sci.*, **541**, 101, 2003. doi:10.1016/S0039-6028(03)00873-2.

[8] R. Westerström, M. E. Messing, S. Blomberg, A. Hellman, H. Grönbeck, J. Gustafson, N. M. Martin, O. Balmes, R. van Rijn, J. N. Andersen, K. Deppert, H. Bluhm, Z. Liu, M. E. Grass, M. Hävecker and E. Lundgren. "Oxidation and reduction of Pd(100) and aerosol-deposited Pd nanoparticles". *Phys. Rev. B*, **83**, 2011. doi:10.1103/PhysRevB.83.115440.

[9] J. W. Niemantsverdriet. *Spectroscopy in Catalysis: An Introduction.* WILEY-VCH Verlag, Weinheim, third edition, 2007.

[10] H. Hertz. "Ueber einen Einfluss des ultravioletten Lichtes auf die electrische Entladung". *Ann. Phys.*, **267**, 983, 1887. doi:10.1002/andp.18872670827.

[11] A. Einstein. "Ueber einen die Erzeugung und Verwandlung des Lichtes betreffenden heuristischen Gesichtspunkt". *Ann. Phys.*, **322**, 132, 1905. doi:10.1002/andp.19053220607.

[12] The Nobel Prize in Physics 1921. Nobelprize.org. Nobel Media AB 2014. Web. 6 Sep 2017. `http://www.nobelprize.org/nobel_prizes/physics/laureates/1921/`.

[13] The Nobel Prize in Physics 1981. Nobelprize.org. Nobel Media AB 2014. Web. 7 Sep 2017. `http://www.nobelprize.org/nobel_prizes/physics/laureates/1981/`.

[14] C. N. Berglund and W. E. Spicer. "Photoemission Studies of Copper and Silver: Theory". *Phys. Rev.*, **136**, A1030, 1964. doi:10.1103/PhysRev.136.A1030.

[15] C. N. Berglund and W. E. Spicer. "Photoemission Studies of Copper and Silver: Experiment". *Phys. Rev.*, **136**, A1044, 1964. doi:10.1103/PhysRev.136.A1044.

[16] S. Hüfner. *Photoelectron Spectroscopy - Principles and Applications.* Springer Verlag, Berlin, third edition, 2003.

[17] National Institute of Standards and Technology XPS database, Web. 20 Sep 2017. `https://srdata.nist.gov/xps/ElmSpectralSrch.aspx?selEnergy=PE`.

[18] S. Doniach and M. Šunjić. "Many-electron singularity in X-ray photoemission and X-ray line spectra from metals". *J. Phys. C*, **3**, 285, 1970. doi:10.1088/0022-3719/3/2/010.

[19] D. A. Shirley. "High-Resolution X-Ray Photoemission Spectrum of the Valence Bands of Gold". *Phys. Rev. B*, **5**, 4709, 1972. doi:10.1103/PhysRevB.5.4709.

[20] S. Tougaard and B. Jørgensen. "Inelastic background intensities in XPS spectra". *Surf. Sci.*, **143**, 482, 1984. doi:10.1016/0039-6028(84)90554-5.

[21] J. Stöhr. *NEXAFS Spectroscopy*. Springer-Verlag, Berlin, 1992.

[22] J. Stöhr and D. A. Outka. "Determination of molecular orientations on surfaces from the angular dependence of near-edge x-ray-absorption fine-structure spectra". *Phys. Rev. B*, **36**, 7891, 1987. doi:10.1103/PhysRevB.36.7891.

[23] Oxford online dictionary. Web. 30 Sep 2017. `https://en.oxforddictionaries.com/definition/spectroscopy`.

[24] G. Brown, K. Halbach, J. Harris and H. Winick. "Wiggler and undulator magnets - A review". *Nucl. Instrum. Methods Phys. Res.*, **208**, 65, 1983. doi:10.1016/0167-5087(83)91105-5.

[25] M. Johansson, B. Anderberg and L.-J. Lindgren. "Magnet design for a low-emittance storage ring". *J. Synchrotron Radiat.*, **21**, 884, 2014. doi:10.1107/S160057751401666X.

[26] W. Grizolli, F. Hennies, J. Knudsen, R. Nyholm, R. Sankari and J. Schnadt. "Use of astigmatic re-focusing at HP-XPS endstation". *J. Phys. Conf. Ser.*, **425**, 152005, 2013. doi:10.1088/1742-6596/425/15/152005.

[27] D. E. Starr, Z. Liu, M. Hävecker and H. B. A. Knop-Gericke. "Investigation of solid/vapor interfaces using ambient pressure X-ray photoelectron spectroscopy". *Chem. Soc. Rev.*, **42**, 5833, 2013. doi:10.1039/c3cs60057b.

[28] H. Siegbahn and K. Siegbahn. "ESCA applied to liquids". *J. Electron Spectrosc. Relat. Phenom.*, **2**, 319, 1973. doi:10.1016/0368-2048(73)80023-4.

[29] H. Siegbahn. "Electron spectroscopy for chemical analysis of liquids and solutions". *J. Phys. Chem.*, **89**, 897, 1985. doi:10.1021/j100252a005.

[30] K. Y. Richard W. Joyner, M.Wyn Roberts. "A "high-pressure" electron spectrometer for surface studies". *Surf. Sci.*, **87**, 501, 1979. doi:10.1016/0039-6028(79)90544-2.

[31] D. F. Ogletree, H. Bluhm, G. Lebedev, C. S. Fadley, Z. Hussain and M. Salmeron. "A differentially pumped electrostatic lens system for photoemission studies in the millibar range". *Rev. Sci. Instrum.*, **73**, 3872, 2002. doi:10.1063/1.1512336.

[32] N. Johansson. *The new HPXPS instrument at MAX-lab: A powefull tool for In Situ catalysis investigations*. Master's thesis, Lunds Universitet, 2012.

[33] J. Zhou, S. Blomberg, J. Gustafson, E. Lundgren and J. Zetterberg. "Visualization of Gas Distribution in a Model AP-XPS Reactor by PLIF: CO Oxidation over a Pd(100) Catalyst". *Catalysts*, **7**, 29, 2017. doi:10.3390/catal7010029.

[34] D. F. Ogletree, H. Bluhm, E. D. Hebenstreit and M. Salmeron. "Photoelectron spectroscopy under ambient pressure and temperature conditions". *Nucl. Instrum. Meth. A*, **601**, 151, 2009. doi:10.1016/j.nima.2008.12.155.

[35] H. Bluhm. "Photoelectron spectroscopy of surfaces under humid conditions". *J. Electron Spectrosc. Relat. Phenom.*, **177**, 71, 2010. doi:10.1016/j.elspec.2009.08.006.

[36] H. Siegbahn, M. Lundholm, M. Arbman and S. Holmberg. "On the Measurement of Binding Energies in Liquid ESCA and the Relation to Electrochemical Half-Cell Emfs". *Phys. Scr.*, **27**, 241, 1983. doi:10.1088/0031-8949/27/4/003.

[37] E. J. Crumlin, H. Bluhm and Z. Liu. "*In situ* investigation of electrochemical devices using ambient pressure photoelectron spectroscopy". *J. Electron Spectrosc. Relat. Phenom.*, **190**, 84, 2013. doi:10.1016/j.elspec.2013.03.002.

[38] R. T. Poole, R. C. G. Leckey, J. G. Jenkin and J. Liesegang. "Calibration procedures for photoelectron spectrometers". *J. Phys. E: Sci. Instrum.*, **6**, 201, 1973. doi:10.1088/0022-3735/6/3/003.

[39] EnviroESCA, SPECS GmbH, Web. 23 Aug 2017, `http://enviro.specs.de/cms/front_content.php?idcat=209`.

[40] HiPP-3, Scienta Omicron, Web 24 Sept 2017, `<http://www.scientaomicron.com/en/products/355/1188>`.

[41] H. Ali-Löytty, M. W. Louie, M. R. Singh, L. Li, H. G. S. Casalongue, H. Ogasawara, E. J. Crumlin, Z. Liu, A. T. Bell, A. Nilsson and D. Friebel. "Ambient-Pressure XPS Study of a Ni–Fe Electrocatalyst for the Oxygen Evolution Reaction". *J. Phys. Chem. C*, **120**, 2247, 2016. doi:10.1021/acs.jpcc.5b10931.

[42] M. Favaro, B. Jeong, P. N. Ross, J. Yano, Z. Hussain, Z. Liu and E. J. Crumlin. "Unravelling the electrochemical double layer by direct probing of the solid/liquid interface". *Nat. Commun.*, **7**, 12695, 2016. doi:10.1038/ncomms12695.

[43] A. R. Head, O. Karslıoğlu, T. Gerber, Y. Yu, L. Trotochaud, J. Raso, P. Kerger and H. Bluhm. "CO adsorption on Pd(100) studied by multimodal ambient pressure X-ray photoelectron and infrared reflection absorption spectroscopies". *Surf. Sci.*, **665**, 51, 2017. doi:10.1016/j.susc.2017.08.009.

[44] S. Nemšák, A. Shavorskiy, O. Karslioglu, I. Zegkinoglou, A. Rattanachata, C. S. Conlon, A. Keqi, P. K. Greene, E. C. Burks, F. Salmassi, E. M. Gullikson, S.-H. Yang, K. Liu, H. Bluhm and C. S. Fadley. "Concentration and chemical-state profiles at heterogeneous interfaces with sub-nm accuracy from standing-wave ambient-pressure photoemission". *Nat. Commun.*, **5**, 5441, 2014. doi:10.1038/ncomms6441.

[45] H. R. G. Binnig. "Scanning tunneling microscopy". *Surf. Sci.*, **126**, 236, 1983. doi:10.1016/0039-6028(83)90716-1.

[46] The Nobel Prize in Physics 1986. Nobelprize.org. Nobel Media AB 2014. Web. 15 Aug 2017. `http://www.nobelprize.org/nobel_prizes/physics/laureates/1986/`.

[47] G. Attard and C. Barnes. *Surfaces*. Oxford University Press Inc., New York, 1998.

[48] L. Kuipers, R. W. M. Loos, H. Neerings, J. ter Horst, G. J. Ruwiel, A. P. de Jongh and J. W. M. Frenken. "Design and performance of a high-temperature, high-speed scanning tunneling microscope". *Rev. Sci. Instrum.*, **66**, 4557, 1995. doi:10.1063/1.1145289.

[49] J. Wintterlin, J. Trost, S. Renisch, R. Schuster, T. Zambelli and G. Ertl. "Real-time STM observations of atomic equilibrium fluctuations in an adsorbate system: O/Ru(0001)". *Surf. Sci.*, **394**, 159, 1997. doi:10.1016/S0039-6028(97)00604-3.

[50] C. T. Herbschleb, P. C. van der Tuijn, S. B. Roobol, V. Navarro, J. W. Bakker, Q. Liu, D. Stoltz, M. E. Cañas-Ventura, G. Verdoes, M. A. van Spronsen, M. Bergman, L. Crama, I. Taminiau, A. Ofitserov, G. J. C. van Baarle and J. W. M. Frenken. "The ReactorSTM: Atomically resolved scanning tunneling microscopy under high-pressure, high-temperature catalytic reaction conditions". *Rev. Sci. Instrum.*, **85**, 083703, 2014. doi:10.1063/1.4891811.

[51] L. Nguyen, L. Liu, S. Assefa, C. Wolverton, W. F. Schneider and F. F. Tao. "Atomic-Scale Structural Evolution of Rh(110) during Catalysis". *ACS Catal.*, **7**, 664, 2017. doi:10.1021/acscatal.6b02006.

[52] M. A. van Spronsen, J. W. M. Frenken and I. M. N. Groot. "Surface science under reaction conditions: CO oxidation on Pt and Pd model catalysts". *Chem. Soc. Rev.*, **46**, 4347, 2017. doi:10.1039/C7CS00045F.

[53] B. Hendriksen, S. Bobaru and J. Frenken. "Oscillatory CO oxidation on Pd(100) studied with in situ scanning tunneling microscopy". *Surf. Sci.*, **552**, 229, 2004. doi:10.1016/j.susc.2004.01.025.

[54] P. Sutter. *Scanning Tunneling Microscopy in Surface Science*, pages 969–1024. Springer New York, New York, 2007. doi:10.1007/978-0-387-49762-4_15.

[55] J. Kepler, Strena seu de Nive Sexangula. 1611, Frankfurt: G. Tampach, Web 14 Sep 2017. `http://www.thelatinlibrary.com/kepler/strena.html`.

[56] C. Kittel. *Introduction to Solid State Physics*. Wiley, Hoboken, 8th edition, 2005.

[57] P. W. Bridgman. "Certain Physical Properties of Single Crystals of Tungsten, Antimony, Bismuth, Tellurium, Cadmium, Zinc, and Tin". *P. Am. Acad. Arts Sci.*, **60**, 305, 1925. doi:10.2307/25130058.

[58] I. Langmuir. "Chemical Reactions at Low Pressures". *J. Am. Chem. Soc.*, **37**, 1139, 1915. doi:10.1021/ja02170a017.

[59] I. Langmuir. "The Condensation and Evaporation of Gas Molecules". *Proceedings of the National Academy of Sciences*, **3**, 141, 1917. doi:10.1073/pnas.3.3.141.

[60] I. Langmuir. "The Adsorption of Gases on Plane Surfaces of Glass, Mica and Platinum". *J. Am. Chem. Soc.*, **40**, 1361, 1918. doi:10.1021/ja02242a004.

[61] The Nobel Prize in Chemistry 1932. Nobelprize.org. Nobel Media AB 2014. Web. 5 Sep 2017. `http://www.nobelprize.org/nobel_prizes/chemistry/laureates/1932/`.

[62] O. Björneholm, A. Nilsson, H. Tillborg, P. Bennich, A. Sandell, B. Hernnäs, C. Puglia and N. Mårtensson. "Overlayer structure from adsorbate and substrate core level binding energy shifts: CO, CCH3 and O on Pt(111)". *Surf. Sci.*, **315**, L983, 1994. doi:10.1016/0039-6028(94)90530-4.

[63] M. Tüshaus, E. Schweizer, P. Hollins and A. Bradshaw. "Yet another vibrational study of the adsorption system Pt(111)-CO". *J. Electron Spectrosc. Relat. Phenom.*, **44**, 305, 1987. doi:10.1016/0368-2048(87)87031-7.

[64] B. N. J. Persson, M. Tüshaus and A. M. Bradshaw. "On the nature of dense CO adlayers". *J. Chem. Phys.*, **92**, 5034, 1990. doi:10.1063/1.458539.

[65] S. R. Longwitz, J. Schnadt, E. K. Vestergaard, R. T. Vang, I. Stensgaard, H. Brune and F. Besenbacher. "High-Coverage Structures of Carbon Monoxide Adsorbed on Pt(111) Studied by High-Pressure Scanning Tunneling Microscopy". *J. Phys. Chem. B*, **108**, 14497, 2004. doi:10.1021/jp0492218.

[66] R. Toyoshima, M. Yoshida, Y. Monya, K. Suzuki, K. Amemiya, K. Mase, B. S. Mun and H. Kondoh. "A high-pressure-induced dense CO overlayer on a Pt(111) surface: a chemical analysis using in situ near ambient pressure XPS". *Phys. Chem. Chem. Phys.*, **16**, 23564, 2014. doi:10.1039/C4CP04318A.

[67] G. Ertl, P. R. Norton and J. Rüstig. "Kinetic Oscillations in the Platinum-Catalyzed Oxidation of Co". *Phys. Rev. Lett.*, **49**, 177, 1982. doi:10.1103/PhysRevLett.49.177.

[68] T. Engel and G. Ertl. "Elementary Steps in the Catalytic Oxidation of Carbon Monoxide on Platinum Metals". volume 28 of *Advances in Catalysis*, pages 1 – 78. Academic Press, 1979. doi:https://doi.org/10.1016/S0360-0564(08)60133-9.

[69] C. T. Campbell, G. Ertl, H. Kuipers and J. Segner. "A molecular beam study of the catalytic oxidation of CO on a Pt(111) surface". *J. Chem. Phys.*, **73**, 5862, 1980. doi:10.1063/1.440029.

[70] J. Gustafson, R. Westerström, O. Balmes, R. v. R. A. Resta, X. Torrelles, C. T. Herbschleb, J. W. M. Frenken and E. Lundgren. "Reply to "Comment on 'Catalytic Activity of the Rh Surface Oxide: CO Oxidation over Rh(111) under Realistic Conditions"'". *J. Phys. Chem. C*, **114**, 22372, 2010. doi:10.1021/jp108816j.

[71] J. Gustafson, R. Westerström, A. Mikkelsen, X. Torrelles, O. Balmes, N. Bovet, J. N. Andersen, C. J. Baddeley and E. Lundgren. "Sensitivity of catalysis to surface structure: The example of CO oxidation on Rh under realistic conditions". *Phys. Rev. B*, **78**, 2008. doi:10.1103/PhysRevB.78.045423.

[72] J. Gustafson, S. Blomberg, N. M. Martin, V. Fernandes, A. Borg, Z. Liu, R. Chang and E. Lundgren. "A high pressure x-ray photoelectron spectroscopy study of CO oxidation over Rh(100)". *J. Phys.: Condens. Matter*, **26**, 055003, 2014. doi:10.1088/0953-8984/26/5/055003.

[73] S. Blomberg, M. J. Hoffmann, J. Gustafson, N. M. Martin, V. R. Fernandes, A. Borg, Z. Liu, R. Chang, S. Matera, K. Reuter and E. Lundgren. "In Situ X-Ray Photoelectron Spectroscopy of Model Catalysts: At the Edge of the Gap". *Phys. Rev. Lett.*, **110**, 2013. doi:10.1103/PhysRevLett.110.117601.

[74] V. R. Fernandes, M. V. den Bossche, J. Knudsen, M. H. Farstad, J. Gustafson, H. J. Venvik, H. Grönbeck and A. Borg. "Reversed Hysteresis during CO Oxidation over Pd 75 Ag 25 (100)". *ACS Catal.*, **6**, 4154, 2016. doi:10.1021/acscatal.6b00658.

[75] R. Toyoshima, M. Yoshida, Y. Monya, Y. Kousa, K. Suzuki, H. Abe, B. S. Mun, K. Mase, K. Amemiya and H. Kondoh. "In Situ Ambient Pressure XPS Study of CO Oxidation Reaction on Pd(111) Surfaces". *J. Phys. Chem. C*, **116**, 18691, 2012. doi:10.1021/jp301636u.

[76] R. van Rijn, O. Balmes, A. Resta, D. Wermeille, R. Westerström, J. Gustafson, R. Felici, E. Lundgren and J. W. M. Frenken. "Surface structure and reactivity of Pd(100) during CO oxidation near ambient pressures". *Phys. Chem. Chem. Phys.*, **13**, 13167, 2011. doi:10.1039/c1cp20989b.

[77] J. Schnadt, J. Knudsen, J. N. Andersen, H. Siegbahn, A. Pietzsch, F. Hennies, N. Johansson, N. Mårtensson, G. Öhrwall, S. Bahr, S. Mähl and O. Schaff. "The New Ambient Pressure X-ray Photoelectron Spectroscopy Instrument at MAX-lab". *J. Synchrotron Radiat.*, **19**, 701, 2012. doi:10.1107/S0909049512032700.

[78] S. K. Calderón, M. Grabau, L. Óvári, B. Kress, H.-P. Steinrück and C. Papp. "CO oxidation on Pt(111) at near ambient pressures". *J. Chem. Phys.*, **144**, 044706, 2016. doi:10.1063/1.4940318.

[79] J. Grant. "Some studies on the Ir(111) surface using LEED and Auger electron spectroscopy". *Surf. Sci.*, **25**, 451, 1971. doi:10.1016/0039-6028(71)90264-0.

[80] K. Ueda, K. Suzuki, R. Toyoshima, Y. Monya, M. Yoshida, K. Isegawa, K. Amemiya, K. Mase, B. S. Mun, M. A. Arman, E. Grånäs, J. Knudsen, J. Schnadt and H. Kondoh. "Adsorption and Reaction of CO and NO on

Ir(111) Under Near Ambient Pressure Conditions". *Top. Catal.*, **59**, 487, 2015. doi:10.1007/s11244-015-0523-5.

[81] E. Grånäs, M. Andersen, M. A. Arman, T. Gerber, B. Hammer, J. Schnadt, J. N. Andersen, T. Michely and J. Knudsen. "CO Intercalation of Graphene on Ir(111) in the Millibar Regime". *J. Phys. Chem. C*, **117**, 16438, 2013. doi:10.1021/jp4043045.

[82] M. Bianchi, D. Cassese, A. Cavallin, R. Comin, F. Orlando, L. Postregna, E. Golfetto, S. Lizzit and A. Baraldi. "Surface core level shifts of clean and oxygen covered Ir(111)". *New J. Phys.*, **11**, 063002, 2009. doi:10.1088/1367-2630/11/6/063002.

[83] Z. Liang, T. Li, M. Kim, A. Asthagiri and J. F. Weaver. "Low-temperature activation of methane on the IrO 2 (110) surface". *Science*, **356**, 299, 2017. doi:10.1126/science.aam9147.

[84] Y. B. He, A. Stierle, W. X. Li, A. Farkas, N. Kasper and H. Over. "Oxidation of Ir(111): From O−Ir−O Trilayer to Bulk Oxide Formation". *J. Phys. Chem. C.*, **112**, 11946, 2008. doi:10.1021/jp803607y.

[85] L. Anastasia and E. Negishi. *Handbook of Organopalladium Chemistry for Organic Synthesis.* Wiley, New York, 2002.

[86] A. D. Meijere and F. Diederich. *Metal-Catalyzed Cross-Coupling Reactions.* Wiley, Weinheim, 2004.

[87] X.-F. Wu, P. Anbarasan, H. Neumann and M. Beller. "From Noble Metal to Nobel Prize: Palladium-Catalyzed Coupling Reactions as Key Methods in Organic Synthesis". *Angew. Chem. Int. Ed.*, **49**, 9047, 2010. doi:10.1002/anie.201006374.

[88] M. M. B. Nilay Hazari, Patrick R. Melvin. "Well-defined nickel and palladium precatalysts for cross-coupling". *Nat. Rev. Chem.*, **1**, 0025, 2017. doi:10.1038/s41570-017-0025.

[89] C. González-Arellano, A. Abad, A. Corma, H. García, M. Iglesias and F. Sánchez. "Catalysis by Gold(I) and Gold(III): A Parallelism between Homo- and Heterogeneous Catalysts for Copper-Free Sonogashira Cross-Coupling Reactions". *Angew. Chem. Int. Ed.*, **46**, 1536, 2007. doi:10.1002/anie.200604746.

[90] G. Kyriakou, S. K. Beaumont, S. M. Humphrey, C. Antonetti and R. M. Lambert. "Sonogashira Coupling Catalyzed by Gold Nanoparticles: Does

Homogeneous or Heterogeneous Catalysis Dominate?" *ChemCatChem*, **2**, 1444, 2010. doi:10.1002/cctc.201000154.

[91] A. Corma, R. Juárez, M. Boronat, F. Sánchez, M. Iglesias and H. García. "Gold catalyzes the Sonogashira coupling reaction without the requirement of palladium impurities". *Chem. Commun.*, **47**, 1446, 2011. doi:10.1039/C0CC04564K.

[92] S. Sisodiya, L. R. Wallenberg, E. Lewin and O. F. Wendt. "Sonogashira coupling reaction over supported gold nanoparticles: Influence of support and catalyst synthesis route". *Appl. Catal., A*, **503**, 69, 2015. doi:10.1016/j.apcata.2015.07.001.

[93] J. Oliver-Meseguer, I. Dominguez, R. Gavara, A. Leyva-Pérez and A. Corma. "Disassembling Metal Nanocrystallites into Sub-nanometric Clusters and Low-faceted Nanoparticles for Multisite Catalytic Reactions". *ChemCatChem*, **9**, 1429, 2017. doi:10.1002/cctc.201700037.

[94] T. Ishida, H. Koga, M. Okumura and M. Haruta. "Advances in Gold Catalysis and Understanding the Catalytic Mechanism". *Chem. Rec.*, **16**, 2278, 2016. doi:10.1002/tcr.201600046.

[95] P. C. Mercedes Boronat. "Combined theoretical and spectroscopic mechanistic studies for improving activity and selectivity in heterogeneous catalysis". *Catal. Today*, **285**, 166, 2017. doi:10.1016/j.cattod.2016.11.048.

[96] C. Sánchez-Sánchez, F. Yubero, A. R. González-Elipe, L. Feria, J. F. Sanz and R. M. Lambert. "The Flexible Surface Revisited: Adsorbate-Induced Reconstruction, Homocoupling, and Sonogashira Cross-Coupling on the Au(100) Surface". *J. Phys. Chem. C*, **118**, 11677, 2014. doi:10.1021/jp501321u.

[97] V. K. Kanuru, G. Kyriakou, S. K. Beaumont, A. C. Papageorgiou, D. J. Watson and R. M. Lambert. "Sonogashira Coupling on an Extended Gold Surface in Vacuo: Reaction of Phenylacetylene with Iodobenzene on Au(111)". *J. Am. Chem. Soc.*, **132**, 8081, 2010. doi:10.1021/ja1011542.

[98] K. Sonogashira, Y. Tohda and N. Hagihara. "A convenient synthesis of acetylenes: catalytic substitutions of acetylenic hydrogen with bromoalkenes, iodoarenes and bromopyridines". *Tetrahedron Lett.*, **16**, 4467, 1975. doi:10.1016/S0040-4039(00)91094-3.

[99] M. Boronat, D. Combita, P. Concepción, A. Corma, H. García, R. Juárez, S. Laursen and J. de Dios López-Castro. "Making C–C Bonds with Gold:

Identification of Selective Gold Sites for Homo- and Cross-Coupling Reactions between Iodobenzene and Alkynes". *J. Phys. Chem. C*, **116**, 24855, 2012. doi:10.1021/jp3071585.

[100] D. Syomin and B. E. Koel. "Adsorption of iodobenzene (C6H5I) on Au(111) surfaces and production of biphenyl (C6H5–C6H5)". *Surf. Sci.*, **490**, 265, 2001. doi:10.1016/S0039-6028(01)01319-X.

[101] C. Sanchez-Sanchez, N. Orozco, J. P. Holgado, S. K. Beaumont, G. Kyriakou, D. J. Watson, A. R. Gonzalez-Elipe, L. Feria, J. F. Sanz and R. M. Lambert. "Sonogashira Cross-Coupling and Homocoupling on a Silver Surface: Chlorobenzene and Phenylacetylene on Ag(100)". *J. Am. Chem. Soc.*, **137**, 940, 2015. doi:10.1021/ja5115584.

[102] M. Boronat, T. López-Ausens and A. Corma. "Making C–C Bonds with Gold Catalysts: A Theoretical Study of the Influence of Gold Particle Size on the Dissociation of the C–X Bond in Aryl Halides". *J. Phys. Chem. C*, **118**, 9018, 2014. doi:10.1021/jp500806w.

[103] F. P. Netzer, F. Allegretti and S. Surnev. "Low-dimensional oxide nanostructures on metals: Hybrid systems with novel properties". *J. Vac. Sci. Technol. B.*, **28**, 1, 2010. doi:10.1116/1.3268503.

[104] G. Vurens, M. Salmeron and G. Somorjai. "Structure, composition and chemisorption studies of thin ordered iron oxide films on platinum (111)". *Surf. Sci.*, **201**, 129, 1988. doi:10.1016/0039-6028(88)90602-4.

[105] M. Ritter, W. Ranke and W. Weiss. "Growth and structure of ultrathin FeO films on Pt(111) studied by STM and LEED". *Phys. Rev. B*, **57**, 7240, 1998. doi:10.1103/PhysRevB.57.7240.

[106] W. Ranke, M. Ritter and W. Weiss. "Crystal structures and growth mechanism for ultrathin films of ionic compound materials: FeO(111) on Pt(111)". *Phys. Rev. B*, **60**, 1527, 1999. doi:10.1103/PhysRevB.60.1527.

[107] W. Weiss and W. Ranke. "Surface chemistry and catalysis on well-defined epitaxial iron-oxide layers". *Prog. Surf. Sci.*, **70**, 1, 2002. doi:10.1016/S0079-6816(01)00056-9.

[108] L. R. Merte, L. C. Grabow, G. Peng, J. Knudsen, H. Zeuthen, W. Kudernatsch, S. Porsgaard, E. Lægsgaard, M. Mavrikakis and F. Besenbacher. "Tip-Dependent Scanning Tunneling Microscopy Imaging of Ultrathin FeO Films on Pt(111)". *J. Phys. Chem. C*, **115**, 2089, 2011. doi:10.1021/jp109581a.

[109] Y. J. Kim, C. Westphal, R. X. Ynzunza, H. C. Galloway, M. Salmeron, M. A. Van Hove and C. S. Fadley. "Interlayer interactions in epitaxial oxide growth: FeO on Pt(111)". *Phys. Rev. B*, **55**, R13448, 1997. doi:10.1103/PhysRevB.55.R13448.

[110] J. Knudsen, L. R. Merte, L. C. Grabow, F. M. Eichhorn, S. Porsgaard, H. Zeuthen, R. T. Vang, E. Lægsgaard, M. Mavrikakis and F. Besenbacher. "Reduction of FeO/Pt(111) thin films by exposure to atomic hydrogen". *Surf. Sci.*, **604**, 11, 2010. doi:10.1016/j.susc.2009.10.008.

[111] W. Zhang, Z. Li, Y. Luo and J. Yang. "First Principles Study on the Geometric and Electronic Structures of the FeO/Pt(111) Surface". *J. Phys. Chem. C*, **113**, 8302, 2009. doi:10.1021/jp810751j.

[112] L. Giordano, G. Pacchioni, J. Goniakowski, N. Nilius, E. D. L. Rienks and H.-J. Freund. "Interplay between structural, magnetic, and electronic properties in a FeO/Pt(111) ultrathin film". *Phys. Rev. B*, **76**, 075416, 2007. doi:10.1103/PhysRevB.76.075416.

[113] W. Weiss. "Structure and composition of thin epitaxial iron oxide films grown onto Pt(111)". *Surf. Sci.*, **377-379**, 943, 1997. doi:10.1016/S0039-6028(96)01526-9.

[114] Y.-N. Sun, Z.-H. Qin, M. Lewandowski, E. Carrasco, M. Sterrer, S. Shaikhutdinov and H.-J. Freund. "Monolayer iron oxide film on platinum promotes low temperature CO oxidation". *J. Catal.*, **266**, 359, 2009. doi:10.1016/j.jcat.2009.07.002.

[115] Y.-N. Sun, L. Giordano, J. Goniakowski, M. Lewandowski, Z.-H. Qin, C. Noguera, S. Shaikhutdinov, G. Pacchioni and H.-J. Freund. "The Interplay between Structure and CO Oxidation Catalysis on Metal-Supported Ultrathin Oxide Films". *Angew. Chem. Int. Ed.*, **49**, 4418, 2010. doi:10.1002/anie.201000437.

[116] L. Giordano, M. Lewandowski, I. M. N. Groot, Y.-N. Sun, J. Goniakowski, C. Noguera, S. Shaikhutdinov, G. Pacchioni and H.-J. Freund. "Oxygen-Induced Transformations of an FeO(111) Film on Pt(111): A Combined DFT and STM Study". *J. Phys. Chem. C*, **114**, 21504, 2010. doi:10.1021/jp1070105.

[117] M. Lewandowski, Y. Sun, Z.-H. Qin, S. Shaikhutdinov and H.-J. Freund. "Promotional effect of metal encapsulation on reactivity of iron oxide supported Pt catalysts". *Appl. Catal., A*, **391**, 407, 2011. doi:10.1016/j.apcata.2010.04.030.

[118] M. Lewandowski, I. Groot, S. Shaikhutdinov and H.-J. Freund. "Scanning tunneling microscopy evidence for the Mars-van Krevelen type mechanism of low temperature CO oxidation on an FeO(111) film on Pt(111)". *Catal. Today*, **181**, 52, 2012. doi:10.1016/j.cattod.2011.08.033.

[119] L. Giordano, G. Pacchioni, C. Noguera and J. Goniakowski. "Identification of Active Sites in a Realistic Model of Strong Metal Support Interaction Catalysts: The Case of Platinum(111)-Supported Iron Oxide Film". *ChemCatChem*, **6**, 185, 2014. doi:10.1002/cctc.201300642.

[120] L. Giordano, G. Pacchioni, C. Noguera and J. Goniakowski. "Spectroscopic Evidences of Charge Transfer Phenomena and Stabilization of Unusual Phases at Iron Oxide Monolayers Grown on Pt(111)". *Top. Catal.*, **56**, 1074, 2013. doi:10.1007/s11244-013-0072-8.

[121] F. Ringleb, Y. Fujimori, H.-F. Wang, H. Ariga, E. Carrasco, M. Sterrer, H.-J. Freund, L. Giordano, G. Pacchioni and J. Goniakowski. "Interaction of Water with FeO(111)/Pt(111): Environmental Effects and Influence of Oxygen". *J. Phys. Chem. C*, **115**, 19328, 2011. doi:10.1021/jp207332n.

[122] A. S. Walton, J. Fester, M. Bajdich, M. A. Arman, J. Osiecki, J. Knudsen, A. Vojvodic and J. V. Lauritsen. "Interface Controlled Oxidation States in Layered Cobalt Oxide Nanoislands on Gold". *ACS Nano*, **9**, 2445, 2015. doi:10.1021/acsnano.5b00158.

[123] V. Fernandes. *Palladium alloy model systems for understanding the surface properties of Pd-based membranes and catalysis.* Phd. thesis, Norwegian University of Science and Technology, 2014.

[124] M. Shipilin, E. Lundgren, J. Gustafson, C. Zhang, F. Bertram, C. Nicklin, C. J. Heard, H. Grönbeck, F. Zhang, J. Choi, V. Mehar, J. F. Weaver and L. R. Merte. "Fe Oxides on Ag Surfaces: Structure and Reactivity". *Top. Catal.*, **60**, 492, 2016. doi:10.1007/s11244-016-0714-8.

[125] G. A. Somorjai, R. W. Joyner and B. Lang. "The Reactivity of Low Index [(111) and (100)] and Stepped Platinum Single Crystal Surfaces". *P. Roy. Soc. A-Math. Phy.*, **331**, 335, 1972. doi:10.1098/rspa.1972.0181.

[126] F. Tao, S. Dag, L.-W. Wang, Z. Liu, D. R. Butcher, H. Bluhm, M. Salmeron and G. A. Somorjai. "Break-Up of Stepped Platinum Catalyst Surfaces by High CO Coverage". *Science*, **327**, 850, 2010. doi:10.1126/science.1182122.

[127] R. Westerström, J. Gustafson, A. Resta, A. Mikkelsen, J. N. Andersen, E. Lundgren, N. Seriani, F. Mittendorfer, M. Schmid, J. Klikovits, P. Varga, M. D. Ackermann, J. W. M. Frenken, N. Kasper and A. Stierle. "Oxidation of Pd(553): From ultrahigh vacuum to atmospheric pressure". *Phys. Rev. B*, **76**, 2007. doi:10.1103/PhysRevB.76.155410.

[128] J. Gustafson, A. Resta, A. Mikkelsen, R. Westerström, J. N. Andersen, E. Lundgren, J. Weissenrieder, M. Schmid, P. Varga, N. Kasper, X. Torrelles, S. Ferrer, F. Mittendorfer and G. Kresse. "Oxygen-induced step bunching and faceting of Rh(553): Experiment and ab initio calculations". *Phys. Rev. B*, **74**, 2006. doi:10.1103/PhysRevB.74.035401.

[129] G. Hoogers and D. King. "Adsorbate-induced step-doubling reconstruction of a vicinal metal surface: oxygen on Rh(332)". *Surf. Sci.*, **286**, 306, 1993. doi:10.1016/0039-6028(93)90414-F.

[130] A. L. Walter, F. Schiller, M. Corso, L. R. Merte, F. Bertram, J. Lobo-Checa, M. Shipilin, J. Gustafson, E. Lundgren, A. X. Bríon-Ríos, P. Cabrera-Sanfelix, D. Sánchez-Portal and J. E. Ortega. "X-ray photoemission analysis of clean and carbon monoxide-chemisorbed platinum(111) stepped surfaces using a curved crystal". *Nat. Commun.*, **6**, 8903, 2015. doi:10.1038/ncomms9903.

[131] S. Blomberg, J. Zetterberg, J. Zhou, L. R. Merte, J. Gustafson, M. Shipilin, A. Trinchero, L. A. Miccio, A. M. na, M. Ilyn, F. Schiller, J. E. Ortega, F. Bertram, H. Grönbeck and E. Lundgren. "Strain Dependent Light-off Temperature in Catalysis Revealed by Planar Laser-Induced Fluorescence". *ACS Catal.*, **7**, 110, 2016. doi:10.1021/acscatal.6b02440.

[132] Q. Fu, W.-X. Li, Y. Yao, H. Liu, H.-Y. Su, D. Ma, X.-K. Gu, L. Chen, Z. Wang, H. Zhang, B. Wang and X. Bao. "Interface-Confined Ferrous Centers for Catalytic Oxidation". *Science*, **328**, 1141, 2010. doi:10.1126/science.1188267.

[133] M. M. Biener, J. Biener, R. Schalek and C. M. Friend. "Growth of nanocrystalline MoO3 on Au(111) studied by in situ scanning tunneling microscopy". *J. Chem. Phys.*, **121**, 12010, 2004. doi:10.1063/1.1808422.

[134] X. Deng, J. Lee, C. Wang, C. Matranga, F. Aksoy and Z. Liu. "In Situ Observation of Water Dissociation with Lattice Incorporation at FeO Particle Edges Using Scanning Tunneling Microscopy and X-ray Photoelectron Spectroscopy". *Langmuir*, **27**, 2146, 2011. doi:dx.doi.org/10.1021/la1049716.

[135] H. Zeuthen, W. Kudernatsch, L. R. Merte, L. K. Ono, L. Lammich, F. Besenbacher and S. Wendt. "Unraveling the Edge Structures of Platinum(111)-Supported Ultrathin FeO Islands: The Influence of Oxidation State". *ACS Nano*, **9**, 573, 2015. doi:10.1021/nn505890v.

[136] J. Fester, M. García-Melchor, A. S. Walton, M. Bajdich, Z. Li, L. Lammich, A. Vojvodic and J. V. Lauritsen. "Edge reactivity and water-assisted dissociation on cobalt oxide nanoislands". *Nat. Commun.*, **8**, 14169, 2017. doi:10.1038/ncomms14169.

[137] J. Kramer, C. Tegenkamp, W. Ernst and H. Pfnür. "Growth and surface morphology: epitaxial MgO films and the Ag(1,1,19) substrate". *Surf. Sci.*, **537**, 265, 2003. doi:10.1016/S0039-6028(03)00634-4.

[138] J. Schoiswohl, M. Sock, Q. Chen, G. Thornton, G. Kresse, M. G. Ramsey, S. Surnev and F. P. Netzer. "Metal supported oxide nanostructures: model systems for advanced catalysis". *Top. Catal.*, **46**, 137, 2007. doi:10.1007/s11244-007-0324-6.

[139] G. Ketteler and W. Ranke. "Heteroepitaxial Growth and Nucleation of Iron Oxide Films on Ru(0001)". *J. Phys. Chem. B*, **107**, 4320, 2003. doi:10.1021/jp027265f.

[140] G. Ketteler and W. Ranke. "Epitaxial iron oxide growth on a stepped Pt(9 11 11) surface". *J. Vac. Sci. Technol. A.*, **23**, 1055, 2005. doi:10.1116/1.1889441.

[141] J. Mol. "Industrial applications of olefin metathesis". *J. Mol. Catal. A: Chem.*, **213**, 39, 2004. doi:10.1016/j.molcata.2003.10.049.

[142] C. Copéret and J.-M. Basset. "Strategies to Immobilize Well-Defined Olefin Metathesis Catalysts: Supported Homogeneous Catalysis vs. Surface Organometallic Chemistry". *Adv. Synth. Catal.*, **349**, 78, 2007. doi:10.1002/adsc.200600443.

[143] W. Zhang, J. L. Loebach, S. R. Wilson and E. N. Jacobsen. "Enantioselective Epoxidation of Unfunctionalized Olefins Catalyzed by (Salen)manganese Complexes". *J. Am. Chem. Soc.*, **112**, 2801, 1990. doi:10.1021/ja00163a052.

[144] W. Zhang and E. N. Jacobsen. "Asymmetric Olefin Epoxidation with Sodium Hypochlorate Catalyzed by Easily Prepared Chiral Mn(III) Salen Complexes". *J. Org. Chem.*, **56**, 2296, 1991. doi:10.1021/jo00007a012.

[145] E. N. Jacobsen, W. Zhang, A. R. Muci, J. R. Ecker and L. Deng. "Highly enantioselective epoxidation catalysts derived from 1,2-diaminocyclohexane". *J. Am. Chem. Soc.*, **113**, 7063, 1991. doi:10.1021/ja00018a068.

[146] R. Irie, K. Noda, Y. Ito, N. Matsumoto and T. Katsuki. "Catalytic asymmetric epoxidation of unfunctionalized olefins using chiral (salen)manganese(III) complexes". *Tetrahedron*, **2**, 481, 1991. doi:10.1016/S0957-4166(00)86102-9.

[147] K. Gupta and A. Sutar. "Catalytic activities of Schiff base transitional metal complexes". *Coord. Chem. Rev.*, **252**, 1420, 2008. doi:10.1016/j.ccr.2007.09.005.

[148] N. C. Maity, G. V. Rao, K. Prathap, S. H. Abdi, R. I. Kureshy, N. ul H. Khan and H. C. Bajaj. "Organic carbonates as solvents in macrocyclic Mn(III) salen catalyzed asymmetric epoxidation of non-functionalised olefins". *J. Mol. Cat. A-Chem.*, **366**, 380, 2013. doi:10.1016/j.molcata.2012.10.021.

[149] P. G. Cozzi. "Metal-Salen Schiff base complexes in catalysis: practical aspects". *Chem. Soc. Rev.*, **33**, 410, 2004. doi:10.1039/B307853C.

[150] W. Adam, C. Mock-Knoblauch, C. R. Saha-Möller and M. Herderich. "Are Mn^{IV} Species Involved in Mn(Salen)-Catalyzed Jacobsen-Katsuki Epoxidations? A Mechanism Elucidation of Their Formation and Reaction Modes by EPR Spectroscopy, Mass-Spectral Analysis, and Product Studies: Chlorination versus Oxygen Transfer". *J. Am. Chem. Soc.*, **122**, 9685, 2000. doi:10.1021/ja0005082.

[151] I. Kuźniarska-Biernacka, A. P. C. Ana R. Silva, J. ao Pires and C. Freire. "Direct immobilisation versus covalent attachment of a Mn(III)salen complex onto an Al-pillared clay and influence in the catalytic epoxidation of styrene". *J. Mol. Cat. A-Chem.*, **278**, 82, 2007. doi:10.1016/j.molcata.2007.08.022.

[152] I. Kuźniarska-Biernacka, A. P. C. Ana R. Silva, J. ao Pires and C. Freire. "Anchoring of Chiral Manganese(III) Salen Complex onto Organo Clay and Prous Clay Heterostructure and Catalytic Activity in Alkene Epoxidation". *Catal. Lett.*, **134**, 63, 2010. doi:10.1007/s10562-009-0232-4.

[153] A. M. Garcia, V. Morena, S. X. Delgado, A. e. Ramirez, L. A. . Vargas, M. A. Vicente, A. Gil and L. A. Galeano. "Encapsulation of SALEN- and SALHD-Mn(III) complexes in an Al-pillared clay for bicarbonate-assisted

catalytic epoxidation of cyclohexene". *J. Mol. Cat. A-Chem.*, **416**, 10, 2016. doi:10.1016/j.molcata.2016.01.034.

[154] H. Gaspar, M. Andrade, C. Periera, A. Pereira, S. Rebelo, J.P.Araújo, J.Pires, A. Carvalho and C. Freire. "Alkene epoxidation by manganese(III) complexes immobilized onto nanostructured carbon CMK-3". *Catal. Today*, **203**, 103, 2013. doi:10.1016/j.cattod.2012.04.018.

[155] J. Huang, X. Fu, G. Wang, Q. Miao and G. Wang. "Axially coordinated chiral salen Mn(III) anchored onto azole onium modified ZnPS-PVPA as effective catalysts for asymmetric epoxidation of unfunctionalized olefins". *Dalton Trans.*, **41**, 10661, 2012. doi:10.1039/c2dt30081h.

[156] P. Das, A. R. Silva, A. p. Carvalho, J. ao Pires and C. Freire. "Organofunctionalized mesoporous supports for Jacobsen-type catalyst: Laponite versus MCM-41". *J. Mater Sci.*, **44**, 2865, 2009. doi:10.1007/s10853-009-3379-x.

[157] F. Maia, R. Silva, B. Jarrais, A. R. Silva, C. Freire, M. F. Pereira and J. L. Figueiredo. "Pore tuned activated carbons as supports for an enantioselective molecular catalyst". *J. Colloid Interf. Sci.*, **328**, 314, 2008. doi:10.1016/j.jcis.2008.09.030.

[158] J. Huang, L. Yuan and J. Cai. "Constraining asymmetric organometallic catalysts within mesoporous supports ZnPS-BrPPAS boosts their enantioselectivity". *J. Mol. Cat. A-Chem.*, **416**, 147, 2016. doi:10.1016/j.molcata.2015.10.011.

[159] M. D. Angelino and P. E. Laibinis. "Polymer-Supported Salen Complexes for Heterogeneous Asymmetric Synthesis: Stabilityu and Selectivity". *J. Polym. Sci. A1.*, **37**, 3888, 1999. doi:10.1002/(SICI)1099-0518(19991101)37:21<3888::AID-POLA2>3.0.CO;2-B.

[160] A. R. Silva, J. L. Figueiredo, C. Freire and B. de Castro. "Manganese(III) salen complexes anchored onto activated carbon as heterogeneous catalyst for the epoxidation of olefins". *Microporous Mesoporous Mater.*, **68**, 83, 2004. doi:10.1016/j.micromeso.2003.12.002.

[161] R. Ji, K. Yu, L.-L. Lou, Z. Gu and S. Liu. "Mesoporous Silica Supported Unsymmetric Chiral Mn(III) Salen Complex: Synthesis, Characterization and Effect of Pore Size on Catalytic Performance". *J. Inorg. Organomet. Polym.*, **20**, 675, 2010. doi:10.1007/s10904-010-9395-0.

[162] V. L. P. Fragola, F. Lupo, A. Pappalardo, G. T. Sfrazzetto, R. M. Toscano, F. P. Ballistreri, G. A. Tomaselli and A. Gulino. "A surface-confined O=Mn^{V}(salen) oxene catalyst and high turnover values in asymmetric epoxidation of unfunctionalized olefins". *J. Mater. Chem.*, **22**, 20561, 2012. doi:10.1039/c2jm34847k.

[163] A. Mohammadinezhad, M. A. Nasseri and M. Salimi. "Cellulose as an efficient support for Mn(salen)CL: application for catalytic oxidation of sulfides to solfoxides". *RSC Adv.*, **4**, 39870, 2014. doi:10.1039/C4RA06450J.

[164] H. T. Ban, T. Kase and M. Murata. "Manganese Based Transition Metal Complexes as New Catalyst for Olefin Polymerizations". *J. Polym. Sci. A1.*, **39**, 3733, 2001. doi:10.1002/pola.10021.

[165] F. Jutz, J.-D. Grunwaldt and A. Baiker. "Mn(III)(salen)-catalyzed synthesis of cyclic organic carbonates from propylene and styrene oxide in "supercritical" CO_2". *J. Mol. Cat. A-Chem.*, **279**, 94, 2008. doi:10.1016/j.molcata.2007.10.010.

[166] F. Jutz, J.-D. Grunwaldt and A. Baiker. "*In Situ* XAS study of the Mn(III)(salen)Br catalyzed synthesis of cyclic organic carbonates from epoxides and CO_2". *J. Mol. Cat. A-Chem.*, **297**, 63, 2009. doi:10.1016/j.molcata.2008.10.009.

[167] I. Bar-Nahum, H. Cohen and R. Neumann. "Organometallic-Polyoxometalate Hybrid Compounds: Metallosalen Compounds Modified by Keggin Type Polyoxometalates". *Inorg. Chem.*, **42**, 3677, 2003. doi:10.1021/ic034095s.

[168] Q. Wu, S.-W. Lin, Y. G. Li and E.-B. Wang. "New supramolecular hybrids based on A-type Anderson polyoxometalates and Mn-Schiff-base complexes". *Inorg. Chim. Acta*, **382**, 139, 2012. doi:10.1016/j.ica.2011.10.028.

[169] A. Schwarz, D. Z. Gao, K. Lämmle, J. Grenz, M. Watkins, A. Shluger and R. Wiesendanger. "Determining Adsorption Geometry, Bonding and Translational Pathways of a Metal-Organic Complex on an Oxide Surface: Co-Salen on NiO(001)". *J. Phys. Chem. C*, **117**, 1105, 2013. doi:10.1021/jp311702j.

[170] K. Lämmle, T. Trevethan, A. Schwarz, M. Watkins, A. Shluger and R. Wiesendanger. "Unambiguous Determination of the Adsorption Geometry of a Metal-Organic Complex on a Bulk Insulator". *Nano Lett.*, **10**, 2965, 2010. doi:10.1021/nl101290t.

Paper I

Sonogashira cross-coupling over Au(111): From UHV to ambient pressure

N Johansson[1], S Sisodiya[2], P Shayesteh[1], S Chaudhary[1,4], J N Andersen[1,3], J Knudsen[1,3], O F Wendt[2], and J Schnadt[1,3]

[1]Division of Synchrotron Radiation Research, Department of Physics, Lund University, Box 118, 221 00 Lund, Sweden

[2]Centre for Analysis and Synthesis, Department of Chemistry, Lund University, Box 124, 221 00 Lund, Sweden

[3]MAX IV Laboratory, Lund University, Box 118, 221 00 Lund, Sweden

E-mail: joachim.schnadt@sljus.lu.se

Abstract. We have studied the reaction of phenylacetylene with chloro-, bromo-, and iodobenzene on the Au(111) surface as a model system for the gold-catalysed Sonogashira cross-coupling. Both ultrahigh vacuum (UVV)-based and ambient pressure X-ray photoelectron spectroscopy show that iodo- and chlorobenzene (IB and CB) undergo the cross-coupling reaction towards diphenylacetylene. Bromobenzene, in contrast, does not react in the ultrahigh vacuum experiments. Further, at ambient pressure signs are found for poisoning of the Au(111) surface by a carbon species formed in the reaction. The understanding obtained in the reaction experiments are based on a thorough investigation of the adsorption of PA, IB, CB, and BB on the Au(111) surface by soft X-ray absorption spectroscopy and temperature-dependent X-ray photoelectron spectroscopy. In particular, the experiments provide the orientation of the intact adsorbates with respect to the surfaces at liquid nitrogen temperature. Dissociation in the temperature regime between -80 and -15°C is observed for iodo- and chlorobenzene, but not for BB, in agreement with that only IB and CB, but not BB, react PA to form diphenylacetylene. The difference is tentatively attributed to a difference in surface orientation of the different halobenzenes.

Keywords: Au(111), halobenzene, XPS, XAS, APXPS, Sonogashira cross-coupling

[4] Present address: Department of Physics, Indian Institute of Technology Ropar, Rupnagar, Punjab-140001, India

1. Introduction

Metal-catalysed cross-coupling reactions to form C-C bonds are of paramount importance in organic synthesis with a range of application in the production of fine chemicals and pharmaceuticals [1-3]. Most often molecular species or metal nanoparticles based on palladium or nickel have been used as catalysts [4]. Among cross-coupling reactions, the Sonogashira cross-coupling, cf. Scheme 1, is unique in that it uses unfunctionalized acetylenes as a coupling partner, thus forming a product with one sp-hybridized carbon atom [5]. It is also unique in that gold is active in the Sonogashira cross-coupling, primarily in the form of gold nanoparticles [6-12]. Also extended gold surfaces [Au(111)] have been shown to mediate the cross-coupling between IB and PA [13, 14]. The latter finding unambiguously shows that cross-coupling also can take place under heterogeneous conditions, and a mechanism for the heterogeneous coupling was also proposed which involves C–I bond cleavage on the gold surface [15]. This is in agreement with previous studies on the adsorption and dissociation of IB on Au(111), where it was found that IB dissociates on the Au(111) surface at 175 K, producing, among other things, biphenyl and I_2 [16]. It has also been shown that the Au(111) facets of Au nanorods are more effective in mediating the Sonogashira coupling reaction compared to their Au(100) facets [17]. While basic knowledge on the Sonogashira coupling over gold thus is readily available, the details of the reaction mechanism remain not fully clarified [18], and investigations which address these details are needed to further the field.

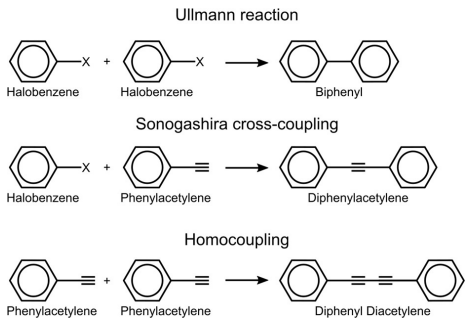

Scheme 1. Coupling reactions that are reported to occur on the extended Au(111) surface.

A general trend in cross-coupling reactions is the development of catalysts that allow the use of less reactive, but cheaper and more available bromo- and particularly CBs [19]. For the gold-catalysed Sonogashira reaction this concept has, however, hardly been explored at all. All examples include IBs, while, to our knowledge, to-date only two studies exist which address the Sonogashira coupling of BB and CB. Boronat et al. [20] investigated the dissociation of IB, BB, and CB over extended Au(111) surfaces and Au nanoparticles using density functional theory (DFT), and it was found that all three compounds adhere to similar dissociation mechanism on the Au(111) surface, with IB having the lowest activation energy and CB the highest. Oliver-Meseguer et al. investigated the Sonogashira cross-coupling over Au nanoparticles and -clusters for a variety of iodo-, bromo-, and chlorobenzene derivatives with aliphatic and aromatic alkynes

[10]. Their findings agree with Boronat et al. insofar as chlorobenzene derivatives resulted in lower yields. Experimental data on unfunctionalized BB and CB are not available so far, however.

Here we present an analogous experimental study using X-ray photoelectron spectroscopy (XPS) and ambient pressure XPS (APXPS) to investigate the interaction of IB, BB, and CB with PA. From our spectroscopy data we conclude that the Au(111) surface mediates the Sonogashira cross-coupling between PA and both IB and CB in UHV and at ambient pressure, while no cross-coupling is found for BB. This is partly attributed to the dissociation of the C-I bond of IB and the low bond angle between CB and the substrate. We find also, however, that at elevated temperature in ambient pressure the Au(111) surface is inactivated rapidly by formation of a carbon species. This surface poison is not seen in the UHV measurements, which illustrates the importance of approaching real pressure and temperature conditions in surface studies on catalysis.

2. Experimental

The temperature-dependent X-ray photoelectron spectroscopy (TDXPS) and temperature-dependent reaction XPS (TDRXPS) experiments were performed at beamline D1011 [21] and the APXPS experiments at the SPECIES beamline [22] on the MAX-II electron storage ring of the National Swedish Synchrotron Radiation Facility MAX IV Laboratory in Lund. The D1011 experimental system consists of a preparation chamber separated by a gate valve from an analysis chamber, both with a base pressure in the 10^{-10} mbar range. The preparation chamber hosts standard surface science equipment for sample preparation and characterization. The analysis chamber is equipped with a Scienta SES-200 electron energy analyser and a partial electron yield detector. The APXPS end station [23, 24] at the SPECIES beamline consists of a preparation chamber and an analysis chamber separated by a gate valve, both with a base pressure in the low 10^{-10} mbar range. The preparation chamber houses standard surface science equipment for cleaning and sample characterization. The analysis chamber houses a reaction cell inside the main vacuum system that, after docking to the SPECS Phoibos 150 NAP electron energy analyser, enables acquisition of X-ray photoelectron (XP) spectra at pressures up to 25 mbar. This scheme allows for quick switching (~10 min) between UHV and ambient pressure investigations effectively bridging the *pressure gap* and linking previous UHV results to ambient pressure data.

For the TDXPS and TDRXPS measurements the Au(111) crystal was mounted on the sample manipulator in a tungsten wire, while for the APXPS measurements the crystal was mounted on a transferrable stainless steel sample plate. In both cases, the sample temperature was measured by a type K thermocouple, mounted in a hole in the side of the Au(111) crystal. The sample was cleaned by Ar^+-sputtering using an acceleration voltage of 1 kV, followed by thermal annealing at 550°C. During the TDXPS and TDRXPS experiments, the Au(111) support was cooled using liquid nitrogen as specified below. CB (C_6H_5Cl), BB (C_6H_5Br), IB (C_6H_5I), and PA (C_6H_5CCH) were provided through a leak valve from a UHV-tight glass test tube. The reagents were degassed prior to dosing by several freeze-pump-thaw cycles. For the TDXPS and TDRXPS measurements, they were then dosed onto the liquid nitrogen-cooled Au(111) support at a temperature of -

160°C. Doses are given in quantities of L (1 L = 1 Langmuir = 1.33×10^{-6} mbar×s), while for the APXPS measurements the compounds were dosed onto the Au(111) crystal at a pressure of about (0.2±0.05) mbar. Coverages were estimated from the attenuation of the Au $4f_{7/2}$ line, assuming the same electron attenuation properties as benzene for all chemicals, with an electron inelastic mean free path (IMFP) of 11.7 Å [25]. Monolayer (ML) reference spectra were obtained from the temperature-dependent X-ray photoelectron (TDXP) spectra by identifying the point of multilayer desorption. Here, a ML is defined in terms of surface saturation, i.e. the coverage when no further molecule can be accommodated in the first adsorbate layer on the Au(111) surface anymore, but instead growth of a second layer would start. For the XAS and XPS measurements the compounds were dosed onto the Au(111) surface at pressures in the 10^{-9} mbar range, and coverages of 0.75 ML (1.1 L dose), 0.6 ML (1.1 L), 0.3 ML (0.2 L), and 0.3 ML (0.1 L) of PA, CB, BB, and IB were achieved. In the TDXPS experiments, initial multilayers were prepared on the Au(111) surface by dosing the pure compounds at pressures in the 10^{-8} mbar range. These multilayers correspond to coverages of 3.1 ML (PA), 5.4 ML (CB), 1.9 ML (BB), and 5 ML (IB), respectively. For the TDRXPS measurements 0.4 ML (0.5 L) of PA were dosed onto the Au(111) surface pre-covered by 0.7 ML CB, 0.15 ML BB, and 0.4 ML IB, respectively. All TDXP and TDRXP spectra were measured in sets of C 1s, Au 4f, and halogen core level spectra (Cl 2p/Br 3d/I 4d for CB/BB/IB) during the heating run. For the TDXPS measurements, approximate heating rates of 3.2°C/min, 5.3°C/min, 4.2°C/min, and 4°C/min were used for the PA, CB, BB, and IB preparations. In the TDRXPS measurements the heating rates were about 4.1°C/min, 4.4°C/min, and 5.3°C/min for the preparations of PA on CB, BB, and IB, respectively.

All XP spectra were collected in normal emission geometry with the light incident at a 45º angle relative to the surface. All XP, TDXP, TDRXP, and ambient pressure x-ray photoelectron (APXP) spectra were calibrated to the Au $4f_{7/2}$ component of a Au 4f spectrum. The Au 4f spectrum itself was calibrated to a Fermi energy-calibrated Au $4f_{7/2}$ line acquired on the clean Au(111) surface. All XP spectra were acquired with an analyser pass energy of 50 eV. The C 1s, Cl 2p, and all temperature-dependent X-ray photoelectron (TDXP) spectra were measured with a photon energy of 380 eV at an overall experimental resolution of 215 meV. The Br 3d spectrum of the monolayer was collected using photons of an energy of 180 eV with an overall resolution of 185 meV, while the I 3d spectrum was measured using photons of an energy of 725 eV at an overall resolution of 350 meV. A Shirley-type background was removed from all Au 4f spectra, while a polynomial background was used in the case of C 1s and halogen core level lines. For all C 1s TDXP spectra the binding energy is given in terms of the feature's peak maximum position. All analysis was performed within the programming environment Igor Pro, using the built-in minimization algorithm and Voigt functions [26, 27] for fitting. Potential beam damage was evaluated by measuring subsequent fast C 1s XP spectra in the same spot, and it was found not to be an issue.

The XAS data were acquired using a multichannel plate-based partial electron yield detector mounted under the sample at a 90° angle to the incoming photon beam. All X-ray absorption (XA) spectra were acquired using a retardation voltage of 150 V. The energy scale of the XA spectra was calibrated from a measurement of Au 4f XP spectra excited by first- and second-order light transmitted by the beamline's monochromator.

The uncertainty of the calibration is less than 50 meV. A linear background was fitted to the pre-edge of the XAS data and then removed from the spectrum. To normalize the data with respect to beamline flux, the spectra were divided by the time-dependent storage ring beam current in each point and a beamline transmission spectrum measured with a photodiode mounted just before the end station. To normalize the sample response the XA spectra were also divided by an identically treated XA spectrum measured on a clean Au(111) substrate. Finally, each spectrum was normalized to the intensity at the highest-energy point of the spectrum in order to normalize to the continuum of states. XA spectra were recorded as a function of X-ray incidence angle θ, which is given with respect to the surface. The uncertainties of the measured intensities are estimated from the deviation depending on reference point for continuum of states normalization and precision in resonance energy.

3. Results and Discussion

3.1 Halobenzene adsorption on Au(111)

We start by considering the adsorption of the halobenzenes on the Au(111) surface. We will analyze the orientation of the adsorbed compounds with respect to the Au(111) surface using XAS as well as the nature of the surface chemical species as a function of sample temperature. Particular focus will be on the question whether the halobenzenes dissociate on the surface or not.

3.1.1 XAS results. In figure 1 angle-resolved C K-edge XA spectra of submonolayers of the halogenated benzenes and PA on Au(111) are shown (for details on the coverage see Experimental section). All spectra were acquired at a temperature of -160°C. Also shown in the figure are the intensities of the C 1s → $\pi^*(LUMO_{phenyl})$ transition as a function of incidence angle for all compounds. A summary of the XAS assignments is shown in Table 1. We will now discuss these data separately for each adsorbate.

Figure 1(a) contains the data for PA on Au(111). Resonances are found at 285.1 eV, 285.9 eV, 287.4 eV, 288.0 eV, 289.5 eV, and 294.0 eV photon energy. The energy of the resonance at 285.1 eV is similar to that of the C 1s → $\pi^*(1e_{2u})$ transition of benzene, which has been observed at 285 eV [28]. The line is therefore assigned to the C 1s → $\pi^*(LUMO_{phenyl})$ transition, while the resonance at 285.9 eV is assigned to the C 1s → $\pi^*(LUMO_{acetylene})$ transition in accordance with measurements on acetylene [29]. In principle, the $LUMO_{phenyl}$ resonance should contain fine structure due to the six chemically inequivalent C atoms in PA [30], but this structure is not resolved in our measurements. In accordance with XAS data obtained on a multilayer of PA on Cu(111) [31], Rh(100) [32], and Pt(111) [33] the resonance at 287.4 eV is assigned to a PA C 1s → σ*(C-H) transition. These studies attributed additional resonances at ~288.7 eV and 289.4 eV photon energy to a mixed high-energy C 1s → π*/ C 1s → σ*(C-H) resonance and a further high-energy C 1s → π* resonance. In contrast, no resonance is found at 288.7 eV in the present data, but the resonance at 288.0 eV has the distinct angular dependence of a C 1s → π* transition. In agreement with the finding reported on the literature, the resonance at 289.5 eV is assigned to a C 1s → π* transition, but with a contribution of the C 1s → σ*(C-H) transition, as seen from the angular dependence. Finally, the resonance

at 294.0 eV is assigned to a C 1s → σ*(C-C) transition in view of its energy which is similar to that found for the corresponding resonance of benzene [34].

Figure 1(b) shows the height of the C 1s → π*(LUMO$_{phenyl}$) transition for the different light incidence angles. Since the height of the resonance is easier to determine than its intensity, which would require a deconvolution of the peak, it is here taken as a good approximation to the latter. Assuming a sixfold symmetry of the Au(111) surface, which implies the existence of three physically identical rotational domains, and assuming that all phenyl groups have the same angle to the surface, one can fit the data as outlined in Ref. [35]. In the present case the curve fit yields an angle of (15 ± 4)° between the plane of the phenyl group and the Au(111) surface.

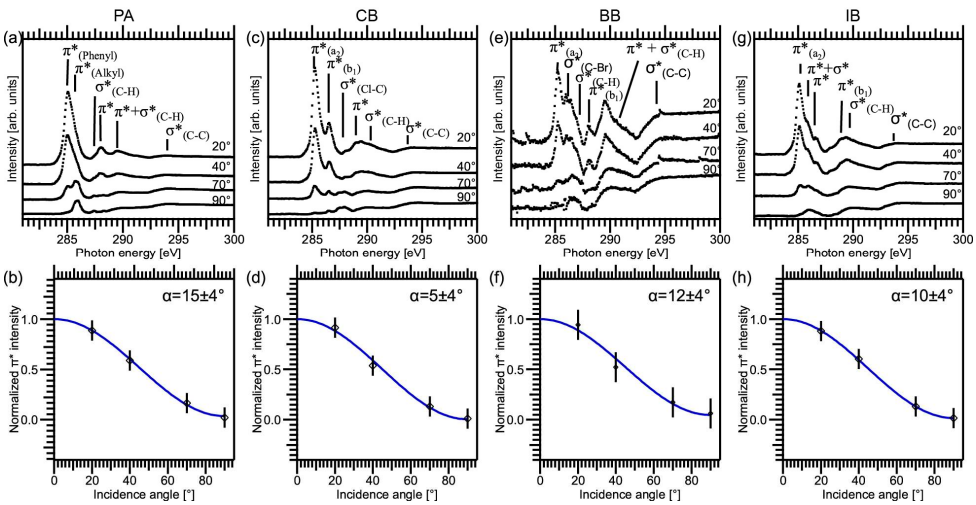

Figure 1. C 1s XAS data for submonolayer preparations of PA, CB, BB, and IB on a Au(111) surface. (a), (c), (e), and (g) show the angle-resolved XA spectra of PA, CB, BB, and IB. The incidence angle is given with respect to the surface. (b), (d), (f), and (h) show the corresponding intensities of the C 1s → LUMO transitions.

Figure 1(c) contains the angle-resolved XA spectra for a submonolayer of CB/Au(111). Clearly identifiable resonances are found at 285.2 eV, 286.7 eV, 287.8 eV, 289.0 eV, 290.3 eV, and 294.1 eV photon energy. The appearance of the low-energy part of the spectrum in the 285-287 eV photon energy range is related to the presence of the Cl heteroatom, the introduction of which reduces the molecular symmetry from D_{6h} to C_{2v}. The change of symmetry splits the doubly degenerate π*(e_{2u}) orbital of benzene into a_2 and b_1 components [14, 36, 37], where the a_2 orbital is spread over the five non-Cl-bonded carbon atoms – i.e. it does not have any weight on the Cl-bonded carbon atom – and the b_1 orbital with much weight on the Cl-neighbouring C atom. The energy of the C 1s level of this C atom can be expected to be chemically shifted towards higher binding energy due to the high electronegativity of Cl, which should also increase the XAS transition energy. Therefore, the resonance at 286.7 eV is assigned to the C 1s → π*(b_1) transition, while the low-energy peak

at 285.2 eV is due to the C 1s → π*(a_2) transition. At 287.8 eV photon energy a resonance is identifiable in the spectra measured at incidence angles of θ=90° and 70°. The angular dependence of this resonance corresponds to that of a σ* orbital. In an XAS study of CB adsorbed on the Cu(111) surface, Yang *et al.* [36] found a resonance in this energy regime and attributed it to a transition into an antibonding σ*(C-Cl) orbital, an assignment which we follow here, based on the observed angle dependence. The line at 289 eV is assigned to a higher-lying C 1s → π* resonance, while the resonances at 290.3 eV and 294.1 eV are assigned to C 1s → σ*(C-H) and σ*(C-C) transitions.

As for PA, we have plotted the intensity for the lowest π* resonance – the π*(a_2) resonance – in figure 1(d) to allow an identification of the angle of the molecule with respect to the surface. A curve fit based on the same assumptions as before indicates a low tilt angle of (5 ± 4)° of the phenyl group with respect to the surface. Thus, the CB molecules lie very flat on the Au(111) surface in comparison to PA.

Figure 1(e) shows the angle-resolved C K-edge XA spectra of BB/Au(111). Resonances are found at 285.2 eV, 286.5 eV, 287.0 eV, 288.0 eV, 289.5 eV, and 293.7 eV photon energy. In accordance with data on multilayers of BB on Pt(111) [37] the resonances can be assigned as follows: As for CB, the benzene C 1s → π*(e_{2u}) resonance is split into the C 1s → π*(a_2) and C 1s→ π*(b_1) components at 285.2 eV and 288.0 eV photon energy, respectively. Hence, the dependence of the π*(b_1) energy on the electronegativity of the heteroatom is further confirmed. Also in agreement with the assignments for CB, the line at 286.5 eV photon energy is assigned to a C 1s → σ*(C-Br) transition [37], while the resonance at 287.0 eV photon energy is due to a C 1s → σ*(C-H) transition. The line at 289.5 eV is partly assigned to a higher-lying C 1s → π* transition due to its characteristic angle behaviour. However, at the same energy also a C 1s → σ* resonance is found as is obvious from the intensity in the spectra obtained at θ=90°. This line is assigned to a C 1s → σ*(C-H) transition in accordance with what is discussed above. The last resonance at 293.7 eV photon energy is assigned to the C 1s → σ*(C-C) transition. Figure 1(f) shows the intensity of the π*(a_2) resonance for the different acquisition angles. The fit reveals that the angle between the surface and the benzene ring is (12 ± 4)°.

Finally, figure 1(g) shows the angle-resolved XAS data of IB/Au(111). Resonances are observed at 285.1 eV, 285.9 eV, 286.5 eV, 288.9 eV, 289.7 eV, and 293.7 eV photon energy. Again, the lowest-energy resonances at 285.1 eV and 285.9 eV photon energy are assigned to the C 1s → π*(a_2) and C 1s → π*(b_1) transitions, which together form the C 1s →π*($LUMO_{phenyl}$) peak. The assignment is in agreement with an earlier study of IB/Cu(111) [36]. The difference in energy between the π*(a_2) and π*(b_1) components is considerably smaller in comparison to the shift introduced by Cl and Br (0.75 eV as compared to 1.5 eV/1.3 eV). The decrease in splitting is easily explained from the lower C 1s binding energy of the C atom neighbouring the heteroatom, which is due to the smaller electronegativity of iodine compared to that of chlorine. An additional broad resonance is found at 285.9 eV photon energy, especially visible in the θ=90° spectrum. Due to its width and angle dependence this resonance is assigned to a C 1s → σ*(I-C) transition similar to that of CB [36] and BB. The resonance at 286.5 eV photon energy is attributed to a C 1s→π* transition due to the

apparent angle dependency. This resonance is not reported in previous studies of IB/Au(111), although it is present in the XA spectrum of a multilayer of IB adsorbed on the Au(111) surface (cf. figure S1 in the Supplementary Information). Hence, it is considered to be an intrinsic π* resonance of IB. The resonance at 288.9 eV photon energy is assigned to the C 1s → π*(b_1) transition in accordance with previous studies [14]. The resonances at 289.7 eV and 293.7 eV are assigned to C 1s → σ*(C-H) and σ*(C-C) transitions, respectively. As for the other halogenated benzenes, figure 1(h) shows the intensity of the C 1s→π*(a_2) intensity as a function of X-ray incidence angle. Making the same assumptions as above, a phenyl tilt angle of (10 ± 4)° is found for IB/Au(111).

XA spectra on multilayers of all molecules were also measured (not shown). In these spectra no angle dependence of the XAS signal is seen. Hence, the molecules in the multilayers do not bind in a preferred direction and are randomly ordered with respect to the Au(111) support. The loss of order is attributed to weak intermolecular interactions.

Table 1: Energies of the XAS resonances and angles between the Au(111) substrate and phenyl ring of the compounds.

	transition	hν [eV]	α[°]
PA	C 1s → π*(Phenyl)	285.1	15±4
	C 1s → π*(Alkyl)	285.9	
	C 1s → σ*(C-H)	287.4	
	C 1s → π*	288.0	
	C 1s → π*+ σ*(C-H)	289.5	
	C 1s → σ*(C-C)	294	
CB	C 1s → π*(a_2)	285.2	5±4
	C 1s → π(b_1)	286.7	
	C 1s → σ*(Cl-C)	285.2	
	C 1s → π*	286.7	
	C 1s → σ*(C-H)	285.2	
	C 1s → σ*(C-C)	286.7	
BB	C 1s → π*(a_2)	285.2	12±4
	C 1s → σ*(Br-C)	286.5	
	C 1s → σ*(C-H)	287.0	
	C 1s → π(b_1)	288.0	
	C 1s → π* + σ*(C-H)	289.5	
	C 1s → σ*(C-C)	293.7	
IB	C 1s → π*(a_2)	285.1	10±4
	C 1s → π*+ σ*	285.9	
	C 1s → π*	286.5	
	C 1s → π*	288.9	
	C 1s → σ*(C-H)	289.7	
	C 1s → σ*(C-C)	293.7	

3.1.2 XPS results. Figure 2 shows the XP spectra of the submonolayer preparations of PA, CB, IB, and BB on Au(111). All spectra were acquired at a temperature of -160°C, and a summary of the assigned binding energies is shown in Table 2.

Starting with the C 1s XP spectrum of PA in figure 2(a), a single peak with a clearly discernible shoulder on the high-binding energy side is observed. From peak deconvolution by least-square curve fitting, the main component is found to have a binding energy of 283.9 eV, which corresponds to the expected C 1s energy of the sp^2-hybridized C atoms in PA. The shoulder component at 284.5 eV is due to the sp-hybridized carbon atoms in the acetylene moiety. The intensity of the high binding energy component is one third of the total C 1s signal, which is the ratio expected from the molecular stoichiometry.

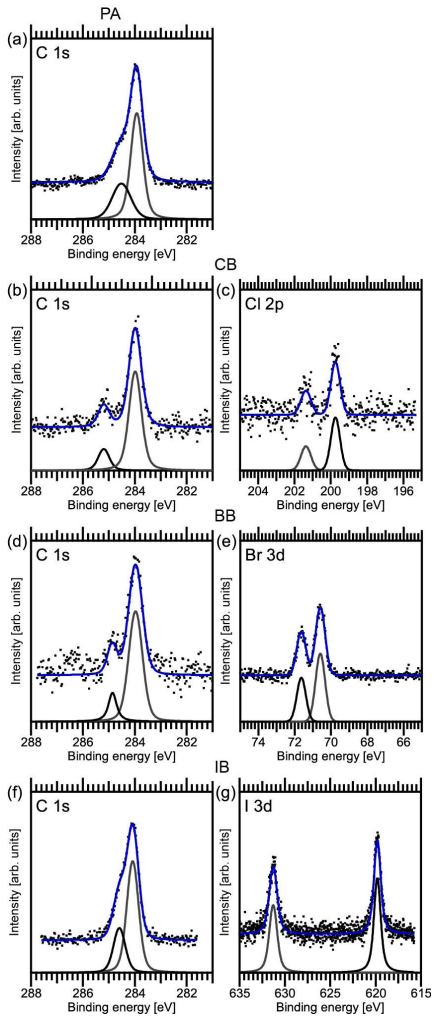

Figure 2. XP spectra of the submonolayer preparations. (a) C 1s spectrum of PA, (b) C 1s and (c) Cl 2p spectra of CB, (d) C 1s and (e) Br 3d spectra of BB, and (f) C 1s and (g) I 3d spectra of IB.

Figures 2(b), (d), and (f) show the C 1s spectra of the CB, BB, and IB submonolayers adsorbed on the Au(111) surface. In all three cases two components are observed: the main component at around 284.0 eV is

due to the five out of six sp^2-hybridized carbons in the phenyl moieties which are bonded to other C and H atoms, while the high-binding energy peak at 285.2/284.9/284.6 eV (CB/BB/IB) is attributed to the carbon atom bonded to the chlorine/bromine/iodine heteroatom. The intensity ratio between the two components is 1:6/1:5/1:4 (CB/BB/IB), in relatively good, but not perfect agreement with the stoichiometry.

Figures 2(c), (e), and (g) show the corresponding Cl 2p/Br 3d/I 3d spectra. In all three cases a single doublet is sufficient to explain the lineshapes. The binding energies of the doublet components are 199.7 eV and 201.4 eV for the Cl $2p_{3/2}$ and Cl $2p_{1/2}$ lines in CB, 70.6 eV and 71.6 eV for the Br $3d_{5/2}$ and Br $3d_{3/2}$ lines in BB, and 619.8 eV and 631.3 eV for the I $3d_{5/2}$ and I $3d_{3/2}$ lines in IB, respectively.

The Cl $2p_{3/2}$ binding energy reported for atomic Cl/Au(111) is ~197.4 eV [38, 39], quite much lower than what is found here. Hence, it is concluded that chlorobenzene adsorbs non-dissociatively at the liquid nitrogen temperature employed here. The conclusion is also supported by the shape of the C 1s spectrum in figure 2(b) as two distinct C 1s species are found.

The situation is the same for the adsorption of BB on the Au(111) surface at liquid nitrogen temperature: at 70.6 eV this Br 3d binding energy is higher than what has been reported previously for Br involved in C-Br bonds (69.7 eV [40]), but also significantly distinct from the energy found for Br-Au (67.8 eV) [40]. Therefore, these components are assigned to the Br-C species of BB, which thus adsorbs intact on the Au(111) surface at -160°C.

Likewise, the I 3d binding energy for IB is higher than what would be expected for the adsorption of atomic I on Au(111). Even though the values found here are in slight disagreement with Ref. [14] with respect to absolute energy and separation of the components, we nevertheless conclude on a non-dissociative bonding of IB to the Au(111) surface at liquid nitrogen temperature; the disagreement is instead attributed to experimental uncertainties.

Thus, all halogenated benzenes tested here adsorb non-dissociatively on the Au(111) surface at liquid nitrogen temperature. The C 1s binding energy correlates well with the electronegativity of the heteroatom (3.0, 2.8, and 2.5 for Cl, Br, and I, respectively), and the chemical shifts in the C 1s spectra can thus be explained in the standard initial state picture.

3.2 TDXPS results.

Figures 3 and 4 show the C 1s and halogen (Cl 2p/Br 3d/I 4d) TDXP spectra obtained on pure PA, CB, BB, and IB multilayers adsorbed on the Au(111) support (for coverages and heating rates, see the Experimental section). A summary of the results is found in Table 2. We will start our discussion with the C 1s spectra.

Figures 3(a), (c), (e), and (g) show image plots of all C 1s TDXP spectra. In these plots three general trends can be identified: (i) a region with a multilayer that desorbs rapidly, as marked by a rapid, large drop in intensity, and a downshift in binding energy at -122°C, -120°C, -103°C, and -96°C for PA, CB, BB, and IB [figures 3(a)/(c)/(e)/(g)], respectively. (ii) After the multilayer is desorbed, a monolayer coverage remains

where a slight continuous downshift in binding energy is seen in the C 1s spectra until about -15°C for PA and IB, -34°C for CB, and -30°C for BB. At these temperatures the samples enter the (iii) dissociation/desorption region, where the C 1s intensity decreases slowly. At the end of the temperature run a C 1s signal remains for PA, IB, and CB, but only a minute amount is left for BB. This is an indication that BB mostly desorbs in intact form.

Table 2. Summary of the XPS, TDXPS, and TDRXPS results.

		XPS		TDXPS			TDRXPS		
		C 1s [eV]	X[eV]	T [°C]	Main C 1s [eV]	X [eV]	T[°C]	C 1s [eV]	X[eV]
PA	multilayer			< -122	284.4	-			
	monolayer	283.9		-122 to -15	284.0	-			
	submonolayer			>-15	284.0	-			
CB, X=Cl $2p_{3/2}$	multilayer			< -120	284.4	200.4			
	monolayer	284.0	199.7	-120 to -34	284.1	199.8	<-60	284.2	199.9
	submonolayer			> -43	283.9	-	> -60	283.8, 283.9	
BB, X=Br $3d_{5/2}$	multilayer			< -103	284.5	70.2			
	monolayer	284.0	70.6	-103 to -30	284.1	69.7	< -20	284.0	69.8
	submonolayer			>-30	-	-			
IB, X=I $4d_{5/2}$	multilayer			< -96	284.6	50.8			
	monolayer	284.1		-96 to -15	284.1	50.3	<-5	284.2	50.4
	submonolayer			> -15	283.9	48.9	> -5	283.8, 284.0	

In more detail, figure 3(b) shows selected XP spectra of PA/Au(111) from the TDXPS series in figure 3(a). The spectrum acquired at -158°C shows a slightly asymmetric peak with a maximum at 284.5 eV binding energy. This peak can be deconvoluted by fitting with two sets of two peaks each (cf. figure S2 in the Supplementary Information) corresponding to photoemission from the monolayer and multilayer (cf. Table 2). Upon heating there is an initial increase in intensity in the spectrum recorded at -129°C. This increase is assigned to thermal drift during heating. Apart from that, the spectral shape remains the same until -97°C, at which temperature only the monolayer component remains. At higher temperature an asymmetric peak remains at 283.9 eV binding energy, assigned to a persisting submonolayer of PA. Clearly, this species is adsorbed more strongly compared to the majority of the PA adsorbates. Hence, the persisting submonolayer is assigned to PA bound to a minority adsorption site, e.g. defects, terrace steps, or elbows of the herringbone reconstruction on the Au(111) surface. Determination of the exact adsorption site would require further experiments, e.g. by means of scanning tunnelling microscopy.

Selected XP spectra from the CB, BB and IB TDXPS series are shown in figures 3(d), (f), and (h). For all compounds the main C 1s component is found at 284.5-284.6 eV binding energy with the addition of a shoulder component at the high binding energy side, which is not resolved in the IB case. After entering the dissociation/desorption temperature regime, the main C 1s components are found at about 284 eV binding energy in agreement with the corresponding submonolayer spectra in figure 2. At higher temperature the shoulder component vanishes for CB [cf. the spectrum at -53°C in figure 3(d)], and in the IB case the main C 1s component asymmetry is reduced and the peak shifts downward in binding energy. This is in contrast to

the behaviour of the C 1s line of BB, which only is reduced in intensity, but does not shift anymore in binding energy. For both CB and IB the C 1s component of the final product is found at 283.9 eV binding energy, i.e. at an energy where the signal of sp^2-hybridized carbon is expected. Since the C-Cl shoulder is not present in the final spectrum of the CB series, and since the asymmetry of the final IB C 1s peak has largely disappeared, the spectrum at highest temperature is assigned to biphenyl (BP) for both CB and IB. BP is a result of the homocoupling reaction between the phenyl radicals which remain after C-halogen bond dissociation [16]. This signal is not found in the BB case, and thus we conclude that BB does not dissociate on the Au(111) surface.

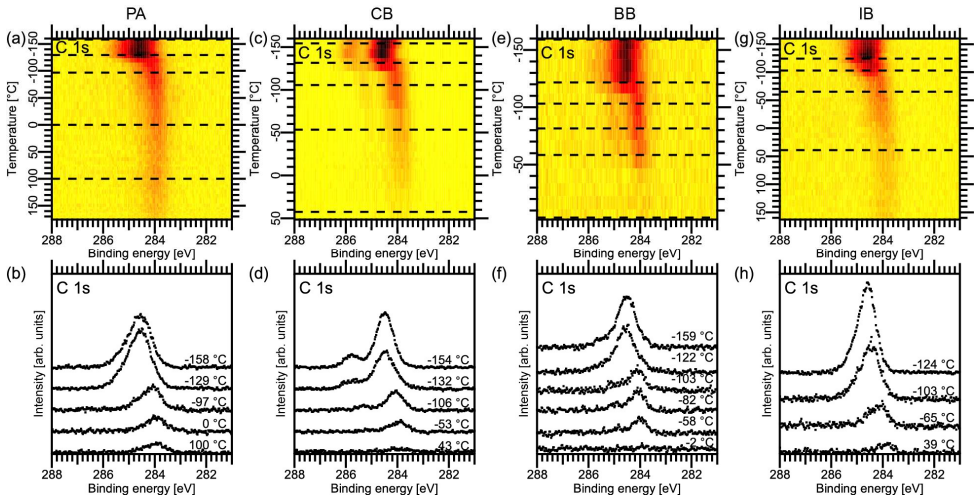

Figure 3. C 1s TDXP spectra. (a), (c), (e), and (g) show C 1s image plots obtained on multilayer preparations of PA, CB, BB and IB on Au(111). (b), (d), (f), and (h) show selected C 1s spectra marked by the dashed lines in the corresponding surface plot.

Figure 4 shows the Cl 2p, Br 3d, and I 4d TDXP spectra acquired simultaneously as the corresponding C 1s TDXP spectra in figure 3. Figures 4 (a), (c), and (e) contain image plots with all Cl 2p, Br 3d, and I 4d spectra measured during the heating run, while figures 4(b), (d), and (f) show selected spectra marked by the dashed lines in the image plots.

The image plots in figures 4(a), (c), and (e) exhibit the same trends as observed in the C 1s spectra, cf. figures 3 (c), (e), and (g). At low temperature a well-resolved doublet is seen in the Cl 2p and I 4d spectra, whereas for Br 3d a single, broad component is observed. At about -120°C there is a downshift in binding energy and loss in intensity in the I 4d, Cl 2p, and Br 3d core level spectra, which is consistent with desorption of the halobenzene multilayers. Additionally, a new component appears in the I 4d image plot on the low-binding energy side at an energy typical of an atomic I-Au species. In the Br 3d spectrum a doublet is clearly resolved in the temperature regime above -120°C. Hence, in accordance with what is seen in the C 1s spectra, the transition from the multilayer to monolayer signal is obvious for all three halobenzenes. After

reaching -24°C (-30°C) the doublet vanishes in the Cl 2p and Br 3d spectra. In contrast, only the monolayer I 4d doublets vanishes at -15°C, while the low-energy doublet persists up to the highest temperature.

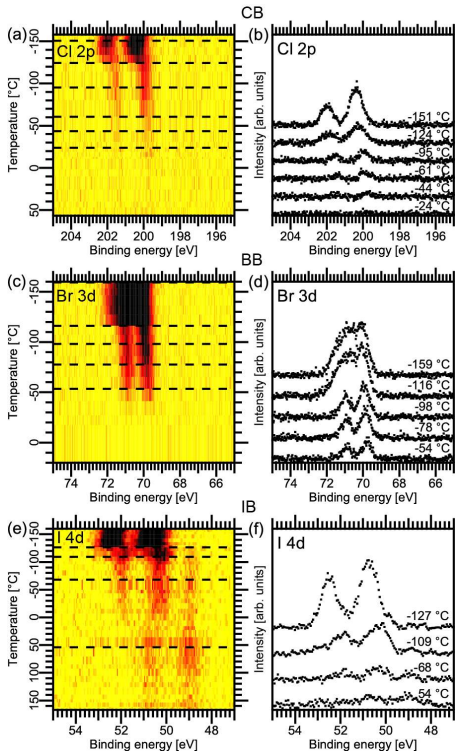

Figure 4. Panels (a), (c), and (e) show image plots of the Cl 2p, Br 3d, and I 4d TDXP spectra. Panels (b), (d), and (f) show selected spectra as marked by the dashed lines in (a), (c), and (e).

Using the above assignments all halogen spectra are fitted using doublets for the multilayer, monolayer and, in the case of IB, atomic I-Au(111) species. The integrated area of these doublets is plotted in figures 5(a), (b), and (c) as a function of temperature. Clearly, the atomic I-Au(111) species [figure 5(c)] remain on the surface until the end of the heating run. This is clear proof of IB dissociation on the Au(111) surface, as already indicated by the evolution of the C 1s spectra. In contrast, the halogen core level signals of CB and BB vanish at 0°C (CB) and -25°C (BB). The Br 3d signal disappears at the same temperature as the C 1s signal vanishes, which implies that BB desorbs in intact form from the Au(111) substrate, as was already concluded above. The Cl 2p signal vanishes at about -40°C, but a C 1s signal remains. Therefore, CB dissociates on the Au(111) surface during the temperature run. In line with this, upon dissociation the formation of an atomic Cl-Au(111) species would be expected, visible in the Cl 2p spectra. The absence of a Cl 2p signal is unexpected, especially since Cl_2 adsorbs dissociatively on Au(111) [20] and desorbs first at 370°C as Cl_2 and as atomic Cl at 520°C [38]. The absence cannot be explained by a low signal either, since the subshell Cl 2p photoionization cross section at the employed photon energy is considerably higher than

that of C 1s. Even though there are six times as many C atoms as Cl on the surface, the signal should not be negligible, and, moreover, summation of the last four spectra do not show any Cl 2p signal (not shown). It has been shown that H reacts with Cl adsorbed on the Au(111) surface via the Langmuir-Hinshelwood mechanism [41] after which HCl desorbs from the surface at sufficiently high temperature. The desorption temperature of HCl can be estimated by a Redhead analysis using a pre-factor of 10^{13} and a barrier towards desorption of 0.22 eV [42]. The thus estimated approximate desorption temperature is -185°C, which would agree with the above data. It is, however, unlikely that any H originates from C-H bond breaking, since this reaction is not catalysed by the Au(111) surface [43]. Cl could potentially react with H dissolved in the Au(111) single crystal, but we do not consider this possibility particularly likely.

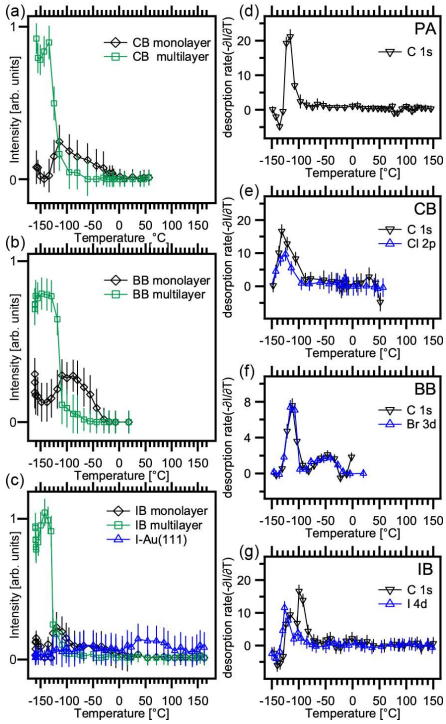

Figure 5. Integrated areas of the monolayer and multilayer components obtained from the TDXPS data for (a) CB, (b) BB, (c) and IB. (c) also shows the evolution of the atomic I-Au(111) species. The graphs are normalized to unity at -160°C. Panels (d), (e), (f), and (g) show TPD-like spectra for PA, CB, BB, and IB obtained from the integrated intensities of the C 1 s (black) and halogen (blue) core level lines.

Instead, we consider the influence of adsorption geometry on the surface reaction. From the XAS measurements it is clear that CB adsorbs in a very flat geometry, induced by the interaction between the phenyl moiety and Au surface. Thus, two CB molecules could interact through the Cl heteroatoms, which subsequently forms Cl_2 and two Ph-Au species which react to BP, while the Cl_2 is released directly into

vacuum. While we cannot confirm this hypothesis at present, this is the most likely explanation at hand. The hypothesis would have to be confirmed in future experiments using e.g. mass spectrometry.

Figures 5(d), (e), (f), and (g) show TPD-like spectra created from the TDXPS data. The spectra are the negative of the derivative with respect to temperature of the integrated surface signal of the C 1s and halogen spectra. Figure 5(d) shows the desorption peak of PA, while figures 5(e), (f), and (g) show the desorption features as found from the C 1s (black) and halogen core levels (blue) [Cl 2p, Br 3d, and I 4d] for CB, BB, and IB, respectively. Starting the discussion with PA, the main desorption peak is found at -120ºC in agreement with previous studies [13]. The desorption temperature points to the formation of diphenyl diacetylene (DPDA) [14] as a result of PA homocoupling. While DPDA thus should be present on the sample at temperatures lower than -120°C, its spectral fingerprint in the C 1s core level line is virtually impossible to differentiate from that of PA. We thus cannot provide a final confirmation of DPDA formation, but consider the temperature-based evidence strong.

Turning now to the halogenated benzenes, the main desorption features of CB and BB are found at -125ºC, and -116ºC, respectively. The Cl 2p and Br 3d-derived desorption rates are in close agreement with the C 1s-derived ones, in particular for BB. This indicates multilayer desorption, in good agreement with the C 1s TDXPS assignment. In addition, a small, wide feature is seen in both BB spectra in figure 5(f). This feature is located at a temperature of -46ºC, which agrees with BB monolayer desorption. In contrast, the IB desorption peaks exhibit a different behaviour. Here, in the C 1s desorption rate two distinct peaks are found at -116ºC and -95ºC. In the corresponding I 4d spectrum only one major desorption peak is found at -127ºC. Clearly, the desorption mechanism of IB from Au(111) contains multiple channels, and we assign the difference in desorption rates derived from the C 1s and I 4d XP spectra to C-I bond dissociation: the first C 1s TPD peak and the I 4d TPD peak are assigned to multilayer desorption, while the peak at -95°C is assigned to a C species desorbing from the Au(111) surface subsequent to C-I bond dissociation. Here, no peak is seen in the I 4d derived spectrum as the atomic I-Au(111) species do not desorb at these temperatures.

The desorption energies can be approximated to a 30% accuracy using a Redhead analysis assuming an exponential pre-factor of 10^{13}, first order desorption kinetics, and using the temperatures obtained from a Gaussian fitted to the main C 1s derived desorption peaks. This yields desorption energies for multilayer desorption energies of 44 kJ/mol (PA), 40 kJ/mol (CB), 45 kJ/mol (BB), and 49 kJ/mol (IB), and 63 kJ/mol for the BB monolayer desorption.

From the above results we conclude that the C-I bond in IB dissociates and there are strong indications even for dissociation of the C-Cl bond in CB. In contrast, there is no sign of C-Br bond dissociation in BB. The bond dissociation energies are high for all three compounds [44] and cannot explain the observed differences, especially since the dissociation energy trend is C–Cl > C–Br > C–I. As was determined above

(Table 1), what differs between the three compounds is their orientation with respect to the surface. At 5° CB has a very small tilt angle, which seems to favour dissociation, likely due to a weakened chlorine-phenyl bond due to the stronger interaction of the phenyl moiety with the surface. BB exhibits a comparatively large tilt, 15°, which disfavours dissociation. With a 10° tilt angle IB is an intermediate case, but the tilt angle seems to allow a sufficiently strong interaction between the surface and the phenyl moiety to promote dissociation; the C–I bond is also the weakest. A striking difference between CB and IB is that the split-off iodine atoms remain at the surface, while the chlorine atoms do not. Obviously the mechanisms of dissociation on the Au(111) surface are different for the two compounds.

3.3 TDRXPS results.

Figure 6 presents the C 1s spectra acquired during the TDRXPS measurements. In these experiments PA was dosed onto the Au(111) surface pre-dosed with halobenzenes, and then the sample was heated and XP spectra were acquired (for heating rates and coverages, see the Experimental section). A summary of the TDRXPS results is presented in Table 2.

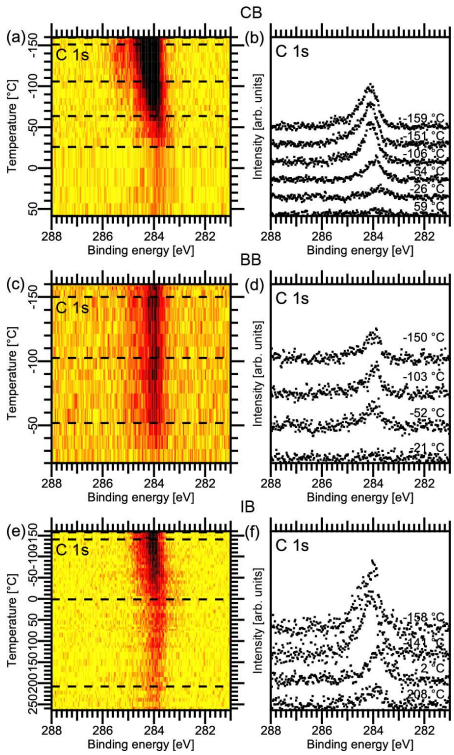

Figure 6. C 1s TDRXPS spectra for PA dosed on (a) CB, (c) BB, and (e) IB. Panels (b), (d), and (f) show selected spectra from (a), (c), and (e) as marked by the dashed lines.

Figures 6 (a), (c), and (e) show image plots of all C 1s spectra acquired during the TDRXPS measurements for PA on CB/Au(111), BB/Au(111), and IB/Au(111), respectively. Apart from a loss of intensity with increasing temperature, two trends can be identified: (i) in the CB and IB case there is a downshift of the photoemission lines in binding energy until roughly -26°C for CB and room temperature for IB, after which the spectral features shift slightly upwards in binding energy; (ii) in the BB case there is no change in binding energy at all until the C 1s line vanishes at about -20°C. Considering the selected spectra in figures 6(b), (d), and (f) for PA on CB, BB, and IB, it is clear that the energy separation of the main C 1s component from that of the C atom bound to the halogen heteroatom is less pronounced compared to what is seen for the halobenzene-only preparation in the spectra in figure 3; moreover, the separation is more clearly seen in the CB and BB spectra than for IB. In all three preparations multiple C species are present, and we can conclude that PA is co-adsorbed with all halogenated benzenes. For both CB and IB, the lowest-energy line is located at 283.8 eV binding energy. This component was not seen in the spectra of the halobenzene-only preparations and is thus assigned to the interaction between CB/IB and PA. Upon further heating, the main C 1s component shifts to 284 eV binding energy for both CB and IB, while for BB no C 1s signal is found.

In order to assign the nature of the low-binding energy species, the most common reaction products between CB and IB with PA need to be considered. For IB+PA over Au(111) three main products have previously been reported: BP, DPDA, and diphenylacetylene (DPA) [14]. From TDXPS BP was above found to have a photoemission line with a binding energy of 283.9 eV, which is not observed here. DPDA desorbs from the surface at -120°C (cf. figure 5), and no photoemission line at 283.8 eV was found in those measurements. Hence, both BP and DPDA are excluded as the species that gives rise to the low-binding energy component. Instead we assign the component at 283.8 eV binding energy in the IB and CB TDRXPS spectra to DPA. This leads us to conclude that both IB and CB are active for the Sonogashira cross-coupling reaction over Au(111), whereas BB is not since no DPA feature is seen in the BB C 1s spectra.

Continuing with the halogen core levels, figure 7 shows the Cl 2p, Br 3d, and I 4d spectra acquired during the TDRXPS measurements as image plots in panels (a), (c), and (e) and selected spectra in (b), (d), and (f). In all three cases a single doublet is seen at the submonolayer binding energies of 199.9 eV (Cl $2p_{3/2}$)/69.8 eV (Br $3d_{5/2}$)/50.4 eV (I$4d_{5/2}$) up to temperatures of -66°C (CB), -30°C (BB), and -5°C (IB) in agreement with the monolayer desorption temperatures, cf. Table 2. While no shift in binding energy is seen prior to desorption for IB and BB, for CB there is a slight downshift of the Cl 2p signal, which is assigned to the strong coverage dependence of the CB lines seen in the TDXPS measurements. The presence of the submonolayer halobenzene features is a clear proof of halobenzene coadsorption with PA.

The PA+BB measurements warrant further discussion. As can be seen from the spectra in figures 6 and 7, both the C 1s and Br 3d signal disappear at about -40°C. Thus, no adsorbates remain on the Au(111) surface. As seen from the TDXPS measurements in figures 3 and 5, PA alone forms DPDA and, moreover, a submonolayer of PA persists on the surface up to at least 150°C. In this submonolayer PA is bound more strongly to the surface at minority adsorption sites. A plausible explanation for the absence of PA on the

surface at temperature above -40°C when PA+BB are co-dosed would be that the prime adsorption site of BB is the minority adsorption site of PA (i.e. defects, terrace steps, or herringbone elbows). The pre-adsorbed BB (0.4 ML) would block the sites and the less strongly bound PA would desorb intact. Alternatively, we cannot exclude the homocoupling reaction towards DPDA, which would desorb already at -120°C [13]. In either case, since no temperature-dependent changes are observed in neither the Br 3d nor C 1s spectra, BB does not participate in the reaction.

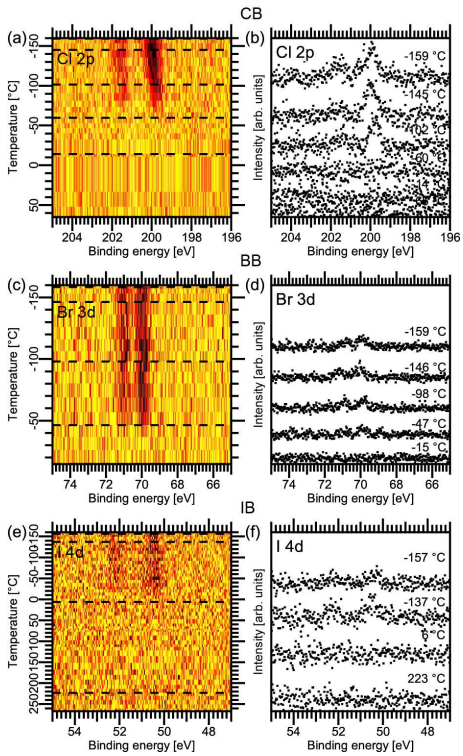

Figure 7. TDRXPS spectra. (a) Cl 2p, (c) Br 3d, and (e) I 4d data as image plots. (b), (d), and (f) shows selected spectra marked by the dashed lines.

With respect to the TDRXPS reaction of IB with PA, we find that no atomic I-Au(111) species is present on the surface. Since Au(111) greatly facilitates C-I bond cleaving (cf. the TDXPS measurements in figure 4) this absence is unexpected. The Sonogashira cross-coupling reaction mechanism provides, however, an explanation: in order for cross-coupling between IB and PA to take place, the C-H bond on the acetylene moiety must be cleaved, a reaction which is generally not catalysed by Au(111). The presence of atomic I-Au(111) might facilitate the cleaving and lead to the formation of HI, which would desorb from the Au(111) surface. The remaining phenyl- and phenylacetylenyl groups would form DPA. This scheme is also valid for

the CB case. Therefore, the absence of atomic halogen species on the Au(111) surfaces is an indication of the occurrence of a Au(111)-catalysed Sonogashira cross-coupling reaction between PA and CB/IB.

From the results of the above TDRXPS experiments we can conclude that both CB and IB undergo a Sonogashira cross-coupling reaction with PA to DPA with a characteristic C 1s photoemission peak at 283.8 eV binding energy. The reaction proceeds via C-Cl/C-I bond cleavage followed by HCl/HI formation. In contrast, a Au(111)-catalysed Sonogashira cross-coupling reaction between BB and PA does not take place, which is paralleled by a lack of BB dissociation on the Au(111) surface.

3.4 Halobenzene and phenylacetylene adsorption and reaction at ambient pressure

3.4.1 APXPS results: individual compounds. APXPS was used to study the reaction of PA with CB and IB under *in situ* conditions, i.e. at relevant pressure and temperature. Since in particular the C 1s APXP spectra represent a rather complex convolution of lines from PA on the one hand and CB/IB on the other, we start by discussing the temperature-dependent APXP spectra of the individual compounds recorded at a pressure of 0.2 mbar. The heating rates are summarized in the experimental section, and the resulting spectra are plotted in figure 8. All plots are divided into two sections: (i) the top part was acquired during heating of the Au(111) crystal, while (ii) the bottom part was measured as the sample cooled in the vapour.

We start our discussion with the C 1s image plots and selected spectra in figures 8 (a) and (b) for PA, (c) and (d) for CB, and (e) and (f) for IB. For PA and CB the image plots show two distinct peaks, while only a single peak is seen for IB. At room temperature the PA, CB, and IB main peaks are located at 283.9 eV, 284.0 eV, and 284.2 eV binding energy, in agreement with monolayer or submonolayer coverages of PA, CB, and IB (cf. figure 2 and table 2). The main peak in the PA spectrum is asymmetric due to the presence of the acetylene component at 284.5 eV. In the CB spectrum the C-Cl component is seen as a low-energy shoulder of the peak at ~285.6 eV (see below), while the C-I component is found at 284.7 eV in the IB spectrum. Hence, we observe adsorption of not more than a single adsorbate layer, when the Au(111) surface is exposed to 0.2 mbar of PA, CB, or IB at room temperature.

The PA and CB spectra exhibit high binding energy peaks at 285.6 eV binding energy for PA and 285.7 eV for CB. These lines are assigned to the PA and CB vapour signals. In contrast, at room temperature no gas phase peak is seen for IB. This initial absence of the IB gas phase is attributed to thermal drift during the heating, which reduces the distance between sample and entrance aperture of the electrostatic lens system of the electron energy analyser [45], leading to a reduced pressure over the surface.

With increasing temperature the PA C 1s surface peaks shifts to slightly higher binding energy. Also the CB C 1s surface lines shift towards higher energy, albeit first after an initial downshift of the main component to 283.9 eV, which is accompanied by a reduction in intensity of the C-Cl component. These observations are in line with the formation of BP at around 150°C. Returning to the subsequent upshift of the C 1s lines of both PA and CB, they come along with an increase in asymmetry and width and a simultaneous upshift of the gas phase C 1s lines. The gas phase component shift shows that the surface work function changes as a result of

the formation of a carbon structure at the surface of unclear exact nature. In contrast, due to desorption, the C 1s signal of IB greatly diminishes at temperatures higher than room temperature, and only a minute signal persists. At about 340°C the IB C 1s signal, however, increases again and a component is seen at 284.5 eV binding energy, an energy which is higher than that of the room temperature species. Instead, it is near the binding energy assigned to the IB multilayer (cf. table 2). Multilayer condensation at elevated temperature seems highly unlikely, though (see also below). Hence, we conclude that also IB reacts to an unknown carbon surface structure at elevated temperature. During the cooling cycle no major shifts in binding energy are seen; a slight increase in asymmetry of the main C 1s component, indicative of further reaction of the carbon surface structure, and the appearance of a component at 286.3 eV binding energy are, however, apparent in the IB spectra. The binding energy shift between this new component and the main C 1s line is similar to that between the surface species of CB and PA on the one hand and their gas phase components on the other. Hence, the signal is assigned to IB in the gas phase.

From the discussion of the C 1s spectra obtained during exposure of the Au(111) surface to 0.2 mbar of PA, CB, and IB we can conclude that all three compounds adsorb non-dissociatively on the Au(111) surface at room temperature; for IB this picture will, however, be modified slightly below. Upon heating CB reacts to BP at moderate temperature, while IB desorbs. In all cases unknown carbon surface structures are formed at higher temperature.

Further understanding is achieved from consideration of the halogen (Cl 2p and I 4d) core levels. Figures 8(g) and (i) show image plots of the halogen lines, while (h) and (j) show the corresponding selected spectra. At room temperature two overlapping doublets are seen in both cases, corresponding to a majority and a minority species. The Cl $2p_{3/2}$ and I $4d_{5/2}$ components of the majority species are observed at 199.7 eV and 49.2 eV binding energy, respectively. The former is assigned to the monolayer or submonolayer signal of CB consistent with the assignment based on the C 1s spectra, while the latter is due to an atomic I-Au(111) species, in accordance with our TDXPS data. The Cl $2p_{3/2}$ and I $4d_{5/2}$ components of the minority species are hidden by the signals of the more intense majority signal; their positions can be identified reliably from curve fitting, and their locations are 201.2 eV and 50.3 eV binding energy. In accordance with its binding energy (see TDXPS results above) the I 4d minority species is assigned to a (sub-)monolayer of IB. Both the CB and IB (sub-)monolayer features disappear upon heating to elevated temperature.

The Cl minority species at 201.2 eV does not have a binding energy which has been identified previously. The signal persists throughout the entire heating and cooling cycle, but shifts towards higher binding energy in the cooling half-cycle. This behaviour, its persistence throughout the entire heating/cooling cycle and its shift, as well as its relative high binding energy let us assign the doublet to the CB gas phase signal; the shift during the cooling cycle is given rise to by the surface modification in the form of a carbon-containing overlayer as reported above and a concomitant work function shift.

Just above 340°C the atomic I-Au(111) species desorbs and the corresponding doublet disappears from the spectra. This is clear evidence of that the C 1s signal at this temperature does not originate from an IB

multilayer. As the cooling cycle starts two additional I 4d doublets are seen. The first doublet has its I $4d_{7/2}$ component located at 51 eV binding energy, which correspond to an IB multilayer. Thus, IB is seen to re-condense on the surface as the temperature is lowered. The high-energy component, located at 52.5 eV binding energy, is assigned to gas phase IB, based on the observed core level shift. Its appearance is simultaneous with the appearance of the IB vapour line in the C 1s spectra and can be attributed to an enlarged distance between sample and analyser aperture. This observation further reinforces the assignment.

From the APXPS measurements it is concluded that there is a large degree of C-I bond cleavage up to a temperature of 340°C. In fact, the surface is nearly completely covered by atomic I as seen from the lack of C 1s signal. It seems likely that the phenyl radicals form BP, which desorbs from the surface. As I desorbs from the surface, an unknown carbon structure is formed, and IB condensates on top of this structure when the temperature is lowered below 250°C. However, the atomic I-Au(111) species is not found and thus the Au(111) surface has become inactive for C-I bond scission.

Both PA and CB produce a carbon surface structure at higher temperature, and no atomic Cl-Au(111) species is seen, in agreement with the TDXPS measurements. However, the large C signal is indicative of C-Cl bond scission. Interestingly, CB does not re-condensate on top of this structure, as seen from the absence of a CB multilayer signal during the cooling half-cycle. Possibly, we did not measure at sufficiently low temperature; alternatively, the C structure inhibits CB adsorption.

3.4.2 APXPS results: Sonogashira coupling conditions. Using the above discussion as a basis, we continue with the APXPS data obtained at reaction conditions. A mixture of PA with either CB or IB was dosed onto the Au(111) surface at a pressure of about 0.2 mbar. During exposure the crystal underwent a heating and cooling cycle (see experimental section), and APXP spectra were recorded at the same time. The acquired C 1s, Cl 2p, and I 4d spectra are shown in figure 9.

The C 1s data will be addressed first. Figures 9(a) and (c) show image plots of all C 1s spectra acquired during reaction conditions, while figures 9(b) and (f) show the selected spectra for PA+CB and PA+IB, respectively. The surface species are found at about 284 eV binding energy with the gas phase components at about 285.5 eV with an additional component at about 287 eV, which is assigned to a gas phase species from a gas phase spectrum of the PA+CB mixture (cf. Fig S3). For CB, this agrees well with what was found for the single compound at ambient pressure. The exact composition of the adsorbate overlayer is difficult to assign as PA and CB monolayers have near-identical binding energies; we therefore limit ourselves to assigning the surface peak to a combination of CB and PA (sub-)monolayers. In contrast, in the PA+IB case, in comparison to pure IB, the surface species is located at a considerably lower binding energy (-0.3 eV). This energy agrees with that observed for the pure PA system, and thus, this component is assigned to (sub-)monolayer-coverage PA on the Au(111) surface, although a contribution of a (sub-)monolayer IB species cannot be excluded, either. During the temperature ramp the surface species signal for both gas mixtures shifts to lower binding energy, namely 283.8 eV, at 185°C for CB and 170°C for IB. This species is assigned to DPA on the basis of TDXPS results discussed above. Upon further heating, the lines of the surface species

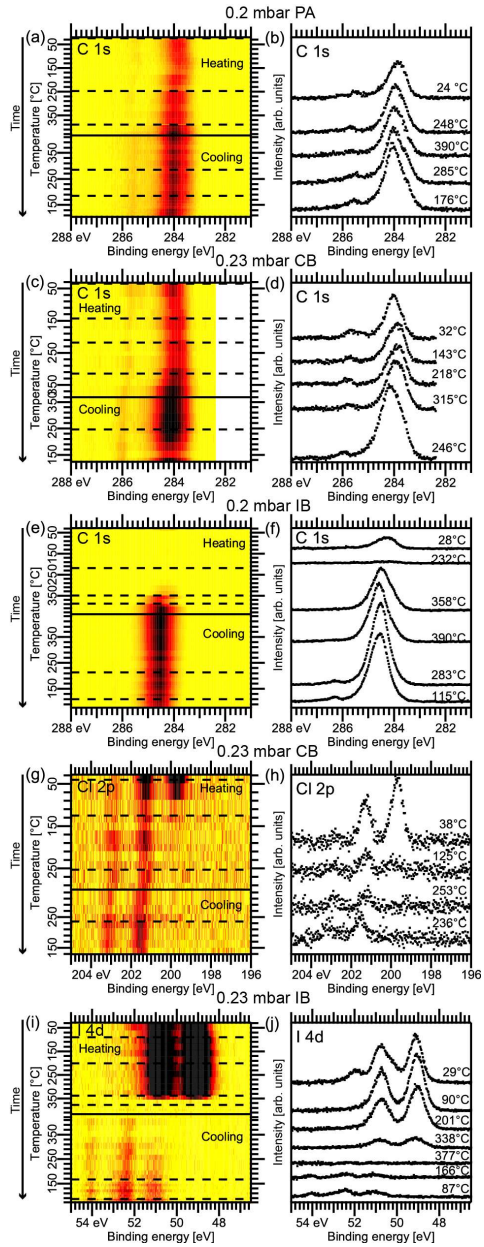

Figure 8. APXP spectra of the individual compounds. Panels (a), (c) and (e) show image plots of the C 1s spectra acquired for PA, IB and CB. (b), (d), and (f) show selected C 1s spectra as marked by the dashed lines in the image plots. (g) and (i) show image plots of the I 4d and Cl 2p spectra of IB and CB. (h) and (j) show the corresponding selected spectra.

in both systems shift to 284.1 eV, where they remain during the entire cooling half cycle. This is a similar binding energy as that found for the unknown carbon surface structure formed upon dosing either pure PA or CB at ambient pressure. It is distinct from what was found for pure IB.

The influence of PA is clear in the PA+IB case since the signal of a surface C species is seen throughout the entire heating/cooling cycle. The observation agrees with the presence of a (sub-)monolayer of PA on the Au(111) surface. In the CB+PA case, the binding energy of the surface species agrees with that of a monolayer of CB, but at the same time it is difficult to differentiate between PA and CB, since their surface species have near-identical binding energies. In both vapour mixtures the surface species shifts to the binding energy assigned to DPA at moderate temperature, indicative of the Sonogashira cross-coupling reaction. The surface is, however, passivated by an unknown carbon species when heating above 340°C.

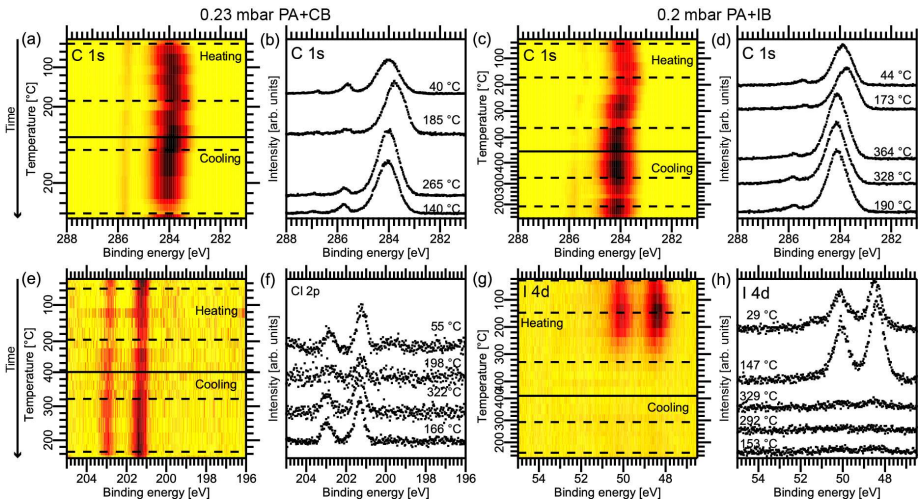

Figure. 9. APXPS characterization during Sonogashira coupling reaction conditions. (a) and (c): C 1s image plots taken during exposure of the Au(111) surface to (a) PA+IB and (c) PA+CB. (b) and (d) show the corresponding selected spectra marked by the dashed lines. (e) and (g): I 4d and Cl 2p image plots. (f) and (h): corresponding selected I 4d and Cl 2p spectra.

Turning to the halogen core levels measured at reaction conditions, we consider the image plots of the Cl 2p and I 4d core levels in figures 9(e) and (g) and selected spectra in figures 9(f) and (h). At room temperature two doublets are seen in the Cl 2p spectra with Cl $2p_{3/2}$ components at 201.2 eV and 199.8 eV binding energy. The peaks are assigned to gas phase CB and (sub-)monolayer CB, respectively, in agreement with the TDXPS finding reported above. Thus, as stipulated based on the shape of the C 1s spectra non-dissociatively adsorbed CB is present on the surface. Similarly, two doublets are seen in the room temperature I 4d spectra assigned to atomic I-Au(111) (I $4d_{7/2}$ peak at 48.4 eV) and submonolayer IB (I $4d_{7/2}$ peak at 49.6 eV). The latter has an energy which is lower than expected for a monolayer (50.3 eV), but distinctly higher than the energy of an atomic I-Au(111) species. Hence, PA does not inhibit C-I bond cleavage on the Au(111) surface,

and, in fact, submonolayers of PA and IB are found to be present at the surface. So is the atomic I-Au(111) species, which also implies the presence of phenyl radicals. Just above room temperature the submonolayer components vanish, and at 300°C the intensity related to the atomic I-Au(111) species greatly diminishes. Only the gas phase CB species is present in the Cl 2p spectra during cooling while a minute I-Au(111) signal is seen in the I 4d spectra.

From the *in situ* APXP spectra we conclude on the observation of the Sonogashira cross-coupling reaction over the Au(111) surface at the conditions employed here (0.2 mbar, 185°C [CB]/170°C [IB]). For IB we initially, i.e. at room temperature, find the coexistence of an IB/PA (sub-)monolayer with the atomic I-Au(111) species, although we did not see this atomic species in the UHV TDRXPS experiments. Hence, C-I bond scission is faster than formation of the iodine compounds that desorb from the surface, tentatively HI. At reaction temperature, we instead observe the signal of the atomic species simultaneously with the C 1s line assigned to DPA in the TDRXPS experiments. This DPA component was not observed in the case of the pure compounds, and thus it results from the interaction of PA with CB and IB. In contrast and in line with the CB/PA UHV TDRXPS measurements, neither an atomic Cl-Au(111) nor a CB mono/multilayer species is seen during the Sonogashira cross-coupling reaction, although the DPA reaction product is visible. Hence, the residence time of CB, and subsequently Cl, on the Au(111) surface is so short that we are unable to see it with XPS at reaction temperature. This behaviour contrasts with the observations for the CB/PA reaction mixture.

For both gas mixtures the surface is inactivated at temperatures above 300°C by the formation of an unknown carbon structure, which is similar in binding energy to the structure formed by adsorption of PA alone, but distinct from that observed for pure IB. Hence, PA plays a major role in the deactivation of the Au(111) surface. This is clearly demonstrated in the I 4d spectra: The atomic I-Au(111) species coexists with the C structure during the cooling half cycle, albeit at a greatly diminished signal strength. Thus, the C species covers the surface, including overgrowing the I-Au(111) species. Additionally, no re-condensation of IB or CB is found, which entails that the surface has become completely passivated towards CB and IB adsorption. Hence, no further Sonogashira cross-coupling reaction is possible.

4. Conclusions

In this study we have compared the adsorption of the I, Cl, and Br halobenzenes on a Au(111) single crystal surface and we have studied the temperature-dependent reaction behaviour of these compounds with phenylacetylene and the interaction of CB and IB with PA at ambient pressure. The bond angles between the compounds and surface have been determined using XAS, and all XPS and XAS lines have been assigned. At monolayer coverage the molecules are near-flat lying, while at coverages higher than one monolayer there is no directional dependence. It is shown that iodobenzene dissociates on the Au(111) support, while there is some indication of possible dissociation for chlorobenzene. There is no sign of bromobenzene dissociation at the employed conditions. This is in disagreement with the DFT study by Boronat *et al.* [20], in which it is suggested that IB and BB would dissociate prior to CB. This discrepancy is attributed to the low bond angle

of CB which allows for a greater Au-Ph interaction, which, in turn, enables C-Cl bond scission. After bond dissociation a single C species is left on the surface for IB and CB, but not for BB. The species is assigned to biphenyl formed in a Ullmann homocoupling reaction of the phenyl radicals. Interestingly, the atomic I-Au(111) species is found after bond scission, but no atomic Cl-Au(111) is observed. This discrepancy suggests different bond dissociation mechanisms.

In the reaction measurements, achieved by co-dosing the halobenzenes and PA, there is indication of formation of DPA in both the IB and CB cases, but not for BB. This disagrees with the findings of Olivier-Meseguer et al. [10] who found CB derivatives to be the least reactive. Unfunctionalized BB and CB were not addressed, however. Further, we find that PA, CB, and IB adsorb on the Au(111) surface at ambient conditions (BB was not investigated). IB undergoes C-I bond cleavage as seen by a I-Au(111)-dominated surface, while a unknown carbon surface structure forms in the PA and CB vapours. Here, future mass spectrometry as well as ex situ and in situ infrared spectroscopy investigations that assign both the adsorbed and desorbed molecular species before, during, and after the reaction may play a vital role to fully understand the difference in the reaction mechanisms between chloro- and IB.

At ambient reaction conditions both CB and IB undergo the Sonogashira cross-coupling reaction at slightly elevated temperature when mixed with phenylacetylene. The Au(111) surface becomes inactivated by further heating as a passivating C structure forms. In both the UHV and APXPS measurements, no Cl surface species is seen during reaction measurement, while for IB the atomic I-Au(111) species is seen in the reaction at ambient pressure, but not in the UHV reaction. Additionally, the temperatures at which DPA is found are higher at ambient conditions, which we conclude is due to the different surface structures. Hence, it is demonstrated that investigations at ambient conditions are vital in order to deduce the adsorbate structures and mechanisms of real catalysts.

Acknowledgements

We gratefully acknowledge the assistance of the staff at the MAX IV Laboratory. The Faculty of Science at Lund University is gratefully acknowledged for financial support.

References:

1. Anastasia L and Negishi E 2002, in: Negeshi, E (ed.) *Handbook of Organopalladium Chemistry for Organic Synthesis*. (New York: Wiley)
2. Meijere A D and Diederich F(eds) 2004, *Metal-Catalyzed Cross- Coupling Reactions,*. (Weinheim: Wiley)
3. Wu X-F, Anbarasan P, Neumann H, and Beller M, 2010, *Angew. Chem. Int. Ed.*, **49**, 9047.
4. Hazari N, Melvin P R, and Beromi M M, 2017, *Nature Reviews Chemistry*, **1**, 0025.
5. Sonogashira K, Tohda Y, and Hagihara N, 1975, *Tetrahedron Lett.*, **16**, 4467.
6. González-Arellano C, Abad A, Corma A, García H, Iglesias M, and Sánchez F, 2007, *Angew. Chem. Int. Ed.*, **46**, 1536.
7. Kyriakou G, Beaumont S K, Humphrey S M, Antonetti C, and Lambert R M, 2010, *ChemCatChem*, **2**, 1444.
8. Corma A, Juárez R, Boronat M, Sánchez F, Iglesias M, and García H, 2011, *Chem. Commun.*, **47**, 1446.
9. Sisodiya S, Wallenberg L R, Lewin E, and Wendt O F, 2015, *Applied Catalysis A: General*, **503**, 69.
10. Oliver-Meseguer J, Dominguez I, Gavara R, Leyva-Pérez A, and Corma A, 2017, *ChemCatChem*, **9**, 1429.
11. Ishida T, Koga H, Okumura M, and Haruta M, 2016, *The Chemical Record*, **16**, 2278.
12. Boronat M and Concepción P, 2017, *Catal. Today*, **285**, 166.
13. Sánchez-Sánchez C, Yubero F, González-Elipe A R, Feria L, Sanz J F, and Lambert R M, 2014, *J. Phys. Chem. C.*, **118**, 11677.
14. Kanuru V K, Kyriakou G, Beaumont S K, Papageorgiou A C, Watson D J, and Lambert R M, 2010, *J. Am. Chem. Soc.*, **132**, 8081.
15. Boronat M, Combita D, Concepción P, Corma A, García H, Juárez R, Laursen S, and de Dios López-Castro J, 2012, *The Journal of Physical Chemistry C*, **116**, 24855.
16. Syomin D and Koel B E, 2001, *Surf Sci.*, **490**, 265.
17. Lin J, Abroshan H, Liu C, Zhu M, Li G, and Haruta M, 2015, *J. Catal.*, **330**, 354.
18. Karak M, Barbosa L C A, and Hargaden G C, 2014, *RSC Adv.*, **4**, 53442.
19. Sanchez-Sanchez C, Orozco N, Holgado J P, Beaumont S K, Kyriakou G, Watson D J, Gonzalez-Elipe A R, Feria L, Fernández Sanz J, and Lambert R M, 2015, *J. Am. Chem. Soc.*, **137**, 940.
20. Boronat M, Lopez-Ausens T, and Corma A, 2014, *J. Phys. Chem. C.*, **118**, 9018.
21. Nyholm R, Svensson S, Nordgren J, and Flodström A, 1986, *Nucl. Instrum. Meth. A.*, **246**, 267.
22. Urpelainen S, et al., 2017, *J. Synchrotron Rad.*, **24**, 344.
23. Schnadt J, et al., 2012, *J. Synchrotron Rad.*, **19**, 701.
24. Knudsen J, Andersen J N, and Schnadt J, 2016, *Surf Sci.*, **646**, 160.
25. Tanuma S, Powell C J, and Penn D R, 1994, *Surf. Interface Anal.*, **21**, 165.
26. Humlíček J, 1982, *J. Quant. Spectrosc. Radiat. Transfer*, **27**, 437.
27. Schreier F, 1992, *J. Quant. Spectrosc. Radiat. Transfer*, **48**, 743.
28. Horsley J A, Stöhr J, Hitchcock A P, Newbury D C, Johnson A L, and Sette F, 1985, *J. Chem. Phys.*, **83**, 6099.
29. Hitchcock A P and Brion C E, 1977, *J. Electron. Spectrosc.*, **10**, 317.
30. Carravetta V, Polzonetti G, Iucci G, Russo M V, Paolucci G, and Barnaba M, 1998, *Chem. Phys. Lett.*, **288**, 37.
31. Iucci G, Carravetta V, Altamura P, Russo M V, Paolucci G, Goldoni A, and Polzonetti G, 2004, *Chem. Phys.*, **302**, 43.
32. Iucci G, Carravetta V, Paolucci G, Goldoni A, Russo M V, and Polzonetti G, 2005, *Chem. Phys.*, **310**, 43.

33. Polzonetti G, Carravetta V, Russo M V, Contini G, Parent P, and Laffon C, 1999, *J. Electron. Spectrosc.*, **98-99**, 175.
34. Weiss K, Gebert S, Wühn M, Wadepohl H, and Wöll C, 1998, *J. Vac. Sci. Technol. A*, **16**, 1017.
35. Stöhr J and Outka D A, 1987, *Physical Review B*, **36**, 7891.
36. Yang M X, Xi M, Yuan H, Bent B E, Stevens P, and White J M, 1995, *Surf Sci.*, **341**, 9.
37. Lee A F, Chang Z, Hackett S F J, Newman A D, and Wilson K, 2007, *J. Phys. Chem. C.*, **111**, 10455.
38. Kastanas G N and Koel B E, 1993, *Appl. Surf. Sci.*, **64**, 235.
39. Gao W, Baker T A, Zhou L, Pinnaduwage D S, Kaxiras E, and Friend C M, 2008, *J. Am. Chem. Soc.*, **130**, 3560.
40. Simonov K A, Vinogradov N A, Vinogradov A S, Generalov A V, Zagrebina E M, Mårtensson N, Cafolla A A, Carpy T, Cunniffe J P, and Preobrajenski A B, 2014, *J. Phys. Chem. C.*, **118**, 12532.
41. Rettner C T, 1994, *The Journal of Chemical Physics*, **101**, 1529.
42. Lykke K R and Kay B D, 1990, *The Journal of Chemical Physics*, **92**, 2614.
43. Syomin D, Kim J, Koel B E, and Ellison G B, 2001, *The Journal of Physical Chemistry B*, **105**, 8387.
44. Linde D R, 1993, *Handbook of Chemistry and Physics*. 74th ed. (Boca Raton: CRC Press)
45. Ogletree D F, Bluhm H, Lebedev G, Fadley C S, Hussain Z, and Salmeron M, 2002, *Rev. Sci. Instrum.*, **73**, 3872.

Sonogashira cross-coupling over Au(111): From UHV to ambient pressure

N Johansson[1], S Sisodiya[2], P Shayesteh[1], S Chaudhary[1], J N Andersen[1,3], J Knudsen[1,3], O F Wendt[2], and J Schnadt[1,3]

[1]Division of Synchrotron Radiation Research, Department of Physics, Lund University, Box 118, 221 00 Lund, Sweden

[2]Centre for Analysis and Synthesis, Department of Chemistry, Lund University, Box 124, 221 00 Lund, Sweden

[3]MAX IV Laboratory, Lund University, Box 118, 221 00 Lund, Sweden

E-mail: joachim.schnadt@sljus.lu.se

Supplementary material

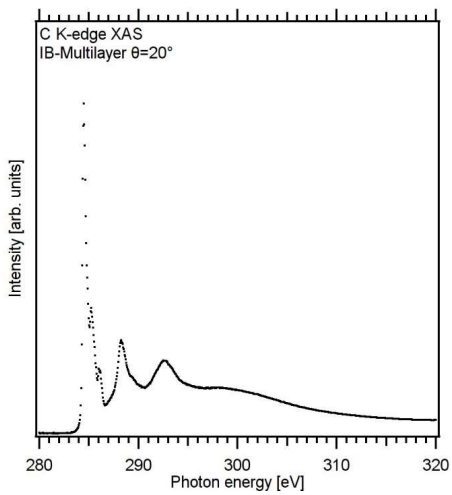

Figure S1: C K-edge NEXAFS of a multilayer coverage of IB.

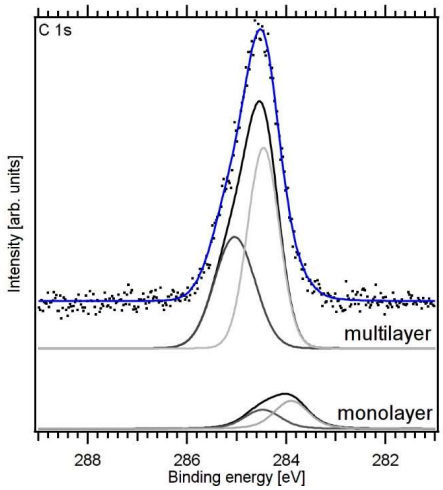

Figure S2: Fit of the multilayer coverage of PA on Au(111)

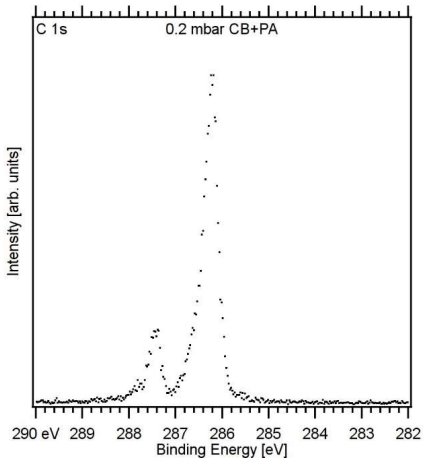

Figure S3: Gas phase APXP spectrum of CB+PA with the sample retracted.

Paper II

Mn-salen supported by Au(111): adsorption and catalysis

N. Johansson[1], O. Snezhkova[1], S. Chaudhary[1], E. Monazami[2], F. Ericson[3], R. Jensen[4], A.-L. Christoffersen[4], A. R. Head[1], S. Urpelainen[5], B. N. Reinecke[1], I. Chorkendorff[4], P. Reinke[2], P. Persson[3], J. Knudsen[1,5], and J. Schnadt[*1,5]

[1]*Division of Synchrotron Radiation Research, Department of Physics, Lund University, Box 118, 221 00 Lund, Sweden*

[2]*Department of Materials Science & Engineering, University of Virginia, PO Box 400745, Charlottesville, VA 22904-4745, United States of America*

[3]*Division of Theoretical Chemistry, Department of Chemistry, Lund University, Box 124, 221 00 Lund, Sweden*

[4]*Department of Physics, Technical University of Denmark, Fysikvej, 2800 Kgs. Lyngby, Denmark*

[5]*MAX IV Laboratory, Lund University, Box 118, 221 00 Lund, Sweden*

Abstract

We have investigated the adsorption of Mn-salen on a Au(111) surface as well as the catalytic properties of both the Au(111)-supported Mn-salen complex and pristine Mn-salen powder. X-ray photoelectron spectroscopy and scanning tunneling microscopy, carried out in ultrahigh vacuum, show that Mn-salen initially grows layer by layer on the Au(111) surface. The layers can easily be distinguished in the x-ray photoelectron spectra, and a more careful analysis of the x-ray photoelectron spectra in combination with density functional theory calculations allows the extraction of geometric information from the intensity ratio of the sp^2 to sp^3-type carbon ratio. In the preparation of a Mn-salen multilayer a fraction of the Mn-salen complexes are oxidized to oxo-Mn-salen, likely due to a combination of higher sublimation temperature and presence of oxidative contaminants in the Mn-salen chemical. Ambient pressure x-ray photoelectron spectroscopy and simultaneous mass spectroscopy show that the oxo-Mn-salen complexes in the multilayer are active for the combustion of propylene at room temperature. In contrast, microreactor characterization shows that pristine Mn-salen becomes active for propylene combustion first at a temperature of 150°C.

*Electronic address: joachim.schnadt@sljus.lu.se

1 Introduction

If it was possible to design an ideal catalyst, it would be characterized by a high activity and perfect selectivity towards the desired chemical reaction product, it would be stable and be produced at low cost, it would be "green" and thus avoid the use of solvents and production of byproducts, it would be produced from abundant materials, and it would be easy to separate it from the reaction products. With respect to these different aspects, heterogeneous and homogeneous catalysts have different advantages as well as disadvantages. Heterogeneous catalysts – often the preferred choice in large-scale technical and industrial applications – ease the separation of the catalyst material from the product [1] and often avoid the use of solvents, but suffer typically from a limited selectivity and even activity [2]. Homogeneous catalysts, in contrast, typically excel at high activity and selectivity [3], but are difficult to separate from the reaction products. The high activity and selectivity of homogeneous catalysts can be achieved due to the possibility of tailoring the active site towards the chemical reaction of interest [4, 5]. This is much more difficult to achieve with heterogeneous catalysts, which, as the solid surface materials they are, feature are large number of different active sites [1]. Single-site heterogeneous catalysis aims at marrying the advantages of homogeneous and heterogenous catalysts [6]. One of the routes towards this goal is the immobilization of a homogeneous, molecular catalyst on a surface [1].

Here we investigate a simple example of a surface-adsorbed molecular catalyst, which is known to be an excellent homogeneous catalyst for a wide range of chemical reactions. The goal is to study the catalyst's catalytic activity as well as its electronic and geometric structure by surface science methods and to thus draw on the unprecedented level of detail of such methods. The molecular catalyst in question is a Mn(III)-salen complex [bis(3,5,di-t-butylsalycylidene), 1,2, cyclohexane diaminomanganese(III)chloride](cf. Fig. 1). We will refer to it as "Mn-salen".

Mn-salen and its derivatives are effective for oxidation reactions such as the asymmetric epoxidation of unfunctionalized olefins [7–24] and sulfide oxidation [25], but also processes such as olefin polymerization [26] and cyclic organic synthesis from carbonates [27]. The complex has been subject to extensive scrutiny since it first was shown to be active for the enantioselective epoxidation of olefins [7, 8]. Its action as a homogeneous catalysts, but also as an immobilized heterogenous catalyst has been investigated in numerous studies. For example, Mn-salen – or closely resembling derivatives – have been immobilized by anchoring to silica [23, 27, 28], quartz [24] and clay [13–15] supports as well as mesoporous materials [18, 20], by attachment to polyoxometalates [29, 30], activated carbon [19, 22], polymers [21], cellulose [25] and nanostructured carbon [16]. Thus, much effort has been put into investigating the catalytic capabilities of Mn-salen complexes. Surprisingly, however, only very few surface science studies concerned with salen complexes have been reported to-date. To the best of our knowledge, the only surface science

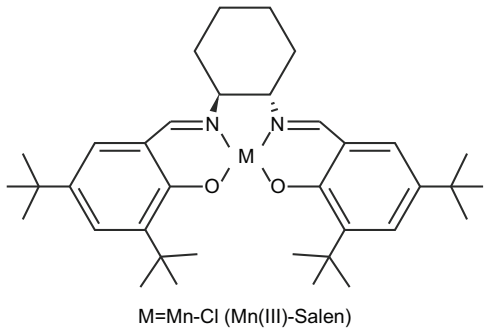

Figure 1: Molecular structure of Mn-salen.

investigations on metal salen complexes concern the adsorption of Co-salen on NaCl surfaces [31,32]. These two studies demonstrated that a surface preparation of a metal salen complex can easily be achieved by thermal sublimation. The ease of preparation of an adequate surface science systems makes is the more suprising that surface science characterization of this important catalytic system is essentially completely missing so far.

In the study we employ x-ray photoelectron spectroscopy (XPS), scanning tunneling microscopy (STM), density functional theory (DFT), ambient pressure XPS (APXPS) and catalytic microreactor measurements to study the adsorption and catalytic properties of Mn-salen in some detail. The most interesting finding is that the surface-adsorbed Mn-salen complex is active in the room-temperature combustion of propylene, as is observed from APXPS and mass spectrometry data. This stands in stark contrast to the oxidative activity of the untreated molecular powder, which becomes active for oxidation first a much higher temperature. The unexpected room-temperature activity of surface-adsorbed Mn-salen is tentatively assigned to a priming of the Mn-salen complex during deposition of a multilayer.

2 Experimental

The XPS measurements were performed at beamline I311 [33] at the MAX-II electron storage ring of the national Swedish synchrotron radiation facility MAX IV Laboratory, Lund, and at beamline 11.0.2 of the Advanced Light Source (ALS) at the Lawrence Berkeley National Laboratory, USA. The instrument at beamline I311 is composed of separate preparation and analysis chambers, connected by a gate valve. The base pressure in both chambers is in the 10^{-11} mbar range. The analysis chamber is equipped with a Scienta SES 200 electron energy analyzer. Similarly, the instrument at ALS beamline 11.0.2 [34] features an analysis chamber, separated by a gate valve from the preparation chamber. Here, both chambers have a base pressure in the 10^{-10} mbar range. The analyzer is a SPECS Phoibos 150 with a differentielly

pumped electrostatic pre-lens. The APXPS measurements were carried out at the APXPS instrument at beamline 9.3.2 [35] at the ALS. This end station, likewise equipped with separate preparation and analysis chambers with a base pressure in the 10^{-10} mbar range, features a Scienta R4000 HiPP electron energy analyzer for APXPS experiments.

At beamline I311 the Au(111) crystal was mounted on the sample manipulator by a tungsten wire, which was used for direct heating. The temperature was monitored by a type K thermocouple clamped into a hole in the side of the crystal. In the experiments at the ALS, the Au(111) crystal was mounted on a transferable sample holder equipped with a ceramic boron nitride butter heater. The temperature was monitored using a type K thermocouple clamped to the surface of the crystal.

The Au(111) crystal was cleaned by cycles of Ar^+ sputtering at an ion energy of 1 kV followed by annealing to 500°C. The sample cleanness was monitored using XPS. The Mn-salen powder was purchased from Sigma-Aldrich and degassed *in vacuo* at 100-150° for two hours prior to deposition. For low-coverage deposition the Mn-salen powder was heated to about 180° during sublimation, while multilayer coverages were obtained by Mn-salen sublimation at a temperature of 220°C.

Photon energies of 390, 520, 650, and 720 eV were used for measurements of the C 1s and Cl 2p, N 1s, O 1s, and Mn 2p core levels, respectively. At beamline I311 the overall experimental resolution was 0.06/0.12/0.14 eV for measurement of the C 1s/Cl 2p/N 1s and O 1s core levels, while the overall experimental resolution was about 0.25 eV for all core levels during the measurements at the ALS. The x-ray photoelectron (XP) spectra acquired at beamline I311 were directly calibrated to the Fermi energy, while the spectra obtained in the experiments at the ALS were calibrated to a Au 4f spectrum measured directly after each spectrum. This Au 4f spectrum in turn was calibrated to a Au 4f x-ray photoelectron (XP) spectrum of the clean Au(111) crystal calibrated to the Fermi energy.

The oxidation of propylene was monitored simultaneously by APXPS and mass spectrometry using a quadrupole mass spectrometer mounted on the second differential pumping stage of the HiPP electron energy analyser. The monitored masses were 32 u (O_2), 42 u (propylene), 44 u (CO_2) and 58 u (propylene oxide). Complementing reactivity measurements were carried out in a microreactor setup at the Danish Technical University. The setup and its operating procedures are described in Ref. [36]. The reactivity data were obtained by deviating a fraction of the gas from the reactor outlet into a gas chromatograph.

STM measurements were performed on an Omicron room-temperature STM at the University of Virginia, Charlottesville, USA. Here, a Au(111) layer grown on mica was used as the support rather than a Au(111) single crystal. The surface was cleaned by flame annealing and subsequently inserted into the vacuum system. The cleanness of the substrate was confirmed by STM before Mn-salen deposition. All STM data were recorded in constant current mode.

3 Computational Details

Supporting DFT calculations were performed using the Gaussian G09 program [37] using the B3LYP hybrid functional [38] together with the valence double-zeta quality with effective core potentials (ECP) basis set LANL2DZ [39–41]. DFT typically describe well metal complexes, and good agreement with experimental results have been demonstrated for the B3LYP functional [42]. The calculations were performed for an isolated Mn-salen complex, i.e. the supporting surface was not taken into consideration.

The core-ionized systems were modelled using the Z+1 approximation. Core-level XPS binding energy shifts were obtained from the difference between the energies of the ground and core-ionized states of the molecule. In the ground state calculation the geometries were fully optimized. The geometries of the core-excited complexes were not further relaxed, but were assumed to be identical to the relaxed ground state geometries.

4 Results and Discussion

4.1 Core level spectra

Fig. 2 shows the O 1s, N 1s, C 1s and Cl 2p core level XP spectra acquired on three different preparations of Mn-salen adsorbed on a Au(111) surface. The top spectra are for a multilayer with a thickness of approximately 60 Å, as determined from the attenuation of the Au 4f substrate line. This multilayer was prepared using a sublimation temperature of 220 °C. The middle and bottom spectra were obtained on considerably lower coverages of Mn-salen on Au(111), prepared using a sublimation temperature of 180°C. The coverage is lowest for the bottom spectra, while the middle spectra represent an intermediate situation. It is seen, and will be further elucidated below, that all spectra in the middle row can be explained from a combination of the bottom spectra with an additional component at the higher binding energy side. The only exception is the Cl 2p spectrum. This suggests that the bottom spectra were measured on a submonolayer – or maximum monolayer – coverage, while the middle spectra were obtained on a preparation with a completed first and a partial second layer of Mn-salen. For simplicity we will refer to the latter preparation as a "bilayer". All spectra in Fig. 2 were curve-fitted as described below. We did not further analyze the Mn 2p spectra, which show the expected presence of Mn on the surface (cf. figure S1 in the Supplementary information). Since the Mn 2p binding energy coincides with that of the Au 4p support line, it is difficult to extract additional information from these spectra.

Starting with a general overview of the spectral appearances, the submonolayer O 1s and N 1s spectra are both characterized by a single component at 530.9 eV and 398.9 eV binding energy, respectively. The submonolayer Cl 2p intensity is low, but the spectral shape is in agreement with a single doublet at a Cl

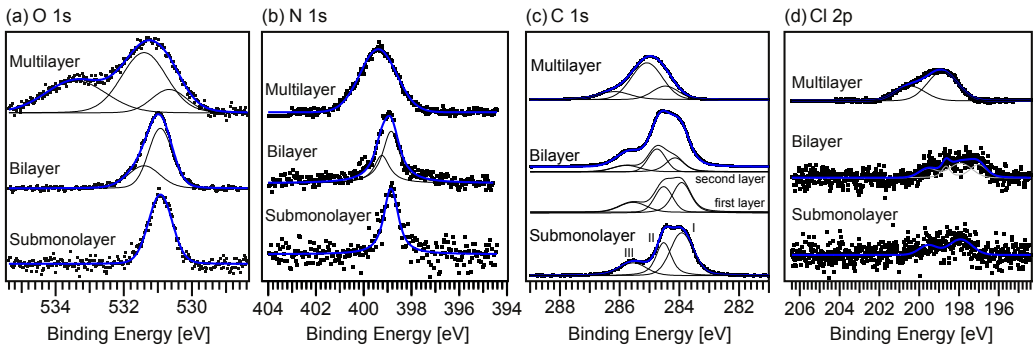

Figure 2: XP spectra of Mn-salen adsorbed on a Au(111) surface.

$2p_{3/2}$ binding energy of 197.9 eV. In the submonolayer C 1s signal, in contrast, multiple components are discernible. Overall, the observation of a single type of O, N and Cl is in agreement with intact adsorption of Mn-salen on the Au(111) support; the sublimation procedure does not decompose the complex.

Increasing the coverage to that of the bilayer preparation leads to a broadening of the O 1s, N 1s and C 1s signals. Their first moments shift to slightly higher binding energies (shifts of 0.4/0.2/0.17 eV in the O 1s/N 1s/C 1s XP spectra), in agreement with the formation of more than a single adsorbate layer. Moreover, the O 1s and N 1s signals become asymmetric towards higher binding energy. The Cl 2p signal, however, shifts to lower binding energy by -0.5 eV.

Finally, at multilayer coverage, the spectral appearance is changed significantly. Common for all core levels is a large increase in the width of the features and shifts towards higher binding energies. In addition, a component has developed on the high-binding energy side of the main peak in the O 1s spectrum. An estimate of the thickness of the multilayer from the attenuation of the substrate Au 4f signal suggest a layer thickness of approximately 60 Å.

We will now examine the XP spectra in more detail. The N 1s submonolayer spectrum can be curve-fitted with one component located at 398.9 eV binding energy. This first-layer component is re-used in the curve-fit of the bilayer spectrum. The asymmetry on the high-binding energy side of the spectrum requires a new component at 399.2 eV binding energy, characteristic of the added layer. The multilayer N 1s XP spectrum can be fitted by a single multilayer component at 399.4 eV binding energy, i.e. an energy which is very similar to that of the second layer in the bilayer preparation, in line with the expectation that a major shift between second layer and multilayer is not expected. The multilayer component is, however, much broader than the corresponding bilayer and submonolayer components, which leads us to conclude that varying chemical environments exist in the multilayer. Hence, the multilayer is characterized by significant molecular disorder.

The C 1s XP spectra in Fig. 2(c) exhibit a more complex appearance with several different components. In order to gain a principal understanding of the lineshape, we used DFT to calculate the core-level shifts of an isolated gas phase Mn-salen complex in the Z+1 approximation. Given the expected limited interaction between neighboring molecules in the multilayer – it should be dominated by van der Waals forces and possibly dipole interactions – it seems fair to model the corresponding spectrum using the calculational results. In the calculations we assume the central Mn ion to be in a quintet state, in agreement with earlier results [43]; we also found, however, that the C 1s and O 1s core-level shifts do not critically depend on the spin state of the Mn ion. The results of the calculations are shown in Fig. 3 and Table 1. On average, the phenyl carbon atoms, excluding the oxygen-bonded carbon atoms, are found to have the lowest binding energies (with an average shift of -2.1 eV relative to the binding energy of the cyclohexane C6 carbon atom, cf. Fig. 3(a)). Next lowest is the average C 1s binding energy of the tert-butyl groups with a shift of -1.55 eV relative to the C6 atom. The difference of $\sim$0.6 eV between the phenyl and tert-butyl C 1s binding energies are in very good agreement with experiment [44]. The cyclohexane carbon atoms, excluding the nitrogen-bonded carbon atoms, have an average core-level shift of -0.59 eV relative to the binding energy of the C6 atom. As one would expect intuitively, the oxygen- and nitrogen-bonded carbon atoms have the highest binding energies with an average shift of -0.16 eV relative to the C6 binding energy. Somewhat unexpectedly, the oxygen-bonded carbon atoms have lower C 1s binding energies than the nitrogen-bonded ones; this can be explained from the fact that the oxygen-bonded carbon atoms are part of the phenyl rings with excellent properties for core-hole screening in the final state. Further, we note that the variation of the C 1s shifts of the tert-butyl carbon atoms are large: they range from -1.0 to -2.1 eV.

One can now group the core-level shifts in terms of whether the photoemitting carbon atom is nitrogen- or oxygen-bonded ($C_{N,O}$), sp^3-hybridized or sp^2-hybridized, where we exclude the nitrogen- and oxygen-bonded carbon atoms from the latter two groups. If one places a Gaussian at each of the calculated relative binding energies (normalized and with a width of 0.4 eV), one obtains the $C_{N,O}$, sp^3 and sp^2 components depicted in Fig. 3(b) together with the overall theoretical spectrum. The shape of the spectrum is in semi-quantitative agreement with the shape of the experimental multilayer C 1s spectrum in Fig. 2(b). It clearly overestimates the intensity of the high-binding energy shoulder, which raises the question of the reliability of the unexpectedly large variation in the tert-butyl core-level shifts. Nevertheless, the calculations provide us with a general understanding of the composition of the C 1s line with three different components due to the $C_{N,O}$, sp^3 and sp^2 peaks as defined above.

The three $C_{N,O}$, sp^3 and sp^2 components were used in a curve fit of the C 1s multilayer spectrum in Fig. 2(c). The binding energies of these components are found to be 286.2, 285.1 and 284.5 eV, respectively. The widths of all components are rather large, which reinforces the notion of varying chemical environments

and disorder in the multilayer. The sp^3 to sp^2 intensity ratio is 3.2, i.e. it is larger than what the Mn-salen stoichiometry suggests. The most likely explanation is that the tert-butyl groups of the outermost layer of Mn-salen molecules point towards the vacuum.

As in the case of the C 1*s* multilayer spectrum, a comparable, but more well-defined structure with three components is found for the submonolayer C 1*s* XP spectrum. In comparison to the multilayer spectrum the components are down-shifted, in line with an efficient screening of the final state core hole by the metallic Au(111) support. Again, we identify (i) the component at 285.6 eV binding energy with oxygen- and nitrogen-bonded carbon, $C_{N,O}$, (ii) that at 284.5 eV with sp^3-type C and (iii) that at 283.9 eV with sp^2-type C. The $C_{N,O}$ component comprises 18% of the total intensity of the C 1*s* signal, in good agreement with what is expected from the stoichiometry (17%). The sp^3- and sp^2-type C intensities sum up to 31% and 51% of the intensity of the C 1*s* line, respectively, yielding a sp^3 to sp^2 intensity ratio of 0.6. This is considerably lower than what is expected from the 2:1 stoichiometry of the complex. Part of the deviation can possibly be explained from the large variation of C 1s binding energies of the sp^3-hybridized carbon atoms, which we identified in the DFT calculations; probably this variation implies that our peak assignment is quantitatively not entirely correct. Further, we can state that the deviation of the sp^3 to sp^2 intensity ratio from the expected value cannot result from a conversion of sp^3-type into sp^2-hybridized carbon, since a room temperature dehydrogenation of the cyclohexane moiety is highly unlikely given the inertness of the Au(111) support and since a dissociation of the tert-butyl groups seems equally unlikely. What could contribute to the low sp^3 to sp^2 intensity ratio is a geometric factor: is seems as if the sp^3-hybridized carbon atoms on average are closer to the surface than the sp^2-hybridized ones. Possibly, the tert-butyl groups point towards to the Au(111) surface, which would lead to a stronger attenuation of the photoelectrons emitted by these groups in comparison to that of photoelectrons emitted by the phenyl moieties.

The components in the bilayer C 1*s* XP spectrum are less well defined than those in the submonolayer spectrum. In order to model the lineshape we assume the first-layer signal to be unchanged and to be complemented by second-layer components. For the second-layer signal we retain the $C_{N,O}$, sp^3 and sp^2 peaks, but let them shift to higher binding energy by 0.27 eV (retaining the relative shifts) and allow relative intensity variation between the sp^3 and sp^2 components. In contrast, we fix the $C_{N,O}$ contribution to 18% of the second-layer intensity. The resulting fit agrees well with the experimental data. The sp^3 to sp^2 intensity ratio in the second-layer signal is now 1.1, still quite much lower than what is expected from the stoichiometry, but considerably large than what was observed for the first layer.

The submonolayer O 1s XP spectrum in Fig. 2(a) is explained by a single component located at 530.3 eV binding energy. This first-layer component is, again, re-used as the low-binding energy component in

the curve-fit of the bilayer. This allows us to pin down the location of the high-binding energy component which gives rise to the observed asymmetry; this second-layer component is found at a binding energy of 531.4 eV. Also here assuming that the multilayer signal should be similar in energy to that of the second layer, the curve-fit of the multilayer re-uses this component. In the multilayer the component is seen to be considerably broadened, in the same way as was observed for the multilayer N 1s and C 1s spectra. Moreover, in order to achieve a good fit the line due photoemission from the pristine complex needs to be accompanied by two additional components at 533.4 eV and 530.7 eV binding energy.

In an effort to understand these two new components in the O 1s spectrum of the multilayer, we calculated the O 1s core-level shifts of an oxo-Mn(V)-salen complex. The modified central part of the complex is shown in Fig. 3(a), while the corresponding theoretical spectrum, constructed from the core-level shifts as the theoretical spectrum of the pristine Mn-salen complex, is shown in Fig. 3(c). We find two components separated by 2.75 eV from each other, with the high-binding energy component being due to the original oxygen ligands to the Mn ion, while the low-energy component is due to the new oxo ligand. The separation is in excellent agreement with the separation of 2.7 eV between the two new components in the experimental multilayer spectrum in Fig. 2(a). Also the experimental intensity ratio of 2.3:1 agrees very well with the stoichiometric ratio. The analysis leads us to conclude that an oxidation of the Mn-salen complex was experienced in the preparation of the multilayer. The difference between the low-coverage preparations of submonolayer and bilayer and the high-coverage multilayer preparation was the sublimation temperature, since higher a sublimation temperature were required in order to achieve a high coverage (220°C vs 180°C for the lower-coverage preparations). The exact reason for the oxidation remains unclear, however, and we only can speculate that impurities in the molecular powder, such as water, are responsible.

Finally, we turn to an analysis of the Cl 2p spectra in Fig. 2(d). In agreement with what was found for the O 1s and N 1s submonolayer spectra, a single species with a Cl $2p_{3/2}$ binding energy of 197.9 eV can explain the corresponding Cl 2p spectrum. This Cl species is assigned to Cl bound to the molecular complex. Curve-fitting the bilayer spectrum requires two doublets, one of which corresponds to that of the first layer and a second doublet at a binding energy of 197.0 eV binding energy. The second-layer downshift is suprising: the energy of the new species is comparable to what is expected for atomic Cl bound to a Au(111) surface [45, 46]. Intuitively, splitting of the Cl ligand would have been expected for the first rather than the second layer; at present, we cannot give any explanation. The mutilayer Cl 2p line is broad, but agrees with a single multilayer component at 198.8 eV binding energy.

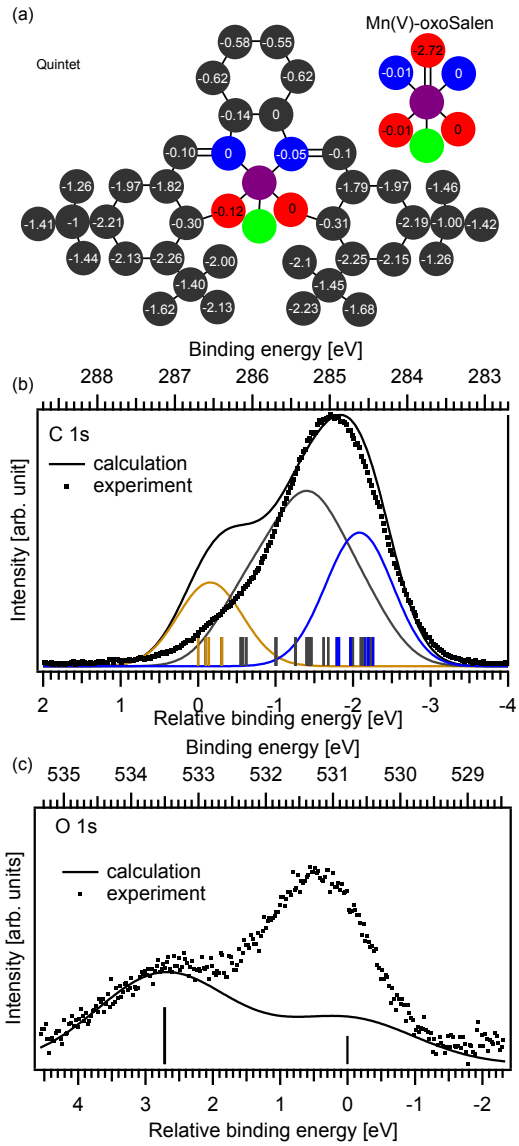

Figure 3: DFT calculations. (a) Calculated core-level shifts for each of the atoms in Mn-salen. (b) Experimental multilayer C 1*s* XP spectrum of Mn(III)-salen/Au(111) and comparison to a spectrum assembled from the calculated core-level shifts. (c) Experimental multilayer O 1*s* XP spectrum and comparison to a spectrum assembled from the calculated core-level shifts of the oxo-Mn(V)-salen complex (see inset of (a)).

Photoemitting atom	Core-level shift (eV)
C-$\underline{C}H_2$-C in cyclohexane	-0.58
	-0.55
	-0.62
	-0.62
O-$\underline{C}$H-C in cyclohexane	0
O-$\underline{C}$H-C in cyclohexane	-0.14
C-$\underline{C}$-C in tert-butyl	-1
	-1
	-1.40
	-1.45
C-$\underline{C}H_3$ in tert-butyl	-1.26
	-1.41
	-1.44
	-2.00
	-1.62
	-2.13
	-2.1
	-2.23
	-1.68
	-1.46
	-1.42
	-1.26
C-$\underline{C}$H-C and C-$\underline{C}$-C_2 in phenyl	-1.97
	-2.21
	-2.13
	-2.26
	-1.79
	-1.97
	-2.19
	-2.15
	-2.25
	-1.82
O-$\underline{C}$-C_2 in phenyl	-0.30
	-0.31
C-$\underline{C}$H-N	-0.10
	-0.1

Table 1: DFT C 1*s* core-level shifts calculated for an isolated Mn-salen complex. The photoemitting atom is underlined.

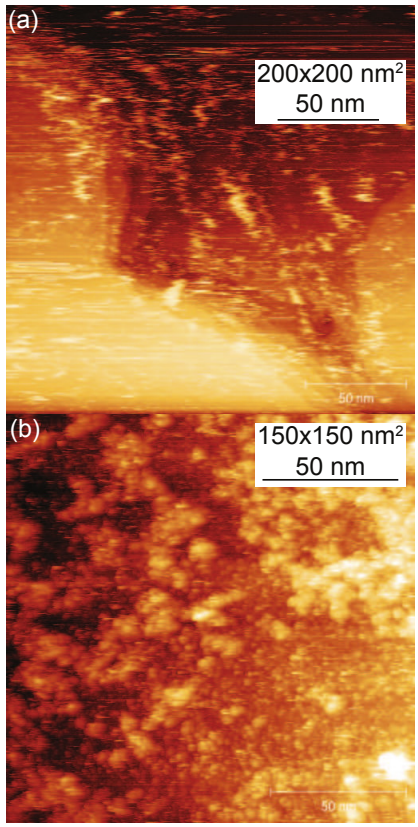

Figure 4: STM images obtained on (a) a submonolayer of Mn-salen/Au(111) (V=1.6 V, I=1 nA) and (b) a coverage of Mn-salen larger than a monolayer (V=-1.91 V, I=0.045 nA).

4.2 Scanning tunneling microscopy

In an effort to investigate the validity of the layer approach as applied to the analysis of the core-level spectra, room-temperature STM measurements were conducted. STM images were acquired of submonolayer and bilayer preparations. Not unexpectedly, STM imaging of a multilayer preparation was not possible. Representative STM images of the submonolayer and bilayer are shown in Fig. 4(a) and (b).

Fig. 4(a) clearly illustrates the high mobility of the Mn-salen adsorbates on the Au(111) surface. The image shows Au(111) terraces covered in fuzzy streaks due to the moving Mn-salen molecules. Extensive scanning at the same position was found to clear the area. Increasing the coverage above a monolayer and heating to 140°C for 15 min leads to a changed appearance of the STM images (Fig. 4(b)). Roughly, areas with two different heights are discernible, which suggests that the assumption made in the XPS analysis

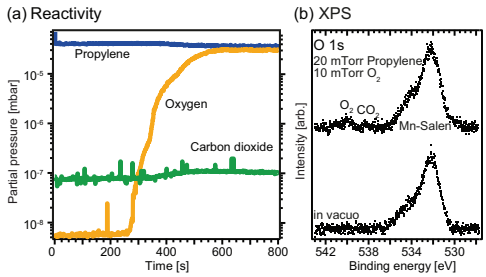

Figure 5: (a) QMS and (b) APXPS data for propylene oxidation over a Au(111)-supported multilayer of Mn-salen.

of, at least initial, layer-by-layer growth is suitable. In more detail, the surface is covered by sphere-like structures with fairly uniform nm-sizes, but also larger aggregates. These aggregates point towards the clustering of Mn-salen adsorbates.

4.3 Reactivity measurements: APXPS and microreactor experiments

APXPS and simultaneous quadrupole mass spectrometry (QMS) were used to study the catalytic oxidation of propylene over Au(111)-supported Mn-salen. O_2 was used as the oxidant. The resulting QMS data together with corresponding APXPS data are shown in Fig. 5.

Initially, i.e. at time $t = 0$ s in Fig. 5(a), the sample is exposed to 20 mTorr C_3H_6 (blue line). At this point, the CO_2 and O_2 partial pressures are at their background levels. As 10 mTorr O_2 are leaked into the chamber at $t \approx 300$ s, the measured O_2 partial pressure rises rapidly while the C_3H_6 partial pressure decreases. No change is observed in the mass 58 signal, which would have corresponded to the production of propylene epoxide (not shown). In contrast, the CO_2 partial pressure is seen to increase from its background level, indicative of propylene combustion.

Fig. 5(b) shows the O 1*s* ambient pressure x-ray photoelectron (APXP) spectra of the Mn-salen film as prepared in vacuum (bottom) and in the 10 mTorr O_2 + 20 mTorr C_3H_6 reaction mixture (top). The bottom spectrum exhibits a single peak at 532.1 eV binding energy with a shoulder at the high energy side, i.e. the appearance is that of a Mn-salen multilayer as discussed above. In the O_2/C_3H_6 reaction mixture a doublet with components located at 539.8 eV and 541.0 eV binding energy is observed as well as a second peak at 538.4 eV binding energy. The doublet is the characteristic signal of gas phase O_2 with two components due to core polarization. The lower-energy peak is attributed to gas phase CO_2, easily identifiable due to its shift relative to the O_2 gas phase signal. Clearly, in reaction conditions a substantial amount of CO_2 is found above the sample surface.

Hence, CO_2 is observed in both the QMS and APXPS signals. Together, this excludes alternative explanations for the appearance of a CO_2 signal other than a combustion reaction. If the CO_2 signal had been produced by the mass spectrometer filament, it would not have been observed in the APXP spectra, as the gases do not flow back to the sample. Likewise, we can also exclude that the O_2 feed gas is contaminated by CO_2, since the corresponding APXPS intensities are comparable to each other, but very different, by about two orders of magnitude, in the QMS data. If the O_2 feed had been contaminated, the QMS and APXPS intensity ratios should have been similar. In a control experiment on a clean Au(111) surface we also ensured that no CO_2 was observed (not shown), so that we can exclude any reaction on sample holder parts. Clearly, the CO_2 originates indeed from the sample, and we conclude that a Mn-salen multilayer is active in the combustion of propylene at room temperature.

The catalytic properties of Mn-salen were further investigated by reactivity measurements in a microreactor. After filling the reactor with Mn-salen powder, a mixture of O_2 and C_3H_6 was flowed through the reactor, using Ar as the carrier gas. As in the APXPS experiments, the oxygen and propylene partial pressures were 10 and 20 mTorr, respectively. The reactivity data from the experiment are shown in figure 6.

Initially, all partial pressures were given time to stabilize. After around 1.5 h heating was started, and the temperature was increased in two steps to first 90°C and then 120°C. First at 150°C, large changes of the partial pressures are observed: the CO_2 and H_2O partial pressures increase drastically, while the O_2 and C_3H_6 partial pressures drop. Within the time frame of the experiment, the increase in CO_2 and H_2O partial pressure is only partly reverted towards the initial levels. Moreover, no reaction is seen if the same experiment is carried out without any Mn-salen powder in the reactor. This leads us to conclude that propylene combustion indeed is catalyzed by Mn-salen. Given that Mn-salen is active for the homogeneous epoxidation of unfunctionalized alkenes, it is not very surprising that Mn-salen also should catalyze the heterogeneous combustion of propylene.

The complete combustion of propylene over Mn-salen is thus observed in APXPS and microreactor experiments. The temperature is, however, very different in the two cases: in the APXPS experiments we observed the room temperature combustion of propylene, while the experiments in the microreactor required a temperature of 150° for the combustion to proceed. We hypothesize that the difference in temperature can be attributed to a difference in the initial state of the Mn-salen material.

The homogeneous epoxidation reaction over the Mn-salen complex proceeds via an oxo-Mn-salen intermediate [47]. In the XPS analysis above, we found a large fraction of the Mn-salen complexes in the multilayer to carry an oxo ligand to the Mn center, and we speculated that the oxidation – and hence 'priming' of the catalyst – occurred during the sublimation at around 220°C of the Mn-salen complex onto

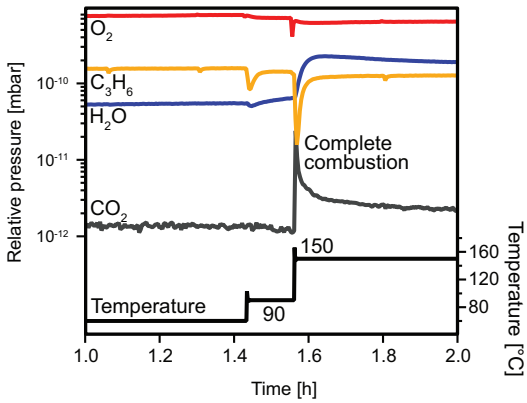

Figure 6: Reactivity for propylene oxidation over Mn-salen powder measured in a microreactor. The graph shows the partial pressures of CO_2, O_2, propylene (C_3H_6) and H_2O during heating of the catalyst.

the Au(111) surface, likely due to the presence of contaminants in the chemical. In contrast, no previous heating and thus no priming was carried out in the microreactor experiments; heating to temperatures above 150°C was done first during the catalysis experiments in the presence of O_2. In this way, continuous formation of of oxo-Mn-salen complexes is ensured and the reaction can persist for longer time.

5 Conclusions

We have performed a combined XPS, DFT and STM study to investigate the adsorption of the Mn-salen complex on a Au(111) surface. The XP spectra of submonolayer, bilayer and multilayer preparations have been analyzed carefully, and we find a preference for the Mn-salen complexes to adsorb in the first layer with the tert-butyl groups towards the Au surface. The multilayer is largely characterized by disorder and varying chemical environments, but there are indications that the tert-butyl groups of the outermost layer point outwards. The multilayer was prepared at a higher sublimation temperature, which led to the oxidation of a fraction of Mn-salen complexes towards an oxo-Mn-salen species. The oxo-Mn-salen has previously been identified to catalyze alkane oxidation reactions.

In reactivity experiments we find that a Au(111)-supported multilayer of Mn-salen is active for the combustion of propylene at room temperature. This surprising low-temperature activity is ascribed to the priming of the multilayer film with oxo ligands. A reactivity experiment carried out in a microreactor using pristine, un-primed Mn-salen, show combustion activity first at 150°C. The results suggest that Mn-salen could be a potent room-temperature catalyst if it could be supplied with oxo ligands, e.g. from a sufficiently potent oxidant. Using a less oxygen-rich reaction mixture might enable the partial oxidation

of alkanes. For propylene this is particularly interesting, since a partial oxidation could result in the formation of propylene oxide, a chiral compound.

6 Acknoledgements

The staff at the MAX IV Laboratory and the Advanced Light Source are gratefully acknowledged for their assistance during the beamtimes.

References

[1] J. M. Thomas. *Chem. Cat. Chem.*, 2:127, 2010.

[2] R. T. Vang, K. Honkala, S. Dahl, E. Kruse Vestergaard, J. Schnadt, E. Lægsgaard, B. S. Clausen, J. K. Nørskov, , and F. Besenbacher. *Nat. Mater.*, 4:160, 2005.

[3] D. Astruc. *Organometallic Chemistry and Catalysis*. Springer, Berlin, Heidelberg, 2007.

[4] F. Zaera. *Top. Catal.*, 34:129, 2005.

[5] A. Corma and H. Garcia. *Top. Catal.*, 48:8, 2008.

[6] J. M. Thomas. *Proc. R. Soc. A*, 468:1884, 2012.

[7] W. Zhang, J. L. Loebach, S. R. Wilson, and E. N. Jacobsen. *J. Am. Chem. Soc.*, 112:2801–2803, 1990.

[8] W. Zhang and E. N. Jacobsen. *J. Org. Chem.*, 56:2296–2298, 1991.

[9] K. C. Gupta and A. K. Sutar. *Coord. Chem. Rev.*, 252:1420–1450, 2008.

[10] N. C. Maity, G. V.S. Rao, K.J. Prathap, S. H.R. Abdi, R. I. Kureshy, N. H. Khan, and H. C. Bajaj. *J. Mol. Cat. A: Chem.*, 366:380–389, 2013.

[11] P. G. Cozzi. *Chem. Soc. Rev.*, 33:410–421, 2004.

[12] W. Adam, C. Mock-Knoblauch, C. R. Saha-Möller, and M. Herderich. *J. Am. Chem. Soc.*, 122:9685–9691, 2000.

[13] I. Kuźniarska-Biernacka, A. R. Silva, A. P. Carvalho, J. Pires, and C. Freire. *J. Mol. Cat. A: Chem.*, 278:82–91, 2007.

[14] I. Kuźniarska-Biernacka, A-R. Silva, A. P. Carvalho, J. Pires, and C. Freire. *Catal. Lett.*, 134:63–71, 2010.

[15] A. M. Garcia, V. Morena, S. X. Delgado, A. E. Ramirez, L. A . Vargas, M. Á. Vicente, A. Gil, and L. A. Galeano. *J. Mol. Cat. A: Chem.*, 416:10–19, 2016.

[16] H. Gaspar, M. Andrade, C. Periera, A.M. Pereira, S.L.H Rebelo, J.P.Araújo, J.Pires, A.P. Carvalho, and C. Freire. *Catal. Today*, 203:103–110, 2013.

[17] J. Huang, X. Fu, G. Wang, Q. Miao, and G. Wang. *Dalton Trans.*, 41:10661–10669, 2012.

[18] P. Das, A. R. Silva, A. P. Carvalho, J. Pires, and C. Freire. *J. Mater. Sci.*, 44:2865–2875, 2009.

[19] F. Maia, R. Silva, B. Jarrais, A. R. Silva, C. Freire, M. F.R. Pereira, and J. L. Figueiredo. *J. Colloid Interf. Sci.*, 328:314–323, 2008.

[20] J. Huang, L. Yuan, and J. Cai. *J. Mol. Cat. A: Chem.*, 416:147–153, 2016.

[21] M. D. Angelino and P. E. Laibinis. *J. Polym. Sci. Pol. Chem.*, 37:3888–3898, 1999.

[22] A. R. Silva, J. L. Figueiredo, C. Freire, and B. de Castro. *Micropor. Mesopor. Mat.*, 68:83–89, 2004.

[23] R. Ji, K. Yu, L.-L. Lou, Z. Gu, and S. Liu. *J. Inorg. Organomet. P.*, 20:675–683, 2010.

[24] V. La Paglia Fragola, F. Lupo, A. Pappalardo, G. Trusso Sfrazzetto, R. M. Toscano, F. P. Ballistreri, G. A. Tomaselli, and A. Gulino. *J. Mater. Chem.*, 22:20561, 2012.

[25] A. Mohammadinezhad, M. Ali Nasseri, and M. Salimi. *RSC Adv.*, 4:39870, 2014.

[26] H. T. Ban, T. Kase, and M. Murata. *J. Polym. Sci. Pol. Chem.*, 39:3733–3738, 2001.

[27] F. Jutz, J.-D. Grunwaldt, and A. Baiker. *J. Mol. Cat. A: Chem.*, 279:94–103, 2008.

[28] F. Jutz, J.-D. Grunwaldt, and A. Baiker. *J. Mol. Cat. A: Chem.*, 297:63–72, 2009.

[29] I. Bar-Nahum, H. Cohen, and R. Neumann. *Inorg. Chem.*, 42:3677–3684, 2003.

[30] Q. Wu, S.-W. Lin, Y. G. Li, and E.-B. Wang. *Inorg. Chem. Acta*, 382:139–145, 2012.

[31] K. Lämmle, T. Trevethan, A. Schwarz, M. Watkins, A. Shluger, and R. Wiesendanger. *Nano Lett.*, 10:2965–2971, 2010.

[32] A. Schwarz, D. Z. Gao, K. Lämmle, J. Grenz, M. Watkins, A. Shluger, and R. Wiesendanger. *J. Phys. Chem. C*, 117:1105–1112, 2013.

[33] R. Nyholm, J. N. Andersen, U. Johansson, B. N. Jensen, and I. Lindau. *Nucl. Instrum. Res. Meth. A*, 467-468, Part 1:520, 2001.

[34] H. Bluhm, K. Andersson, T. Araki, K. Benzerara, G.E. Brown, J.J. Dynes, S. Ghosal, M.K. Gilles, H.-C. Hansen, J.C. Hemminger, A.P. Hitchcock, G. Ketteler, A.L.D. Kilcoyne, E. Kneedler, J.R. Lawrence, G.G. Leppard, J. Majzlam, B.S. Mun, S.C.B. Myneni, A. Nilsson, H. Ogasawara, D.F. Ogletree, K. Pecher, M. Salmeron, D.K. Shuha, B. Tonner, T. Tyliszczak, T. Warwick, and T.H. Yoon. *J. Electron Spectroscopy Rel. Phen.*, 150:86, 2006.

[35] M. E. Grass, P. G. Karlsson, F. Aksoy, M. Lundqvist, B. Wannberg, B. S. Mun, Z. Hussain, and Z. Liu. *Rev. Sci. Instrum.*, 81:053106, 2010.

[36] T. R. Henriksen, J. L. Olsen, P. Vesborg, I. Chorkendorff, and O. Hansen. *Rev. Sci. Instrum.*, 80:124101, 2009.

[37] M. J. Frisch, G. W. Trucks, H. B. Schlegel, G. E. Scuseria, M. A. Robb, J. R. Cheeseman, G. Scalmani, V. Barone, B. Mennucci, G. A. Petersson, H. Nakatsuji, M. Caricato, X. Li, H. P. Hratchian, A. F. Izmaylov, J. Bloino, G. Zheng, J. L. Sonnenberg, M. Hada, M. Ehara, K. Toyota, R. Fukuda, J. Hasegawa, M. Ishida, T. Nakajima, Y. Honda, O. Kitao, H. Nakai, T. Vreven, J. A. Montgomery, J. E. Peralta, F. Ogliaro, M. Bearpark, J. J. Heyd, E. Brothers, K. N. Kudin, V. N. Staroverov, R. Kobayashi, J. Normand, K. Raghavachari, A. Rendell, J. C. Burant, S. S. Iyengar, J. Tomasi, M. Cossi, N. Rega, J. M. Millam, M. Klene, J. E. Knox, J. B. Cross, V. Bakken, C. Adamo, J. Jaramillo, R. Gomperts, R. E. Stratmann, O. Yazyev, A. J. Austin, R. Cammi, C. Pomelli, J. W. Ochterski, R. L. Martin, K. Morokuma, V. G. Zakrzewski, G. A. Voth, P. Salvador, J. J. Dannenberg, S. Dapprich, A. D. Daniels, Ö. Farkas, J. B. Foresman, J. V. Ortiz, J. Cioslowski, and D. J. Fox, Gaussian 09, Revision E.01, Tech. Rep. (Gaussian, Inc.).

[38] A. D. Becke. *J. Chem. Phys.*, 98:5648, 1993.

[39] W. R. Wadt and P. J. Hay. *J. Chem. Phys.*, 82:270, 1985.

[40] P. J. Hay and W. R. Wadt. *J. Chem. Phys.*, 82:284, 1985.

[41] W. R. Wadt and P. J. Hay. *J. Chem. Phys.*, 82:299, 1985.

[42] C. J. Cramer and D. G. Truhlar. *Phys. Chem. Chem. Phys.*, 11:10757, 2009.

[43] J. Krzystek and J. Telser. *J. Magn. Res.*, 162:454, 2003.

[44] I. Biswas, H. Peisert, T. Schwieger, D. Dini, M. Hanack, M. Knupfer, T. Schmidt, , and T. Chassé. *J. Chem. Phys.*, 122:064710, 2005.

[45] W. Gao, T. A. Baker, L. Zhou, D. S. Pinnaduwage, E. Kaxiras, and C. M. Friend. *J. Am. Chem. Soc.*, 130(11):3560, 2008.

[46] G. N. Kastanas and B. E. Koel. *Appl. Surf. Sci.*, 64(3):235 – 249, 1993.

[47] J. Clayden, N. Greeves, S. Warren, and P. Wothers. *Organic Chemistry.* Oxford University Press, Oxford, 2001.

Mn-salen supported by Au(111): adsorption and catalysis

N. Johansson[1], O. Snezhkova[1], S. Chaudhary[1], E. Monazami[2], F. Ericson[3], R. Jensen[4], A.-L. Christoffersen[4], A. R. Head[1], S. Urpelainen[5], B. N. Reinecke[1], I. Chorkendorff[4], P. Reinke[2], P. Persson[3], J. Knudsen[1,5], and J. Schnadt[*1,5]

[1]*Division of Synchrotron Radiation Research, Department of Physics, Lund University, Box 118, 221 00 Lund, Sweden*

[2]*Department of Materials Science & Engineering, University of Virginia, PO Box 400745, Charlottesville, VA 22904-4745, United States of America*

[3]*Division of Theoretical Chemistry, Department of Chemistry, Lund University, Box 124, 221 00 Lund, Sweden*

[4]*Department of Physics, Technical University of Denmark, Fysikvej, 2800 Kgs. Lyngby, Denmark*

[5]*MAX IV Laboratory, Lund University, Box 118, 221 00 Lund, Sweden*

Supplementary material

[*]Electronic address: joachim.schnadt@sljus.lu.se

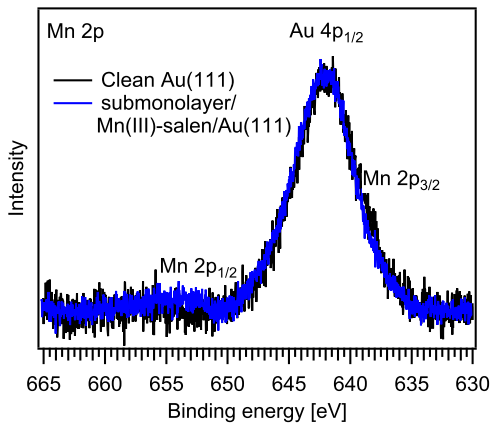

Figure S1: Mn 2p region X-ray photoelectron spectra acquired of the clean Au(111) (black line) substrate and the submonolayer coverage (blue line). The spectra are dominated by the Au $4p_{1/2}$ peak which coincides with the Mn $2p_{3/2}$ peak. The blue spectrum show a small signal of Mn $2p_{1/2}$ at 653 eV binding energy.

Paper III

IOP Publishing Journal of Physics: Condensed Matter
J. Phys.: Condens. Matter **00** (2017) 000000 (10pp) UNCORRECTED PROOF

Ambient pressure phase transitions over Ir(1 1 1): at the onset of CO oxidation

N Johansson[1], M Andersen[2], Y Monya[3], J N Andersen[4], H Kondoh[3], J Schnadt[1,4] and J Knudsen[1,4]

[1] Division of Synchrotron radiation research, Department of Physics, Lund University, Box 118, 221 00 Lund, Sweden
[2] Chair for Theoretical Chemistry and Catalysis Research Center, Technische Universität München, Lichtenbergstr. 4, 85747 Garching, Germany
[3] Department of Chemistry, Keio University, 3-14-1 Hiyoshi, Kohoku-ku, Yokohama 223-8522, Japan
[4] MAX IV Laboratory, Lund University, Box 118, 221 00 Lund, Sweden

E-mail: jan.knudsen@sljus.lu.se

Received 16 July 2017, revised 25 August 2017
Accepted for publication 5 September 2017
Published

Abstract

In this study we report on the adsorbate structures on an Ir(1 1 1) surface during the phase transition from the inactive to the active state during CO oxidation. The CO oxidation over Pt(1 1 1) is used as a reference case. Where Pt(1 1 1) either is inactive and CO covered or active and O covered, Ir(1 1 1) exhibits a transition state with co-existing chemisorbed O and CO. The observed structural differences are explained in terms of DFT-calculated adsorption energies. For Pt(1 1 1) the repulsive CO–O interaction makes co-existing chemisorbed CO and O unfavourable, while for Ir(1 1 1) the stronger O and CO adsorption allows for overcoming the repulsive interaction. At the onset of CO oxidation over Ir(1 1 1), a CO structure containing defects forms, which enables O_2 to dissociatively adsorb on the Ir(1 1 1) surface, thus enabling the CO oxidation reaction. At the mass transfer limit, the Ir(1 1 1) surface is covered by a chemisorbed O structure with defects; hence, the active surface is predominately chemisorbed O covered at a total pressure of 0.5 mbar and no oxide formation is observed.

Keywords: CO oxidation, Ir(1 1 1), Pt(1 1 1), XPS, DFT, APXPS

(Some figures may appear in colour only in the online journal)

1. Introduction

CO oxidation over transition metal surfaces has been studied extensively due to its technological importance ranging from automobile exhaust conversion to hydrogen gas purification for fuel cell applications. It also serves as a probe reaction for the identification of active sites and phases on simplified model systems. To this end, low-index transition metals surfaces have been used in an effort to identify and understand these active sites and phases.

One question that has been studied and debated extensively is whether the surface is metallic or covered by a thin or thick surface oxide at reaction conditions upon reaching the mass transfer limit (MTL). Here, the MTL refers to the creation of a boundary layer in the gas phase above the surface in which CO is depleted due to the rapid oxidation at the surface.

For Rh it has been demonstrated that a thin surface oxide is formed on the Rh(1 1 1) [1] and the Rh(1 0 0) [2] surfaces in CO:O_2 mixtures at total pressures between 10 and 300 mbar using surface x-ray diffraction (SXRD) upon reaching the MTL. In contrast, a chemisorbed oxygen phase has been observed in the MTL in a corresponding ambient pressure x-ray photoemission spectroscopy (APXPS) study of the Rh(1 0 0) [3] surface at lower pressures between 0.01 to 1 mbar. Another important finding from the same APXPS study is that the transition from the unreactive and CO poisoned surface, found at low temperatures, to the active chemisorbed oxygen phase, found at higher temperature, happened instantaneously at a total pressure between 0.1 and 1 mbar. Co-existence of CO and oxygen is only observed at 0.01 mbar total pressure.

Pd is another late transition metal over which the oxidation of CO has been extensively studied. The Pd(1 0 0) and Pd(1 1 1)

JNL:CM PIPS: AA8A44 TYPE: SPE TS: NEWGEN DATE:13/9/17 EDITOR: IOP SPELLING: UK

surfaces have, for example, been studied with APXPS [4–6], the Pd(1 0 0) surface with SXRD [7], and the Pd(1 1 0) surface with high pressure scanning tunnelling microscopy (HPSTM) [8]. In summary, these studies have shown that the surfaces are poisoned by adsorbed CO at low temperatures, while surface oxides or bulk-like oxides are formed in the MTL at higher temperatures depending on the CO:O_2 ratio. For the Pd(1 0 0) surface it has been demonstrated [4, 5, 8] that the switching between the inactive and CO-covered surface and the oxide surface is fast and co-existence of CO and the oxide phases was not observed.

In contrast to both Rh and Pd, no surface oxide has been observed for Pt(1 1 1) in APXPS studies performed at CO oxidation conditions [9, 10]. Here, a chemisorbed oxygen phase or a clean surface without adsorbates [10] have been reported in the MTL at total pressures around 1 mbar at oxygen rich CO:O_2 mixtures. An oxide has, however, been reported to form on Pt(1 1 1) in pure O_2 in the mbar regime at elevated temperatures [11].

For Ir surfaces oxygen adsorption [12] and oxidation in pure oxygen [13–16] as well as CO adsorption at UHV [17–19] conditions and in the mbar regime [20, 21] have been studied, but to our knowledge no *in situ* CO oxidation study has been published. At UHV conditions and low CO exposure, a $(\sqrt{3} \times \sqrt{3})$R30°-CO structure is formed similarly to that of other Pt-group metals [17]. At low temperature (<250 K), or at high exposure, a $(2\sqrt{3} \times 2\sqrt{3})$R30°-7CO structure is obtained with a coverage of 0.58 ML. The actual structure consists of hexagonal CO clusters containing seven CO molecules in atop position. In mbar pressure and at room temperature, these clusters are observed to grow to a size of 19 CO molecules adsorbed in a $(3\sqrt{3} \times 3\sqrt{3})$R30°-19CO structure with a coverage of 0.70 ML [20, 21]. Regarding oxygen exposure, low doses onto Ir(1 1 1) results in a p(2 × 2)-O structure, which transforms into a more dense p(2 × 1)-O structure at high oxygen exposure [12]. At O_2 pressures in the mbar regime, an IrO_2 surface oxide forms on Ir(1 0 0) [13] and Ir(1 1 1) [14]. This structure can also be formed at UHV conditions by employing oxygen plasma [15, 16]. Recently, it is found that this IrO_2 surface oxide is active for low-temperature methane activation [13]. Hence, an active surface oxide is formed on Ir in pure oxygen, but it remains an open question whether this oxide is also present at reaction conditions for the CO oxidation reaction in the MTL as reported for Pd and Rh surfaces, or if Ir behaves more like Pt(1 1 1), where metallic or chemisorbed O phases have been reported.

In this contribution we report on our APXPS and density functional theory (DFT) study on CO oxidation over Ir(1 1 1) and Pt(1 1 1). We find that the Ir(1 1 1) surface is covered by a chemisorbed oxygen phase in the MTL similar to that on Pt(1 1 1). A clear difference between the two surfaces is, however, that Pt(1 1 1) exhibits a sharp transition from a surface with adsorbed CO and without oxygen to an surface without CO and with oxygen—i.e. no coexistence of CO and oxygen is observed, while Ir(1 1 1) exhibits a smooth transition involving phases in which chemisorbed O and CO coexist. Our DFT calculations confirm that O_2 adsorption on Pt(1 1 1) is favourable only at CO coverages close to zero, while O_2 adsorption on Ir(1 1 1) is favourable for a CO coverage of about 0.4 ML at the experimentally studied reaction conditions. The calculations reveal that the reason for this difference is not caused by differences in O–CO interactions, which are found to be rather similar for the two metals, but to the overall stronger binding of O and CO to Ir(1 1 1) compared to Pt(1 1 1). The stronger O–Ir and CO–Ir interactions are sufficient to overcome the repulsive O–CO interaction found in high-coverage mixed adsorbate structures, allowing for the coexistence of O and CO on the Ir(1 1 1) surface at reaction conditions.

2. Experimental

The experiments were performed at the APXPS end station [9] of beamline I511 [22] on the MAX-II ring of the National Swedish Synchrotron Radiation Facility, the MAX IV Laboratory. The system has a base pressure in the low 10^{-10} mbar regime and is equipped with a SPECS Phoibos 150 NAP electron energy analyser. The analysis chamber hosts a dedicated reaction cell which allows for APXPS measurements at pressures up to 25 mbar when attached to the analyser. All ambient pressure x-ray (APXP) spectra were measured in normal emission geometry with 45° angle to the incoming photons. The Ir 4f spectra were acquired at a photon energy of 390 eV at an overall resolution of 360 meV, while the O 1s spectra were acquired at 650 eV at an overall resolution of 900 meV. All APXP spectra were calibrated to the Fermi energy measured directly after each spectrum. A polynomial background was removed from all O 1s spectra prior to curve fitting for which Voigt functions were used. Doniach-Šunjić functions convoluted with Gaussians were fitted to the Ir 4f lines together with a linear background.

The Pt(1 1 1) and Ir(1 1 1) single crystals were mounted on a transferrable stainless steel sample plate. The temperature was monitored with a chromel–alumel thermocouple spot welded to the side of the crystals. Both crystals were cleaned by 1.5 kV Ar^+ sputtering followed by annealing to 900 K. Before measurements the crystals were heated to 900 K in 10^{-7} mbar O_2 followed by vacuum annealing at 900 K for Ir(1 1 1) and 1000 K for Pt(1 1 1) in order to remove carbon from the surface. The cleanness of the surfaces was confirmed by XPS.

The pressure in the reaction cell was measured with a commercial Ceravac (CTR100) full range pressure gauge placed outside of the reaction cell on the exhaust pipe used for flow mode measurement. A pressure regulator on the exhaust pipe controlled in closed loop by the CTR100 pressure gauge ensured a constant gas pressure in the reaction cell. Gas inlet flows to the cell were controlled by commercial flow controllers (Brooks Instruments GF125 Analog I/O). Before entering the system, the CO gas passed through a commercial gaskleen II purifier manufactured by PALL, which removed volatile Ni carbonyls. Flows of 1.35–1.4 standard-cubic-centimeters per minute (sccm) O_2—where standard refers to 1 bar and 25 °C—and 0.15 sccm CO were employed over both crystals. In the Pt(1 1 1) case, a constant total pressure of 0.25 mbar with

resulting partial pressures of 0.225 mbar O_2 and 0.025 mbar CO was used while in the Ir(1 1 1) case a constant total pressure of 0.5 mbar was used, yielding partial pressures of 0.45 mbar O_2 and 0.05 mbar CO.

A small fraction of the outlet gas from the cell was leaked into a small UHV chamber through a leak valve. This small chamber is equipped with a Dycor LCD residual gas analyser used to measure the time-resolved partial pressure of CO, O_2, and CO_2 simultaneously. As the base pressure of this chamber with the leak valve fully closed was observed to decrease as function of time, most likely due to CO degassing from the filament of the residual gas analyser and due to prior pressure variations within the chamber originating from adjusting the leak rate into the chamber, we subtracted an exponential background from the measured partial pressures. Finally, the partial pressures within the cell were calculated from the total pressure measured by the CTR100 gauge and the background corrected partial pressures measured by the residual gas analyser assuming a constant calibration factor (i.e. gas diffusion and pumping are assumed to be identical for CO, O_2, and CO_2).

3. Computational details

The DFT calculations were performed with the plane-wave code Quantum ESPRESSO [23] (PWSCF v.5.0.2, svn rev. 10452) using ultrasoft pseudopotentials[5]. Electronic exchange and correlation effects were described using the RPBE functional [24]. Like most DFT functionals, the RPBE functional predicts the low-coverage adsorption site for CO on Pt(1 1 1) to be the fcc hollow site [25, 26], while experiments have identified the adsorption site as the atop site [27]. Still, the RPBE functional is one of the most accurate functionals for the overall adsorption energy of CO on Pt(1 1 1) [26], and at higher coverages it correctly identifies the preference for atop-bridge adsorption sites over fcc-hcp adsorption sites [25]. For CO on Ir(1 1 1) the RPBE functional predicts atop adsorption site [28] in agreement with experimental investigations [21].

The calculations for Ir(1 1 1) and Pt(1 1 1) were carried out as periodic slab calculations using DFT-optimized lattice constants (Pt: 4.016 Å, Ir: 3.902 Å), various unit cell sizes (see below) and four metal layers. The two bottom layers were kept fixed at their bulk-truncated positions, while the two top layers and all adsorbates were relaxed until the maximum force on each atom fell below 0.05 eV $Å^{-1}$. A vacuum region of 12 Å perpendicular to the surface separated the slab from its periodic images and a dipole correction was applied [29]. The Brillouin zone was sampled with a (4×4) $\boldsymbol{k}$-point grid for the smallest (3×3) and $(2\sqrt{3} \times 2\sqrt{3})$ supercells and a (2×2) $\boldsymbol{k}$-point grid for the larger (4×4) and $(\sqrt{19} \times \sqrt{19})$ supercells. Cutoffs of 500 eV and 5000 eV were used for the orbitals and the charge density, respectively. Vibrational zero-point energies (ZPEs) of O and CO were calculated in the harmonic approximation as implemented in the atomic simulation environment (ASE) code [30] at a coverage of 0.11 monolayers (ML). The ZPEs were assumed to be coverage independent.

Differential CO adsorption energies $\Delta E_{CO}^{diff.}$ are calculated according to the formula:

$$\Delta E_{CO}^{diff.} = E_{surf,nCO} - E_{surf,(n-1)CO} - E_{CO(g)},$$

where $E_{surf,nCO}$ ($E_{surf,(n-1)CO}$) is the energy of the Pt(1 1 1) or Ir(1 1 1) surface with n ($n-1$) adsorbed COs and $E_{CO(g)}$ is the energy of a gas phase CO molecule.

The temperature at which CO desorption becomes significant is estimated as the temperature where the transition state theory expression for the CO desorption rate constant $k_{CO}^{des.}$, which is given as

$$k_{CO}^{des.} = \frac{k_B T}{h} e^{\frac{\Delta E_{CO}^{diff.\,ZPE}}{k_B T}},$$

reaches a significant value (e.g. $1\,s^{-1}$). Here k_B is the Boltzmann constant, T is the temperature, h is Planck's constant and $\Delta E_{CO}^{diff.\,ZPE}$ is the ZPE-corrected differential CO adsorption energy (equal to the negative of the desorption energy). However, for finite CO pressures also CO adsorption will occur, which in our case shifts the temperature at which a given CO is expected to vacate the surface to higher temperatures. We assume that CO adsorption and desorption at these higher temperatures are in equilibrium, which allows us to estimate the vacancy formation temperature for a given CO as the temperature where the Gibbs free energy of adsorption becomes zero. Gibbs free energies of gas phase molecules were calculated in the ideal gas approximation using the ASE thermochemistry module and experimental vibrational frequencies from [31].

O_2 dissociative adsorption energies are calculated according to the formula:

$$\Delta E_{O_2}^{ads.} = E_{surf,nCO,2O} - E_{surf,nCO} - E_{O_2(g)},$$

where $E_{surf,nCO}$ ($E_{surf,nCO,2O}$) is the energy of the Pt(1 1 1) or Ir(1 1 1) surface with nCOs (nCOs and 2O atoms) adsorbed and $E_{O_2(g)}$ is the energy of an O_2 gas phase molecule.

4. Results and discussion

CO oxidation over Pt(1 1 1) in the mbar regime has been studied before with APXPS as discussed in the introduction [9, 10], but since it is here used as a reference system for CO oxidation on Ir(1 1 1) we discuss it in some detail. Figure 1 compares selected O 1s APXP spectra, reactivity data, and work function measurements for CO oxidation over Pt(1 1 1) and Ir(1 1 1). These data were recorded in a flow of O_2 and CO maintaining a 9:1 mixture (see experimental for details) while stepwise heating the Ir(1 1 1) surface in steps of 25–50 K and continuously heating the Pt(1 1 1) surface at a rate of 4 K min^{-1}.

Beginning with the O 1s spectra acquired at 450 K and 500 K for Pt(1 1 1) (figure 1(a)); four components are observed. The components located at binding energies of 539 eV (O_{2a}) and 537.9 eV (O_{2b}) are assigned to molecular O_2 in the gas phase. The splitting of 1.1 eV between these two components

[5] Ultrasoft pseudopotentials are taken from the Quantum ESPRESSO pseudopotential library and were generated using the 'atomic' code by A Dal Corso in 2012 (v.5.0.2 svn rev. 9415).

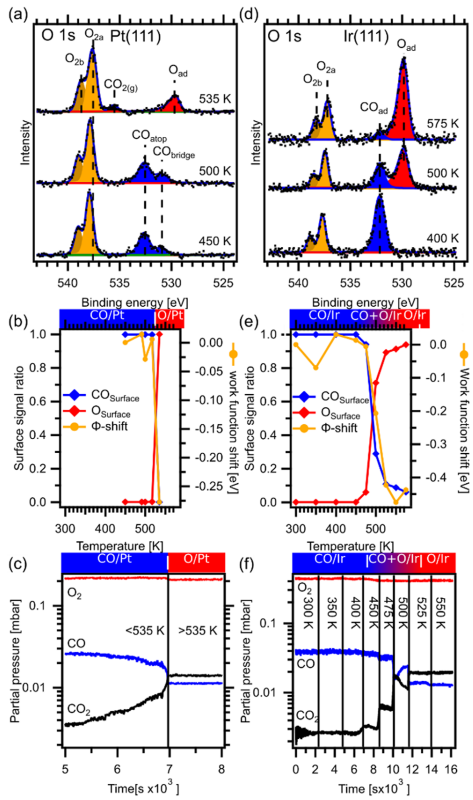

Figure 1. (a) O 1s APXP spectra acquired in a CO:O_2 mixture over Pt(1 1 1) at different temperatures, (b) the ratio between the surface species and the shift in O_2 binding energy calculated from the deconvolution of the O 1s APXP spectra, and (c) Pt(1 1 1) reactivity data. Panels (d)–(f) show the corresponding figures for Ir(1 1 1).

is a result of the coupling of the core hole to the valence state of the O_2 molecule. The corresponding CO gas phase component expected at 536.8 eV (−1.1 eV with respect to O_{2b}) [4], is hidden by the large O_{2a} and O_{2b} components and it is therefore not included in the curve fitting of the spectrum. The two remaining components located at 532.6 eV and 530.9 eV are assigned to CO adsorbed in atop (CO_{atop}) and bridge (CO_{bridge}) sites, respectively, in agreement with previous work on CO adsorption structures formed at UHV [32] and mbar [33] conditions. No chemisorbed O species are found in the O 1s spectra acquired 450 K and 500 K.

At 535 K the O 1s spectrum changes dramatically. The binding energy of the two O_2 gas phase components (O_{2a} and O_{2b}) both shift by −0.4 eV indicating that the surface work function changes by this amount, neglecting the small difference caused by the potential difference from the sample surface to the gas volume probed [34] and space-charge effects. Furthermore, the CO_{atop} and CO_{bridge} components vanish. Additionally, two new components develop: one at 535.6 eV assigned to CO_2 in the gas phase ($CO_{2(g)}$) and another one at 529.8 eV assigned to chemisorbed O (O_{ad}) bound in threefold hollow sites on the Pt(1 1 1) surface [32]. Clearly, the CO_2 production observed in the gas phase coincides with the change from a CO covered surface to an oxygen-covered surface.

Deconvolution of the corresponding Pt $4f_{7/2}$ spectrum acquired at 535 K (see figure S1 in the SI (stacks.iop.org/JPhysCM/00/0000/mmedia)) reveals a significantly reduced surface component (Pt_{surf}) and development of an oxygen-induced component (Pt_O) shifted by +0.62 eV with respect to the surface component. These Pt surface atoms form bonds with O atoms adsorbed in the hollow site [32]. From the relative intensity ratio between the Pt_O and Pt_{surf} components and from the knowledge of hollow adsorption site of the O atoms we estimate the total oxygen coverage to be (0.21 ± 0.02) ML at 535 K, close to the theoretical coverage of 0.25 ML of a p(2 × 2)-O structure [32]. Further, we note that we do not find any support for oxidation of the Pt(1 1 1) surface at our experimental conditions for the CO oxidation reaction even though the gas phase just above the surface is CO depleted in our case and oxidation has been observed before on Pt(1 1 1) in pure oxygen [11].

The above discussed qualitative observations of the O 1s spectra acquired at different temperatures are quantified by curve fitting all the O 1s spectra acquired (see figure S2(a)) and plotting the relative intensities of the chemisorbed CO (CO_{atop} + CO_{bridge}) and O (O_{ad}) components together with the work function shift of the O_2 gas phase components (O_{2a} and O_{2b}) as a function of temperature, see figure 1(b). The surface changes quickly from CO to O covered and from our data, a co-existing structure of adsorbed CO and O at any temperature can be excluded. The transition occurs between 520 K and 535 K, i.e. within a 15 K window. Additionally, the work function shift clearly correlates with the phase change.

Using the estimated oxygen coverage at 535 K as an internal absolute coverage calibration and using the O_2 gas phase components as internal intensity calibration it is possible to calculate the CO coverage from the O 1s spectra acquired at temperatures below 535 K (see figure S3). This analysis reveals an approximately constant CO coverage of (0.33 ± 0.06) ML between 450 and 500 K. At 517 K the coverage drops to (0.25 ± 0.05) ML and at 535 K no CO is found on the surface.

CO adsorption on Pt(1 1 1) has been studied previously both at UHV conditions and in the mbar regime. The UHV studies revealed the following structures and site coverages: p(4 × 4)—3/16 atop—0.19 ML, c(4 × 2) or c($\sqrt{3}$ × 2)rect—2/8 atop and 2/8 bridge—0.50 ML [32, 35], c($\sqrt{3}$ × 5)rect—4/10 atop, 2/10 bridge—0.60 ML, c($\sqrt{3}$ × 3)rect—3/6 atop and 1/6 bridge—0.66 ML, c($\sqrt{3}$ × 7)rect—8/14 atop and 2/14 bridge—0.71 ML [36, 37]. Dense hexagonal and pressure dependent moiré structures with continuously varying coverages are formed at higher pressures between 10^{-6} mbar and 1000 mbar [37] The most dense structure is a ($\sqrt{19}$ × $\sqrt{19}$) R23.4°-13CO structure—7/19 atop and 6/19 bridge—0.68 ML, and this phase has recently been confirmed in an APXPS study performed at room temperature [33].

Comparing the experimentally determined CO coverage of (0.33 ± 0.06) ML at 450–500 K and (0.25 ± 0.05) ML at 517 K with the known structures discussed above, coexistence of the p(4 × 4) phase with a 0.19 ML atop coverage and the c(4 × 2) phase with 0.25 ML atop and 0.25 ML bridge coverage fits best with our experimental data. We note that without any structural characterization it is impossible to say whether these phases really form or if we just have disordered surface structures. It is, however, clear that compared to the previous APXPS study [33] of Pt(1 1 1) in pure CO at room temperature where a dense ($\sqrt{19} \times \sqrt{19}$)R23.4°-13 phase with 0.68 ML coverage was found; the CO phases formed at 450 K and above in our CO:O_2 mixtures have coverages closer to the low-coverage structures observed in UHV. This makes very much sense as CO desorption from Pt(1 1 1) starts just above room temperature with the main desorption peak centred around 410 K [38]. At temperatures above 450 K we therefore expect the CO on the surface to be in equilibrium with the CO in the gas phase.

We now turn to the reactivity data displayed in figure 1(c) and acquired simultaneously with the APXPS data. Here, the rapid change from a CO-covered surface to an O-covered surface is mirrored as we observe no, or very low, activity below 530 K. At about 530 K there is a large increase in the CO_2 signal and a simultaneous decrease in the CO signal, which shows that the surface transitions directly from an inactive CO-poisoned state to an active phase where the large majority of the surface is oxygen-covered. This behaviour is identical to that of the Pd(1 0 0) surface; at the mass transfer limit the Pd(1 0 0) surface is, however, oxidized, whereas in the case of Pt(1 1 1) the surface species are chemisorbed O atoms adsorbed in the threefold hollow sites.

Last we compare our work to the published APXPS work by Calderón *et al* on CO oxidation over Pt(1 1 1) [10]. In agreement with our work, they found CO adsorbed at bridge and atop sites at moderate temperatures in a CO:O_2 mixture of 1:10 and a total pressure of 1.1 mbar. Upon increasing the temperature, the CO coverage decreased and the CO_2 production slowly increased and at 563 K they observed a dramatic increase of CO_2 in the gas phase in reasonable agreement with our value of 530 K. The authors concluded, however, that the surface is adsorbate-free when it is highly active and within the MTL. In contrast, we find clear evidence for adsorbed oxygen, with a coverage close to a p(2 × 2)-O structure, in the MTL both in the O 1s and Pt 4f spectra at almost identical pressures and gas mixtures as Calderón *et al* used. We can only speculate about the reason for the disagreement, but we find it likely that a surface structure with an oxygen coverage close to the one of a p(2 × 2)-O structure also formed in their study. This phase might have been invisible in their O 1s spectra due to a quite high detection limit (~0.15 ML) of their instrument, which the authors mention themselves [10].

The corresponding CO oxidation data for Ir(1 1 1) are shown in figures 1(d)–(f). Beginning with the O 1s spectra acquired at 400 K in panel (d) three peaks are observed. The two components at 538.8 eV (O_{2a}) and 537.7 eV (O_{2b}) are assigned to gas phase O_2 in accordance with the Pt(1 1 1) case, while the last component at 532.2 eV is assigned to CO molecules adsorbed in atop positions (CO_{ad}) [21]. We note that the ratio between the adsorbed CO and gas phase O_2 components is larger as compared to the data for Pt(1 1 1) displayed in panel (a) even though the total pressure is higher in the Ir(1 1 1) experiment. This difference is caused by a slightly different cone-sample distance, but it does not affect any of our conclusions. No chemisorbed O species are found and we therefore conclude that only CO is adsorbed at 400 K. Upon increasing the temperature to 500 K a shift of −0.2 eV is seen in the binding energies of the components assigned to O_2 indicating a surface work function shift. Further, the intensity of the CO_{ad} component is reduced and a new component is seen at 529.9 eV. This component is assigned to O adsorbed in threefold hollow sites on the Ir(1 1 1) surface (O_{ad}) [12]. As the CO_{ad} and the O_{ad} components are observed in the same spectrum we conclude that chemisorbed CO and O coexists on the Ir(1 1 1) surface at 500 K in contrast to the Pt(1 1 1) case where we never observed coexistence of CO and O. After further heating the Ir(1 1 1) surface to 575 K, the gas phase O_2 components shift further by −0.3 eV and the intensity of the CO_{ad} component is reduced further. Now, the surface is almost completely O covered and only a small signal from adsorbed CO remains.

Analogous to the Pt(1 1 1) case, figure 1(e) shows the relative intensities of the adsorbed species (CO_{ad} and O_{ad}) and the work function shift as measured from the O_2 gas phase components as a function of temperature (for curve fitted O 1s spectra see figure S2(b)). Inspection of this figure clearly demonstrates that adsorbed CO and O coexists on the surface and that the transition from a CO to O covered surface occurs in a large 100 K interval (between 450 K and 550 K). Further, the surface work function correlates with the intensity of the O_{ad} components which gives further evidence for a continuously changing surface structure. This is in contrast to the phase transition from a pure CO to pure O covered Pt(1 1 1) surface.

Finally, we address the activity data for Ir(1 1 1) displayed in figure 1(f). Three different temperature regimes can be observed: (i) in the CO/Ir region (below 450 K) no CO_2 production is observed. In this region the surface is completely covered by CO and inactive, i.e. CO poisoned. (ii) Stepwise temperature increase (450 K, 475 K, and 500 K) in the CO + O/Ir region leads to a stepwise increase in CO_2 production. In this region the CO_2 turnover is highly dependent on temperature. By plotting the increase in CO_2 partial pressure against the inverse of the temperature (see figure S4) and fitting the Arrhenius equation to this data, we approximate the activation energy for CO oxidation over Ir(1 1 1) at the present conditions to be 1.04 eV. (iii) Finally, in the O/Ir region (above 525 K) the reaction reaches the mass transfer limit and the CO_2 production does not increase any further when the sample temperature is increased to e.g. 575 K.

From the above discussion the following can be concluded: In the case of Pt(1 1 1) there is a sharp transition from an inactive CO covered surface into a mass transfer-limited active surface that is covered by O with no observed coexistence of adsorbed CO and O. In contrast, the transition from inactive and CO-covered Ir(1 1 1) surface to mass transfer limited surface involves phases of coexisting chemisorbed CO and O.

Indeed, the Ir surface is only O dominated at the mass transfer limit. Hence, the Ir(1 1 1) surface only becomes depleted of CO if the gas just above the surface is fully depleted of CO as a consequence of the fast oxidation taking place on the surface.

To deduce adsorbate coverages, we now direct our attention to the Ir $4f_{7/2}$ APXP spectra. All acquired Ir $4f_{7/2}$ spectra were fitted by five components over the total temperature range. These components correspond to bulk atoms (Ir_B—60.9 eV), clean surface atoms (Ir_S—60.3 eV), surface atoms bound to CO_{atop} (Ir_{CO}—61.1 eV), and surface atoms bound to one O_{ad} atom (Ir_{O1}—60.7 eV) or two O_{ad} atoms (Ir_{O2}—61.1 eV). All spectra were fitted using a global algorithm allowing for simultaneous fitting of all Ir $4f_{7/2}$ spectra with correlated coefficients (see figure S5). In all spectra, the binding energies for the corresponding components were set to be the same while the intensity was allowed to vary within restrictions. The intensity of all components was restricted so that the ratio between the bulk component intensity (I_B) and the sum of the surface component intensities ($I_S + I_{CO} + I_{O1} + I_{O2}$) remained the same for all spectra. In addition, we know the coverage ratio between oxygen and CO $\left(\frac{\theta_O}{\theta_{CO}}\right)$ from our deconvolution of the O 1s spectra. The oxygen and CO coverage can also be found from the Ir 4f spectra. Since CO adsorbs in atop sites, the coverage of CO is calculated by $I_{CO}/(I_{CO} + I_S + I_{O1} + I_{O2})$. In the O case, the coverage is calculated by $(I_{O1}/3 + 2 \times I_{O2}/3)/(I_{CO} + I_S + I_{O1} + I_{O2})$ since O adsorbs in threefold hollow sites. Combining these three equations the following constraint for the I_{O1} intensity is obtained: $I_{O1} = 3I_{CO} \cdot \frac{\theta_O}{\theta_{CO}} - 2I_{O_2}$. This constraint ensures that the relative CO and O coverages calculated from the Ir 4f curve fitting are identical to the ones obtained from the O 1s curve fitting. Finally, we note that this way of constraining the curve fitting has the benefit that the contribution to the Ir 4f signal from Ir_{CO} and Ir_{O2}, which appear at identical binding energies, can be distinguished. The spectra measured at 300 K, 450 K, and 500 K are shown in figure 2(a), demonstrating the fit results for the CO/Ir (bottom spectrum), CO + O/Ir (middle spectrum), and O/Ir (top spectrum) regions, while all spectra are shown in figure S5.

From the Ir 4f curve fitting presented in figure S5, the absolute coverages of adsorbed CO and O can be calculated as discussed above. The measured CO and O coverages as a function of the surface temperature are shown in figure 2(b). The CO coverage at room temperature is about (0.7 ± 0.03) ML, and with increasing temperature the CO coverage diminishes as follows: $(0.54 \pm 0.02)/(0.41 \pm 0.03)/(0.15 \pm 0.02)/(0.03 \pm 0.01)$ ML at 450/475/500/575 K, respectively. At 475 K and above, chemisorbed O is observed at the following increasing coverages: $(0.03 \pm 0.06)/(0.28 \pm 0.06)/(0.4 \pm 0.04)$ ML at 475/500/575 K, respectively.

In light of the above stated CO coverages likely adsorbate structures will be discussed. Ball models of the $(3\sqrt{3} \times 3\sqrt{3})$R30°-19CO and $(2\sqrt{3} \times 2\sqrt{3})$R30°-7CO structures discussed in the introduction and the p(2 × 2)-O and p(2 × 1)-O structures are shown in figure 2(c). Their

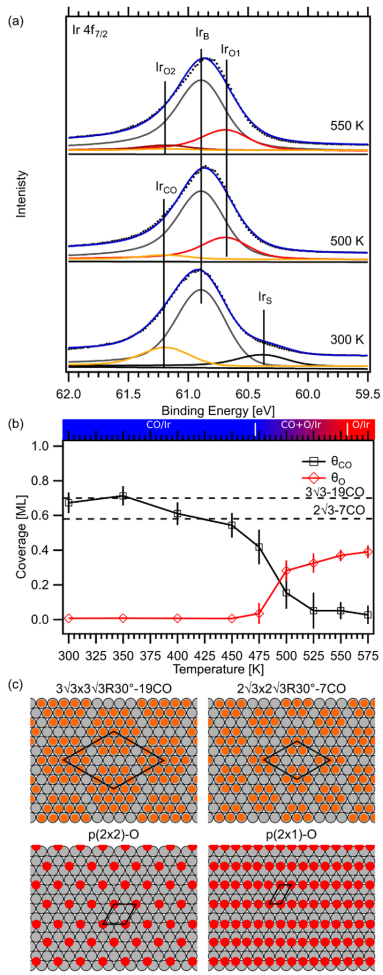

Figure 2. (a) Ir $4f_{7/2}$ APXP spectra acquired at 300 K, 500 K, and 550 K, (b) coverage of CO and O for all measured temperatures. (c) Ball model of dense CO and O structures.

respective theoretical coverages are 0.7 ML, 0.58 ML, 0.25 ML, and 0.5 ML. The coverage of the $(3\sqrt{3} \times 3\sqrt{3})$R30°-19CO phase agrees with the CO coverage from the Ir 4f spectra below 400 K; thus we conclude that we observe the same CO coverage in a O:CO mixture as in pure CO at room temperature [21]. Between 400 K and 450 K the coverage agrees with that of the $(2\sqrt{3} \times 2\sqrt{3})$R30°-7CO structure, i.e. temperatures above 400 K destabilize the high density $(3\sqrt{3} \times 3\sqrt{3})$R30°-19CO structure. At the onset of CO oxidation, the (0.41 ± 0.03) ML CO coverage could agree with a $(2\sqrt{3} \times 2\sqrt{3})$R30°-7CO structure with two removed CO molecules. The removal of these molecules would thus make

sufficient room for O_2 adsorption and dissociation, as seen by the co-existence of chemisorbed O in both the O 1s and the Ir 4f APXP spectra. At 500 K, the (0.28 ± 0.06) ML O coverage fits with the coverage of a p(2 × 2)-O structure found for O over Ir(1 1 1) [12]. This structure contains one Ir atom per unit cell not bound to O, which accommodates a CO_{atop} species since no Ir_S component is seen at these temperatures. However, the (0.15 ± 0.02) ML coverage is less than one CO per (2 × 2) unit cell. At increasing temperature the O coverage increases suggesting the formation of a slightly more dense p(2 × 1)-O structure as seen from the occurrence of the Ir_{O2} component [12]. However, the O structure does not reach full coverage which is attributed to the ongoing CO oxidation.

From the above discussed Ir 4f spectra we conclude that the surface is covered by a CO phase fitting a $(3\sqrt{3} \times 3\sqrt{3})$R30°-19CO at room temperature, but is re-structured to the slightly less dense phase fitting a $(2\sqrt{3} \times 2\sqrt{3})$R30°-7CO structure at moderate temperature. At the transition to the active state a phase with a CO coverage matching a $(2\sqrt{3} \times 2\sqrt{3})$R30°-CO structure with defects covers the majority of the surface along with co-adsorbed O. Further heating transforms the surface to a phase having a coverage close to a p(2 × 2)-O structure with co-adsorbed CO on the unbound Ir atom. At the mass transfer limit in O rich conditions at 0.5 mbar, the oxygen coverage suggests a p(2 × 1)-O structure with defects.

4.1. DFT calculations for Pt(1 1 1)

As we found experimental CO coverages between 0.4 and 0.25 ML (see figure S3) we begin our theoretical work by investigating the stability of the CO structures shown in figures 3(a)–(c) with coverages of 0.68 ML, 0.50 ML, and 0.19 ML [32, 33, 35], respectively, by calculating the differential CO adsorption energies (see table 1). The calculations illustrate the well-known repulsive interactions between COs in high-coverage structures, which reduce the CO binding from about 1.4 eV at low coverage to about 0.77 eV at the highest coverage of 0.68 ML. These values are further reduced by the vibrational zero-point energy (ZPE) which we estimate to be around 0.21 eV/CO. Using the ZPE-corrected differential CO adsorption energies we estimate the CO vacancy formation temperature as the temperature where the Gibbs free energy of CO adsorption becomes zero. The entropy of gas phase CO is calculated for the experimentally used CO pressure of 0.02 mbar, while the entropy of adsorbed CO is neglected. The resulting vacancy formation temperatures (see table 1) of 425 K (470 K) for the 0.50 ML (0.19 ML) structure are in reasonable agreement with the experimental measurement of a CO coverage of 0.33 ML at 450–500 K, keeping in mind that a DFT error on the CO adsorption energy of 0.1 eV would result in a temperature shift of about 30 K.

Having confirmed that the CO coverage on Pt(1 1 1) will be close to zero at the experimentally observed transition to the active state at around 520 K, we proceed to calculate the O_2 dissociative adsorption energy for the clean (4 × 4) Pt(1 1 1) surface and for the 0.19 ML CO structure. We assume that O_2 dissociates into two neighbouring O atoms adsorbed in fcc sites as shown in figure 3(c). The dissociative adsorption energies shown in table 1 are further reduced by the vibrational ZPE which we estimate to be around 0.06 eV/O. From these energies the repulsive CO–O interaction energy in the mixed adsorbate structure can be calculated to 0.18 eV/O. Since barriers for O_2 adsorption onto Pt(1 1 1) have been found to be rather low (about 0.3–0.4 eV) and fairly independent of the CO coverage [39, 40], we assume that O_2 adsorption and desorption at 520 K are equilibrated. The Gibbs free energies of adsorption are calculated in the same way as described for CO and are presented in table 1 for an O_2 pressure of 0.2 mbar and a temperature of 520 K. It is seen that O_2 adsorption only becomes favourable for CO coverages between 0–0.19 ML, which is in good agreement with the experimental observation that no mixed O–CO adsorbate structures form.

Table 1. Calculated differential CO adsorption energies $\Delta E_{CO}^{diff.}$ (in eV, excl. ZPEs), CO vacancy formation temperatures $T_{CO}^{vac.}$ (in K) calculated (incl. ZPEs) for a CO pressure of 0.02 mbar, O_2 dissociative adsorption energies $\Delta E_{O_2}^{ads.}$ (in eV, excl. ZPEs) and Gibbs free energies of dissociative O_2 adsorption $\Delta G_{O_2}^{ads.}$ (in eV) calculated (incl. ZPEs) for an O_2 pressure of 0.2 mbar and a temperature of 520 K for Pt(1 1 1) at various CO coverages θ_{CO} (in ML).

θ_{CO}	0.68	0.50	0.19	Clean
$\Delta E_{CO}^{diff.}$	−0.77	−1.25	−1.39	—
$T_{CO}^{vac.}$	270	425	470	—
$\Delta E_{O_2}^{ads.}$	—	—	−1.39	−1.74
$\Delta G_{O_2}^{ads.}$	—	—	0.06	−0.29

4.2. DFT calculations for Ir(1 1 1)

For Ir(1 1 1) the experimental determined CO coverage fits that of a $(2\sqrt{3} \times 2\sqrt{3})$R30°-7CO structure with defects at the transition to the active state at a temperature of about 475 K. We therefore concentrate our DFT calculations on this structure. The differential CO adsorption energies for various COs as labelled in figure 3(d) and the vacancy formation temperatures are shown in table 2. The CO vibrational ZPE on Ir is found to be around 0.21 eV, which is the same as the value found on Pt. The data show that single CO vacancies are expected to form from about 420 K (central CO in cluster) to about 465 K (edge CO). This is in good agreement with the experimentally measured temperature-dependent coverages in figure 2(b), where it is seen that the coverage drops below the 0.58 ML expected for the $(2\sqrt{3} \times 2\sqrt{3})$R30°-7CO structure at around 425 K. Since only desorbed edge COs are expected to make room for O_2 adsorption (see figure 3(e)), we use this structure as the starting point for investigating the differential adsorption energy of a second CO (see table 1). The structure with the least strongly bound second CO removed is shown in figure 3(f). This structure is expected to form at about 475 K, which is also in very good agreement with the experimental data in figure 2(b).

For the relevant structures with one and two COs removed, we calculate the O_2 dissociative adsorption energy and the Gibbs free energy of O_2 adsorption for an O_2 pressure of 0.4 mbar and a temperature of 475 K. Also for Ir(1 1 1), barriers

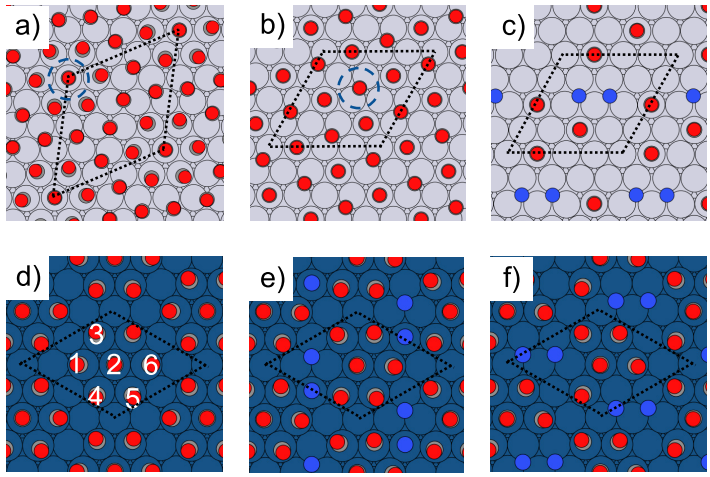

Figure 3. DFT-optimized structures of the experimentally observed CO adsorption structures on Pt(1 1 1) at a CO coverage of (a) 0.68 ML, (b) 0.50 ML, and (c) 0.19 ML. In (a) and (b) the least bound CO is highlighted by a dashed blue circle. In (c) is also indicated the adsorption of two O atoms in neighbouring fcc sites (individual O atoms are shown in light blue, whereas O atoms in CO are shown in red). The lower panels show (d) the experimentally observed $(2\sqrt{3} \times 2\sqrt{3})$R30°-7CO structure on Ir(1 1 1), (e) the structure in (d) with CO (1) desorbed and two O atoms adsorbed in fcc and atop positions, and (f) the structure in (d) with COs (1,5) desorbed and two O atoms adsorbed in neighbouring fcc sites. The used DFT supercells are indicated with dashed black lines.

Table 2. Calculated differential CO adsorption energies $\Delta E_{CO}^{diff.}$ (in eV, excl. ZPEs) for COs in the $(2\sqrt{3} \times 2\sqrt{3})$R30°-7CO structure on Ir(1 1 1) (the CO labels are indicated in figure 3(d)), CO vacancy formation temperatures $T_{CO}^{vac.}$ (in K) calculated (incl. ZPEs) for a CO pressure of 0.04 mbar, O_2 dissociative adsorption energies $\Delta E_{O_2}^{ads.}$ (in eV, excl. ZPEs) and Gibbs free energies of dissociative O_2 adsorption $\Delta G_{O_2}^{ads.}$ (in eV) calculated (incl. ZPEs) for an O_2 pressure of 0.4 mbar and a temperature of 475 K for O_2 adsorption onto defected CO structures with COs desorbed according to the given CO labels.

CO labels	(1)	(2)	(1) → (1,3)	(1) → (1,4)	(1) → (1,5)	(1) → (1,6)
$\Delta E_{CO}^{diff.}$	−1.36	−1.22	−1.43	−1.44	−1.40	−1.42
$T_{CO}^{vac.}$	465	420	490	490	475	485
$\Delta E_{O_2}^{ads.}$	−1.27	—	—	—	−2.35	—
$\Delta G_{O_2}^{ads.}$	0.04	—	—	—	−1.04	—

for O_2 adsorption have been found to be very small (about 0.06 eV) [41], which allows us to focus only on the thermodynamics of O_2 adsorption. The O vibrational ZPE on Ir is found to be around 0.08 eV, which is similar to the value found on Pt. The structures considered are shown in figures 3(e) and (f) and the energies are given in table 2. The data show that O_2 adsorption is slightly unfavourable for the structure with only one CO removed, but highly favourable for the structure with two COs removed. Hence, our DFT calculations corroborate the experimental suggestion that a defected $(2\sqrt{3} \times 2\sqrt{3})$R30°-(7-2)CO structure forms along with co-adsorbed O at the transition to the active phase for CO oxidation.

4.3. Comparison of Ir(1 1 1) and Pt(1 1 1)

The experimental measurements and DFT calculations presented so far demonstrate very different behaviours of the Pt(1 1 1) and the Ir(1 1 1) surface at the transition from the CO-poisoned to the active state of the catalyst. Whereas on Pt all COs have to desorb from the surface before O_2 adsorption becomes favourable, the Ir surface allows for a coexistence of CO and O on the surface. These differences could arise either from the stronger adsorption of O and CO on Ir as compared to Pt or to differences in the O–CO repulsive interactions in the mixed structures. On Pt the repulsive O–CO interaction energy in the mixed structure formed by adsorbing O_2 onto the 0.19 ML CO structure (see figure 3(c)) was calculated to 0.18 eV/O. When calculating the corresponding structures on Ir(1 1 1) we arrive at a repulsive CO–O interaction energy of 0.10 eV/O. In comparison, the adsorption energies of isolated CO molecules or O atoms calculated using (3×3) supercells vary a lot more. CO adsorption energies amount to −1.36 eV (Pt) and −1.71 eV (Ir), while O adsorption energies amount to −0.80 eV (Pt) and −1.41 eV (Ir) with respect to O_2 in the gas phase. We therefore conclude that the important difference between Ir and Pt is the much stronger binding of CO and O to Ir as compared to Pt, which is sufficient to overcome the repulsive CO–O interactions and allows for mixed CO–O adsorbate structures to form on Ir(1 1 1).

5. Conclusion

We have studied the oxidation of CO over Ir(1 1 1) using APXPS and DFT and compared it to the oxidation of CO over Pt(1 1 1). While the Pt(1 1 1) surface exhibits a sharp step-like transition from CO poisoned to mass transfer-limited activity, the Ir(1 1 1) surface shows a stepwise increase in activity between 450 and 525 K after which the MTL is reached. The difference is explained in terms of the adsorption energies of O and CO on the Pt(1 1 1) and Ir(1 1 1) surfaces. In the Pt(1 1 1) case, co-existence of adsorbed O and CO is unfavourable as the adsorption energies of CO and O are small compared to the CO–O repulsive interaction, resulting in the sharp phase transition observed with APXPS. On Ir(1 1 1) the O and CO adsorption energies are large enough to overcome the CO–O repulsive interaction, which explains the observed co-existence. Based on comparison to previous experimental structure determinations [12, 20, 21], since we do not have any structural characterizations ourselves, the following adsorbate structures are suggested. At room temperature, the Ir(1 1 1) surface is covered by the $(3\sqrt{3} \times 3\sqrt{3})$R30°-19CO structure which turns into the $(2\sqrt{3} \times 2\sqrt{3})$R30°-7CO structure at moderate temperature. At the transition to the active state, a $(2\sqrt{3} \times 2\sqrt{3})$R30°-(7-2) CO structure with defects forms, which allows sufficient room for O_2 to adsorb dissociatively. Further heating results in a $p(2 \times 2)$-O-covered surface with CO adsorbed at atop sites in the non-O-bonded Ir atoms. At the MTL a $p(2 \times 1)$-O structure containing defects covers the Ir(1 1 1) surface. Thus, we have assigned the surface structures preceding and during CO oxidation over Ir(1 1 1) at ambient pressure.

Our study unambiguously demonstrates that the surface phase at the MTL is predominately chemisorbed O at the employed conditions (0.5 mbar, 1.35 sccm O_2 and 0.15 sccm CO) and we can exclude any major IrO_2 formation. This is in contrast to both Rh and Pd, where oxide formation has been observed at the MTL and where a rapid switching from a CO poisoned to an oxidized surface occurs.

Acknowledgments

The staff at the MAX IV Laboratory is hereby gratefully acknowledged for their assistance during the beamtime. JK is grateful for support from project grant 2012-3850 financed by the Swedish Research Council.

ORCID iDs

N Johansson https://orcid.org/0000-0002-1402-1502
M Andersen https://orcid.org/0000-0002-9943-1534
J Schnadt https://orcid.org/0000-0001-9375-831X

References

[1] Gustafson J, Westerström R, Balmes O, Resta A, van Rijn R, Torrelles X, Herbschleb C T, Frenken J W M and Lundgren E 2010 *J. Phys. Chem.* C **114** 4580
[2] Gustafson J, Westerström R, Mikkelsen A, Torrelles X, Balmes O, Bovet N, Andersen J N, Baddeley C J and Lundgren E 2008 *Phys. Rev.* B **78** 045423
[3] Gustafson J, Blomberg S, Martin N M, Fernandes V, Borg A, Liu Z, Chang R and Lundgren E 2014 *J. Phys.: Condens. Mater* **26** 055003
[4] Blomberg S *et al* 2013 *Phys. Rev. Lett.* **110** 117601
[5] Fernandes V R, Bossche M V d, Knudsen J, Farstad M H, Gustafson J, Venvik H J, Grönbeck H and Borg A 2016 *ACS Catal.* **6** 4154
[6] Toyoshima R, Yoshida M, Monya Y, Kousa Y, Suzuki K, Abe H, Mun B S, Mase K, Amemiya K and Kondoh H 2012 *J. Phys. Chem.* C **116** 18691
[7] van Rijn R, Balmes O, Resta A, Wermeille D, Westerström R, Gustafson J, Felici R, Lundgren E and Frenken J W M 2011 *Phys. Chem. Chem. Phys.* **13** 13167
[8] Hendriksen B L M, Bobaru S C and Frenken J W M 2004 *Surf. Sci.* **552** 229
[9] Schnadt J *et al* 2012 *J. Synchrotron Radiat.* **19** 701
[10] Krick Calderón S, Grabau M, Óvári L, Kress B, Steinrück H P and Papp C 2016 *J. Chem. Phys.* **144** 044706
[11] Miller D J, Öberg H, Kaya S, Sanchez Casalongue H, Friebel D, Anniyev T, Ogasawara H, Bluhm H, Pettersson L G M and Nilsson A 2011 *Phys. Rev. Lett.* **107** 195502
[12] Bianchi M, Cassese D, Cavallin A, Comin R, Orlando F, Postregna L, Golfetto E, Lizzit S and Baraldi A 2009 *New. J. Phys.* **11** 063002
[13] Liang Z, Li T, Kim M, Asthagiri A and Weaver J F 2017 *Science* **356** 299
[14] He Y B, Stierle A, Li W X, Farkas A, Kasper N and Over H 2008 *J. Phys. Chem.* C **112** 11946
[15] Chung W-H, Tsai D-S, Fan L-J, Yang Y-W and Huang Y-S 2012 *Surf. Sci.* **606** 1965
[16] Rai R, Li T, Liang Z, Kim M, Asthagiri A and Weaver J F 2016 *Surf. Sci.* **652** 213
[17] Grant J T 1971 *Surf. Sci.* **25** 451
[18] Comrie C M and Weinberg W H 1976 *J. Chem. Phys.* **64** 250
[19] Boyle R W, Lauterbach J, Schick M, Mitchell W J and Weinberg W H 1996 *Ind. Eng. Chem. Res.* **35** 2986
[20] Gråsäs E, Andersen M, Arman M A, Gerber T, Hammer B, Schnadt J, Andersen J N, Michely T and Knudsen J 2013 *J. Phys. Chem.* C **117** 16438
[21] Ueda K *et al* 2015 *Top. Catal.* **59** 487
[22] Denecke R, Väterlein P, Bässler M, Wassdahl N, Butorin S, Nilsson A, Rubensson J E, Nordgren J, Mårtensson N and Nyholm R 1999 *J. Electron. Spectrosc.* **101–3** 971
[23] Giannozzi P *et al* 2009 *J. Phys.: Condens. Mater* **21** 395502
[24] Hammer B, Hansen L B and Nørskov J K 1999 *Phys. Rev.* B **59** 7413
[25] Feibelman P J, Hammer B, Nørskov J K, Wagner F, Scheffler M, Stumpf R, Watwe R and Dumesic J 2001 *J. Phys. Chem.* B **105** 4018
[26] Janthon P, Viñes F, Sirijaraensre J, Limtrakul J and Illas F 2017 *J. Phys. Chem.* C **121** 3970
[27] Steininger H, Lehwald S and Ibach H 1982 *Surf. Sci.* **123** 264
[28] Krekelberg W P, Greeley J and Mavrikakis M 2004 *J. Phys. Chem.* B **108** 987
[29] Bengtsson L 1999 *Phys. Rev.* B **59** 12301
[30] Ask Hjorth L *et al* 2017 *J. Phys.: Condens. Mater* **29** 273002
[31] *NIST Chemistry WebBook, NIST Standard Reference Database Number 69* (Gaithersburg, MD: National Institute of Standards and Technology) Retrieved 10 July 2017 p 20899
[32] Björneholm O, Nilsson A, Tillborg H, Bennich P, Sandell A, Hernnas B, Puglia C and Mårtensson N 1994 *Surf. Sci.* **315** L983
[33] Toyoshima R, Yoshida M, Monya Y, Suzuki K, Amemiya K, Mase K, Mun B S and Kondoh H 2014 *Phys. Chem. Chem. Phys.* **16** 23564

[34] Crumlin E J, Bluhm H and Liu Z 2013 *J. Electron. Spectrosc.* **190** 84
[35] Tüshaus M, Schweizer E, Hollins P and Bradshaw A M 1987 *J. Electron. Spectrosc.* **44** 305
[36] Persson B N J, Tüshaus M and Bradshaw A M 1990 *J. Chem. Phys.* **92** 5034
[37] Longwitz S R, Schnadt J, Vestergaard E K, Vang R T, Stensgaard I, Brune H and Besenbacher F 2004 *J. Phys. Chem.* B **108** 14497
[38] Tränkenschuh B, Fritsche N, Fuhrmann T, Papp C, Zhu J F, Denecke R and Steinrück H P 2006 *J. Chem. Phys.* **124** 074712
[39] McEwen J S, Bray J M, Wu C and Schneider W F 2012 *Phys. Chem. Chem. Phys.* **14** 16677
[40] Shan B, Kapur N, Hyun J, Wang L, Nicholas J B and Cho K 2009 *J. Phys. Chem.* C **113** 710
[41] Xu Y and Mavrikakis M 2002 *J. Chem. Phys.* **116** 10846

Ambient pressure phase transitions over Ir(111): At the onset of CO oxidation

N Johansson[1], M Andersen[2], Y Monya[3], J N Andersen[4], H Kondoh[3], J Schnadt[1,4], and J Knudsen[1,4]

[1]Division of Synchrotron radiation research, Department of Physics, Lund University, Box 118, 221 00 Lund, Sweden

[2]Chair for Theoretical Chemistry and Catalysis Research Center, Technische Universität München, Lichtenbergstr. 4, 85747 Garching, Germany

[3]Department of Chemistry, Keio University, 3-14-1 Hiyoshi, Kohoku-ku, Yokohama 223-8522, Japan

[4]MAX IV Laboratory, Lund University, Box 118, 221 00 Lund, Sweden

E-mail: jan.knudsen@sljus.lu.se

Supplementary material

Oxygen coverage at 535 K

The O coverage at Pt(111) in the mass transfer limit (MTL) is calculated from the relative areas of the Pt 4f components in figure S1. The XP spectrum is deconvoluted by three components assigned to bulk Pt atoms (Pt_B), clean Pt surface atoms (Pt_S), and Pt surface atoms bound to O (Pt_O). Since O atoms adsorb at hollow sites on Pt(111) the O coverage is calculated by:

$$\theta_O = \frac{I_O}{3(I_O + I_S)},$$

where I_O is the integrated intensity of the Pt_O component and I_S the integrated intensity of the Pt_S component. The resulting coverage is (0.21±0.02) monolayer (ML). In this fit we exclude the onset of oxide formation since: (i) the Pt_S component is clearly distinguishable at 70.6 eV binding energy and (ii) the high energy component ("4O") [1] at about 71.7 eV binding energy is not seen.

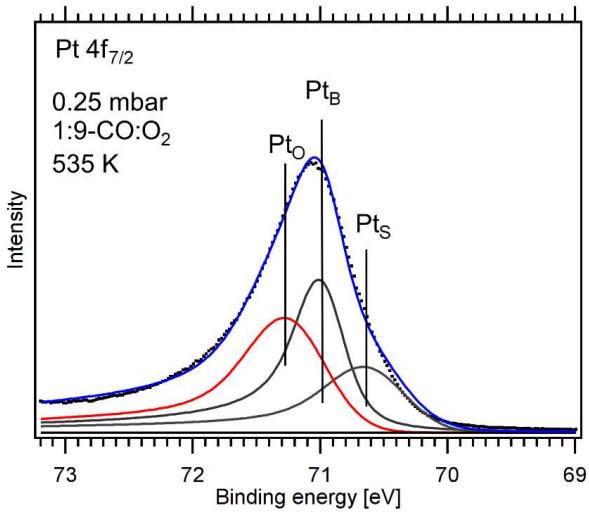

Figure S1. Pt $4f_{7/2}$ spectrum acquired while the CO oxidation reaction is in the MTL using 390 eV photons.

Deconvolution of O 1s spectra of Pt(111) and Ir(111)

Figure S2 shows the O 1s spectra and resulting curvefitting for different temperatures in $CO:O_2$ mixtures for Pt(111) and Ir(111). See experimental sections for flows and pressures.

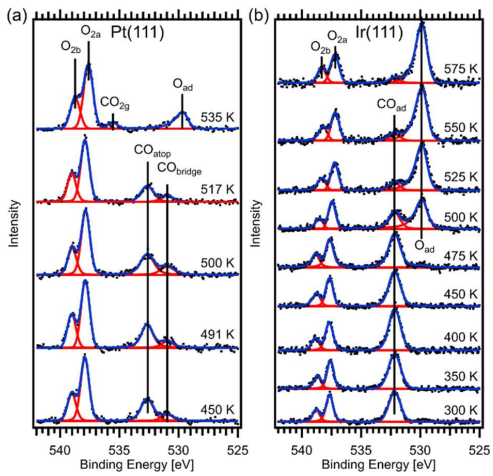

Figure S2. Panels (a) and (b) show all O 1s spectra acquired during the CO oxidation experiments over Pt(111) and Ir(111), respectively. The spectra are normalized to the O_{2a} maximum

CO coverage on Pt(111)

From the O 1s XP spectra acquired over Pt(111) the CO coverage can be estimated since we know that the O coverage at 535 K is (0.21±0.02) ML (cf. figure S1). By assuming that the gas phase components have a constant area, the ratio between the adsorbed O and the gas phase O can be used to approximate the temperature dependent coverage. The error induced by the some of the O_2 being converted to CO_2 is negligible. The O coverage at 535 K is calculated by

$$\theta_O(535) = k \cdot \frac{I_{Oad}(535)}{I_{O2}(535)} = 0.21\ ML,$$

where $I_{Oad}(535)$ is the integrated signal of the O_{ad} component at 535 K, $I_{O2}(535)$ is the integrated signal of gas phase O_2 (O_{2a}+O_{2b}) and k is the calibration factor. Since the O coverage at 535 K is known, we can solve for k. The temperature dependent CO coverage then becomes

$$\theta_{CO}(T) = k \cdot \frac{I_{COad}(T)}{I_{O2}(T)},$$

where $I_{COad}(T)$ is the integrated CO signal at the specific temperature and $I_{O2}(T)$ is the integrated gas phase signal at the corresponding temperature (T). The resulting coverages are plotted in figure S3.

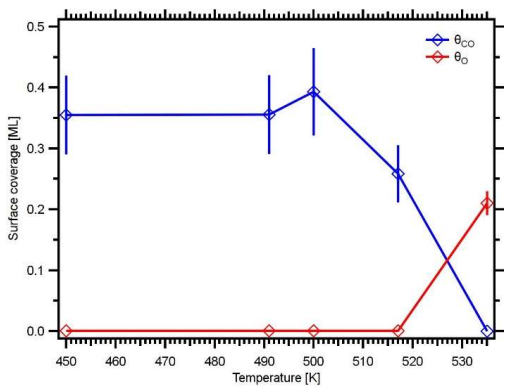

Figure S3. The temperature dependent adsorbate coverage as calculated from the Pt(111) O 1s XP spectra.

Activation energy on Ir(111)

The activation energy for CO oxidation over Ir(111) at a 9:1 O_2:CO ratio with a total pressure of 0.5 mbar is calculated with the Arrhenius expression

$$k = Ae^{-\frac{E_A}{k_b T}},$$

where k is the rate constant, A is the exponential pre-factor, E_A is the activation energy and T is the temperature. In figure S3 an Arrhenius plot of the CO_2 reactivity data is shown. The change in rate constant is measured by the change in CO_2 partial pressure. The fitted (blue line) yields an activation energy of 1.04 eV. The error bars on each datapoint is estimated from the change in CO_2 partial pressure from the start of the temperature until the next change of temperature.

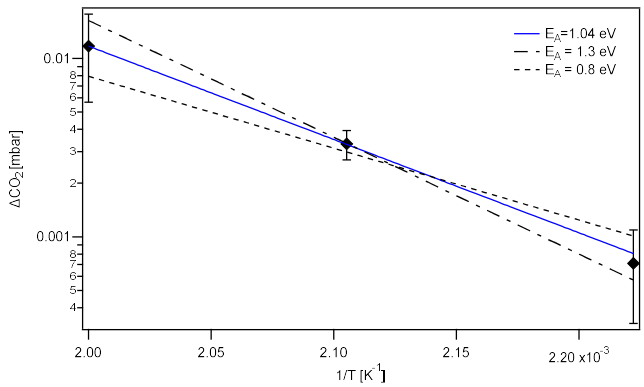

Figure S4. Arrhenius plot generated from the CO_2 reactivity data measured with the mass spectrometer for Ir(111). The blue line represents the fit to the data while the dashed and dash-dotted lines are used to estimate the uncertainty in the determination of the activation energy.

Curvefitting of Ir 4f spectra

Figure S4 shows the Ir $4f_{7/2}$ spectra recorded at different temperatures and the corresponding curve fits. All Ir 4f spectra were calibrated to the fermi level measured directly after each spectrum. Prior to fitting a Shirley-type background were removed from the Ir 4f line and the Ir 4f spectra were normalized to the maximum of the Ir $4f_{7/2}$ signal. The fitting function consists of five Doniach-Šunjić functions with identical shape, i.e. Lorenzian FWHM, Gaussian FWHM, and asymmetry. The components used in the fit are Ir_B, Ir_S, Ir_{CO}, Ir_{O1}, and Ir_{O2}, corresponding to bulk Ir, clean Ir surface atoms, Ir surface atoms atoms bound to CO, Ir surface atoms bound to one O atom, and Ir surface atoms bound to two O atoms, respectively. All spectra were fitted using a global analysis algorithm allowing for simultaneous fitting of all Ir spectra with correlated coefficients. In all spectra, the binding energies for the corresponding components were set to be the same while the intensity was allowed to vary. The Intensity of all components were restricted so that the ratio between Bulk and total surface contribution was the same for all spectra. Additionally, the intensity ratio between the Ir_O components (Ir_{O1}+Ir_{O2}) and the Ir_{CO} component for each temperature is determined by the ratio between the O_{ad} and CO_{ad} components from the corresponding O 1s spectrum.

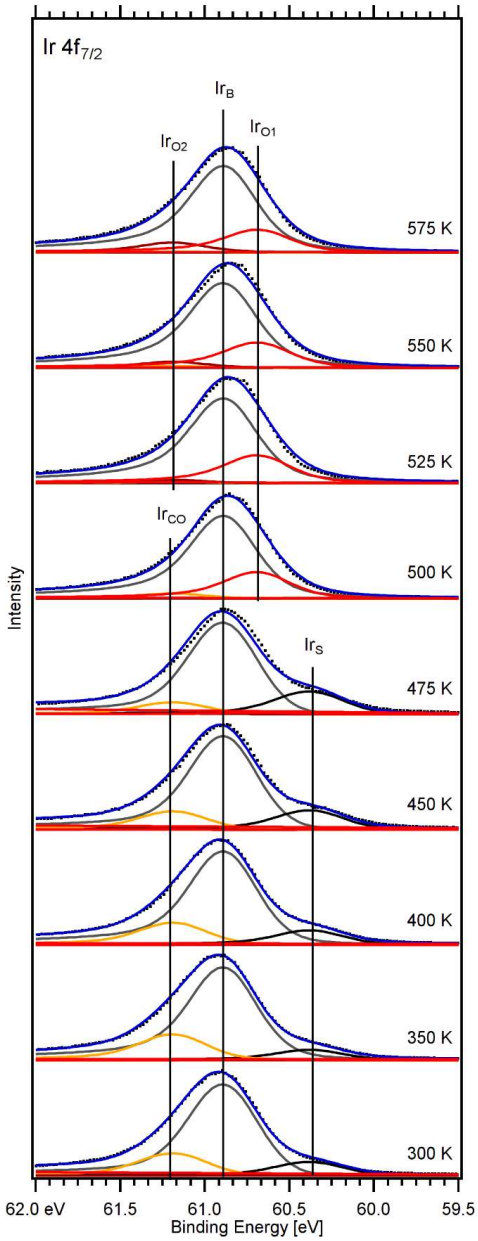

Figure S5. The curvefited Ir 4f spectra for the different temperatures.

References

1. Miller D J, Öberg H, Kaya S, Sanchez Casalongue H, Friebel D, Anniyev T, Ogasawara H, Bluhm H, Pettersson L G M, and Nilsson A, 2011, *Phys. Rev. Lett.,* **107,** 195502

Paper IV

Top Catal (2016) 59:506–515
DOI 10.1007/s11244-015-0521-7

ORIGINAL PAPER

Oxidation of Ultrathin FeO(111) Grown on Pt(111): Spectroscopic Evidence for Hydroxylation

Niclas Johansson[1] · Lindsay R. Merte[1,2] · Elin Grånäs[1] · Stefan Wendt[2] · Jesper N. Andersen[3] · Joachim Schnadt[1] · Jan Knudsen[3]

Published online: 6 January 2016

Abstract Using high resolution and ambient pressure X-ray photoelectron spectroscopy we show that the catalytically active FeO_2 trilayer films grown on Pt(111) are very active for water dissociation, in contrast to inert FeO(111) bilayer films. The FeO_2 trilayer is so active for water dissociation that it becomes hydroxylated upon formation, regardless of the applied preparation method. FeO_2 trilayers were grown by oxidation of FeO(111) bilayer films either with molecular oxygen in the mbar regime, or by NO_2 and atomic oxygen exposures, respectively, in the ultrahigh vacuum regime. Because it was impossible to prepare clean FeO_2 without any hydroxyls we propose that catalytically highly active FeO_2 trilayer films are generally hydroxylated. In addition, we provide spectroscopic fingerprints both for Pt(111)-supported FeO(111) and FeO_2 films that can serve as reference for future in situ studies.

Keywords Spectroscopy · Iron oxide monolayers · Ultrathin films · Hydroxylation

✉ Jan Knudsen
jan.knudsen@sljus.lu.se

[1] Division of Synchrotron Radiation Research, Department of Physics, Lund University, Box 118, 221 00 Lund, Sweden

[2] Interdisciplinary Nanoscience Center (iNANO) and Department of Physics and Astronomy, Aarhus University, 8000Aarhus C, Aarhus, Denmark

[3] Division of Synchrotron Radiation Research and the MAX IV Laboratory, Department of Physics, Lund University, Box 118, 221 00 Lund, Sweden

1 Introduction

The ultrathin FeO(111) bilayer film grown on Pt(111) is one of best studied hetero-oxide hybrid system that couples a subnanometer sized oxide phase to a metal surface [1]. It was first grown and characterized in 1988 by Vurens et al. [2] Since then the FeO(111) bilayer film on Pt(111) has been characterized in great detail using the combination of scanning tunneling microcopy (STM) and low energy electron diffraction (LEED) [3–7], X-ray photoelectron diffraction [8], and density functional theory (DFT) [7, 9, 10]. From these studies it is known that the FeO(111) bilayer consist of hexagonal closed packed O- and Fe-layers with the O-layer at the surface and the Fe-layer sandwiched between the surface O-layer and the Pt(111) support. Due to a small misfit angle (0.6°) between the FeO(111) film and the Pt(111) support and the lattice mismatch between the FeO lattice ($\sim$ 3.1 Å) and the Pt(111) substrate (2.77 Å) a characteristic moiré pattern with a $\sim$ 25 Å periodicity is formed.

Numerous interesting properties of the FeO(111) films have been discovered in various studies that focused on: (i) the reduction of the film by atomic hydrogen [11–13]; (ii) reduction of the film by CO [14]; (iii) nanopattering using the films moiré structure [15–18]; (iv) adsorption of molecules on the film [5, 19–22]; and (v) catalytic activity of the film [23, 24].

One of the reactivity studies published by Sun et al. in 2009 [23] revealed that an oxygen-rich FeO_x ($1 < x < 2$) trilayer phase is formed when FeO(111) bilayer films are exposed to O_2 pressures in the mbar regime at elevated temperatures. The formation of this oxygen-rich FeO_x phase at reaction conditions was linked to the enhanced CO oxidation activity observed for ultrathin FeO(111) as compared to clean Pt(111) and nm-thick Fe_3O_4(111). In the

following, the O-enriched FeO_x phase will be referred to as FeO_2 trilayer. Since its discovery, the FeO_2 trilayer phase has been studied extensively by a variety of techniques, including STM [25–28], Auger electron spectroscopy (AES) [25], and DFT [26, 29, 30]. In a study by Giordano et al. [10] it was shown that the transition from FeO(111) to FeO_2 strongly depends on the specific region, leading to oxygen enrichment in specific areas of the FeO(111) moiré unit cell. In addition, it was shown that the FeO_2 trilayer islands have a O–Fe–O–$Pt_{substrate}$ stacking. Compared with the FeO(111) bilayer film, the FeO_2 islands thus contain O atoms at the interface between the oxide film and the Pt(111) substrate. Finally, high resolution STM studies revealed a $(\sqrt{3} \times \sqrt{3})R30^\circ$ superstructure on the FeO_2 trilayer islands. On the basis of DFT calculations it was suggested that this superstructure originates from a energetically preferred location of O-interphase atoms atop the Pt atoms of the substrate [10]. In two more recent studies by Giordano et al. [29, 30] theoretical core level shifts (CLS's), work function changes between FeO(111) and FeO_2, and OH stretching frequencies were reported and the mapping of the local activity at different sites showed that oxygen easily can be adsorbed and released at the FeO(111)/FeO_2 boundaries, which might explain the high CO oxidation activity. Studies by Lewandowski et al. [27] showed (i) that the FeO_2(111) phase is also formed on Pt particles supported on Fe_3O_4(111) upon annealing in O_2 in the mbar pressure range, and (ii) that CO_2 formation occurs via a Mars-van Krevelen mechanism, where CO reacts with the FeO_2 trilayer film, thereby reducing it, while O_2 oxidizes FeO back to FeO_2 [28]. This proposed mechanism by Lewandowski et al. fits well with the reaction mechanism proposed in the DFT study by Giordano et al. [30] All the studies addressing the FeO_2 trilayer mentioned above considered the formation of FeO_2 by O_2 and its reduction by CO. However, a recent study by Ringleb et al. demonstrates that hydroxylated FeO_2 can be formed from FeO(111) if H_2O and O_2 are dosed simultaneously at near ambient pressure, leading to a H-O-Fe-O-$Pt_{substrate}$ structural motive [31].

Indeed, a lot of efforts have been devoted in determining the topology, local electronic structure, and reactive sites of FeO_2 trilayer films using STM and DFT. However, spectroscopic information on the electronic structure of FeO_2 films is still lacking. Solely the study by Ringleb et al. [31] reports on X-ray photoelectron spectroscopy (XPS) data, but in this study the FeO_2 surface was intentionally hydroxylated, as it was produced by co-dosing of O_2 and H_2O onto a FeO(111) bilayer film.

Here we present a spectroscopic investigation of the FeO_2 trilayer film grown on Pt(111). We report XPS and X-ray absorption spectroscopy (XAS) fingerprints for bilayer FeO(111) and trilayer FeO_2. The FeO_2 trilayer films were formed by oxidizing FeO(111) either with molecular oxygen in the mbar regime or with NO_2 and atomic oxygen, respectively, dosed in the ultrahigh vacuum (UHV) regime. Independent of the preparation method we observe spectroscopic evidence for a significant degree of hydroxylation on the FeO_2 trilayer films, and our STM data are fully consistent with this conclusion. Ambient pressure X-ray photoelectron spectroscopy (APXPS) measurements conducted while oxidizing FeO(111) to FeO_2 further reveals that the onset and degree of hydroxylation correlate with the coverage of FeO_2 trilayer islands. Altogether, our observations are strong evidence for an astonishing high activity of the FeO_2 trilayer towards water dissociation. Furthermore, our experimental data suggest that Pt(111)-supported FeO_2 trilayer films are generally hydroxylated, regardless of the applied preparation recipe.

2 Experimental

High resolution X-ray photoelectron spectroscopy (HRXPS) and XAS in UHV were performed at beamline I311 of the MAX IV Laboratory in Lund, Sweden. The beamline as well as the endstation are described in detail elsewhere [32]. High-pressure experiments in the mbar range were performed at the APXPS endstation of beamline I511. The APXPS instrument is capable of performing in situ experiments in pressures up to $\sim$5 mbar in a dedicated reaction cell inside the main analysis chamber. A description of the instrument and the beamline can be found in refs. [33] and [34], respectively.

In the HRXPS and the APXPS experiments, the Pt(111) crystal was cleaned by repeated cycles of Ar^+ sputtering followed by annealing to 870 K in 1×10^{-7} mbar O_2. After annealing the crystal was subsequently flashed to 970 K. The cleanness of the crystal was probed by LEED and XPS. To grow the FeO(111) bilayer film, Fe was deposited onto Pt(111) with an e-beam evaporator. The deposited Fe was oxidized by heating the crystal to 870 K in $1 \cdot 10^{-6}$ mbar O_2. This procedure is known to result in a FeO(111) bilayer film, which grows layer-by-layer up to a coverage of about 2.5 ML [4]. The coverage of the FeO film in the XPS experiments was calibrated by saturating the surface with CO at room temperature. As CO only binds to the exposed Pt surface at room temperature the intensity of the C 1s and O 1s signal can be used directly to follow the growth of the film. By cycles of Fe deposition (submonolayer amounts) at room temperature and subsequent oxidation, we tuned the coverage of FeO to the point where the C 1s signal disappeared. We define a monolayer (ML) as a complete coverage of a bilayer FeO(111) film, noting

that the FeO(111) lattice is expanded by about 12 % [13] resulting in 0.8 layer coverage with respect to the Pt(111) surface density. All sample temperatures given in our work are measured with a type K thermocouple spot-welded to the edge of the Pt(111) single crystal surface. In the APXPS experiments we used O_2 (99.9999 % purity) without further purification. The base pressure of the APXPS chamber was $\sim 5 \times 10^{-10}$ mbar. In the HRXPS measurements performed at beamline I311 we used NO_2 (99.5 % purity) for the oxidation. The NO_2 was dosed at a maximum pressure of 1×10^{-7} mbar at room temperature. No filaments were on during NO_2 exposure and a cold cathode gauge was used to measure the pressure when NO_2 was dosed. The base pressure of the HRXPS setup was $\sim 1 \times 10^{-10}$ mbar. The XPS spectra shown in this paper are calibrated to the Fermi level. All O 1s spectra were acquired using a photon energy of 650 eV. In our experiments, this yields a resolution of 580, 950 and 250 meV for UHV, mbar and NO_2 experiments, respectively. The Pt 4f and Fe 3p/Pt 5p regions were recorded with a photon energy of 190 eV, yielding corresponding resolutions of 110 meV for the Pt 4f and 330 meV for the Fe 3p/Pt 5p levels. Polynomial backgrounds were subtracted from all spectra before or during the curve fitting. For Pt 4f spectra Doniach-Šunjić (DS) functions convoluted with Gaussians line shapes were used for the curve fitting. O 1s spectra were deconvoluted using asymmetric Voigt functions. Due to the open-shell nature of Fe, fitting of Fe 3p features is non-trivial. For simplicity we used three DS components convoluted with Gaussians for curve fitting of the Fe 3p features.

The Fe L-edge XAS spectra were recorded in normal incidence in Auger yield mode by collecting electrons with a kinetic energies between 540 and 550 eV using a SES-200 analyzer. The photon energy of the XAS spectra was calibrated by measuring the Pt 4f peak using first and second order light from the monochromator.

STM measurements were conducted in a separate UHV system in Aarhus with a base pressure of $\sim 2 \times 10^{-10}$ mbar, using a home-built Aarhus STM operated at room temperature with a mechanically cut Pt–Ir tip. Preparation of the Pt(111) crystal and growth of the FeO film were conducted in the same way as for the spectroscopy measurements. To form the FeO_2 trilayer, the bilayer FeO(111) film was exposed to atomic oxygen at 385 K using a thermal atom source (Oxford Applied Research TC-50) operated at a power of 54 W with a chamber background O_2 pressure of 2×10^{-8} mbar. Exposure for 8 min under these conditions followed by flash annealing to 500 K was found to produce a film that was nearly saturated with FeO_2 trilayer islands, similar to a previous study of the oxidation of FeO/Pd(111) [35] conducted using the same experimental system.

3 Results and Discussion

The spectroscopic and structural properties of Pt(111)-supported FeO(111) bilayer films are well documented in the literature [5, 13]. Nevertheless, to facilitate a direct comparison of the XPS data acquired on FeO_2 we first show the spectra of clean Pt(111) surface (top Fig. 1) and the bilayer FeO(111) film (middle Fig. 1). Subsequently, the spectroscopic and structural properties of FeO_2 will be discussed. Ball models and LEED images for the different preparation steps are also shown in Fig. 1.

3.1 Spectroscopic Fingerprints of FeO

Before growing of the FeO(111) film the spectral features corresponding to a clean Pt(111) surface is discussed. No signal is observed in the O 1s region. In the Pt $4f_{7/2}$ line bulk (Pt_B) and surface (Pt_S) components are observed at 70.94 and 70.52 eV [36], respectively. The small component observed at 51.40 eV originates from the Pt 5p core level of the clean Pt(111) surface. Following the growth of 1 ML FeO(111) a single O 1s peak is observed at 529.4 eV (denoted I). In the Pt $4f_{7/2}$ region the previously observed surface component disappears and one single component is observed at 70.94 eV, i.e. the position of the bulk component of the Pt(111). The CLS of the topmost layer of Pt atoms that binds to Pt atoms beneath and Fe atoms above is thus indistinguishable from that of the Pt bulk atoms. In the Fe 3p region a component with first moment—i.e. 'center of mass'—at 54.99 eV and peak maximum at 54.11 eV is observed. The spectra acquired here on FeO(111) are in good agreement with those published previously [5, 13]. The cleanliness of our FeO(111) films was further confirmed by acquiring survey scans, which showed no sign of the presence of other elements than Fe, O, and Pt. The ordering of the film was checked with LEED, which revealed the expected floret patterns due to the film's moiré structure (see the insets in Fig. 1). Careful inspection of the individual diffraction spots reveal an arc shape that could indicate the formation of slightly rotated FeO(111) domains on the sample. Most likely a higher oxidation temperature after iron deposition would have given sharp spots without any arc shape.

3.2 Spectroscopic Fingerprints of FeO_2

For the formation of the FeO_2 trilayer film the FeO(111) film was oxidized by dosing 0.6 mbar O_2 while annealing

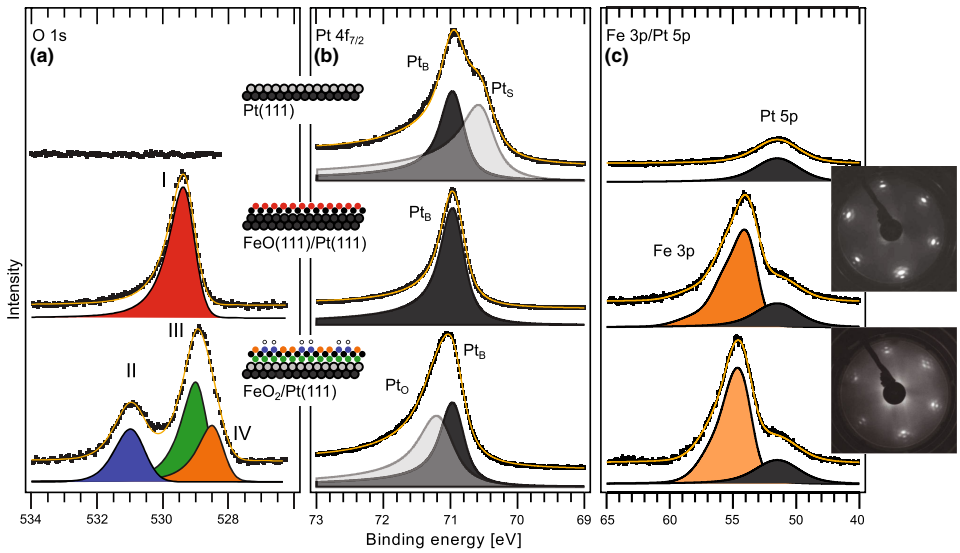

Fig. 1 XP spectra acquired on the clean Pt(111) crystal (*top*), with a bilayer FeO(111) overlayer (*middle*), and with a trilayer FeO_2 overlayer (*bottom*). *Panel a* shows the O 1s core levels, while *panels b, c* show Pt $4f_{7/2}$ and Fe 3p/Pt 5p regions, respectively. LEED images of FeO(111) and FeO_2 overlayers acquired in the XPS setup with energies of 62 and 65 eV, respectively, are also included in the figure.

the sample at 500 K. Subsequently the sample was cooled to room temperature in an oxygen atmosphere. Following the oxidation, the main O 1s peak shifts to lower binding energy and a shoulder component develops at the high binding energy side. The full width at half maximum (FWHM) of the main O 1s peak of the FeO_2 trilayer film is significantly larger (1.1 eV) than the FWHM of the O 1s component (I) observed on the bilayer FeO(111) (0.9 eV) suggesting that more than one component should be used for its deconvolution. On the basis of this observation we fitted the main O 1s peak by two components with similar widths as component I positioned at 529.0 eV (III) and 528.5 eV (IV), respectively. Our experimental CLS of −0.4 eV (III) and −0.9 eV (IV) with respect to component I of FeO(111) agree very well with DFT-calculated final state CLS of −0.4 eV (interface O) and −0.7 eV (surface O) reported by Giordano *et al.* [29] Accordingly, we assign component III to interface O atoms sandwiched between Pt and Fe atoms and component IV to surface O atoms in FeO_2.

The shoulder component (II) located at 531.0 eV is shifted by +2.5 eV with respect to component IV originating from surface O atoms in FeO_2. Core-level shifts of ∼2 eV have previously been observed for hydroxylation of oxide films such as FeO(111) (2.2 eV) [13], Fe_3O_4(111) (2.1 eV) [37], α-Al_2O_3(0001) (1.9–2.0) [38], and α-Fe_2O_3(0001) (1.9–2.2 eV) [38]. On this basis we assign the shoulder component (II) to OH groups. Comparing the relative area of the OH component II (49%) and the FeO_2 surface component IV (51%) we conclude that approximately half of the surface O atoms in the FeO_2 film are hydroxylated. However, it should be noted that the area of component IV is very sensitive to the peak widths of component IV and III. Thus, the real coverage of OH-groups could easily be higher or lower than 0.5 ML.

In contrast to the FeO(111) film, the FeO_2 trilayer film contains interface O atoms in direct contact with the topmost layer of Pt atoms. Therefore, we expect the Pt $4f_{7/2}$ spectra of FeO(111) and FeO_2(111) to be clearly distinguishable. Figure 1b confirms this expectation as we find a new component (Pt_O) at 71.15 eV binding energy in addition to the bulk component (Pt_B) at 70.94 eV for the FeO_2(111) film. For comparison, ref. [36] reported a Pt $4f_{7/2}$ binding energy of 71.12 eV for a p(2 × 2)-O chemisorption phase on Pt(111) with O atoms located in the threefold hollow sites.

In the Fe 3p spectrum the oxidation of FeO(111) to FeO_2 causes a CLS of +0.53 eV of the Fe 3p component peak

maximum, suggesting a higher oxidation state of Fe in the FeO_2 film. However, the CLS causes only the first moment to shift by +0.18 eV. Hence, the overall peak has shifted possibly due to multiple changes on the surface. We did not attempt to explicitly curve fit the Fe 3p peak since both the Fe 2p and 3p curve fitting are non trivial [39–41] and beyond the scope of the present study. Instead we used three Doniach-Šunjić (DS) functions to fit the Fe 3p peak in order to determine the integrated area. In Fig. 1c the sum of these three DS functions is plotted as one component shown in orange. By normalizing the spectra to the integrated area of the Pt 5p component we observe a 13 % increase of the Fe 3p component upon oxidation from FeO(111) to FeO_2, fitting well with the fact that more attenuation of the photoelectrons from underlying Pt is expected for FeO_2 than for FeO(111).

Finally, we note that also the LEED pattern acquired on FeO_2 shows a floret pattern, similar to the one observed on the FeO(111) film, but without any arc shape of the individual diffraction spots. First of all this indicates that the in-plane structures of the FeO(111) and FeO_2 surfaces are comparable even though the spectroscopic fingerprints of these two surfaces are very different. Secondly, the disappearance of the arc shape upon FeO_2 formation might be an indication that rotational micro domains disappeared upon oxidation when the interphase O layer became present. Note that the two LEED images shown in Fig. 1 are acquired on the the same sample before and after FeO_2 formation. More experimental work and a careful analysis of many LEED images before and after oxidation are, however, needed to verify our second conclusion.

As mentioned above, our O 1s deconvolution indicates that approximately 50 % of the surface oxygen atoms are hydroxylated. To validate this conclusion we tried to selectively remove the H atoms from the surface, by flashing the FeO_2 trilayer to 580 K. In Fig. 2 we compare the O 1s spectrum of FeO_2 before (bottom) and after (middle) flashing to 580 K. Clearly, component II assigned to the OH groups decrease in intensity upon flashing, while component I assigned to FeO(111) and component IV assigned to surface FeO_2 without OH groups increase in intensity. Further, we note that the FeO_2 interface component decreases in intensity. This is as expected because part of the surface is converted to FeO(111) without an interface component. Hence, flashing in vacuum leads to removal of the hydrogen, as expected, and a partial removal of oxygen leads to the observed trilayer/bilayer mixture. This observation suggests that OH groups help to stabilize the FeO_2 trilayer. Recently, it has been reported by Liu et al. [42] that hydroxyl groups also stabilize ultrathin Zinc oxide films.

The topmost O 1s spectrum in Fig. 2 was acquired after a subsequent room temperature exposure of H_2O

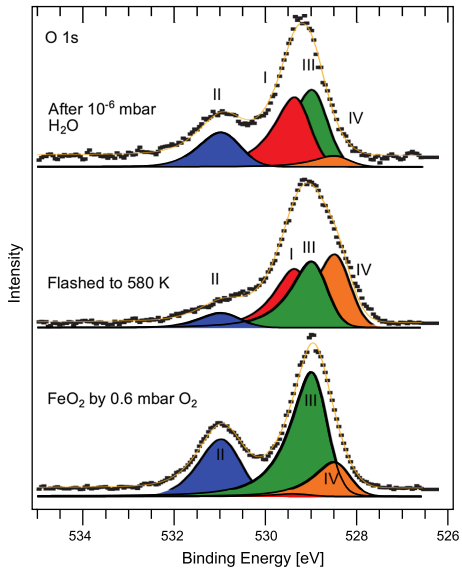

Fig. 2 O 1s spectra of FeO_2(111) before (*bottom*) and after (*middle*) flashing to 580 K. The spectra at the *top* was acquired after exposing the flashed FeO_2(111) film to 1×10^{-6} mbar H_2O for $\sim$15 min

(1×10^{-6} mbar for $\sim$15 minutes) onto this trilayer/bilayer mixture. Clearly, the water exposure leads to re-appearance of the OH-component (II) and a reduced FeO_2 surface component (IV). In contrast, the FeO(111) component (I) and the FeO_2 interface component (III) are unaffected by the water exposure. Hence, the conclusion from these observations is that a surface with FeO_2(111) patches effectively dissociates H_2O, whereas a continuous FeO(111) film is inert with respect to water exposure at room temperature.

For the oxidation of FeO(111) to FeO_2 discussed above a pressure of 0.6 mbar was used. At such high pressures—high as in orders of magnitudes higher than standard UHV techniques—it is difficult to avoid water impurities. In order to reduce the water contamination we also studied the oxidation of FeO(111) by NO_2. Previous surface oxidation studies have shown that NO_2 functions as a very efficient oxidation agent and quite similar to atomic oxygen [43], meaning that the partial pressure of water can be reduced significantly. Figure 3 show a series of O 1s spectra of FeO(111) exposed to an increasing amount of NO_2 dosed at room temperature. As the gas dosing was done in the preparation chamber the sample was transferred between dosing and measurement. After 250 L NO_2 (dosed at

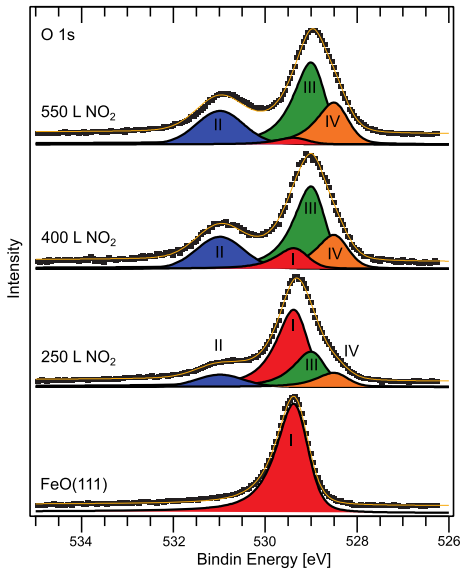

Fig. 3 Trilayer FeO_2 grown with NO_2. The *bottom* spectrum shows bilayer FeO(111) and each spectrum above shows the spectrum after subsequent room temperature NO_2 dosing. Dose shown in the figure is the cumulative NO_2 dose

1×10^{-6} mbar) the OH component (II), the FeO_2 surface component (IV), and the FeO_2 interface component (III) start to become visible. At lower NO_2 doses (not shown) the spectrum looked very similar to that of pristine FeO(111) and only very small changes were observed. With increasing NO_2 dose the components assigned to FeO_2 (II, III, IV) increase in intensity while the FeO(111) component (I) decreases. Between a dose of 400 and 550 L the surface oxidation seems to saturate and the FeO(111) component (I) almost disappears. No N 1s signal was observed upon NO_2 oxidation in any of our experiments suggesting formation of NO or N_2 that immediately desorbs. Comparing the O 1s spectra after O_2 oxidation (Fig. 1a) and the NO_2 oxidation (Fig. 3) of FeO(111) it is evident that the two different oxidation methods are very similar and both result in extensive surface hydroxylation. In none of our NO_2 oxidation experiments we observed FeO_2 interface (II) and surface (IV) components without also observing a OH component (IV). Altogether, these observations suggest that a surface with FeO_2(111) trilayer patches undergoes quickly hydroxylation, whereas the bilayer FeO(111) film does not hydroxylate.

3.3 STM Comparison of FeO and FeO_2

Evidence for spontaneous hydroxylation of the FeO_2 trilayer is also provided by STM measurements. Figure 4 shows STM images of the pristine bilayer FeO film (Fig. 4a) and the oxidized film (Fig. 4b), produced by exposure to atomic oxygen from a thermal cracker. Immediately after exposure at room temperature, it was found to be impossible to establish stable STM imaging, presumably due to the presence of weakly-bound oxygen-containing species on the surface which interact strongly with the STM tip. After flashing the surface to 500 K, however, stable images could be obtained, one of which is shown in Fig. 4b. Similar to previous reports [23, 26, 35], the STM images show bright patches of FeO_2 organized following the moiré superstructure. Atop these patches we observe bright protrusions showing poor short-range order, but typical separations corresponding to $\sqrt{3} \times$ a, or next-nearest-neighbor spacing or larger. This is very similar to what has previously been observed for H adatoms adsorbed on the FeO bilayer [22], and we therefore propose that these protrusions correspond to OH groups which are either residual features following the flash (note that the OH component of the O 1s spectra shown above was not completely removed by heating) or which formed by adsorption while the sample cooled. To distinguish between these two possibilities, it would be interesting to scan on FeO_2 trilayer samples at elevated temperatures. The unintentional adsorption of water upon sample cooling was previously observed in STM studies addressing rutile TiO_2(110) [44]. In an earlier report by Giordano et al. [26] protrusions were observed in STM images similar to those here, but forming a more well-ordered $\sqrt{3} \times \sqrt{3}R30°$ arrangement atop the trilayer patches. In that work the superstructure was attributed to outward relaxation of 1/3 of the Fe ions based on the finding by DFT+U calculations that such a structure was stable. Though we cannot rule out this explanation completely, we find it unlikely that displacement of single ions is responsible for the protrusions observed in the present case, where variability in the number of protrusions observed at each FeO_2(111) patch and their relatively random ordering is suggestive of the presence of foreign species. We furthermore suggest that the superstructure observed in this previous work was also caused by OH groups, the better ordering being attributable to a higher concentration of these species.

3.4 XAS Comparison of FeO and FeO_2

We now take a closer look at the oxidation state of Fe in FeO(111) and FeO_2. In Fig. 5 Fe L_3 spectra of a FeO(111) film and FeO_2 prepared by dosing NO_2 are shown together

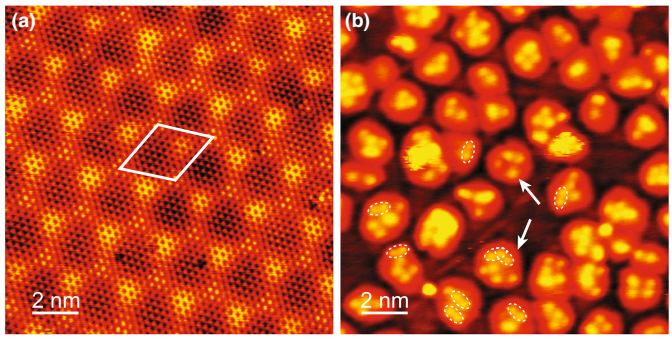

Fig. 4 **a** STM image (65 mV, 3.0 nA) of bilayer FeO/Pt(111), with the moiré coincidence cell marked. **b** STM image (2.0 V, 0.2 nA) of the FeO bilayer following exposure to atomic oxygen and flashing to 500 K. Bright protrusions assigned to OH groups incorporated into patches of the FeO_2 trilayer are indicated with arrows. *Ovals* mark pairs of protrusions separated by a lattice distance of $\sqrt{3}$

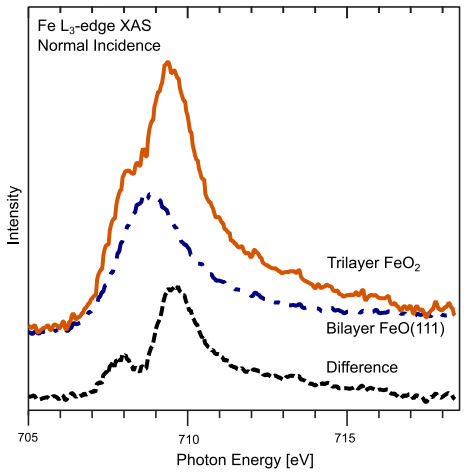

Fig. 5 Normal incidence Fe L_3-edge XAS spectra of a trilayer grown with NO_2 and a bilayer, from which the trilayer was grown. Also shown is the difference between the spectra

with their difference spectra. The spectrum of the FeO(111) bilayer film is, as expected, in accordance with that of Fe^{2+} [5, 45, 46]. For FeO_2 the main component is shifted to higher photon energies and a shoulder is seen at a lower photon energy. Clearly, the iron atoms in FeO_2 are at least partly in a different oxidation state. Indeed, the observed line-shape of the difference spectrum [FeO_2–FeO(111)] is characteristic of an Fe^{3+} oxidation state [45, 46]. Hence, the trilayer is composed of Fe^{2+} and Fe^{3+} contributions. From the relative intensities of the contributions we find that roughly 60 % of the ions are in an Fe^{2+} oxidation state. As previously discussed, no bilayer FeO(111) contributions could be found with XPS. Therefore, the different Fe ion oxidation state must originate from the trilayer FeO_2 patches.

3.5 In Situ Oxidation of FeO to FeO_2 Followed with APXPS

In all our experiments where FeO(111) was oxidized to FeO_2 with O_2, NO_2, and atomic oxygen we observed that the surface is to a large extent hydroxylated. To follow the kinetics of the FeO(111) to FeO_2 transformation and to probe whether the surface first is oxidized to FeO_2 and subsequently becomes hydroxylated we followed the oxidation process in situ with APXPS. In the APXPS experiment the FeO(111) surface was exposed to 0.6 mbar O_2 while the sample temperature was ramped from room temperature to 500 K (Fig. 6). At the same time O 1s XP spectra were measured. Figure 6a shows an image plot of the O 1s spectra acquired in situ while selected O 1s spectra are shown in panel (b). The doublet observed near 538 eV originates from the O_2 gas phase molecules and the peaks near 530 eV originate from surface O species. In the top part of panel (c) in Fig. 6 we plot the relative surface area of all O 1s surface components obtained from simultaneous curve fitting of all O 1s spectra acquired in situ. At 300 K the surface is completely covered by bilayer FeO(111) (I). At a temperature of 315 K after $\sim$20 min of O_2 exposure we observe the onset of the reduction of FeO(111) component (I) and the simultaneous increase of the FeO_2-OH component (II) and the FeO_2 (IV) component. Thus, the FeO_2 surface atoms with and without adsorbed H occurs simultaneously and both components grow with the same rate until a temperature of 360 K is reached. Above this temperature the FeO_2-surface component start to increase faster than the FeO_2-OH component, and above 400 K the OH coverage reaches maximum (33 %) and start to decrease at higher temperatures. Both observations suggest

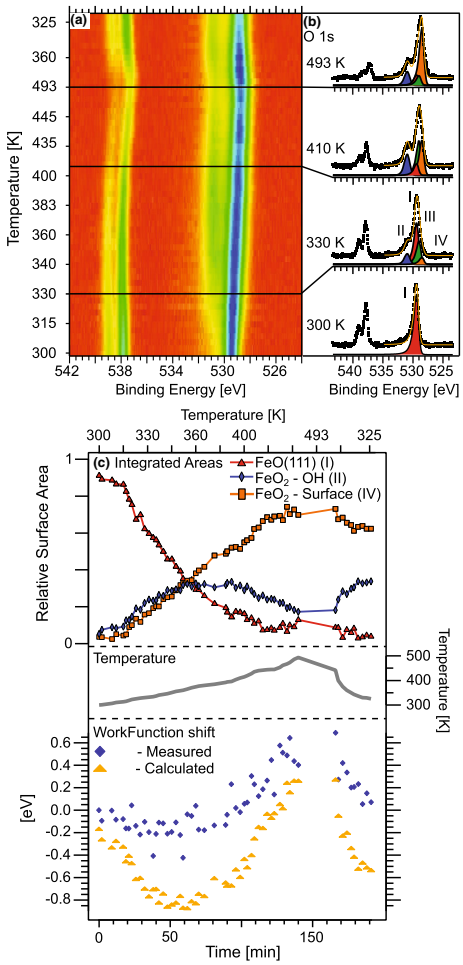

Fig. 6 **a** Image plot of O 1s spectra acquired in 0.6 mbar O_2 while heating the sample from 300 to 500 K followed by subsequent cooling. The temperature profile is plotted in *panel c*. **b** Selected O 1s spectra from *a*. **c** *Top* development of the 3 surface components [FeO(111)(I), FeO_2-OH(II), and FeO_2-Surface (IV)] as function of temperature and exposure time obtained from curve fitting the O 1s spectra shown in *panel a*. *Bottom* measured work function shift as function of temperature and exposure time obtained from the energy shift of the O_2 gas phase peak plotted together with the calculated workfunction shift obtained by combining theoretical values from ref. [29] and the coverage of FeO_2-OH(II) and FeO_2-Surface(IV)

that hydroxylation is suppressed at higher temperature. Even though the OH formation is suppressed at higher temperature we always observe a significant degree of hydroxylation also at the maximum temperature of 500 K (20 %). Upon cooling the OH coverage increase again and the FeO_2-surface component decrease.

Finally, we take a look at the peak position of the O_2 gas phase doublet. In contrast to the O 1s surface atoms that are pinned to the Fermi level the gas phase molecules are pinned to the vacuum level. As a result, the binding energy of gas phase molecules follows surface work function shift during the reaction, in this case, the film growth [47]. It should, however, be kept in mind that the gas phase molecules probed by APXPS are located in a small volume between the sample surface and the grounded electron analyzer aperture. Therefore, the measured binding energy shift of the gas phase molecules is reduced as compared to the work function shift of the sample surface. Nevertheless, at the bottom of Fig. 6c we plot the work function change obtained from the peak position of the O_2 doublet as function of time and temperature. In ref. [29] Giordano et al. calculated the work function change relative to Pt(111) of FeO(111) (+0.31 eV), FeO_2 (+1.72 eV), and FeOOH (-3.89 eV). Using these values and the relative surface coverage of the same components from the top part of Fig. 6c we estimated the expected work function shifts as the FeO(111) film is oxidized and hydroxylated as $\Delta\phi = \Theta(FeO_2 - surface) \cdot 1.41\ \text{eV} - \Theta(FeO_2 - OH) \cdot 4.20\ \text{eV}$. As Fig. 6c demonstrates the estimated work function qualitatively reproduce the measured work function rather well keeping in mind the simplicity of our model and the error bars of the curve fitting. In addition, we note that the calculated work function shift for FeOOH (−3.89 eV) probably overestimates the work function shift in our case, because it was calculated for a full OH coverage, leading to vertical configuration of all OH groups. In our case with partial hydroxylation of the FeO_2, the OH groups are dynamically distorted leading to a reduced effective dipole moment. Altogether we conclude from the data presented in Fig. 6c that: (i) the onset of hydroxylation coincides with the onset of the FeO_2 formation and initially the OH coverage and the FeO_2 formation grows simultaneously, meaning that OH formation is closely connected to the trilayer structure and/or growth; (ii) the degree of hydroxylation is strongly temperature dependent; (iii) the O atoms in the FeO_2 patches are always only partly covered with H atoms, in agreement with our STM observations; (iv) the FeO_2 formation and hydroxylation lead to a measurable work function shift that fits well with our

assignment of the the O 1s components and the calculated work function differences between FeO_2, hydroxylated FeO_2, and FeO(111).

As discussed above, the onset of hydroxylation coincides with the onset of FeO_2 formation, suggesting that hydroxylation occurs during the formation of the FeO_2 trilayer rather than after its formation is completed. On this basis and the fact that hydroxylation also occurred after the formation of FeO_2 patches was completed (see Fig. 2c) we suggest that water dissociates at the FeO_2-FeO(111) interface and at defects that are present mainly during the oxidation process. In contrast, we do not expect that water dissociates on perfect continuous FeO(111) films and on the FeO_2 patches.

Previous studies have shown that FeO bilayer films can be grown also on other Pt facets [48], and many other single-crystalline metal substrates such as Pd(111) [35], Ag(100) [41], Ag(111) [49], Mo(100) [50], Ru(0001) [51] and Au(111) [52, 53]. In other studies it has been found that FeO(111) films encapsulate Fe_3O_4 supported Pt particles [54]. In addition, it has been demonstrated recently that Co–O bilayer films on Au(111) can be transformed to O–Co–O trilayer films , both of which are structurally very similar to the iron oxide phases discussed here [55]. Our finding that the Pt(111) supported FeO_2 trilayer films are generally hydroxylated could thus be relevant both for surface iron oxides on other supports and for other trilayer surface oxides on (111) noble metal surfaces.

4 Conclusions

To conclude, we monitored the FeO(111)/Pt(111) to FeO_2/Pt(111) conversion upon oxidation with different oxidizing agents with HRXPS and APXPS and provided spectroscopic fingerprints of these surface iron oxide phases. Most importantly, we showed that FeO_2 supported by Pt(111) is very active for water dissociation. Once FeO_2 trilayer patches are formed upon oxidation of bilayer FeO(111) films with O_2, NO_2, or atomic oxygen, they immediately become partly hydroxylated. Since we always observe a significant degree of hydroxylation also when FeO(111) is oxidized to FeO_2 at excellent UHV conditions and since our STM data of the hydroxylad FeO_2 patches looks almost identical to previously published STM images of FeO_2 [23, 26] we propose that catalytically highly active FeO_2 trilayer films are generally hydroxylated even at normal UHV conditions. We believe this result is also of relevance for iron oxide films on other supports and for other trilayer oxides grown on (111) noble metal surfaces.

Acknowledgments Financial support from Vetenskapsrådet (Grants Nos. 2010-5080 and 2012-3850) and assistance by the staff at the MAX IV Laboratory are gratefully acknowledged. The work in Aarhus was supported by the Villum Kahn Rasmussen Foundation.

References

1. Surnev S, Fortunelli A, Netzer FP (2013) Chem Rev 113:4314
2. Vurens GH, Salmeron M, Somorjai GA (1988) Surf Sci 201:129
3. Ritter M, Ranke W, Weiss W (1998) Phys Rev B 57:7240
4. Ranke W, Ritter M, Weiss W (1999) Phys Rev B 60:1527
5. Weiss W, Ranke W (2002) Prog Surf Sci 70:1
6. Rienks EDL, Nilius N, Rust HP, Freund HJ (2005) Phys Rev B 71:241404
7. Merte LR, Grabow LC, Peng G, Knudsen J, Zeuthen H, Kudernatsch W, Porsgaard S, Laegsgaard E, Mavrikakis M, Besenbacher F (2011) Jour Phys Chem C 115:2089
8. Kim YJ, Westphal C, Ynzunza RX, Galloway HC, Salmeron M, Van Hove MA, Fadley CS (1997) Phys Rev B 55:R13448
9. Zhang W, Li Z, Luo Y, Yang J (2009) Jour Phys Chem C 113:8302
10. Giordano L, Pacchioni G, Goniakowski J, Nilius N, Rienks EDL, Freund HJ (2007) Phys Rev B 76:075416
11. Huang W, Ranke W (2006) Surf Sci 600:793
12. Merte LR, Knudsen J, Grabow LC, Vang RT, Laegsgaard E, Mavrikakis M, Besenbacher F (2009) Surf Sci 603:L15
13. Knudsen J, Merte LR, Grabow LC, Eichhorn FM, Porsgaard S, Zeuthen H, Vang RT, Laegsgaard E, Mavrikakis M, Besenbacher F (2010) Surf Sci 604:11
14. Merte LR, Knudsen J, Eichhorn FM, Porsgaard S, Zeuthen H, Grabow LC, Laegsgaard E, Bluhm H, Salmeron M, Mavrikakis M, Besenbacher F (2011) J Am Chem Soc 133:10692
15. Nilius N, Rienks EDL, Rust HP, Freund HJ (2005) Phys Rev Lett 95:066101
16. Giordano L, Pacchioni G, Goniakowski J, Nilius N, Rienks EDL, Freund HJ (2008) Phys Rev Lett 101:026102
17. Berdunov M, Mariotto G, Balakrishnan K, Murphy S, Shvets IV (2006) Surf Sci 600:L287
18. Lin X, Nilius N (2008) J Phys Chem C 112:15325
19. Joseph Y, Ranke W, Weiss W (2000) J Phys Chem B 104:3224
20. Leist U, Ranke W, Al-Shamery K (2003) Phys Chem Chem Phys 5:2435
21. Merte LR, Peng C, Bechstein R, Rieboldt F, Farberow CA, Grabow LC, Kudernatsch W, Wendt S, Laegsgaard E, Mavrikakis M, Besenbacher F (2012) Science 336:889
22. Merte LR, Bechstein R, Peng G, Rieboldt F, Farberow CA, Zeuthen H, Knudsen J, Laegsgaard E, Wendt S, Mavrikakis M, Besenbacher F (2014) Nat Commun 5:4193
23. Sun YN, Qin ZH, Lewandowski M, Carrasco E, Sterrer M, Shaikhutdinov S, Freund H (2009) J Catal 266:359
24. Fu Q, Li WX, Yao Y, Liu H, Su HY, Ma D, Gu XQ, Chen L, Wang Z, Zhang H, Wang B, Bao X (2010) Science 328:1141
25. Sun YN, Giordano L, Goniakowski J, Lewandowski M, Qin ZH, Noguera C, Shaikhutdinov S, Pacchioni G, Freund HJ (2010) Angew Chem Int Ed 49:4418
26. Giordano L, Lewandowski M, Groot IMN, Sun YN, Goniakowski J, Noguera C, Shaikhutdinov S, Pacchioni G, Freund HJ (2010) J Phys Chem C 114:21504
27. Lewandowski M, Sun YN, Qin ZH, Shaikhutdinov S, Freund HJ (2011) Appl Catal A 391:407
28. Lewandowski M, Groot IMN, Shaikhutdinov S, Freund HJ (2012) Catal Today 181:52
29. Giordano L, Pacchioni G, Noguera C, Goniakowski J (2013) Top Catal 56:1074
30. Giordano L, Pacchioni G, Noguera C, Goniakowski J (2014) ChemCatChem 6:185

31. Ringleb F, Fujimori Y, Wang HF, Ariga H, Carrasco E, Sterrer M, Freund HJ, Giordano L, Pacchioni G, Goniakowski J (2011) J Phys Chem C 115:19328
32. Nyholm R, Andersen JN, Johansson U, Jensen BN, Lindau I (2001) Nucl Instrum Methods A 467:520
33. Schnadt J, Knudsen J, Andersen JN, Siegbahn H, Pietzsch A, Hennies F, Johansson N, Mårtensson N, Öhrwall G, Bahr S, Mähl S, Schaff O (2012) J Synchotron Radiat 19:701
34. Denecke R, Väterlein P, Bässler M, Wassdahl N, Butorin S, Nilsson A, Rubensson JE, Nordgren J, Mårtensson N, Nyholm R (1999) J Electron Spectro Relat Phenom 101:971
35. Zeuthen H, Kudernatsch W, Peng G, Merte LR, Ono LK, Lammich L, Bai Y, Grabow LC, Mavrikakis M, Wendt S, Besenbacher F (2013) J Phys Chem C 117:15155
36. Björneholm O, Nilsson A, Tillborg H, Bennich P, Sandell A, Hernnäs B, Puglia C, Mårtensson N (1994) Surf Sci 315:L983
37. Joseph Y, Kuhrs C, Ranke W, Ritter M, Weiss W (1999) Chem Phys Lett 314:195
38. Liu P, Kendelewicz T, Brown GE, Nelson EJ, Chambers SA (1998) Surf Sci 417:53
39. Sirotti F, Rossi G (1994) Phys Rev B 49:15682
40. McIntyre NS, Zetaruk DG (1977) Anal Chem 49:1521
41. Merte LR, Shipilin M, Ataran S, Blomberg S, Zhang C, Mikkelsen A, Gustafson J, Lundgren E (2015) J Phys Chem C 119:2572
42. Liu BH, Boscoboinik JA, Cui Y, Shaikhutdinov S, Freund HJ (2015) J Phys Chem C 119:7842
43. Schnadt J, Knudsen J, Hu XL, Michaelides A, Vang RT, Reuter K, Li Z, Lægsgaard E, Scheffler M, Besenbacher F (2009) Phys Rev B 80:075424
44. Wendt S, Schaub R, Matthiesen J, Vestergaard EK, Wahlström E, Rasmussen MD, Thostrup P, Molina LM, Laegsgaard E, Stensgaard I, Hammer B, Besenbacher F (2005) Surf Sci 598:226
45. Laan GVD, Kirkman IW (1992) J Phys Condens Matter 4:4189
46. Cressey G, Henderson CMB, Laan GVD (1993) Phys Chem Miner 20:111
47. Bluhm H (2010) J Electron Spectrosc Relat Phenom 177:71
48. Shaikhutdinov S, Ritter M, Weiss W (2000) Phys Rev B 62:7535
49. Waddill GD, Ozturk O (2005) Surf Sci 575:35
50. Corneille JS, He JW, Goodman DW (1995) Surf Sci 338:211
51. Ketteler G, Ranke W (2003) J Phys Chem B 107:4320
52. Khan NA, Matranga C (2008) Surf Sci 602:93
53. Deng X, Lee J, Wang C, Matranga C, Aksoy F, Liu Z (2011) Langmuir 27:2146
54. Qin ZH, Lewandowski M, Sun YN, Shaikhutdinov S, Freund HJ (2008) J Phys Chem C 112:10209
55. Walton AS, Fester J, Bajdich M, Arman MA, Osiecki J, Knudsen J, Vojvodic A, Lauritsen JV (2015) ACS Nano 9:2445

Paper V

Ultrathin stepped iron oxide films grown on high index Pt surfaces – a new catalytic model system

Elin Grånäs,[*,†,§] Niclas Johansson,[‡] Mohammad A. Arman,[‡] Jacek Osiecki,[¶] Karina Schulte Thånell,[¶] Jesper N. Andersen,[‡,¶] Joachim Schnadt,[‡] and Jan Knudsen[*,‡,¶]

†*Deutsches-Elektron Synchrotron (DESY), Hamburg, Germany*
‡*Division of Synchrotron Radiation Research, Department of Physics, Lund University, Lund, Sweden*
¶*MAX IV Laboratory, Lund University, Lund, Sweden*
§*Division of Synchrotron Radiation Research, Department of Physics, Lund University, Lund, Sweden*

E-mail: elin.granaes@desy.de; jan.knudsen@sljus.lu.se

Abstract

Here we present a new type of model system that mimic the edge sites found on iron oxide surfaces. By growing FeO on vicinal Pt(322) we demonstrate that it is possible to grow homogeneous FeO films with (111) micro-terasses and a high density of homogeneous FeO edge sites. In contrast, to previous work on FeO islands grown on metal substrates which leads to different FeO-metal edge sites, the FeO edge sites created here are identical FeO-FeO sites. These pristine FeO-FeO edge sites are spectroscopically almost invisible, but their presence and high catalytic activity becomes evident upon dosing water. Water dosing at low temperature leads to a large amount of hydroxyl groups when FeO-FeO edge sites are present. We therefore suggest that the pure FeO-FeO sites are terminated by under coordinated Fe atoms similar to what previously has been observed for FeO-metal sites.

Introduction

Iron oxides have potential applications in heterogeneous catalysis, where they have been shown to be active for, e.g. CO oxidation, preferential oxidation of CO (PROX) in excess of H_2, and the water-gas shift reaction (WGS).[1,2] To enable targeted catalyst development, it is necessary to achieve a basic understanding of the relationship between the catalytic function and the atomic structure and composition of the oxide material. To directly and systematically study the structure-reactivity relationship, metal supported ultrathin, nanostructures are commonly used as model surfaces.[3–5]

For planar iron oxide on metal supports the growth mode, surface structure, and defects have been extensively characterized and hence, methods to grow highly perfect epitaxial FeO films have been developed[6–16] and demonstrated on a variety of different metal substrates, such as Pt(111),[10] Cu(100),[17] Ru(0001),[18] Ag(111),[19,20] and Ag(100).[21] Studies on ultrathin iron oxide islands show that coordinatively unsaturated metal sites at edges of the islands are important for the observed

activity.[3,22–24] However, the exact structure of the catalytic active, under-coordinated FeO sites have not been identified experimentally. There are several difficulties with studying the edge sites on such oxide islands, mainly: i) the low number of edge atoms compared to atoms in the basal plane, giving a very low measured signal from the edges compared to the basal plane when using averaging techniques. ii) these systems contain many different edge sites making it very challenging to identify the most active site, and iii) the edge sites are in direct contact with the metal substrate which can heavily modify their properties.

Iron oxide growth on Pt(111) has been extensively studies in the past with a variety of techniques, see for example refs.[10,15,16] and references therein. On Pt(111), FeO grows in a layer-by-layer mode up to approximately 2.5 ML, after which islands of Fe_3O_4 grows on top of and in to the FeO layers.[25] The principle of growing vicinal oxide thin films by using a vicinal single crystals as support has been demonstrated for, for example, MgO, FeO_X, and VO_x.[5,18,26] Ketteler *et al.*[27] shows that FeO has the same general growth behaviour on Pt(9 11 11) as on Pt(111). However, they found that growth of FeO induces step bunching of the substrate and that the FeO does not overgrow the steps.

In this paper, we present an investigation of the growth and reactivity of a vicinal FeO/Pt(322) surface using X-ray photoelectron spectroscopy (XPS), X-ray absorption spectroscopy (XAS), low energy electron diffraction (LEED), and scanning tunnelling microscopy (STM). We show that an highly stepped FeO(111) phase forms when FeO is grown on Pt(322) and that this phase share the symmetry of planar FeO along the step edges, while it is modified orthogonal to the step direction. Further, we show that the well-defined FeO oxide steps sites is equivalent to approximately 20 % of the FeO surface atoms and the produced oxide serves well as a model system for the studies of edge site chemistry, without influence from the substrate. Finally, spectroscopic and microscopic fingerprints are reported.

For the aforementioned PROX and WGS reactions, hydroxyl groups on the oxide surface are important intermediate species. There are numerous publications that have dealt with interactions between the oxide surface and water. Full monolayers planar FeO(111) is known to interact only weakly with H_2O at UHV conditions, while the more oxidised FeO_2 films are very active for water splitting.[28–30] It has also been shown that reduced FeO(111) films[31] and FeO(111) islands on metal substrates[23,32] dissociate water already at UHV conditions. In the case of FeO(111) islands. Deng et al.[23] showed that it is the under coordinated Fe atoms located at the edges of FeO islands that are active for water splitting and Fu et al.[3] has shown that these edge sites also are active for CO oxidation. When studying FeO islands, the edge sites are, of course, in contact with the metal substrate, which may heavily influence the activity of these sites. There is hitherto no study showing if pure FeO-FeO edge sites are also active for water splitting. With the edge sites of the oxide proven to be catalytically active, a natural next step is to investigate surfaces rich in such features. However, generally speaking, studies of vicinal oxide surfaces and their interaction with water, are very scarce despite the unique possibility of atomic scale control of defect (edge) geometry and chemistry. Of other oxides, TiO_2 is the most well-studied both experimentally and theoretically, with respect to the influence of steps and oxygen defects on the interaction between the surface and water.[33–35] Here, the oxygen vacancies on oxide-oxide steps have been shown to be active for water dissociation.[35]

Following the characterization of the FeO-FeO edge sites FeO/Pt(322) we also report on our water adsorption and dissociation study. Through comparisons with FeO/Pt(111) we present unambiguous evidence that pure FeO-FeO edge sites like FeO-metal edge sites also are activity for the water splitting reaction at low temperature.

Experimental details

In our experiments two types of crystals were used: Pt(111) and Pt(322). Pt(322) is a vicinal surface consisting of terraces in the (111) plane and (100) steps. Characterisation of the Pt(322) crystal by STM (see supplementary) gives the average distance between the step edges to be $d_{Pt} = 12.6 \pm 1.5$ Å.

Prior to iron oxide growth the crystals were cleaned with cycles of Ar^+ sputtering at room temperature followed by annealing in $1{\cdot}10^{-7}$ mbar of O_2 at 625 °C [Pt(111)] and 600-670 °C [Pt(322)]. The Pt(111) crystal was also flash annealed to 730 °C after O_2 exposure.

The iron oxide was grown by e-beam deposition of Fe followed by oxidation at 600°C in $1{\cdot}10^{-6}$ mbar O_2. The deposition rates yielded less than 0.2 monolayers (ML) of FeO per minute of Fe deposition. In the XPS measurements, the evaporator was calibrated by FeO growth on Pt(111), where the formation of a complete monolayer was confirmed by the absence of adsorbed CO after exposure to 75 L at room temperature. In the STM measurements the coverage was calibrated by checking for full coverage of FeO in the images. Ketteler et al.[27] have shown that a higher surface order is obtained for low deposition rates (in their case 0.06 ML/min) when growing FeO on a vicinal substrate.

The XPS and XAS measurements were carried out at the I311 beamline[36] at the MAX IV Laboratory. All XP-spectra were collected in normal emission with photon energies of 635 eV for O 1s and 850 eV for Fe 2p. The total energy resolution for the respective core levels, including the light and analyzer, are 130 meV and 320 meV. The O 1s XP spectra were curve fitted using convoluted Doniach-Šunjić and Gaussian functions. Prior to curve fitting a linear background was subtracted from the spectra. During fitting the Lorentzian full width at half maximum for the O 1s core levels was fixed to 0.18 eV, in accordance with ref.[37] The peak positions of the second layer (O_S), and edge (O_E) components were determined from difference spectra [see figure 4(a) and (b)] and kept fixed during curve fitting.

The Fe L-edge X-ray absorption (XA) spectra were collected in normal incidence in Auger yield mode by recording electrons of kinetic energies of between 540 and 550 eV using a Scienta SES 200 electron energy analyzer. The energy scale was calibrated by measuring the Pt 4f core level excited by first- and second order light with a resulting accuracy of 50 meV. A linear background was curve fitted to the pre-edge of each XA spectrum to accommodate for the Pt-background and to calibrate for the response of the crystal, the XA spectra were divided by a XA spectrum acquired of the corresponding clean Pt crystal. All XA spectra are normalized to the continuum of states assigned to the last point of each spectrum. The XA spectra are not normalized to the beamline transmission and, hence, the spectra will only be discussed qualitatively.

The STM measurements were carried out using a commercial Omicron STM1 operated at room temperature. All images shown were recorded in constant current mode. Image post processing was made with the ImageJ software. The base pressure in both vacuum chambers was below $1{\cdot}10^{-10}$ mbar.

Results and discussion

Growth and characterization of FeO on Pt(322)

Before turning to the structure of iron oxide supported by Pt(322) we briefly revisit its growth and structure on Pt(111). FeO(111)/Pt(111) has been extensively studied in the past with a variety of techniques, such as LEED, STM, and XPS. See for example refs.[10,15,16] and references therein. FeO grown on Pt(111) forms a hexagonal bilayer consisting of alternating Fe and O planes, with the Fe^{2+} cations occupying all available octahedral sites between the oxygen atoms. The lattice parameter of FeO is approximately 12 % larger than that of Pt(111) [∼3.1 Å and 2.77 Å resp.], which gives rise to a $(\sqrt{91} \times \sqrt{91})R5.2°$ superstructure with a lattice parameter of ∼26 Å. This superstructure is seen as a hexago-

nal rosette pattern near the substrate spots in LEED images. The superstructure unit cell contain three high symmetry domains, defined by the latteral position of the FeO layer with respect to the underlying Pt substrate. The so called TOP domain has Fe-atoms located atop Pt-atoms, while O-atoms occupy hollow sites with respect to the Pt(111) surface. In the HCP and FCC domains the Fe-atoms are located in hollow sites, while the O-atoms are situated in atop and hollow sites, respectively.

With the FeO/Pt(111) structure in mind, we now turn our attention to the FeO film grown on Pt(322). Figures 1(a) and (b) show selected LEED- and STM images acquired after the growth a FeO film that covers the entire Pt(322) surface. As no Pt(111) patches not covered by FeO are observed, we conclude that the FeO(111) coverage is slightly above 1 ML (see experimental section for coverage calibration).

Starting with the analysis of the LEED image in figure 1(a), it displays relatively sharp and well-defined diffraction spots, indicating a well-ordered surface structure. A closer inspection of the rosette spots formed due to the lattice mismatch between FeO and Pt(322) reveals that they are aligned in the direction of the step edge spacing (highlighted with blue dotted line in the figure). Therefore, we expect the atomic rows of FeO to align along the substrate step direction in real space. The rosette spots are, however, not rotational aligned along the two other high symmetry directions of the substrate, as the superimposed magenta dotted lines in the figure highlight. This observation is very peculiar as it suggests that rotational misalignment of the atomic rows of FeO rotated $\pm 60°$ with respect to the lines running along the step edges. As a result the FeO lattice must be non-uniform with slightly different lattice constants/angels in different directions. Finally, we note that the absence of spot splitting or smearing in the rosette spots indicates that the superstructure periodicity coincide with the periodicity of the surface steps. As we observed slightly different LEED images for different preparations of FeO(111) on Pt(322), we refrain from a detailed analysis and suggesting of a structural model in this work. Instead, we note that the analysis of LEED images from several FeO preparations reveal that the average distance between step edges is 12.7 Å, which fits well with the measured distance for the clean Pt(322) surface without any FeO(111) cover (see figure S1 in the SI). Therefore, we have to conclude that the growth of FeO(111) on Pt(322) do not induce any significant step bunching. The LEED analysis also reveals an average atomic spacing of the FeO lattice of approximately 3.1 Å fitting well with the values reported on clean Pt(111).

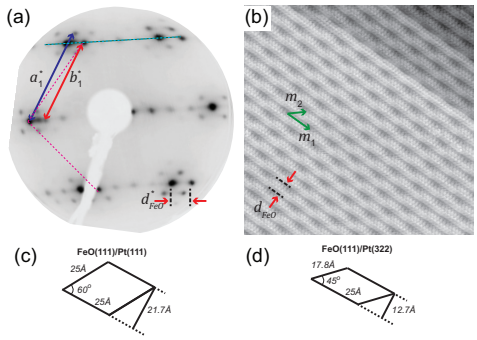

Figure 1: (a) LEED pattern of FeO/Pt(322), taken at 52 eV. a_1^* and b_1^* represent the interatomic spacing in Pt(322) and FeO respectively. d_{FeO}^* corresponds to the average distance between step edges. The satellite spots around the FeO spots originate from the superstructure. (b) STM image of FeO/Pt(322) with the lattice vectors of the superstructure (m_1 and m_2) and the step distance (d_{FeO}) marked. 20×20 nm^2. (c) Moiré unit cell of FeO(111) grown on Pt(111). (d) Moiré unit cell of FeO(111) grown on Pt(322).

Following the LEED analysis, we continue with the STM characterization. As expected from the LEED investigations; STM survey images of the FeO films grown on Pt(322) display large areas of a well-ordered stepped FeO(111) film. A small fraction of less well-ordered areas are, however, also observed. These areas contain an increased number of kinks, double steps, and terraces of 2-3 times the width. We conclude, however, both based on the well-ordered LEED images and our STM survey of the sample, that the large fraction of the surface

is covered by well-ordered stepped FeO(111). We find no evidence of induced step bunching for the FeO films on Pt(322) as Ketteler *et al.*[27] observed for submonolayer coverages on Pt(9 11 11).

An STM image from one of the well-ordered areas is shown in figure 1(b). Here, the regular steps can be seen running diagonally across the image, the step-edge-to-step-edge distance, d_{FeO}, is marked by the red arrows. In these well-ordered areas the typical distance between step edges is 11 Å, although occasionally well-ordered areas with a step periodicity of 9 Å are also observed. In the upper right corner of the image two underlying double steps of the Pt(322) are observed below the FeO(111) film. On the terraces the characteristic moiré superstructure of the FeO(111) film is observed as dark-bright undulations. The moiré unit-cell vectors of this superstructure is marked by m_1 and m_2. Clearly, the m_1 vector is very well rotationally aligned with the orientation of the underlying Pt steps and the atomic rows of FeO(111) must, therefore, also be aligned with underlying steps, in agreement with what was concluded based on the LEED analysis. Parallel to the step direction, the lattice distance of the superstructure, m_1, is approximately 25 Å. This is almost identical to what is observed for FeO(111) when grown on Pt(111). In contrast, the moiré lattice distance is significantly affected in the other high-symmetry direction (m_2) where we measure a distance of approximately 17 Å.

The reason for the asymmetric moiré structure can quite easily be understood. In the direction parallel to the step edges of Pt(322), the FeO(111) film growth is unperturbed and the lattice distance of the moiré unit cell is therefore almost unchanged (~ 25 Å) as compared to FeO(111) grown on Pt(111). In contrast, the moiré structure growth is perturbed in the orthogonal direction by the steps separated by 12.7 Å inducing a constrain on the repeating unit. Having a moiré unit cell distance along the step edges of 25 Å, and requiring the orthogonal constraint, results in the moiré cell sketched in fig. 1(d), which should be compared with the unit cell of FeO(111) sketched in panel (c). As seen from the this unit cell, we should measure a periodicity of 17.8 Å at $\pm$ 45° directions with respects to lines running along the step edges. This fits excellent with the measured distance of the m_2 vector and the measured angle between the m_1 and the m_2 vectors of 45°–50°. Further, this is also consistent with our observations from the LEED analysis.

In figure 2(a) a higher resolved STM image is displayed, where the atomic structure of the FeO films can be observed. Here, it is seen that parallel to the steps there are four atomic rows per terrace. In the upper right corner of figure 2(a), the hexagonal atomic lattice of FeO is highlighted, with the blue balls positioned atop of the bright protrusions.

Studies of FeO on Pt(111) have revealed that a number of different, tip-dependent, imaging modes are possible; modes where both atomic species are seen, as well as modes where only either Fe- or O-atoms are visible.[15] In our images, only one type of atoms appears to be visible on the terraces, however, we cannot distinguish if it is Fe- or O-atoms. Regardless of which atomic element that is visible, we can determine the lattice distance of the vicinal FeO film to be 3.1 ± 0.2 Å, as illustrated by the line scan in figure 2(b). This value agrees with that obtained from the LEED measurements and is in perfect agreement with what has been determined for FeO on Pt(111). The superstructure periodicity of approximately 25 Å parallel to the steps is also observed in the line scan in figure 2(b).

In the STM image in figure 2(a) bright zigzag rows are observed at the step edges. These are most likely attributed to confined electronic edge states. In future studies it would be interesting to study this effect using density functional theory simulated STM images. As already meantioned in the discussion of the LEED image, we observed slightly different FeO lattice distances in LEED imaging and we therefore stop our structural discussion at this point and refrain from suggesting an atomic scale model.

To conclude, our STM and LEED characterization show that deposition of Fe onto Pt(322) followed by oxidation result in a well-ordered FeO monolayer with the FeO steps perfectly

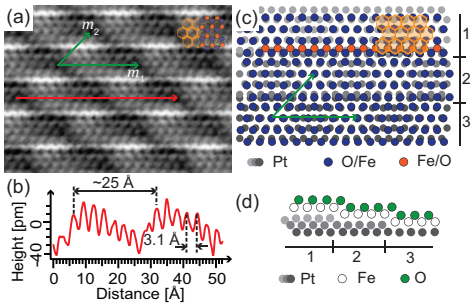

Figure 2: (a) Zoom in STM on a well ordered FeO area, 6.7×4.8 nm^2. m_1 and m_2 indicates the unit cell vectors of the superstructure. The FeO lattice is indicated in the upper right. (b) Line profile along the red line in (a). (c) Ball model of the FeO layer on Pt(322). The Pt-atoms are grey, while the dark blue balls represent the atoms visible in the STM image. On terrace 1 the row of orange balls shows the second element, which is also visible at the step edge in (a). (d) Side view of the model, the Fe-atoms and O-atoms are represented by white and green balls, respectively.

aligned to the substrate steps. Instead of the hexagonal 26×26 Å^2 superstructure observed for FeO(111) on Pt(111), FeO growth on Pt(322) results an asymmetric moiré super structure identical to FeO(111) grown on Pt(111) in the direction along the Pt steps, but perturbed in the orthogonal direction by the step density modulation leading to 25×17 Å superstructure.

Having finished the structural characterization of FeO grown on Pt(322), we now continue with the discussion of our spectroscopic studies of the film. First of all, it is important to verify that the film is a pure FeO film when grown on Pt(322) and share the spectroscopic fingerprints with the film grown on planar Pt(111). Secondly, it is interesting to answer whether or not it is possible to observe spectroscopic evidence for the edge atoms that are minority species with respect to atoms found on the micro terasses. The relative number of these edge atoms is, however, high compared to previous studies of FeO islands and we therefore have fair chance for success here. For comparison, the study by Fu et al. discussed in the introduction[3] had a maximum perimeter density of 0.3 nm/nm^2, while we measure a perimeter density of 0.45 nm/nm^2 in figure 2(b) of one specific edge site.

Starting with the spectroscopic signatures of the Fe atoms in the film the comparison of Fe 2p XP spectra acquired on FeO grown on the stepped and planar substrate are shown in figure 3(a). Clearly the spectra are near-identical with similar peak binding energy positions and shapes. In more detail Fe $2p_{3/2}$ and Fe $2p_{1/2}$ components are observed at 709.0 eV and 722.5 eV, respectively. Between the two components, Fe satellites are observed which originate from a coupling of the iron core hole to the valence band. Further, the Pt 4s peak is observed at 725 eV and overlaps with the Fe $2p_{1/2}$ component. The position of the observed Fe $2p_{3/2}$-peak is very close to what has been found for Fe^{2+}[38] (709 eV compared to 708.4 eV), which is the expected oxidation state of Fe in FeO. The absence of elemental Fe at 706.6 eV shows that the iron is completely oxidized both when grown on the (111) and (322) Pt surfaces. The more oxygen rich iron oxides hematite (Fe_2O_3) and magnetite (Fe_3O_4) contains only Fe^{3+} and a mixture of Fe^{2+} and Fe^{3+}, respectively. Fe^{3+} is generally located at a Fe $2p_{3/2}$ binding energy of 710.2 eV, and the overall Fe 2p spectra for hematite and magnetite differs significantly from that of FeO.[7] To summarize, we do not observe any spectroscopic evidence for different Fe ions in the FeO film grown on Pt(322) as compared to films grown on Pt(111) from our Fe 2p XP spectra.

XAS measurements are usually very sensitive to the oxidation states. In an effort to see the spectroscopic evidence for the edge sites, we performed XAS measurements of the vicinal FeO film. Figure 3(b) compares Fe L-edge XA spectra acquired of FeO/Pt(322) and FeO/Pt(111) systems. Furthermore, a reference acquired on a trilayer FeO_2/Pt(111) oxide film that has a mixture of Fe^{2+} and Fe^{3+} ions[30] is included to have a clear reference for where Fe^{3+} ions should be observed. Similar to the XP spectra, the XA spectra are very similar for

the flat and stepped FeO films. The L_3 resonance is observed at a photon energy of 708.7 eV both for the flat and stepped FeO film and we find no evidence for a component at 709.5 eV in the spectrum from the FeO/Pt(322) film, as observed on the FeO_2 film. Therefore, we conclude that the oxidation state of the stepped FeO/Pt(322) film is pure Fe^{2+} in analog with planar FeO film.

To conclude the analysis of the Fe spectra, the peak position and shape of the Fe 2p spectrum concomitant with the Fe L-edge appearance reveal that film indeed is pure FeO when grown on Pt(322), and magnetite and/or hematite formation induced by the stepped substrate can be excluded. This is contrast to the findings of Ketteler *et al.*,[27] where Fe_3O_4 nucleation was observed already at low coverages. Secondly, we honestly have to say that we are unable to identify any reliable spectroscopic fingerprint of edge-states in our Fe spectra, i.e. as judged from the Fe 2p XP and XA spectra, FeO(111) films grown on Pt(111) and Pt(322) are indistinguishable.

Having finished the analysis of the Fe spectra we continue with the analysis of O 1s spectra acquired for the stepped (FeO/Pt(322)[red]) and planar (FeO/Pt(111)[black]) films (see figure 4(a)). Both spectra show an asymmetric peak with intensity maximum located at approximately 529.4 eV in agrement with previous studies on FeO(111)/Pt(111).[30] Towards higher binding energies, the shape of the spectra are identical for stepped and planar FeO. However at the lower binding energy side the stepped FeO/Pt(322) displays a slight increase in intensity. The blue curve in figure 4(a) corresponds to the difference between the two spectra; here a component located at 529.0 eV can clearly be seen.

At this point it is tempting to assign the 529.0 eV component to oxygen atoms found at the step edges. It is, however, important to remember that the FeO(111) films we prepared have coverages slighly above 1 ML. An alternative reason for the low BE component could, therefore, be a slighly higher coverage of FeO when grown on Pt(322), which could lead to more double-layered FeO having different O 1s components. To excluded this explanation, we prepared a thicker FeO films on Pt(322). In figure 4(b) the O 1s XP spectra of a 2 ML FeO/Pt(322) [red] and 1 ML FeO/Pt(322) [black] are compared. The O 1s spectra of the 2 ML film clearly has an increased intensity on the high binding energy side of the peak, while the spectra are identical at lower binding energies. The blue curve in figure 4(b) shows the difference between the 1 and 2 ML spectra, where the second layer of FeO give rise to a peak located at 529.95 eV.

Based on the comparison of O 1s spectra acquired on well-ordered 1 and 2 ML FeO(111) films grown on Pt(322) and Pt(111) discussed above, the peak assignment becomes clear: O atoms located at FeO terraces ($O_T = 529.4$ eV),

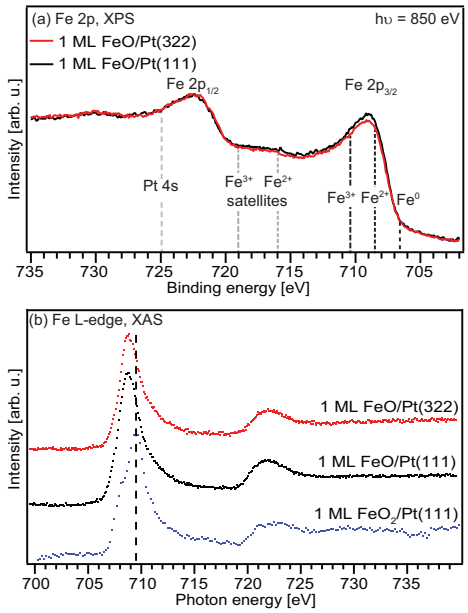

Figure 3: (a) Fe 2p spectra of 1 ML of FeO on Pt(322) [red] and Pt(111) [black]. The dashed lines indicate the binding energy of the indicated specie. (b) XA spectra acquired from FeO/Pt(322)[top], FeO/Pt(111)[middle] and trilayer FeO_2/Pt(111)[bottom]. The FeO_2/Pt(111) XA spectrum is adopted from ref.[30]

O atoms in FeO layers sandwiched between surface FeO and underlying Pt (O_S = 529.95 eV), and finally O atoms located at step edges (O_E = 529.0 eV). Using these 3 components, the measured spectra can be well reproduced for all FeO films on Pt(111) and Pt(322), as can be seen for 1 and 2 ML of FeO/Pt(322) in figure 4 (c) and (d). For the 1 ML FeO(111) film, our curvefitting reveals that the relative area of the edge component, O_E, corresponds to 10-15 % of the total oxide area, which fit well with the expected value based on the STM imaging, remembering that photoelectron diffraction easily can modify the measured intensities significantly. For 2 ML of FeO on both Pt(111) and Pt(322) the area of the O_S component corresponds to approximately 27 % of the total oxide area. The intensity of this component correlates linearly with the deposited FeO coverage fitting well with the assignment.

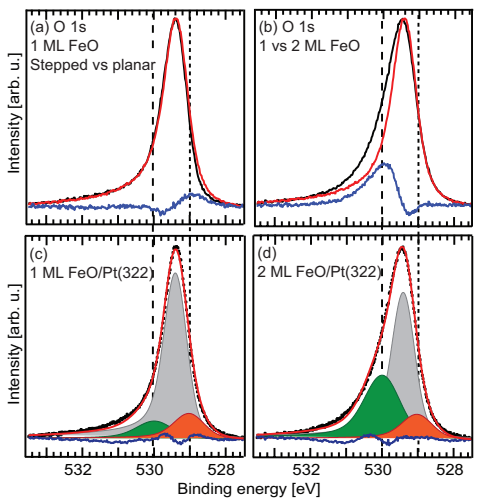

Figure 4: (a) O 1s spectra of 1 ML FeO/Pt(322) [red], 1 ML FeO/Pt(111) [black], and difference spectrum [blue] (b) O 1s spectra of 1 ML FeO/Pt(322) [red], 2 ML FeO/Pt(322) [black], and difference spectrum [blue] (c) 1 ML FeO/Pt(322) and (d) 2 ML FeO/Pt(322) fitted with three components corresponding to oxygen on FeO terraces [grey], FeO step edges [green], and FeO second layer [orange], respectively.

To summarize our spectroscopic data analysis, we showed that vicinal FeO forms on Pt(322) without forming magnetite or hematite, as only Fe^{2+} is observed in both XPS and XAS. In fact, FeO films grown on Pt(322) and Pt(111) have very similar spectroscopic fingerprints and it is almost impossible to observe any difference between the stepped and planar FeO films. The only difference we are able to detect is a weak O_E component in the O 1s component observed as a small broadening at the low energy side of the main peak in the raw spectrum.

Water adsorption on planar and stepped FeO

From the STM imaging we now know that the stepped FeO(111) grown on Pt(322) contains a relatively large amount of step sites, while the spectroscopic characterization revealed that it almost is impossible to observe spectroscopic evidence for the FeO edge sites. An interesting question that remains to be addressed is whether the FeO edge sites have different catalytic properties than the planar FeO(111) surface, which is known to very inert.[7,30] To probe this, we exposed FeO films grown on Pt(322) and Pt(111) to water and used XPS to study the ability of the film to dissociate water. As previously the coverage of the FeO/Pt(322) film was tuned to 1.1 ML, so the only edge sites present on the surface are pure FeO-FeO edge sites - i.e. the oxide edge sites have no direct contact to the metal substrate. Thus, both planar and stepped FeO(111) only have FeO sites exposed to the water, and any difference between the films will be due to the high number of edge sites on the stepped film.

Initially, the two films were exposed to $5 \cdot 10^{-9}$ mbar of H_2O at successively decreasing temperatures while acquiring O 1s spectra, to find the onset temperature for water adsorption, seen as an O 1s component with a BE close to 532.5 eV. For the planar FeO surface, we found the onset of water adsorption starts at -110 °C (see figure S2 in the SI), while it starts at slightly higher temperature (-95 °C) for stepped FeO. The reason for this temperature difference will

be discussed below.

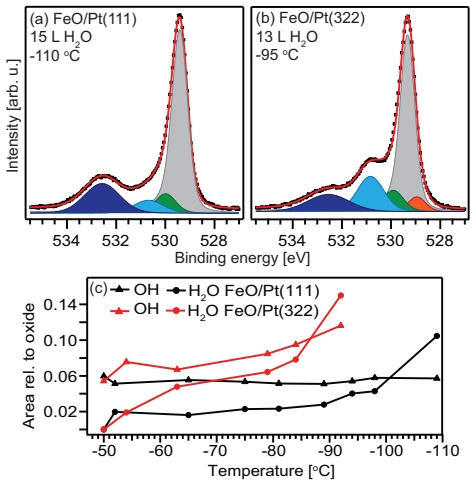

Figure 5: (a) 1 ML FeO/Pt(111) exposed to totally 7.5 L (5e-9 mbar) of H_2O at decreasing temperature, followed by and exposure of 7.5 L at -110 C. (b) 1.1 ML FeO/Pt(322) exposed to 5.5 L (5e-9 mbar) of H_2O at varying temperature, followed by and exposure of 7.5 L at -95 C. The data is shown as black markers, the fitted curve is represented by a red line and the fitted components are: O_T - grey, O_E - orange, O_S - green, O_{OH} - light blue, O_{H_2O} - dark blue. (c) Areas of O_{OH} and O_{H_2O} of the two FeO films during H_2O exposure in 5e-9 mbar at decreasing temperatures. Lines between the markers are only to guide the eye.

After identifying the onset temperature for water adsorption on the two samples, they were exposed to an additional dose of 7.5 L water at this temperature. FeO/Pt(322) was exposed to in total 13 L, with the 7.5 L dosed at -95 °C, while FeO/Pt(111) was exposed to in total 15 L with the 7.5 L dosed at -110 °C. The resulting O 1s spectra are displayed in 5(a) and (b). Here the difference between the two spectra is obvious. For the FeO/Pt(111) film only one peak, located at 532.5 eV and assigned to adsorbed H_2O, can be seen aside from the main oxide peak. In contrast for the FeO/Pt(322) film there is an additional peak located at 530.8 eV and assigned to OH groups.[39]

The two spectra were fitted using the previously discussed O_T, O_E, O_S, and two additional components: O_{OH} shifted +1.3 and +1.5 eV from O_T for FeO/Pt(111) and FeO/Pt(322), respectively, and O_{H_2O} shifted 3.2 eV from O_T. The variations in the peak position of OH is most likely due to coverage differences, as observed on other surfaces. On the stepped FeO film, the area of the OH component is 24 % relative to the total oxide signal, while it is only 10 % on the planar FeO film. As can be seen from figure 5(c), this differnece in OH coverage is not due to the different temperatures of the exposure. The area of the H_2O component corresponds to 26 % and 18 % of the total oxide area for FeO/Pt(111) and FeO/Pt(322) respectively.

To summarize, we now found clear spectroscopic evidence for a much larger fraction of OH groups on stepped FeO as compared with the planar oxide surface upon low temperature water exposure. In contrast, it is almost impossible to observe any spectroscopic evidence for the pristine step sites. With these two observations in mind, it is interesting to discuss the atomic scale nature of the FeO edge sites. First of all, the water dissociation at the edge sites suggest that water molecules can adsorb at step sites and subsequently dissociate suggesting that the step sites are Fe terminated. Naturally, the water dissociation will stop once all Fe terminated edge sites are covered by oxygen supplied by the adsorbing water molecules. Secondly, as we expect water molecules to adsorb stronger to Fe terminated edge sites, we expect a higher onset temperature for water adsorption fitting well with our observations.

Conclusions

In conclusion, we have shown that it is possible to grow a new catalytic model system consisting of well-ordered vicinal FeO films on Pt(322), containing a large fraction of identical FeO-FeO step sites. LEED and STM characterization of this FeO film grown on Pt(322) revealed an asymmetric moiré structure identical to FeO(111) grown on Pt(111) in the direc-

tion along the Pt steps, but perturbed in the orthogonal direction by the step density modulation. The spectroscopic fingerprint for the FeO edge sites is, however, weak and almost undetectable for the pure and stepped FeO(111) surface. Only in the O 1s we detect a weak O_E component that we assign to oxygen edge atoms. The spectroscopical invisible FeO edge sites becomes, however, very visible upon low temperature water exposure as they are able to dissociate water very well in contrast to the otherwise inert FeO(111) basal plane, suggesting Fe termination of the edge sites in contrast to the oxygen terminated basal plane. Altogether, our study suggests that pure FeO-FeO step sites are coordinatively unsaturated and, therefore, catalytic active in the same way as what has been found previously for FeO-metal sites. Our work opens up for detailed future studies where FeO edge site chemistry is studied in detail. The catalytic properties of pure FeO-FeO edge sites can for example be compared with FeO-metal edge sites in a systematic way to probe the effect of the substrate on the edge site. Further, it is very likely that the growth recipe can be extended to other known ultrathin films.

Acknowledgement

Financial support from the Swedish Research Council is acknowledged (project grant 2012-3850). The MAX IV Laboratory personnel are acknowledged for support during measurements.

References

(1) Shaikhutdinov, S.; Freund, H.-J. *Annual Review of Physical Chemistry* **2012**, *63*, 619–633.

(2) Pacchioni, G. *Chemistry - A European Journal* **2012**, *18*, 10144–10158.

(3) Fu, Q.; Li, W.-X.; Yao, Y.; Liu, H.; Su, H.-Y.; Ma, D.; Gu, X.-K.; Chen, L.; Wang, Z.; Zhang, H.; Wang, B.; Bao, X. *Science* **2010**, *328*, 1141–1144.

(4) Freund, H.-J. *Surface Science* **2007**, *601*, 14381442.

(5) Schoiswohl, J.; Sock, M.; Chen, Q.; Thornton, G.; Kresse, G.; Ramsey, M. G.; Surnev, S.; Netzer, F. P. *Topics in Catalysis* **2007**, *46*, 137–149.

(6) McIntyre, N. S.; Zetaruk, D. G. *Analytical Chemistry* **1977**, *49*, 1521–1529.

(7) Weiss, W. *Surface Science* **1997**, *377-379*, 943–947.

(8) Fujii, T.; de Groot, F. M. F.; Sawatzky, G. A.; Voogt, F. C.; Hibma, T.; Okada, K. *Physical Review B* **1999**, *59*, 3195–3202.

(9) Chambers, S. A. *Surface Science Reports* **2000**, *39*, 105–180.

(10) Weiss, W.; Ranke, W. *Progress in Surface Science* **2002**, *70*, 1–151.

(11) Merte, L. R.; Knudsen, J.; Grabow, L. C.; Vang, R. T.; Laegsgaard, E.; Mavrikakis, M.; Besenbacher, F. *Surface S* **2009**, *603*, L15–L18.

(12) Santos, B.; Loginova, E.; Mascaraque, A.; Schmid, A. K.; McCarty, K. F.; de la Figuera, J. *Journal of Physics: Condensed Matter* **2009**, *21*, 314011.

(13) Giordano, L.; Lewandowski, M.; Groot, I. M. N.; Sun, Y.-N.; Goniakowski, J.; Noguera, C.; Shaikhutdinov, S.; Pacchioni, G.; Freund, H.-J. *Journal of Physical Chemistry C* **2010**, *114*, 21504–21509.

(14) Yao, Y.; Fu, Q.; Wang, Z.; Tan, D.; Bao, X. *Journal of Physical Chemistry C* **2010**, *114*, 17069–17079.

(15) Merte, L. R.; Grabow, L. C.; Peng, G.; Knudsen, J.; Zeuthen, H.; Kudernatsch, W.; Porsgaard, S.; Laegsgaard, E.; Mavrikakis, M.; Besenbacher, F. *Journal of Physical Chemistry C* **2010**, *115*, 2089–2099.

(16) Spiridis, N.; Wilgocka-Slezak, D.; Freindl, K.; Figarska, B.; Giela, T.; Mlynczak, E.; Strzelczyk, B.; Zajac, M.; Korecki, J. *Physical Review B* **2012**, *85*, 075436.

(17) Koveshnikov, A. N.; Madjoe, R. H.; Karunamuni, J.; Stockbauer, R. L.; Kurtz, R. L. *Journal of Applied Physics* **2000**, *87*, 5929–5931.

(18) Ketteler, G.; Ranke, W. *Journal of Physical Chemistry B* **2003**, *107*, 4320–4333.

(19) Waddill, G. D.; Ozturk, O. *Surface Science* **2005**, *575*, 35–50.

(20) Lewandowski, M.; Hermanowicz, M.; Michalak, N.; Miłosz, Z.; Jurga, S.; Wiesendanger, R. *ResearchGate* **2016**, *1*, 1.

(21) Merte, L. R.; Shipilin, M.; Ataran, S.; Blomberg, S.; Zhang, C.; Mikkelsen, A.; Gustafson, J.; Lundgren, E. *Journal of Physical Chemistry C* **2015**, ASAP.

(22) Biener, M. M.; Biener, J.; Schalek, R.; Friend, C. M. *Journal of Chemical Physics* **2004**, *121*, 12010–12016.

(23) Deng, X.; Lee, J.; Wang, C.; Matranga, C.; Aksoy, F.; Liu, Z. *Langmuir* **2011**, *27*, 2146–2149.

(24) Zeuthen, H.; Kudernatsch, W.; Merte, L. R.; Ono, L. K.; Lammich, L.; Besenbacher, F.; Wendt, S. *ACS Nano* **2015**, *9*, 573.

(25) Weiss, W.; Ritter, M. *Physical Review B* **1999**, *59*, 5201–5213.

(26) Kramer, J.; Tegenkamp, C.; Ernst, W.; Pfnür, H. *Surface Science* **2003**, *537*, 265–275.

(27) Ketteler, G.; Ranke, W. *Journal of Vacuum Science & Technology, A: Vacuum, Surfaces, and Films* **2005**, *23*, 1055–1060.

(28) Ringleb, F.; Fujimori, Y.; Wang, H.-F.; Ariga, H.; Carrasco, E.; Sterrer, M.; Freund, H.-J.; Giordano, L.; Pacchioni, G.; Goniakowski, J. *Journal of Physical Chemistry C* **2011**, *115*, 19328–19335.

(29) Xu, L.; Wu, Z.; Zhang, Y.; Chen, B.; Jiang, Z.; Ma, Y.; Huang, W. *Journal of Physical Chemistry C* **2011**, *115*, 14290–14299.

(30) Johansson, N.; Merte, L. R.; Grånäs, E.; Wendt, S.; Andersen, J. N.; Schnadt, J.; Knudsen, J. *Topics in Catalysis* **2016**, *1*, 1–10.

(31) Knudsen, J.; Merte, L. R.; Grabow, L. C.; Eichhorn, F. M.; Porsgaard, S.; Zeuthen, H.; Vang, R. T.; gsgaard, E. L.; Mavrikakis, M.; Besenbacher, F. *Surface Science* **2010**, *604*, 11–20.

(32) Xu, L.; Wu, Z.; Zhang, W.; Jin, Y.; Yuan, Q.; Ma, Y.; Huang, W. *Journal of Physical Chemistry C* **2012**, *116*, 22921–22929.

(33) Walle, L. E.; Ragazzon, D.; Borg, A.; Uvdal, P.; Sandell, A. *Applied Surface Science* **2014**, *303*, 245–249.

(34) Martinez, U.; Vilhelmsen, L. B.; Kristoffersen, H. H.; Stausholm-Möller, J.; Hammer, B. *Physical Review B* **2011**, *84*, 205434.

(35) Kristoffersen, H. H.; Hansen, J. O.; Martinez, U.; Wei, Y. Y.; Matthiesen, J.; Streber, R.; Bechstein, R.; gsgaard, E. L.; Hammer, F. B.; Wendt, S. *Physical Review Letters* **2013**, *110*, 146101.

(36) Nyholm, R.; Andersen, J. N.; Johansson, U.; Jensen, B. N.; Lindau, I. *Nuclear Instruments and Methods in Physics Research A* **2001**, *467 - 468*, 520 – 524.

(37) Campbell, J. L.; Papp, T. *Atomic Data and Nuclear Data Tables* **2001**, *77*, 1–56.

(38) Biesinger, M. C.; Payne, B. P.; Grosvenor, A. P.; Lau, L. W.; Gerson, A. R.; Smart, R. S. *Applied Surface Science* **2011**, *257*, 2717–2726.

(39) Kendelewicz, T.; Kaya, S.; Newberg, J. T.; Bluhm, H.; Mulakaluri, N.; Moritz, W.; Scheffler, M.; Nilsson, A.; Pentcheva, R.; G. E. Brown, J. *Journal of Physical Chemistry C* **2013**, *117*, 2719–2733.

Supplementary: Ultrathin stepped iron oxide films grown on high index Pt surfaces – a new catalytic model system

Elin Grånäs,[*,†,§] Niclas Johansson,[‡] Mohammad A. Arman,[‡] Jacek Osiecki,[¶] Karina Schulte Thånell,[¶] Jesper N. Andersen,[‡,¶] Joachim Schnadt,[‡] and Jan Knudsen[*,‡,¶]

†*Deutsches-Elektron Synchrotron (DESY), Hamburg, Germany*

‡*Division of Synchrotron Radiation Research, Department of Physics, Lund University, Lund, Sweden*

¶*MAX IV Laboratory, Lund University, Lund, Sweden*

§*Division of Synchrotron Radiation Research, Department of Physics, Lund University, Lund, Sweden*

E-mail: elin.granaes@desy.de; jan.knudsen@sljus.lu.se

Characterisation of Pt(322)

LEED images of the Pt(322) crystal [see figure S1(a)] show the expected hexagonal pattern of the (111) terraces with step-induced spot splitting. Analysis of the LEED images gives an average distance between the step edges of $d_{Pt} = 12.3 \pm 0.5$ Å. However, the LEED spots are slightly elongated in the step direction, indicating some variation in the step periodicity. The average distance between step edges as measured by STM is 12.6 ± 1.5 Å, with the terraces separated by monoatomic steps. The step edges are generally straight, but occasionally an

increased number of kinks are found. A representative STM image is shown in figure S1(b) Calculated based on geometrical consideration d_{Pt} should be 11.44 Å,[1] in fair agreement with the result on our crystal. Tränkenschu *et al.*[2] found the step spacing in Pt(322) to be 5.3 atomic rows (14.7 Å). A ball model of Pt(322) can be seen in figure S1(d).

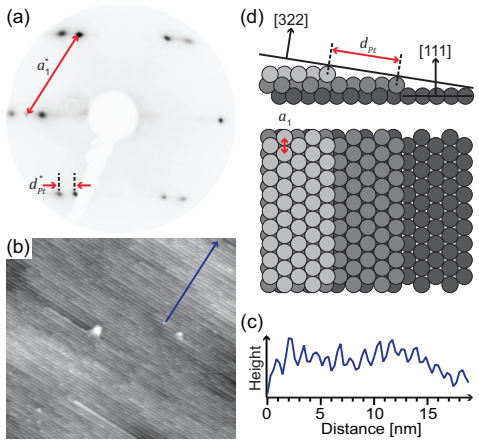

Figure S1: (a) LEED pattern of Pt(322), taken at 65 eV. The step induced spot splitting, perpendicular to the terrace direction is indicated by d^*_{Pt} and the length of the atomic unit cell by a^*_1. (b) STM image of clean Pt(322), 70×80 nm^2. (c) Line scan from the STM image along the blue line in (b). (d) Model of an ideal Pt(322) crystal with the distance d_{Pt} between steps indicated, as well as the interatomic distance, a_1, on the (111) terraces.

Water exposure

O 1s spectra of FeO/Pt(111) and FeO/Pt(322) exposed to $5 \cdot 10^{-9}$ mbar of H_2O at decreasing temperatures. The areas of the fitted components (not shown) are plotted in figure 5(c) in the article. The spectra were fitted using the same components as described in connection to figure 5(a) and (b).

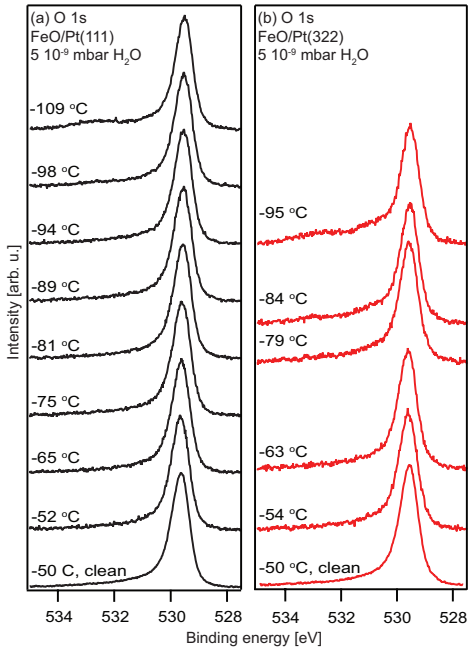

Figure S2: O 1s spectra of (a) 1 ML FeO/Pt(111) and (b) 1.1 ML FeO/Pt(322) exposed to $5 \cdot 10^{-9}$ mbar of H_2O at decreasing temperatures. The temperature are indicated at each spectrum.

References

(1) van Hove, M. A.; Somorjai, G. A. *Surface Science* **1980**, *92*, 489–518.

(2) Traenkenschuh, B.; Papp, C.; Fuhrmann, T.; Denecke, R.; Steinrück, H.-P. *Surface Science* **2007**, *601*, 1108–1117.

Paper VI

JOURNAL OF SYNCHROTRON RADIATION

ISSN 1600-5775

Received 21 September 2016
Accepted 29 November 2016

Edited by J. F. van der Veen

Keywords: RIXS; APXPS; beamlines; MAX IV.

The SPECIES beamline at the MAX IV Laboratory: a facility for soft X-ray RIXS and APXPS

Samuli Urpelainen,[a]* Conny Såthe,[a] Walan Grizolli,[a] Marcus Agåker,[b] Ashley R. Head,[c] Margit Andersson,[a] Shih-Wen Huang,[a] Brian N. Jensen,[a] Erik Wallén,[a,d] Hamed Tarawneh,[a] Rami Sankari,[a] Ralf Nyholm,[a] Mirjam Lindberg,[a] Peter Sjöblom,[a] Niclas Johansson,[c] Benjamin N. Reinecke,[c] M. Alif Arman,[c] Lindsay R. Merte,[c] Jan Knudsen,[a,c] Joachim Schnadt,[a,c] Jesper N. Andersen[a,c] and Franz Hennies[a]

[a]MAX IV Laboratory, Lund University, PO Box 118, SE-221 00 Lund, Sweden, [b]Department of Physics and Astronomy, Uppsala University, PO Box 516, SE-751 20 Uppsala, Sweden, [c]Division of Synchrotron Radiation Research, Department of Physics, Lund University, PO Box 118, 221 00 Lund, Sweden, and [d]Lawrence Berkeley National Laboratory, 1 Cyclotron Road, Berkeley, CA 94720, USA.
*Correspondence e-mail: samuli.urpelainen@maxiv.lu.se

SPECIES is an undulator-based soft X-ray beamline that replaced the old I511 beamline at the MAX II storage ring. SPECIES is aimed at high-resolution ambient-pressure X-ray photoelectron spectroscopy (APXPS), near-edge X-ray absorption fine-structure (NEXAFS), X-ray emission spectroscopy (XES) and resonant inelastic X-ray scattering (RIXS) experiments. The beamline has two branches that use a common elliptically polarizing undulator and monochromator. The beam is switched between the two branches by changing the focusing optics after the monochromator. Both branches have separate exit slits, refocusing optics and dedicated permanent endstations. This allows very fast switching between two types of experiments and offers a unique combination of the surface-sensitive XPS and bulk-sensitive RIXS techniques both in UHV and at elevated ambient-pressure conditions on a single beamline. Another unique property of the beamline is that it reaches energies down to approximately 27 eV, which is not obtainable on other current APXPS beamlines. This allows, for instance, valence band studies under ambient-pressure conditions. In this article the main properties and performance of the beamline are presented, together with selected showcase experiments performed on the new setup.

1. Introduction

Beamline I511 on the MAX II storage ring of the MAX IV Laboratory (formerly MAX-lab), which was decommissioned in 2013, combined successfully two types of spectroscopies: X-ray photoelectron spectroscopy (XPS) under ultrahigh-vacuum (UHV) conditions and resonant inelastic X-ray scattering (RIXS) (Denecke *et al.*, 1999). The beamline was based on the proven SX-700 monochromator design, and had a spherical focusing mirror that allowed a balance between high photon energy resolution and high flux (Reininger & Saile, 1990). Owing to the inclined exit beam of the monochromator the experimental stations were placed at a height of more than 2 m above the experimental hall floor. Switching between the two spectroscopy branches was achieved by an additional switching mirror, causing additional reflection losses in the beam intensity. During the last years of operation, changes in the beamline instrumentation set new demands for the beamline: the existing refocusing optics, and especially the

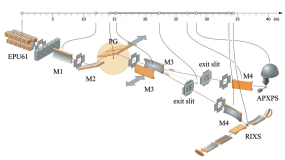

fairly short exit arm for the photoemission branch, were not compatible with the new instrument designed for near ambient-pressure photoelectron spectroscopy (Schnadt *et al.*, 2012). In addition, placing the instrument on an elevated platform resulted in a less stable system compared with a floor-mounted one. On the RIXS branch the development of new spectrometers required a small vertical spot, three to four times smaller than that provided by I511, to take advantage of the new optical designs. The SPECIES beamline was designed to meet the new requirements set by the instrumentation, while still relying on the same experimental techniques, RIXS and XPS; for the latter, the main interest was shifted towards ambient-pressure X-ray photoelectron spectroscopy, APXPS, at pressures up to a few tens of millibars.

The optical design of the beamline is based on a collimated plane-grating monochromator (cPGM), following examples given by successful high-resolution spectroscopy beamlines at BESSY II (Follath *et al.*, 1998; Jiang *et al.*, 2004) and SLS (Strocov *et al.*, 2010). This concept allows a horizontal beam after the monochromator at a reasonable height above the floor (about electron beam height in the ring). The additional switching mirror is rendered obsolete as the switching can be performed by side-deflecting focusing mirrors. The refocusing solutions for both branches are designed in such a way that the beam is horizontal at the experiments.

Owing to the increased demand for circularly polarized light, the new beamline has an elliptically polarizing undulator as a source, instead of the old planar undulator. The beamline covers an energy range of approximately 27–1500 eV with variable polarization. Even when installed at the aging MAX II storage ring, the conditions for spectroscopy studies were good, especially at low photon energies. Further improvements are expected after the move to the MAX IV Laboratory.

In this paper we outline the main properties and performance of the beamline as characterized during operation at the MAX II storage ring. We will also discuss the experimental possibilities and present a few showcases of experiments which have been performed on the new beamline. Future plans and upgrades after installation at the 1.5 GeV electron storage ring at the MAX IV Laboratory are highlighted.

2. Beamline overview

2.1. Source and common optics

The source for the SPECIES beamline is an elliptically polarizing undulator of APPLE-II type (Sasaki *et al.*, 1993) manufactured in-house. The insertion device is called EPU61 and it has 41.5 periods and a period length of 61 mm. It has a frame made of cast iron and the magnets are glued together in pairs in order to minimize the mechanical deformation of the frame and magnet holders during phase shifts. The maximum radiated power is ~720 W at MAX II storage ring. The estimated maximum flux into the beamline is $\sim 10^{15}$ photons s^{-1} into a 0.1% bandwidth. The insertion device was tuned and characterized in a magnetic bench prior to installation at the MAX II storage ring, where the vacuum chamber is 15 mm thick and the minimum gap restricted to 16.5 mm. The RMS phase error for the planar and vertical modes of operation are less than 2.2° over the full gap range 14–200 mm. The EPU61 undulator will be characterized at the new magnetic measurement laboratory prior to installation at the MAX IV Laboratory 1.5 GeV storage ring. In addition, two corrector magnets will be fabricated and installed flanking the undulator to compensate for orbit disturbances due to the changing gap and phase in a feed-forward scheme. The new vacuum chamber has an outer vertical aperture of 12 mm allowing operation over the full gap range.

EPU61 is equipped with passive L-shaped shims of soft magnetic material in order to compensate for the dynamic multipoles that appear in the helical and vertical mode of operation (Chavanne *et al.*, 2000). Commissioning at the MAX II storage ring showed that the device can be operated without disturbing the lifetime of the electron beam too much, except for when very small gaps are used for producing the 45° inclined mode. This is the expected performance of the passive L-shim method, which is unable to compensate fully for the dynamic multipoles in the incline mode of operation. This problem will be addressed at the MAX IV Laboratory by using extra coils in the sextupole magnets flanking the undulator to drive the skew quadrupole field for compensation in a feed-forward scheme.

The beamline utilizes a plane-grating monochromator illuminated with collimated light (cPGM) (Follath *et al.*, 1998) for energy selection. The beamline is split into two branches, one of them dedicated to RIXS and the other to APXPS, by using two different focusing mirrors after the grating and both of the branches have their own exit slits. The main constraints of the geometry of the beamline are imposed by the available space at the old MAX II storage ring and the requirements by the RIXS branch, in which both a good photon energy resolution and a small spot are required. The layout of the beamline is presented in Fig. 1.

The monochromator houses two blazed gratings: an Au-coated one with a ruling density of 1221 lines mm^{-1} and a Ni-coated one with a ruling density of 250 lines mm^{-1}. The Ni-coated grating provides a gain in flux with modest resolution in, roughly, the 200–600 eV photon energy region. Both gratings were transferred from the SX-700 monochromator used at the old I511 beamline as there were no manufacturers for blazed gratings during the procurement phase of this beamline. The Au grating was cleaned from carbon contaminations using UV light-generated ozone under ambient conditions prior to installation. The pre-mirror in the monochromator is internally cooled. In fact, side-cooling would have been sufficient at the MAX II storage ring, but since the beamline was designed to be transferred to the 1.5 GeV ring at the MAX IV Laboratory, and will be subjected to a much higher heat load there, an internal cooling scheme was chosen. All the beamline components were built by FMB Berlin except for the gas absorption cell which was made in-house and based on that designed at Paul Scherrer Institute (Schmitt, 2013).

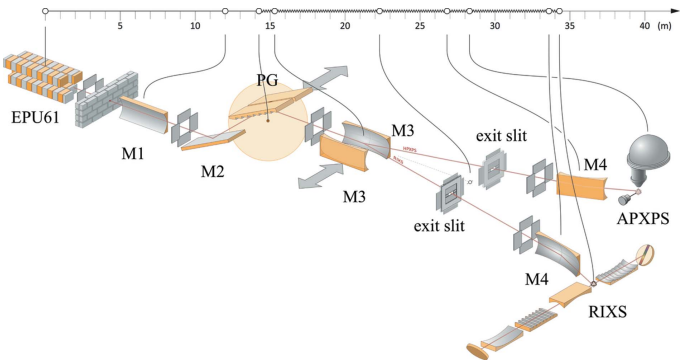

Figure 1
Beamline layout of the SPECIES beamline (courtesy of Johnny Kvistholm). The first mirror (M1) is cylindrical, collimating the beam vertically, whereas both the focusing mirrors (M3) and the refocusing mirror (M4) for the APXPS branch are toroidal. The refocusing mirror (M4) of the RIXS branch is ellipsoidal (rotational ellipse).

For high-resolution cPGM beamlines a stigmatic focusing onto the exit slit is beneficial [for details see, for example, the discussion by Strocov *et al.* (2010)]. Actually, using the first mirror for horizontal focusing results in the highest limit for resolution but at the same time the demagnification to the exit slit is reduced, resulting in a larger spot at the RIXS instrument. Therefore, the focusing mirror also provides the horizontal focusing in the case of the RIXS branch. A stigmatic focus at the RIXS exit slit allows a single, ellipsoidal refocusing mirror to be used for that branch. The photon energy resolution requirement for the APXPS branch is not so stringent and, in addition, the refocusing mirror is toroidal and thus does not require a stigmatic image at the exit slit either. The refocusing stages and their properties are described in more detail below.

2.2. Refocusing stages

The needs set by the APXPS and RIXS experiments are very different: for RIXS a small, high photon density spot is desired whereas for the APXPS the area accepted by the spectrometer aperture should preferably be nearly completely illuminated to reduce the sample damage by radiation. The spectrometers at both branches are preferably mounted horizontally. This facilitates easier alignment of the instruments and simpler sample manipulator design. These requirements exclude conventional Kirkpatrick–Baez pairs based on plane elliptical mirrors, which can be obtained in high quality. The simplest solution for providing a horizontal, focused beam is to use side-deflecting toroidal, or ellipsoidal, mirrors. This solution also reduces the reflection losses compared with a solution based on a Kirkpatrick–Baez pair.

An ellipsoidal mirror was chosen for the RIXS branch, although at very low photon energies the image at the focal plane shows a hint of bow-tie shape: the ray-tracing simulations showed that this does not compromise the energy resolution of the spectrometer. With slope errors of 0.9 and 2.9 arcsec (tangential and sagittal, respectively) the image remains below the required value even when large exit slit openings are used. The benefit of the side-deflecting refocusing mirror is evident: for vertical imaging there is a forgiveness factor of $\sin(2^\circ)$ (Cash, 1987), and the sagittal slope error has a negligible contribution to the vertical image size. Most of the refocusing mirrors for the MAX IV Laboratory soft X-ray beamlines are also ellipsoidal, based on the same argument.

The requirement of a constant spot size at the APXPS branch, independent of photon energy or exit slit opening, demands a more unconventional optical configuration. It can be met by defocusing and controlling the beam waist at the sample location by monochromator magnification (Grizolli *et al.*, 2013). One way of realising this would be by decoupling horizontal and vertical focusing using a Kirkpatrick–Baez pair using an adaptive mirror for vertical focusing. This would compensate for the changes in the object size due to different exit slit openings. However, it is also possible to align the toroidal mirror in such a way that the horizontal focus is at the sample while the vertical focus is some tens of millimeters further downstream (astigmatic focusing). By doing so the vertical beam size becomes more dependent on the divergence of the source rather than its size. In the case of a cPGM monochromator, the vertical divergence at the exit slit plane can easily be controlled by the monochromator settings. This solution allows a single, non-adaptive refocusing mirror, yet providing close-to-constant (vertical) image size at the sample plane independent of the exit slit opening or photon energy. The principle of astigmatic focusing was also tested during the commissioning, and the vertical beam size at the sample was found to be constant, and very close to the expected 100 µm (FWHM).

2.3. Beamline control

SPECIES, being the first beamline to use the standard MAX IV control system, served also as a prototype platform for developing and setting the soft X-ray beamline motion control standard at the MAX IV Laboratory. Here we give a brief description of the control system. A more detailed discussion can be found by Sjöblom *et al.* (2016).

The SPECIES beamline has 56 motorized axes on the beamline and 22 axes on the endstations. The 56 beamline axes were integrated into the control system at the MAX II storage ring, and the remaining 22 axes will be integrated at the new MAX IV Laboratory. The standard motion controller used at

the MAX IV Laboratory is the IcePAP motion controller (Janvier *et al.*, 2013) developed at the ESRF. It controls all of the axes in one system. All motorized axes, except that of the monochromator, are run by stepper motors and the motion is monitored by a set of linear absolute and incremental encoders.

The control system is built in Tango (TANGO, 2015) and uses a Python-based Sardana framework (Coutinho *et al.*, 2011) to communicate with the IcePAP controllers. At the MAX II storage ring, scans and data acquisitions, as well as other functionalities, were run through a set of Taurus GUIs using Sardana, while a graphical synoptic GUI on top of Sardana and Taurus was developed to be used at the MAX IV Laboratory.

The SPECIES monochromator uses Heidenhain RON905UHV angular incremental encoders for the mirror and the grating. Each encoder has four individual analog encoder heads mounted at 90° angle with respect to each other. To process the signals, two IK220 counter cards are installed into two PCs, as one card takes signals from two encoder heads. The analog encoder heads create small built-in cyclic errors. As the heads move across one encoder line two sine-shaped 10 μA_{pp} analog currents phase shifted by $\pi/2$ are produced. The errors are visible when the currents are plotted against each other. Instead of a perfect circle, the graph is a tilting ellipse with an offset from the origin. As the analog input to the IK220 cards has a cyclic error, the ADC encoder output also has a cyclic error as shown in Fig. 2, where the encoder output is not a perfect sawtooth form. Ideally the DAQ output should increase from 0 to 4096 in a linear fashion and then roll over as the motion progresses. Instead of linear, each sawtooth possesses the same wave-like deviation from a straight line. As a result the same DAQ value from each sawtooth needs the same compensation regardless of the photon energy. As each encoder has four individual encoder heads, the error could, to some extent, be averaged out in software by the PC. However, it is not currently possible to send the corrected encoder value back to IcePAP. Instead, analog signals from one of the four encoder heads are forwarded from the IK220 card to an EXE 660B interpolation and digitizer unit.

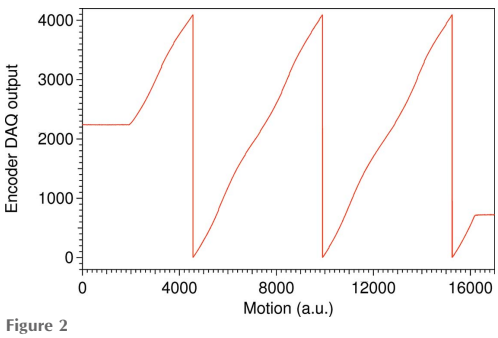

Figure 2
The sinusoidal cyclic error in the sawtooth form of the encoder output that indicates a need of the Heydemann compensation. As the motion progresses, the encoder DAQ should give a linear output from 0 to 4096 and then roll over to create a sawtooth pattern. Instead of a perfectly linear form, there is a periodical error that repeats itself for every sawtooth visible in the plot for one encoder head. Each individual encoder head has its own unique pattern. As a consequence, each DAQ value needs a small correction. As the encoder DAQ is a measure of the mirror and grating pitch angles, and hence the photon energy, it is the energy scale that needs stretching and compressing in the form of Heydemann compensation to correct for the errors.

The EXE 660B produces 400 TTL SSI encoder pulses in every period of analog input signal and these are then forwarded to the IcePAP units. In this setup the encoder errors are fed into IcePAP. The solution to the cyclic error is a Heydemann correction (Heydemann, 1981; Follath & Balzer, 2010) in the Sardana layer. With help of the Heydemann compensation the cyclic error is mapped and the angle output is corrected. Also, when a motion request is sent, the target position is corrected. In the end, the cyclic encoder errors correspond to an energy deviation, and in the 398–402 eV span the maximum error was determined to be approximately 47 meV. The result of introducing the Heydemann correction is shown in Fig. 3, where an N_2 absorption scan is shown with and without applied correction. The spacing between the adjacent peaks ranges from approximately 236 to 208 meV after the compensation. This is in good agreement with previous studies [see, for example, Chen & Sette (1989)].

For the majority of the axes, including those of the monochromator, the IcePAP drivers operate in hardware position closed loops, which make the motors compensate any deviation from a defined position read by the corresponding encoder. In the case of the monochromator, additional care is taken to overcome the non-linear relationship between the angular encoder and the stepper motor operating a sine bar, as the movements otherwise may be slow and inaccurate. During commissioning, measurements showed a resolution of 0.5 µrad for the mirror and 0.3 µrad for the grating pitch motions. The smallest resolvable one-step movement in closed loop, including the settling time, takes 0.1 s for the mirror and the grating.

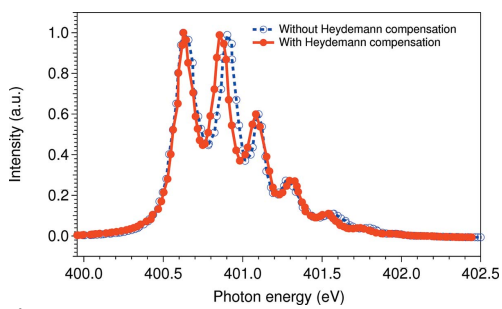

Figure 3
Ion yield spectrum at the N 1*s* absorption edge in N_2. The blue dashed line shows the measured spectrum without the applied software compensation and the red solid line shows the Heydemann compensated spectrum. The spacing between observed adjacent vibrational levels varies between approximately 236 and 208 meV after compensation.

Table 1
Beamline details.

The beam size is given as a full with at half-maximum value.

Beamline name	SPECIES
Source type	EPU61
Mirrors	Au-coated
Monochromator	cPGM
Energy range (keV)	0.03–1.5
Wavelength range (Å)	470–8.3
Beam size (µm)	5 × 25 (RIXS) and 100 × 100 (HP-XPS)
Flux (photons s^{-1})	1×10^{13}–1×10^{11}, $R = 10000$

3. Ancillary facilities

The ancillary facilities at the old MAX II storage ring consisted of a room dedicated to sample mounting and UHV equipment preparation and a basic chemistry laboratory for sample preparation. The new MAX IV Laboratory also provides such facilities and chemistry laboratory spaces as well as some storage space for smaller user equipment.

4. Facility access

The SPECIES beamline is expected to be operational again during late 2017. The beamline will be accessible to non-proprietary users by submitting an application in connection to a call for beam time applications. The applications will be peer-reviewed and beam time will be allocated based on the scientific merits and feasibility of the proposed experiments by the program advisory committee. The beamline is also in a limited fashion accessible to proprietary research.

5. Highlights

5.1. Beamline performance

The beamline was built using a laser tracker coordinate system, which relies on fixed target nests around the beamline location. The initial alignment using this coordinate system gave a good starting point for alignment with light, and with small tuning the first mirror of the beamline was brought onto the axis of undulator radiation.

The commissioning measurements and experiments performed at the SPECIES beamline show that the photon flux at experiments is very close to calculated values (*cf.* Table 1). A flux measurement performed using an IRD AXUV100 photodiode located after the APXPS branch exit slit is presented in Fig. 4. The flux curve was measured into a very small angular opening of approximately 0.04 mrad × 0.04 mrad controlled by a beam-defining aperture after the collimating mirror. The exit slit opening was controlled throughout the scanning in order to keep the bandwidth at 0.1%.

The photon energy resolution of the beamline was measured by studying the absorption spectra of N_2 molecules recorded with a gas cell. The ion yield spectrum at the N_2 $1s \rightarrow \pi_g^*$ excitation region is shown in Fig. 5. Due to the relatively large lifetime broadening of the excited state, the

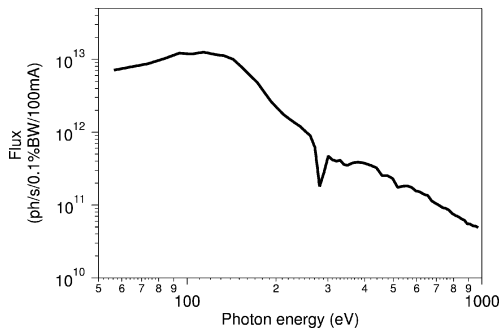

Figure 4
Measured flux after the exit slit on the APXPS branch. The flux curves were measured with a beam-defining aperture (after the collimating mirror) opening of 0.5 mm × 0.5 mm corresponding to approximately 0.04 mrad × 0.04 mrad.

evaluation of the photon energy resolution is difficult by direct deconvolution. A least-squares fit gives a Lorentzian width of 120 meV and a Gaussian width of 50 meV, which corresponds to a resolving power of $R = 8000$. However, using the method presented by Chen & Sette (1989), the instrumental broadening can also be estimated more reliably by calculating the ratio between the intensities of the first valley in the spectrum and the third peak. The ratio determined here gives, according to Chen & Sette (1989), a Gaussian broadening of ∼30–40 meV, or better, resulting in a resolving power $R > 10000$. We therefore conclude that the monochromator reaches the design criteria of reaching a resolving power of 10000.

The energy scale of the monochromator was calibrated using the method that has been succesfully used at BESSY for calibrating plane-grating monochromators (Weiss *et al.*, 2001). For this the same N_2 absorption spectrum as for the resolving power determination was recorded for different fixed focus

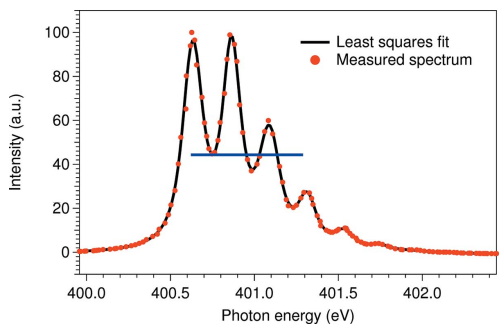

Figure 5
Ion yield spectrum at the N 1*s* absorption edge in N_2. The blue line is to emphasize the first valley and the third vibrational peak: this ratio reflects the experimental resolution. The black curve shows the result of the least-squares fit with a Lorentzian width of 120 meV and a Gaussian width of 50 meV.

constants of the monochromator. Using this method the energy of the first peak of the resonance has been determined to be 400.63 eV. At the same time the relative energy shifts have been observed to be smaller than 10^{-4}.

The effect of using astigmatic focusing at the APXPS branch was studied during commissioning by recording the images of the synchrotron radiation beam spot on a Ce:YAG crystal mounted onto a sample plate using adhesive carbon tape. The images are presented in Fig. 6. The images were captured at the photon energy of 250 eV at two significantly different slit sizes of 50 µm and 500 µm. In order not to saturate the image, the beam intensity was kept approximately constant (monitored by a drain current measurement from the refocusing mirror) by attenuating it with a 200 nm-thick Al window, when using the 500 µm exit slit opening. In the case of stigmatic focus the beam size should be ten times larger at the larger slit conditions, but the images show that the beam size is only marginally affected by the exit slit opening. This indicates that the astigmatic focusing scheme can indeed be used to make the beam size independent of the exit slit opening at the sample position. Furthermore, the images show that the beam sizes match well with the expected 100 µm (FWHM).

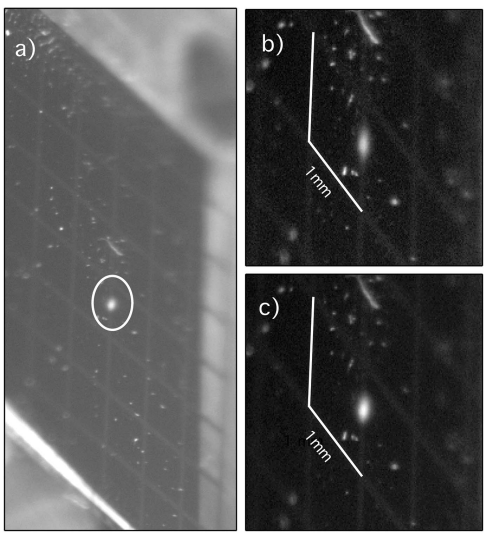

Figure 6
Spot at the APXPS endstation sample position captured at a photon energy of 250 eV. Panel (*a*) shows the Ce:YAG crystal mounted with adhesive carbon tape on a sample holder of the APXPS system. The beam spot is circled. Panels (*b*) and (*c*) show the beam spot at the photon energy of 250 eV and $c_{ff} = 2.25$ for exit slit openings of 500 µm and 50 µm, respectively. The intensity of the photon beam was attenuated by a 200 nm-thick Al window for recording the spot size with the larger slit opening in order to keep the saturation of the YAG crystal at minimum and to be able to compare the spot sizes. The white lines in panels (*b*) and (*c*) show the dimensions of the image (1 mm).

At MAX IV 1.5 GeV storage ring the horizontal spot size and maximum photon energy resolution of the beamline will improve compared with values reached at MAX II storage ring. This follows from the horizontal and vertical source sizes being approximately 50% and 30% smaller, respectively, at the new storage ring. The quality of the optical components was specified in such a way that their effect remains negligible also at the new storage ring. For resolving powers beyond the target value, which might otherwise be achievable, the slope errors of the old grating start to limit the performance.

5.2. RIXS endstation

The RIXS endstation has two grating spectrometers for RIXS measurements. Together these cover the energy range from 27 to 1500 eV. The two spectrometers are mounted horizontally, facing each other, perpendicular to the photon beam (see Fig. 1). The low-energy region of the beamline, 27–200 eV, is covered by a plane-grating spectrometer, PGS (Agåker *et al.*, 2009), whereas a modified grazing-incidence Rowland circle spherical-grating spectrometer, GRACE (Nordgren *et al.*, 1989), covers the energy range 50–1500 eV. In addition to the two spectrometers, a retractable detector for NEXAFS measurements is also available at the endstation.

Both of the RIXS instruments take advantage of the small vertical beam size at the focal plane, imaging the beam spot directly onto the detector without any entrance slits. They are both equipped with multichannel plate delay line detectors which makes it possible to synchronize the detectors to the synchrotron bunch structure. This allows a gating scheme to be implemented, increasing the signal-to-noise level as the synchrotron radiation repetition rate is relatively low compared with the detection time which is in the nanosecond range. To further increase the efficiency of the detectors the front plate is enhanced for UV and X-rays by a coating with a high photo-yield material, such as caesium iodide.

The resolving power of the PGS instrument, $R \simeq 7500$ at 75 eV, matches very well with the achievable resolving power of the beamline ($R > 10000$). The performance of this instrument was tested at BESSY II during a number of commission beam times before being moved to MAX IV Laboratory. The use of a collimating mirror before the grating gives a relatively high acceptance angle, 5000 mrad^2, resulting in reasonable counting rates even with high resolution and the increased number of reflections. The modified GRACE instrument was initially designed much more for covering a wide photon energy range with reasonable resolution (R few thousands) and acceptance (around 1000 mrad^2), but it has been shown to be a very versatile tool for RIXS experiments at synchrotron radiation sources (Kuusik *et al.*, 2013; Magnuson *et al.*, 2012; Nilsson *et al.*, 2010), including free-electron lasers (Kunnus *et al.*, 2012).

The spectrometers at the RIXS station are mounted on a custom chamber, designed for measurements on samples ranging from solids to liquids and the gas phase. The chamber is pumped by two turbomolecular pumps mounted beneath

the experimental region. The design also includes a very compact valve structure, where both vacuum and filter valves are co-located between the instruments and the experimental volume, enabling a separation of the vacuum in the spectrometers and the experimental chamber to protect the optics from contamination. Each spectrometer has its own turbomolecular pump to keep vacuum while the instrument is separated from the experimental chamber vacuum. There is also a differential pumping stage and the possibility to insert a foil between the refocusing mirror (M4) of the beamline and the experimental chamber for protecting the vacuum while running high-pressure experiments.

A small load-lock chamber, enabling docking and sample transfer from a vacuum suitcase, is mounted on top of the experimental chamber. The samples are moved within the system by using a compact, large bore four-axis manipulator designed to hold custom sample rods. The motorization of the manipulator enables sample scanning to avoid radiation damage. The scanning function can also be used for spectral raster imaging. The manipulator rod can be fully extracted from the experimental chamber, into the load lock, while a valve can close the passage between the two chambers. This allows for rapid change of the samples or extraction and replacement of the manipulator rod without breaking the vacuum in the main chamber.

5.3. APXPS endstation

The APXPS endstation is described in detail elsewhere (Schnadt *et al.*, 2012; Knudsen *et al.*, 2016) and is discussed here only briefly. The endstation is dedicated to *in situ* and *operando* studies of the solid–vapor and liquid–vapor interfaces under ambient-pressure conditions using XPS and NEXAFS using partial and total electron yield detection. Although equipped for ambient (in this context up to a few tens of mbars) pressure studies, conventional UHV studies of surfaces are also possible due to the special dockable and retractable ambient pressure (AP) cell. This allows the users to change between high pressure and UHV studies in a matter of minutes without breaking the vacuum, making it possible to prepare and characterize the surface *in situ* before performing the ambient-pressure experiments. In addition, the AP cell itself can be changed relatively easily allowing studies in different sample environments that might require different configurations in terms of, for example, cell materials, cell volumes and sample geometries. Also user modified and specialized cells are possible to mount on the system. This makes the setup extremely versatile and facilitates studies within several disciplines such as catalysis, electrochemistry, corrosion, solar cells, fuel cells as well as liquid, biological and geological samples.

The endstation is equipped with a SPECS PHOIBOS 150 NAP electron energy analyzer. The analyzer features a special head of the electrostatic lens system, on which the AP cell can be docked using a bayonet-like coupling mechanism. The analyzer can be operated in various magnifications, angular dispersion, transmission and acceleration modes optimized for various conditions such as different spot sizes on the sample. To be able to operate at ambient pressure, a pre-stage of differential pumping is necessary between the analyzer and the sample environment. Towards the differential pumping system a small aperture limits the gas flow and different aperture sizes can be used to reach different maximum pressures. Presently, the smallest aperture applied here has a diameter of 300 µm and allows pressures up to roughly 5–10 mbar without compromising the UHV at the electron detector, but in the future it can be replaced by even smaller apertures further increasing the high-pressure limit.

This small aperture, however, limits the maximum geometric acceptance of the spectrometer for the incoming electrons. To take full advantage of the incoming photons, the spot size in the sample plane must match this geometric acceptance. In the case of the 300 µm aperture, an optimum detection efficiency is achieved with a photon spot size of about 100 µm × 100 µm (FWHM) at the sample.

The light is let into the AP cell through a thin Si_3N_4(200 nm)/Al(100 nm) membrane that provides pressure isolation. However, the transmission of this type of window is reasonable only above approximately 250 eV photon energy, and, in order to facilitate the use of the low energies achievable by the SPECIES beamline, pure Al (thickness 200 nm) windows purchased from Luxel are also available. These give reasonable transmission of approximately 60% from 30 to 70 eV, allowing the studies of the valence bands under ambient-pressure conditions in addition to the core-level spectroscopies. Upstream of the endstation a so-called beam stopper ion pump (manufactured by XIA Inc.) is used, allowing five orders of magnitude higher pressure at the inlet side (experiment) compared with the outlet side. The beam stopper pump together with a turbomolecular pump after the endstation allow experiments with low 10^{-4} mbar pressure in the main chamber of the spectrometer without compromising UHV conditions of the beamline. This concept has been used previously on several beamlines at the MAX IV Laboratory (and MAX-lab) with good results (Aksela *et al.*, 1994; Bässler *et al.*, 2001; Urpelainen *et al.*, 2010; Schnadt *et al.*, 2012).

The reaction cell gas composition is controlled through a gas manifold system equipped with mass flow controllers, which allow fast switching of gases. The inlet and outlet lines of the reaction cell are connected to a quadrupole mass spectrometer (QMS), which allows monitoring the reactants and the reaction products *in situ* as a function of time simultaneously with the XPS measurements. By connecting the time stamps of the mass spectra and the X-ray photoelectron spectra, the gas composition measured with the QMS can be correlated to changes on the surface chemistry observed using APXPS.

Another new development at the endstation is a centralized backing pump setup. The SPECIES APXPS setup operates 12 permanent turbomolecular pumps. The system is divided into two groups of 5 and 7 turbomolecular pumps. The group of 5 pumps experiences a heavy gas load, while the other group has to cope with a low, UHV-typical, load of gas only. Both groups of pumps are backed by two centralized backing pump

systems, each pumped by an ACP 40 multi-stage roots pumps. When UHV conditions are reached, the backing pressure requirements are not extremely stringent and a large backing volume can be used instead of continuous pumping in order to maintain the UHV pressures. This allows the operation of the whole setup with only two backing pumps which can be disconnected for maintenance or replacement, while the turbomolecular pumps on the system are still running. This makes the maintenance of the system cost efficient and reduces the amount of down time significantly. The backing system is controlled by the standard PLC system of MAX IV Laboratory.

The setup includes standard sample preparation and characterization tools such as an electron beam heater for annealing, an ion gun for Ar^+ sputtering and a low-energy electron diffraction (LEED) setup for surface structure characterization. The system contains a fast-access load lock, a sample preparation chamber and an analysis chamber, which have independent vacuum systems separated by manual gate valves. This allows for sample preparation at high temperatures and varying the gas atmosphere without compromising the UHV conditions of the analysis chamber. Furthermore, the analyzer and reaction cell vacuums can be isolated from the analysis chamber. The load lock can be vented, loaded and evacuated within approximately half an hour, which facilitates fast sample transfers. In addition, the analysis chamber hosts a sample 'garage', which can hold up to three samples simultaneously for fast switching between samples during measurements both on the UHV manipulator and in the reaction cell.

Other equipment available at the endstation includes equipment (electrospray setups, evaporators *etc.*) for depositing atoms, molecules and clusters on the surfaces, and equipment (light source, optical fiber *etc.*) for photocatalysis experiments. In addition to the synchrotron, an X-ray source with Al and Mg K_α anodes is mounted on the system for offline studies of samples when the RIXS branch is operating and during ring shutdown periods.

Before being installed at MAX IV Laboratory the endstation will be upgraded. The planned upgrades include the construction of a new improved flow cell with a gas flow that is focused onto the target position, a cell and a gas manifold for sulfur-containing and corrosive gases, an electrochemical cell, and the upgrade of the pre-lens of the electron energy analyzer allowing easier and more reliable docking of the reaction cell as well as improved transmission and resolution of the electron analyzer. As a future alternative, the analyzer could be further upgraded to allow imaging measurements.

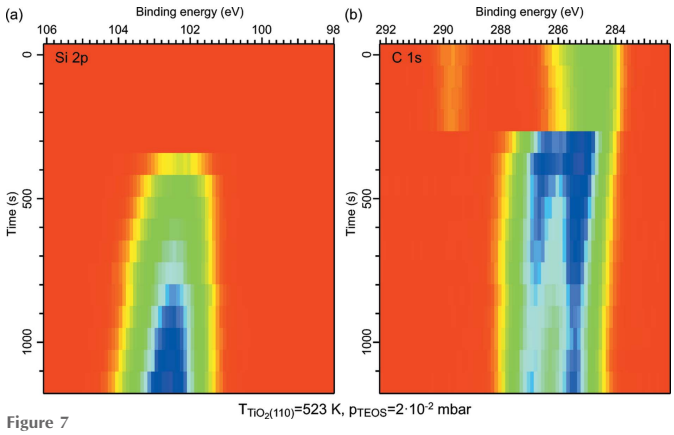

Figure 7
(*a*) Si 2*p* and (*b*) C 1*s* XP spectra series recorded during the exposure of a rutile TiO_2(110) single-crystal held at 523 K to 2×10^{-2} mbar of TEOS. The spectra were measured alternately, and the time stamp is that of the start of the Si 2*p* measurement followed by that of the C 1*s* region. The intensity scale is: blue, high; red, low. The TEOS valve was opened during the initial scans, and the pressure reached the final pressure of 2×10^{-2} mbar after around 300 to 400 s, *i.e.* at the same time as the TEOS Si 2*p* and C 1*s* signals appear. The initial C 1*s* intensity is due to residual gas adsorption. The overall decreasing intensity in the C 1*s* spectra is due to the movement of the sample to avoid beam damage. The Si 2*p* spectra were corrected for this intensity loss, but not the C 1*s* spectra due to problems in the data analysis.

5.4. Atomic layer deposition of SiO_2 on TiO_2(110)

As one example of research carried out at the APXPS endstation of the SPECIES beamline we briefly present some results obtained on the atomic layer deposition (ALD) of SiO_2 on TiO_2(110). ALD is a major technique for the controlled deposition of thin films (Miikkulainen *et al.*, 2013), which builds on the alternating exposure of a substrate to two different precursors. For instance, for the growth of ultrathin oxide layers, metal precursor and oxygen sources are used. In the ideal ALD case, a step-by-step growth is achieved since the adsorption of the precursors on the substrate is self-limited to a single adsorbate layer. This layer can then react with the other precursor.

Although many different ALD processes have been invented, surprisingly little beyond idealized schemes is known about the surface chemistry which takes place during growth and which is decisive for the final film quality. *In situ* techniques applied during growth, *e.g.* APXPS, have the potential to deliver valuable information on this point and thus to help to improve ALD precursors and processes.

For the very first ALD half-cycle of SiO_2 growth on TiO_2(110) from tetraethyl orthosilicate [TEOS, $Si(OC_2H_5O)_4$] and water, *i.e.* for the first exposure of the TiO_2 surface to TEOS at a pressure of 2×10^{-2} mbar, we show the evolution of the Si 2*p* and C 1*s* core levels in Fig. 7 (for details, see figure caption). Clearly visible is the initial appearance of Si 2*p* (102.29 eV), methyl C 1*s* (285.20 eV) and oxygen-bonded carbon C 1*s* (286.37 eV) features due to the adsorption of TEOS on the surface. During TEOS exposure all core levels

shift to higher energy: the Si 2*p* and methyl C 1*s* peaks move to 0.29 eV higher binding energy, and the oxygen-bonded carbon C 1*s* peak shifts by +0.57 eV. In addition, the intensity ratio of the carbon peaks changes slightly. While the overall shift might be due to general band bending, the observation of a deviating shift of the oxygen-bonded carbon peak together with a change of the C 1*s* peak intensity ratio points to the observation of a chemical reaction on the surface. Most likely, ethoxy ligands are split off and bind directly to the surface in a reaction which is unforeseen in the idealized scheme (*cf.* Chaudhary *et al.*, 2015).

In this example each spectrum, taken in swept mode, required 38 s to be completed. Much improved time resolution even down to the millisecond timescale is possible when the electron energy analyzer is used in snapshot rather than in swept mode. For many surface reactions the attainable time resolution is sufficient to allow following of reaction kinetics and measurement of reaction constants, and APXPS therefore renders possible a field of activity which can deliver information on the evolution of surface (and, actually, gas phase) species in direct combination with kinetic data.

5.5. APXPS study of CO oxidation on Ag(100)-supported CO oxide films

Cobalt oxide nanomaterials have attracted attention because of their application potential in the fields of heterogeneous catalysis (Chen *et al.*, 2015; Xie *et al.*, 2009; Fei *et al.*, 2012). In this example we have studied the CO oxidation reaction on Ag(100)-supported Co oxide films using the APXPS setup at the SPECIES beamline.

The starting point in the present example is a CoO(100) film grown on Ag(100). The Co 2*p* spectrum shown at the bottom of Fig. 8(*a*) was recorded under UHV conditions and the shake-up peaks (highlighted with blue arrows) seen at the high binding energy side of the Co $2p_{3/2}$ and Co $2p_{1/2}$ peaks are the fingerprint of the CoO rocksalt phase. In the corresponding C 1*s* spectrum [Fig. 8(*b*)] no carbon-containing species are observed.

Exposing the CoO(100) film to a reaction mixture of a 1:2 mixture of $CO:O_2$ at a total pressure of 1.2 mbar while heating we observe that the Co 2*p* shake-up peaks signaling the CoO rocksalt structure gradually disappears upon heating to 400 K [see Fig. 8(*a*)], due to conversion to a spinel Co_3O_4(100) film. In the corresponding C 1*s* spectrum recorded at 300 K we observe two peaks located at 288.7 eV and 291.2 eV assigned to carbonates (Ferstl *et al.*, 2015) and gas-phase CO molecules, respectively. The intensity of the carbonate component first increases upon heating and reaches a maximum at a temperature of 350 K. At higher temperature the intensity of the carbonate component decreases and at 500 K no carbonates are left on the surface. Upon the film conversion from CoO to Co_3O_4, which takes place at a temperature between 300 K and 400 K, the CO(g) component shifts to 290.8 eV, which indicates a work function shift between the CoO(100) and Co_3O_4(100) surfaces of 0.5 eV, as the binding energies of gas-phase molecules are pinned to the vacuum level which is determined by the surface work function.

Finally, in the C 1*s* spectrum recorded at temperatures of 500 and 550 K we observe a CO_2 gas-phase component at a position of 292.4 eV. Production of CO_2 in the gas phase is also visible in the QMS signal recorded simultaneously both at this temperature and lower temperature, which suggests that the Co_3O_4(100) phase is catalytically active. Unfortunately, we also observed CO_2 production in a reference experiment in which a clean Ag(100) crystal was exposed to an identical gas mixture and heating rate and we are, therefore, unable to correlate the observed CO_2 production to the appearance of the Co_3O_4(100) phase. One tentative explanation for the observed CO_2 production on the clean Ag(100) crystal could be remaining Co oxide on the sample plate left after sputtering.

To conclude, we have shown that Ag(100)-supported CoO(100) thin film is easily converted to Co_3O_4(100) in a 1:2 mixture of $CO:O_2$ at a total pressure of 1.2 mbar. We observed CO_2 production both with APXPS directly above the surface and in the QMS attached to the exhaust gas from the cell. It remains, however, unclear whether the observed CO_2 formation is formed on the Co_3O_4(100) surface or at other hot parts inside the AP cell (Nguyen & Tao, 2016). A final but very important take-home message from our study is, therefore, that reference experiments are essential for correlating

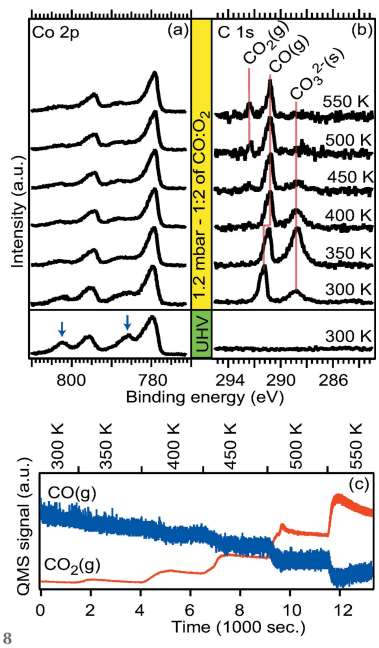

Figure 8
(*a*) Co 2*p* spectra of Ag(100)-supported CoO(100) acquired in UHV at room temperature (bottom) and in 1.2 mbar of a 1:2 $CO:O_2$ mixture at stepwise increasing temperature. (*b*) C 1*s* spectra corresponding to the Co 2*p* spectra shown in panel (*a*). (*c*) CO and CO_2 signals in the exhaust gas from the cell recorded with quadrupole mass spectrometry.

observed reactivity to changes on the sample surface. Furthermore, there is a clear need for improved reactivity cells with more localized heating, so that other reactive surfaces near the single-crystal remain cold when the single-crystal is heated. The MAX IV Laboratory is currently developing such cells for their future APXPS endstations.

6. Summary

The SPECIES beamline offers a platform for electron spectroscopy experiments in UHV and ambient-pressure conditions. The second branch is dedicated to resonant inelastic scattering experiments. This unique combination of these two complementary techniques allows the electronic structure of matter to be studied, both at surfaces and in bulk, and both in UHV and at elevated pressures. Furthermore, the beamline reaches low photon energies suitable for valence band studies, not available at other existing APXPS beamlines at other synchrotron radiation facilities. We have shown that the beamline meets the design parameters very well and performs as expected. The beamline is currently being built up at the 1.5 GeV ring at the MAX IV Laboratory, where it is expected to be operational and opened for regular users in early 2018.

Acknowledgements

We wish to acknowledge Jean-Jacques Gallet and Fabrice Bournel for participating in the ALD experiments and Indiana Pinsard for the ALD data treatment. We thank the staff (past and present) of the MAX IV Laboratory for all the help and participation in the beamline construction, operation and transfer. This work has been financially supported by the Swedish Research Council (2009-5861) and the Knut and Alice Wallenberg Foundation (KWA).

References

Agåker, M., Andersson, J., Englund, C.-J., Olsson, A., Ström, M. & Nordgren, J. (2009). *Nucl. Instrum. Methods Phys. Res. A*, **601**, 213–219.
Aksela, S., Kivimäki, A., Naves de Brito, A., Sairanen, O.-P., Svensson, S. & Väyrynen, J. (1994). *Rev. Sci. Instrum.* **65**, 831–836.
Bässler, M., Ausmees, A., Jurvansuu, M., Feifel, R., Forsell, J.-O., de Tarso Fonseca, P., Kivimäki, A., Sundin, S., Sorensen, S. L., Nyholm, R., Björneholm, O., Aksela, S. & Svensson, S. (2001). *Nucl. Instrum. Methods Phys. Res. A*, **469**, 382–393.
Cash, W. (1987). *Appl. Opt.* **26**, 2915–2920.
Chaudhary, S., Head, A., Sánchez-de-Armas, R., Tissot, H., Olivieri, G., Bournel, F., Montelius, L., Ye, L., Rochet, F., Gallet, J.-J., Brena, B. & Schnadt, J. (2015). *J. Phys. Chem. C*, **119**, 19149–19161.
Chavanne, J., Elleaume, P., Vaerenbergh, P. V. & Gunzel, T. (2000). *Proceedings of the Seventh European Particle Accelerator Conference (EPAC 2000)*, Vienna, Austria, 26–30 June 2000, pp. 2346–2348.
Chen, C. T. & Sette, F. (1989). *Rev. Sci. Instrum.* **60**, 1616–1621.
Chen, Z., Kronawitter, C. X. & Koel, B. E. (2015). *Phys. Chem. Chem. Phys.* **17**, 29387–29393.
Coutinho, T., Cuni, G., Fernandez-Carreiras, D., Klora, J., Pascual-Izarra, C., Reszela, Z. & Sune, R. (2011). *Proceedings of the 13th International Conference on Accelerator and Large Experimental Physics Control Systems (ICALEPCS2011)*, 10–14 October 2011, Grenoble, France, p. 607.
Denecke, R., Väterlein, P., Bässler, M., Wassdahl, N., Butorin, S., Nilsson, A., Rubensson, J.-E., Nordgren, J., Mårtensson, N. & Nyholm, R. (1999). *J. Electron Spectrosc. Relat. Phenom.* **101–103**, 971–977.
Fei, Z., He, S., Li, L., Ji, W. & Au, C.-T. (2012). *Chem. Commun.* **48**, 853–855.
Ferstl, P., Mehl, S., Arman, M. A., Schuler, M., Toghan, A., Laszlo, B., Lykhach, Y., Brummel, O., Lundgren, E., Knudsen, J., Hammer, L., Schneider, M. A. & Libuda, J. (2015). *J. Phys. Chem. C*, **119**, 16688–16699.
Follath, R. & Balzer, A. (2010). *AIP Conf. Proc.* **1234**, 657–660.
Follath, R., Senf, F. & Gudat, W. (1998). *J. Synchrotron Rad.* **5**, 769–771.
Grizolli, W., Hennies, F., Knudsen, J., Nyholm, R., Sankari, R. & Schnadt, J. (2013). *J. Phys. Conf. Ser.* **425**, 152005.
Heydemann, P. L. M. (1981). *Appl. Opt.* **20**, 3382–3384.
Janvier, N., Clement, J. & Farjado, P. (2013). *Proceedings of the 14th International Conference on Accelerator and Large Experimental Physics Control Systems (ICALEPCS2013)*, 6–11 October 2013, San Francisco, CA, USA. p. 766.
Jiang, Y. H., Püttner, R., Martins, M., Follath, R., Rost, J. M. & Kaindl, G. (2004). *Phys. Rev. A*, **69**, 052703.
Knudsen, J., Andersen, J. N. & Schnadt, J. (2016). *Surf. Sci.* **646**, 160–169.
Kunnus, K., Rajkovic, I., Schreck, S., Quevedo, W., Eckert, S., Beye, M., Suljoti, E., Weniger, C., Kalus, C., Grübel, S., Scholz, M., Nordlund, D., Zhang, W., Hartsock, R. W., Gaffney, K. J., Schlotter, W. F., Turner, J. J., Kennedy, B., Hennies, F., Techert, S., Wernet, P. & Föhlisch, A. (2012). *Rev. Sci. Instrum.* **83**, 123109.
Kuusik, I., Käämbre, T., Kooser, K. & Kikas, A. (2013). *J. Electron Spectrosc. Relat. Phenom.* **188**, 32–37.
Magnuson, M., Andersson, M., Lu, J., Hultman, L. & Jansson, U. (2012). *J. Phys. Condens. Matter*, **24**, 225004.
Miikkulainen, V., Leskelä, M., Ritala, M. & Puurunen, R. (2013). *J. Appl. Phys.* **113**, 021301.
Nguyen, L. & Tao, F. (F). (2016). *Rev. Sci. Instrum.* **87**, 064101.
Nilsson, A., Nordlund, D., Waluyo, I., Huang, N., Ogasawara, H., Kaya, S., Bergmann, U., Näslund, L.-Å., Åström, H., Wernet, P., Andersson, K., Schiros, T. & Pettersson, L. (2010). *J. Electron Spectrosc. Relat. Phenom.* **177**, 99–129.
Nordgren, J., Bray, G., Cramm, S., Nyholm, R., Rubensson, J.-E. & Wassdahl, N. (1989). *Rev. Sci. Instrum.* **60**, 1690–1696.
Reininger, R. & Saile, V. (1990). *Nucl. Instrum. Methods Phys. Res. A*, **288**, 343–348.
Sasaki, S., Kakuno, K., Takada, T., Shimada, T., Yanagida, K. & Miyahara, Y. (1993). *Nucl. Instrum. Methods Phys. Res. A*, **331**, 763–767.
Schmitt, T. (2013). Private communication.
Schnadt, J., Knudsen, J., Andersen, J. N., Siegbahn, H., Pietzsch, A., Hennies, F., Johansson, N., Mårtensson, N., Öhrwall, G., Bahr, S., Mähl, S. & Schaff, O. (2012). *J. Synchrotron Rad.* **19**, 701–704.
Sjöblom, P., Lindberg, M., Forsberg, J., Persson, A. G., Urpelainen, S. & Såthe, C. (2016). *AIP Conf. Proc.* **1741**, 030045.
Strocov, V. N., Schmitt, T., Flechsig, U., Schmidt, T., Imhof, A., Chen, Q., Raabe, J., Betemps, R., Zimoch, D., Krempasky, J., Wang, X., Grioni, M., Piazzalunga, A. & Patthey, L. (2010). *J. Synchrotron Rad.* **17**, 631–643.
TANGO (2015). *TANGO*, http://www.tango-controls.org/.
Urpelainen, S., Huttula, M., Balasubramanian, T., Sankari, R., Kovala, P., Kukk, E., Nõmmiste, E., Aksela, S., Nyholm, R., Aksela, H., Garrett, R., Gentle, I., Nugent, K. & Wilkins, S. (2010). *AIP Conf. Proc.* **1234**, 411–414.
Weiss, M., Follath, R., Sawhney, K. & Zeschke, T. (2001). *Nucl. Instrum. Methods Phys. Res. A*, **467–468**, 482–484.
Xie, X., Li, Y., Liu, Z.-Q., Haruta, M. & Shen, W. (2009). *Nature (London)*, **458**, 746–749.

Printed by Media-Tryck, Lund 2017 NORDIC ECOLABEL, 3041 0903

Faculty of Science
Department of Physics
Division of Synchrotron Radiation Research

ISBN 978-91-7753-437-2 (print)
ISBN 978-91-7753-438-9 (pdf)